



UNIVERSITAT DE
BARCELONA

Development of advanced nuclear magnetic resonance methods for biochemical analysis of biofluids and hyperpolarized magnetic resonance spectroscopic imaging for organ-on-chip

Marc Azagra Rodríguez

ADVERTIMENT. La consulta d'aquesta tesi queda condicionada a l'acceptació de les següents condicions d'ús: La difusió d'aquesta tesi per mitjà del servei TDX (www.tdx.cat) i a través del Dipòsit Digital de la UB (diposit.ub.edu) ha estat autoritzada pels titulars dels drets de propietat intel·lectual únicament per a usos privats emmarcats en activitats d'investigació i docència. No s'autoritza la seva reproducció amb finalitats de lucre ni la seva difusió i posada a disposició des d'un lloc aliè al servei TDX ni al Dipòsit Digital de la UB. No s'autoritza la presentació del seu contingut en una finestra o marc aliè a TDX o al Dipòsit Digital de la UB (framing). Aquesta reserva de drets afecta tant al resum de presentació de la tesi com als seus continguts. En la utilització o cita de parts de la tesi és obligat indicar el nom de la persona autora.

ADVERTENCIA. La consulta de esta tesis queda condicionada a la aceptación de las siguientes condiciones de uso: La difusión de esta tesis por medio del servicio TDR (www.tdx.cat) y a través del Repositorio Digital de la UB (diposit.ub.edu) ha sido autorizada por los titulares de los derechos de propiedad intelectual únicamente para usos privados enmarcados en actividades de investigación y docencia. No se autoriza su reproducción con finalidades de lucro ni su difusión y puesta a disposición desde un sitio ajeno al servicio TDR o al Repositorio Digital de la UB. No se autoriza la presentación de su contenido en una ventana o marco ajeno a TDR o al Repositorio Digital de la UB (framing). Esta reserva de derechos afecta tanto al resumen de presentación de la tesis como a sus contenidos. En la utilización o cita de partes de la tesis es obligado indicar el nombre de la persona autora.

WARNING. On having consulted this thesis you're accepting the following use conditions: Spreading this thesis by the TDX (www.tdx.cat) service and by the UB Digital Repository (diposit.ub.edu) has been authorized by the titular of the intellectual property rights only for private uses placed in investigation and teaching activities. Reproduction with lucrative aims is not authorized nor its spreading and availability from a site foreign to the TDX service or to the UB Digital Repository. Introducing its content in a window or frame foreign to the TDX service or to the UB Digital Repository is not authorized (framing). Those rights affect to the presentation summary of the thesis as well as to its contents. In the using or citation of parts of the thesis it's obliged to indicate the name of the author.

Tesi doctoral

**Development of advanced nuclear
magnetic resonance methods for
biochemical analysis of biofluids and
hyperpolarized magnetic resonance
spectroscopic imaging for
organ-on-chip**

Marc Azagra Rodríguez

Irene Marco Rius

Javier Ramón Azcón



UNIVERSITAT DE
BARCELONA

Development of advanced nuclear magnetic resonance methods for biochemical analysis of biofluids and hyperpolarized magnetic resonance spectroscopic imaging for organ-on-chip

Programa de doctorat en Biomedicina

Autor: Marc Azagra Rodríguez

Director/a: Irene Marco Rius i Javier Ramón Azcón

Tutor: Oscar Castaño Linares

Institute for Bioengineering of Catalonia



UNIVERSITAT DE
BARCELONA

ABSTRACT

Nuclear magnetic resonance (NMR) is a powerful analytical technique used to study the structure, dynamics, and interactions of molecules. However, the sensitivity of NMR is limited by the low polarization of nuclear spins at room temperature, which makes it difficult to detect signals from low-concentration species or from small sample volumes. Hyperpolarization techniques, such as dissolution Dynamic Nuclear Polarization (dDNP), and Parahydrogen Induced Polarization (PHIP), have emerged as a promising solution to this problem, as they can boost the NMR signal intensity by several orders of magnitude.

The advancement of organ-on-a-chip (OoC) technology has emerged as a potent platform for investigating biological systems such as tissue and organ physiology *in vitro*. OoCs are microfluidic devices that mimic the structure and function of human organs, and can be used to study disease mechanisms and drug efficacy. However, the merging of NMR and hyperpolarization techniques with OoCs remains largely unexplored.

List of papers and patents

Material in this thesis is patented, published or being prepared for publication in the following list:

1. **Azagra, M.**, Pose, E., De Chiara, F., Perez, M., Avitabile, E., Servitja, J. M., Brugnara, L., Ramón-Azcón, J., & Marco-Rius, I. (2022). Ammonium quantification in human plasma by proton nuclear magnetic resonance for staging of liver fibrosis in alcohol-related liver disease and nonalcoholic fatty liver disease. *NMR in Biomedicine*, 2022, vol. 35, no 9, p. e4745.
2. Yeste, J., **Azagra, M.**, Ortega, M. A., Portela, A., Matajsz, G., Herrero-Gómez, A., Yaewon, K., Sriram, R., Kurhanewicz, J., Vigneron, D., & Marco-Rius, I. (2023). Parallel detection of chemical reactions in a microfluidic platform using hyperpolarized nuclear magnetic resonance. *Lab on a Chip*, 2023, vol. 23, no 23, p. 4950-4958. **First co-author**
3. **Azagra, M.**, Gomez-Cabeza, D., Portela, A., Matajsz, G., Torras, N., Martinez, E., & Marco-Rius, I. (2024). Leveraging Magnetic Resonance Imaging to Study Biocompatible Scaffolds Diffusion and Perfusion for Lab-on-a-Chip Systems. 2024. **First co-author.**
4. Eills, J., **Azagra, M.**, Gómez-Cabeza, D., Tayler, M. C., & Marco-Rius, I. (2024). Polarization losses from the nonadiabatic passage of hyperpolarized solutions through metallic components. *Journal of Magnetic Resonance Open*, 2024, vol. 18, p. 100144.
5. Herrero-Gómez, **Azagra, M.**, & Marco-Rius, I. (2022). A cryopreservation method for bioengineered 3D cell culture models. *Biomedical Materials*, 2022, vol. 17, no

- 4, p. 045023.
6. Mouloudakis, K., Bodenstedt, S., **Azagra, M.**, Mitchell, M. W., Marco-Rius, I., & Tayler, M. C. (2023). Real-time polarimetry of hyperpolarized ^{13}C nuclear spins using an atomic magnetometer. *The Journal of Physical Chemistry Letters*, 2023, vol. 14, no 5, p. 1192-1197.
7. Eills, J., Picazo-Frutos, R., Burueva, D. B., Kovtunova, L. M., **Azagra, M.**, Marco-Rius, I., Budker, I., & Koptug, I. V. (2023). Combined homogeneous and heterogeneous hydrogenation to yield catalyst-free solutions of parahydrogen-hyperpolarized [$1\text{-}^{13}\text{C}$] succinate. *Chemical Communications*, 2023, vol. 59, no 62, p. 9509-9512.
8. Marco Rius, I.; Yeste Lozano, J.; Herrero Gomez, A.; **Azagra, Rodriguez, M.**; Ortega Machuca, MA.; Ramon Azcon, J. System and method for nmr analysis of a physiological condition in an analyte. Patent Reference number: 452021106, Apr 26, 2021.

ACKNOWLEDGEMENTS

En primer lloc m'agradaria agrair de manera molt efusiva i afectiva a la doctora Irene Marco Rius. Ella va ser la persona que va confiar en mi sense coneixe'm per poder realitzar la tesi doctoral en un projecte altament ambiciós i científicament dens. Vaig tenir la sort de ser la primera persona en formar part del seu grup i hem anat creixent poc a poc, des de ser dos a ser-ne gairebé 12! Estic molt orgullós de tot el que has fet fins arribar on estàs ara mateix. Se que no ha sigut fàcil i potser ara encara queda la part més dura, però no tinc cap dubte que arribaràs molt lluny. Agrair-te la confiança dipositada en tot moment, tant per lidiar amb meetings, liderar certs projectes i enviar-me arreu del món per portar el coneixement al nostre laboratori. Dic nostre perquè no puc evitar sentir-lo part de mí, ara i per sempre.

En segon lloc, m'agradaria fer una menció molt especial a tu Alba Herrero ja que sense tu no ho haguéssim fet. És gràcies a tu que tenim un laboratori com toca, amb l'equipament en regla, amb tot endressat i has sapigut mantenir l'ordre del laboratori. Gràcies per tot Alba, aquesta tesi no existiria si no fós en gran part per tu.

It's clear that I was not going to forget you James Eills, my dear English postdoc. You spent a lot of time teaching me, explaining a thousand NMR concepts I didn't understand. You taught me to have criteria, to think like a scientist and to act like one. However, sometimes I think that we should have put on our safety goggles or lab coats more often hahahaha. I won't forget how I improved my English with you and learned to understand these bad English humour you all have. I will never forget you and I hope we will keep in touch.

Gràcies a tu també David. Vas ser com un àngel caigut del cel. Has aportat un coneixement infinit, ganes de treballar, resolitivitat y constancia. Sempre recordaré les hores que ens vam passar al laboratori fent experiments juntament amb una cervesa a la mà fins

altes hores de la nit. Tinc molt bons records amb tu que no oblidaré i tinc clar que la teva amistat perdurà moltíssim.

Lluís m'ha agradat molt compartir aquesta experiència amb tu. Estic segur que sinó hagués estat una etapa molt més avorrida i complicada. Ets de les persones més vàlies i treballadores que conec i espero que segueixi així. Vals moltíssim i espero que ningú et faci canviar mai d'opinió. Trobaré a faltar els partits de futbol i les cates de torró d'amagades jeje.

Alex, has sido una gran inspiración y referencia para mí. Estoy muy agradecido de haber coincidido contigo ya que he tenido un mentor y un amigo durante mucho tiempo. Fueron divertidos los viajes que tuvimos juntos a Oxford donde nos dio tiempo a conocernos más y ver la grandísima persona que eres. No tengo duda que allá donde estés, sea en una universidad o en tu propia empresa te irá de maravilla.

Mariale y Jose también fuísteis una pieza clave al principio de la tesis donde estaba increíblemente perdido en el mundillo de la investigación. Fuísteis unas muy buenas guías para empezar y estoy muy agradecido del tiempo y esfuerzo que dedicasteis para que a día de hoy pueda defender esta tesis.

Gràcies Jordi Redondo a tu també per haver sigut el primer culpable en fer que aquesta tesi sigui una realitat. Vas transmetre en mí aquesta passió per l'RMN i gràcies a això he pogut trobar la meva vocació. Sempre t'estaré agraït.

A very special thanks to IBEC and the European Commission for giving me the opportunity to be hired for the BLOC project and for subsidizing a large part of my stays and research.

Paula, has aparegut al final d'aquest viatge però no per això has tingut un menor impacte. Gràcies per insistir setmana rere setmana com portava els tràmits del dipòsit de tesi i presionar-me carinyosament a espavilar. Fora conyes, has aparegut en un dels moments més difícils de tots i has sigut una peça clau per amainar la tempesta. T'estimo.

Gràcies a tots els meus amics per recolzar-me en tot moment, especialment al Carlos, Marc i Santín per compartir amb mi una gran etapa del doctorat vivint junts i la que recordaré com una de les millors de la meva vida. No oblidaré fins i tot quan van venir a l'Ibec per ajudar-me a omplir nitrogen! Sou uns cracks i us estimo moltíssim!

I per sobre de tot, un agraïment molt molt afectiu i especial per la meva família. Papa

i mama heu sigut sempre un exemple a seguir per l'Alba i per mí, i som literalment el reflexe de la vostra educació, la qual considero extremadament privilegiada. Estic molt orgullós de la feina que heu fet com a pares i estic segur que el 100 % de la població signaria ser la meitat de bons pares que heu sigut vosaltres. Ens heu donat totes les facilitats per arribar a ser el que som i no ho hauriem aconseguit sense vosaltres. Gràcies per tot de tot cor. I a tu també Alba per ser la meva referència des de ben petit. Si t'hi fixes he anat seguint els teus passos formatius des de ben petits. Sempre has dit que jo sóc l'intel·ligent dels dos però no és cert, considero que tu tens moltíssim més potencial que jo i que només et falta una mica de geta perquè la gent se'n adoni. No en tinc cap dubte que arribaràs allà on et proposis i seràs la millor en la teva posició. Us estimo infinit a tots tres.

List of Figures

1.1	1/2 spins energetic diagram	31
1.2	Nuclear 1/2 spin precessing under an external magnetic field.	33
1.3	X and y magnetization evolution over time	36
1.4	Diagram of the hydrogen atom	38
1.5	Slice thickness determination in MRI	42
1.6	MRI frequency encoding readout process	43
1.7	MRI phase encoding gradient diagram	45
1.8	Pulse-acquire gradient echo sequence in MRI	47
1.9	T ₁ and T ₂ weighed MRI images	48
1.10	CSI experiment	49
1.11	Polarization dependency of T/B ₀	51
1.12	Schematic representation of a sample cup	56
1.13	Polarization build-up function	57
1.14	PHIP diagram	59
1.15	Pyruvate metabolic pathway	62
1.16	Metabolic pathways found in the liver	65
1.17	Confocal image of HepG2 cells cluster inside a cryogel	67
3.1	Deuterated solvent optimization	77
3.2	Quantification measurements with DMSO-d ₆ and ammonium chloride	77
3.3	Freeze-drying effect in ammonium chloride	79
3.4	Plasma treatment protocol	80
3.5	Results of the ammonium quantification in human plasma	83
3.6	¹ H NMR spectrum of the plasma sample	84
3.7	Nonparametric Spearman correlations between platelets vs ammonium	86

3.8	Nonparametric Spearman correlations between Child-Plugh score and MELD vs ammonium	88
4.1	Chemical reaction mechanism for cryogel formation	91
4.2	Schematic of the cryogel and the microfluidic device inside the MRI scanner	94
4.3	Custom nylon mesh used to allow perfusion studies in a microfluidic chip	97
4.4	Diffusion studies results	98
4.5	Perfusion studies results	102
4.6	Sagittal MRI images from the microfluidic device before and after the D ₂ O injection	104
4.7	Sagittal MRI images from the microfluidic device before and after the D ₂ O injection with different flow rates, different % of CMC in the scaffolds and different number of scaffolds	106
5.1	Graphical representation of the fourth chapter purpose	110
5.2	Experimental schematic illustration of the fourth chapter	114
5.3	Effect of the angle of the syringe needle in space on the ¹³ C polarization .	115
5.4	Schematic representation of the quantic states population evolution with and without needles effect	117
5.5	Effect of stainless steel ferrules on the ¹³ C polarization	118
5.6	Magnetic field outside the needle produced by itself	120
6.1	Overview of the fifth thesis chapter work	125
6.2	Microfluidic device and its corresponding fabrication mold.	127
6.3	Schematic picture of the saddle coil embedded in the microfluidic device.	132
6.4	Schematic representation to inject a solution in the BLOC chip	133
6.5	Results of the longitudinal relaxation measurements in the BLOC chip with pyruvate and fumarate.	134
6.6	Schematic representation of the setup used in this study	135
6.7	Dynamic curves of the real-time metabolism test using hyperpolarized pyruvate, LDH and NADH	136
6.8	Dynamic curve of the real-time metabolism test using hyperpolarized pyruvate and fumarase	137

6.9	Metabolic study results with 2D cell culture	138
6.10	Kinetic results with HepG2 cells	139
7.1	Pulse length (P90) calibration using three different power references . . .	150
7.2	8-well microfluidic plate for high-throughput DNP-MRSI experiments . .	152
7.3	High-throughput DNP-MRSI assay	154
7.4	Results of the high-throughput MRI analysis with H ₂ O ₂	156
7.5	Plots of the kinetics study with H ₂ O ₂	158
7.6	Representative figure of the results obtained with the multiwell microflu- idic device with the cells study	160

List of Tables

1.1	Variables in a DNP experiment classified by requirement, definition, function and examples.	55
3.1	Presturation effect in proton quantification	78
3.2	Clinical data of patients with different stages of NAFLD and ArLD	82
5.1	Summary of the seven metal syringe needles used in this work	113

ABBREVIATIONS

ALT Alanine transaminase

ALTADENA Adiabatic Longitudinal Transport After Dissociation Engenders Net Alignment

ArLD Alcohol related Liver Disease

AS-ArLD Advanced-Stage Alcohol-Related Liver Disease

AS-NAFLD Advanced-Stage Non-Alcoholic Fatty Liver Disease

AST Aspartate Transaminase

B₀ External magnetic field strength (T)

B₁ Magnetic field strength perpendicular to B₀

BDPA 1,3-bisdiphenylene-2-phenylallyl or α,γ -bisdiphenylene- β -phenylallyl

BILI Bilirubin

CPS1 Carbamoyl Phosphate Synthetase

CSA Chemical shift anisotropy

CSI Chemical Shift Imaging

δ Chemical shift of the nuclear spin (ppm)

dDNP dissolution Dynamic Nuclear Polarization

DHA DeHydroxy Ascorbate

DHA2 DihydroxyAcetone

DMSO DiMethylSulfOxide

DOTA Gadoteric Acid

DSS Sodium trimethylsilylpropanesulfonate

EDTA 2,2',2'',2'''-(Ethane-1,2-diylidinitrilo)tetraacetic acid

FBS Fetal Bovin Serum

FID Free Induction Decay

FOV Field Of View

FWHM Full Width at Half Maximum

GGT Gamma-Glutamyl Transferase

G_{ss} Slice Selection Gradient

G_{FE} Frequency Encoding Gradient

G_{PE} Phase Encoding Gradient

HCC HepatoCellular Carcinoma

HEPES 2-[4-(2-hydroxyethyl)piperazin-1-yl]ethanesulfonic acid

HF High-Field

HP Hyperpolarization/Hyperpolarized

INR International Normalized Ratio

IS-ArLD Initial-Stage Alcohol-related Liver Disease

IS-NAFLD Initial-Stage Non-Alcoholic Fatty Liver Disease

J Coupling constant

γ Gyromagnetic ration of the nuclear spin of interest (rad/sT)

LDH Lactate Dehydrogenase

LOD Limif of Detection

LOD Limit of Quantification

MCT1 MonoCarboxylate Transporter 1

MCV Mean Corpuscular Volume

MELD Model for Endstage Liver Disease

MHz Mega Hertz

MR Magnetic Resonance

MRI Magnetic Resonance Imaging

MRS Magnetic Resonance Spectroscopy

MRSI Magnetic Resonance spectroscopic Imaging

MPC Mythocondrial pyruvate carrier

MW Microwave

NAD⁺ Nicotinamide adenine dinucleotide oxidized

NADH₂ Nicotinamide adenine dinucleotide reduced

NAFLD Non-Alcoholic Fatty Liver Disease

NASH Non-Alcoholic SteatoHepatitis

NMR Nuclear Magnetic Resonance

NS Number of Scans

OCT Ornithine TransCarbamylase

OD Outer Diameter

OoC Organ-on-chip

P/S Penicillin and streptomycine

PET Positron Emission Tomography

PDH Pyruvate DeHydrogenase

PDMS Polydimethylsiloxane

PHIP Parahydrogen Induced Polarization

PFOTS 1H,1H,2H,2H-PerfluorooCtyl-trichlorosilane

PTC Polarization Transfer Catalyst

PTFE Polytetrafluoroethylene

RF Radio Frequency

SABRE Signal Amplification by Reversible Exchange

SABRE-SHEATH Amplification by Reversible Exchange in Shield Enables Alignment
Transfer to Heteronuclei

SEOP Spin Exchange Optical Pumping

SNR Signal-to-Noise Ratio

T₁ Longitudinal relaxation time constant

T₂ Transverse relaxation time constant

T_s Singlet relaxation time constant

TCA TriCarboxylic Acid cycle

TE Echo Time

TFA TriFluoroacetic Acid

TR Repetition Time

TEMPO (2,2,6,6-Tetramethylpiperidin-1-yl)oxyl

PREAMBLE

Dissolution Dynamic Nuclear Polarization has become a powerful technique for metabolic imaging allowing real-time tracking of hyperpolarized substrates administered in a biological system. It has been already applied for clinical studies and the results are promising for early localized cancer diagnosis. However, a clinical hyperpolarisation trial requires administration of hyperpolarized agents, often via intravenous injection, which some patients may find it uncomfortable or stressful. Clinical trials also involve navigating regulatory approvals, ethical considerations and patient consent, which add complexity to the research process. Lastly, the price of most of the reagents is prohibitive, and the cost of each study reaches into several thousand dollars.

This thesis explores a new approach to combine microfluidic platforms to maintain biological *in vitro* models alive in combination with ^{13}C -hyperpolarized magnetic resonance imaging. Organs-on-chip are widely studied for the ability to engineer precise and controlled conditions to grow and manipulate small biological *in vitro* systems in order to study their response to either external stimuli or the metabolism they have by themselves. This approach has a well known focus to replace some of the *in vivo* studies to improve personalized and precision medicine. The aim of this thesis is to study the reproducibility of hyperpolarization analysis while addressing external factors that impact polarization stability. Also to adapt microfluidic systems for an accurate hyperpolarized contrast agent injection and the corresponding metabolic analysis of the *in vitro* models in an MRI scanner using ^{13}C magnetic resonance imaging.

This thesis is structured as follows:

Chapter 1 introduces the topics I will use to describe the investigation carried out during the thesis.

Chapter 2 marked my initiation into the medical and biological field. It was a good

way to approach to the field by using conventional NMR as a means of exploration and investigation. I explored the possibility of diagnosing fatty liver disease non-invasively by quantifying the concentration of ammonium in blood using ^1H NMR spectroscopy. This was the first study to analytically quantify the ammonium levels using NMR spectroscopy in a biologic sample.

Chapter 3 discusses the utility of an MRI spectrometer to track diffusion and perfusion along time of a liquid through porous materials. In microfluidics the perfusion of liquid solutions is widely used for either continuous flow of cell media to maintain the biologic system alive longitudinally, administration of dissolved drugs to change the metabolic behaviour of the system, or even the injection of contrast agents to measure metabolic changes. This study demonstrates the ability of successfully perfusing a solution into different porous material (cryogels and hydrogels) in a wide range of flow rates.

Chapter 4 exemplifies how the magnetic polarization can be easily affected by magnetic materials surrounding the place where the dissolution takes place. In our case I used metallic needles for the injection of the hyperpolarized solution. We realized how fragile and sensible the NMR polarization can be affected by metallic needles or ferrules, making them be completely incompatible with any hyperpolarization technique.

Chapter 5 combines the utilization of a modified 60 MHz benchtop NMR spectrometer with a microfluidic chip probe to test real-time metabolism using customized coils. I will focus on different parts of the setup such as the coil used, the design and fabrication of the microfluidic devices, and the carrier to introduce these devices into the magnet. I will also demonstrate the setup by making T_1 measurements from a hyperpolarized $[1-^{13}\text{C}]$ pyruvate and fumarate. Furthermore I performed multiple analyses testing the metabolism of cells in suspension by injecting pyruvate in the chip fabricated for this project.

Chapter 6 demonstrates how MRSI can be used for *in vitro* analysis on OoC for high-throughput analysis measuring multiple conditions with a single hyperpolarized $[1-^{13}\text{C}]$ pyruvate shot. In this chapter, I initially proved the approach by the chemical reaction between hydrogen peroxide and $[1-^{13}\text{C}]$ pyruvate. Lastly we measured cellular metabolism with different conditions tracking the conversion from $[1-^{13}\text{C}]$ pyruvate to $[1-$

^{13}C]lactate.

Contents

1	INTRODUCTION	30
1.1	Nuclear magnetic resonance spins theory	30
1.2	Polarization and sensitivity	32
1.3	Precession	33
1.4	Spin relaxation	34
1.4.1	Dipole-dipole relaxation	37
1.4.2	Chemical shift anisotropy	37
1.4.3	Quadrupolar relaxation	38
1.5	Atomic fingerprint: Chemical shift	38
1.6	Magnetic Resonance Imaging	40
1.6.1	Fundamental theory of MRI	41
1.6.1.1	Slice selection	41
1.6.1.2	Frequency encoding	42
1.6.1.3	Phase encoding	44
1.6.2	Radiofrequency coils	44
1.6.3	MRI sequences	46
1.6.4	Magnetic Resonance Spectroscopic Imaging	48
1.7	Hyperpolarization-enhanced MRI and MRSI	50
1.7.1	Comparison between hyperpolarized and thermal NMR	50
1.7.2	Hyperpolarization techniques	52
1.7.2.1	Brute Force	53
1.7.2.2	Spin Exchange Optical Pumping (SEOP)	53
1.7.2.3	Dissolution Dynamic Nuclear Polarization (dDNP)	54
1.7.2.4	Para-Hydrogen Induced Polarization (PHIP)	57

1.7.2.5	Signal Amplification by Reversible Exchange (SABRE)	60
1.7.3	Hyperpolarization for metabolic analysis	60
1.7.3.1	Liver disease	63
1.7.3.2	<i>In vitro</i> ^{13}C hyperpolarized MR studies	65
1.8	Microfluidics and organ-on-a-chip devices	66
1.8.1	Scaffolds for 3D-structure cell models	66
2	HYPOTHESES AND OBJECTIVES	68
3	LIVER FIBROSIS STAGING IN LIVER DISEASE BY AMMONIUM QUANTIFICATION IN PLASMA USING ^1H NMR	69
3.1	INTRODUCTION	69
3.2	MATERIALS & METHODS	72
3.2.1	Calibration curve of ammonium chloride in DMSO- d_6	73
3.2.2	Human plasma obtention	73
3.2.3	Human plasma clinical biomarkers	73
3.2.4	Human plasma sample preparation for ammonium assay by ^1H -NMR	73
3.2.5	Ammonium quantification by ^1H -NMR	74
3.2.6	Ammonium chloride standards quantification by ^1H -NMR	74
3.2.7	Data analysis	75
3.2.8	Statistical analysis	75
3.3	RESULTS & DISCUSSION	76
3.3.1	Ammonium quantification	76
3.3.2	Ammonium quantification in human plasma	79
3.3.3	Correlation between ammonium concentration and clinical biomarkers of fatty liver disease	80
3.4	CONCLUSIONS	88
4	LEVERAGING MAGNETIC RESONANCE IMAGING TO STUDY BIO-COMATIBLE SCAFFOLDS DIFFUSION AND PERFUSION FOR LAB-ON-A-CHIP SYSTEMS	89
4.1	INTRODUCTION	89

4.2	MATERIALS & METHODS	94
4.2.1	1% CMC cryogel fabrication	94
4.2.2	10% PEGDA hydrogel fabrication	95
4.2.3	Microfluidic chips fabrication	95
4.2.4	Custom nylon mesh fabrication	96
4.2.5	Magnetic Resonance Imaging for Diffusion and Perfusion Studies .	96
4.2.6	Data Processing and Analysis	97
4.3	RESULTS & DISCUSSION	98
4.3.1	Study of passive diffusion properties of bio-compatible scaffolds using MRI and D ₂ O as a contrast agent	98
4.3.2	Study of the perfusion properties of bio-compatible scaffolds us- ing custom-designed microfluidic systems	100
4.3.3	Perfusion assessment of CMC scaffolds in a 4-well microfluidic device	100
4.3.3.1	Fast perfusion evaluation of 10 % PEGDA hydrogels . .	100
4.3.3.2	Perfusion evaluation of 1 % CMC cryogel scaffolds . .	101
4.3.3.3	Controlled perfusion evaluation of scaffolds using a sy- ringe pump	104
4.3.3.4	Controlled perfusion evaluation of variable % of CMC cryogel scaffolds	105
4.4	CONCLUSIONS	106
5	POLARIZATION LOSSES RESULTING FROM THE NONADIABATIC PASSAGE OF HYPERPOLARIZED SOLUTIONS THROUGH METAL- LIC COMPONENTS	109
5.1	INTRODUCTION	109
5.2	MATERIALS & METHODS	111
5.2.1	HF Experiments with Hyperpolarized [1- ¹³ C]pyruvate .	111
5.3	RESULTS & DISCUSSION	113
5.3.1	HF experiments with hyperpolarized [1- ¹³ C]pyruvate	113
5.3.2	Magnetic field produced by a syringe needle	119
5.4	CONCLUSIONS	121

6	BENCHTOP NMR FOR LAB-ON-A-CHIP	123
6.1	INTRODUCTION	123
6.2	MATERIALS & METHODS	126
6.2.1	Development of a benchtop NMR spectrometer for lab-on-a-chip applications	126
6.2.2	Microfluidic chip device	126
6.2.3	Coil embedded in the microfluidic chip	127
6.2.4	HP fumarate using PHIP	128
6.2.5	Hyperpolarized [1- ¹³ C]pyruvate using dDNP	128
6.2.6	Real-time metabolism study of HepG2 cells	129
6.2.7	Data analysis	130
6.3	RESULTS & DISCUSSION	131
6.3.1	Technical development: spectrometer, carrier, chip and RF coil . .	131
6.3.2	T ₁ measurement of hyperpolarised ¹³ C agents using the customised setup	132
6.3.3	Real-time metabolism detection using the customised setup	134
6.3.3.1	LDH kinetics assessment measuring [1- ¹³ C]pyruvate to [1- ¹³ C]lactate	134
6.3.3.2	Fumarase (FH) kinetics assessment measuring fumarate to L-malate	136
6.3.3.3	Kinetic analysis using HepG2 cell lines	137
6.4	CONCLUSIONS	139
7	HIGH-THROUGHPUT ANALYSIS IN A MULTIWELL MICROFLUIDIC PLATFORM FOR HYPERPOLARIZED MRSI	141
7.1	INTRODUCTION	141
7.2	MATERIALS & METHODS	144
7.2.0.1	Fabrication of the microfluidic platforms for DNP-MR applications	144
7.2.0.2	Hyperpolarization of [1- ¹³ C]pyruvate	145

7.2.0.3	Flip angle calibration using a 10 M ^{13}C -Urea sample . . .	146
7.2.0.4	MRSI data acquisition of the chemical reaction	146
7.2.0.5	MRSI data acquisition of the <i>in vitro</i> analysis	147
7.2.0.6	MRI data processing	149
7.3	RESULTS & DISCUSSION	149
7.3.0.1	Flip angle calibration using a 10 M ^{13}C -Urea sample . .	149
7.3.0.2	Microfluidic multiwell platform for parallel detection of chemical reactions by magnetic resonance	150
7.3.0.3	Microfluidic multiwell platform for the metabolic activ- ity of HepG2 cell line by hyperpolarized spectroscopic imaging	159
7.4	CONCLUSIONS	160
8	CONCLUSIONS	162
	BIBLIOGRAPHY	164

INTRODUCTION

The discipline of nuclear magnetic resonance (NMR) started back in the 1940's from the initial observation of proton magnetic resonance in water in 1946[1], and ethanol in 1951[2]. The technique has been growing since then, focusing on the appreciation of the information it can provide, and hence its potential applications in chemistry, biology, material science, geology and medicine. The founding pioneers of NMR were Felix Bloch and Edward Purcell, recognized with a Nobel Prize in 1952 for their development of new methods for nuclear magnetic precision measurements and discoveries. Briefly, NMR is a physical phenomenon in which some atomic nuclei in a strong magnetic field (B_0) are perturbed by a weak oscillating field (B_1) and react producing an electromagnetic signal with a certain frequency characteristic of each nuclei.

1.1 Nuclear magnetic resonance spins theory

Atoms are particles made up of a nucleus composed of protons and neutrons, which are surrounded by a cloud of electrons. The nuclei of all atoms have a property called nuclear spin quantum number I , which describes the angular momentum of a given particle. The spin number has a value, and it is always greater or equal to 0 and multiple of 1/2[3]. Spin is a crucial property to measure NMR signal. The nuclei spin at a specific angular momentum \vec{P} , and possess an intrinsic property called gyromagnetic ratio γ , a physical constant for any given nuclei defined as the ratio of magnetic moment to its angular momentum. The gyromagnetic ratio quantifies how fast the particle is spinning under certain magnetic field, and rise an associated magnetic moment or $\vec{\mu}$. This magnetic moment is a vector representing the strength and orientation of the magnetic field produced by the

spinning nuclei, and depends on the gyromagnetic ratio and the angular momentum of the spin under study (eq. 1.1)[4]:

$$\vec{\mu} = \gamma \vec{P} \quad (1.1)$$

The number of energetic states depends on the spin number. When spin-1/2 atoms are placed in an external magnetic field B_0 , they have two energetic levels with an associated energy separation that depends linearly on magnetic field[5].

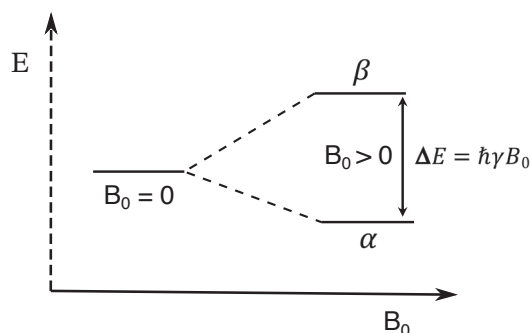


Figure 1.1: Energetic diagram of spins with $I = 1/2$ with and without an external magnetic field B_0 applied. α corresponds to the lowest energetic state, β to the higher energetic state, \hbar to the reduced Plank's constant and γ to the gyromagnetic ratio.

For a given nucleus with quantum number I , there are $(2I + 1)$ possible spin energetic states or angular momentum projection onto a fixed axis, m , in a magnetic field. Therefore, for a nucleus with a spin of $\frac{1}{2}$, such as the ^1H or ^{13}C , there are two possible states denoted as $+\frac{1}{2}$ and $-\frac{1}{2}$.

These two energetic states are usually known as α for the lower energetic state and parallel to B_0 , and β for the higher energetic state and antiparallel to the B_0 . The difference in energy between energetic levels increases with the magnetic field, increasing also the population difference (Fig. 1.1). When measuring an ensemble of spins, each spin can exist in either state α or β , and overall the nuclei have a preference to exist in the lower energy state, α . We will describe the quantitative difference in populations between the two energetic levels at thermal equilibrium in section 1.2.

Those spins with $I = 0$ don't have a nuclear spin so they are non-magnetically active (they do not possess a magnetic moment) and do not produce NMR signal. For example, the relative abundance of the two carbon isotopes are $^{12}\text{C} \% \approx 98.9$ and $^{13}\text{C} \approx 1.1\%$,

being ^{13}C magnetically active with $I = 1/2$ and ^{12}C magnetically invisible with $I = 0$ [6]. This fact is quite unfortunate because, at natural abundance, we can detect only 1 % of the signal from all carbon atoms. Organic molecules always contain carbon atoms, so it is difficult to find strategies to obtain information from them. Luckily, the majority of chemical elements have at least one isotope with positive nuclear spin.

1.2 Polarization and sensitivity

Increasing the inherently low sensitivity of NMR is a challenge since the beginning of the technique, mainly due to the low spin concentration, low-abundant nuclei within the sample, and the low polarization level of the energetic levels[7]. NMR sensitivity is described as the population difference between nuclear energetic levels at a given temperature for the spin $\frac{1}{2}$ system described in figure 1.1, and can be numerically correlated with the Boltzmann distribution formula (eq.1.2)

$$\frac{P_{\beta}}{P_{\alpha}} = e^{\Delta E/K_B T} \quad (1.2)$$

Where P_{β} is the population in the higher energetic state, P_{α} is the population in the lower energetic state, K_B is the Boltzmann constant ($\approx 1.35 \times 10^{-23} \text{m}^2 \text{s}^{-2} \text{K}^{-1}$) and T is the temperature of the sample[8].

The polarization level (P) of an ensemble of spin $\frac{1}{2}$ is given by the equation:

$$P = \frac{P_{\alpha} - P_{\beta}}{P_{\alpha} + P_{\beta}} \quad (1.3)$$

The population rate of the energetic states under the effect of an external magnetic field is well described by the Boltzmann distribution. The polarization level of nuclear spins at 298 K is $3.4 \cdot 10^{-6} \text{T}^{-1}$ for ^1H , and $8.6 \cdot 10^{-7} \text{T}^{-1}$ for ^{13}C . The signal obtained in NMR is polarization level dependent, which means that the maximum signal would be obtained when $p = 1$ and all the spins are in the α state. The level of polarization is proportional to the external magnetic field strength B_0 (Tesla). However, it is inviable to reach $p = 1$ by increasing B_0 with the current technology. Currently, the highest magnetic field strength achieved is 45 T, with a superconducting magnet, which means a polarization level of

10^{-4} at room temperature.

Hyperpolarization was born as a new research field to overcome this inherently low sensitivity, increasing the NMR signal by a factor of 10,000 in the liquid state[9]. This concept will be described in depth in the section 1.7.

1.3 Precession

The magnetic moment of the nuclear spins is not completely aligned towards or against the external magnetic field. There is always a small angle or torque on the magnetic moment, which makes them follow a circular path around the axis of the magnetic field (Fig. 1.2)[10]:

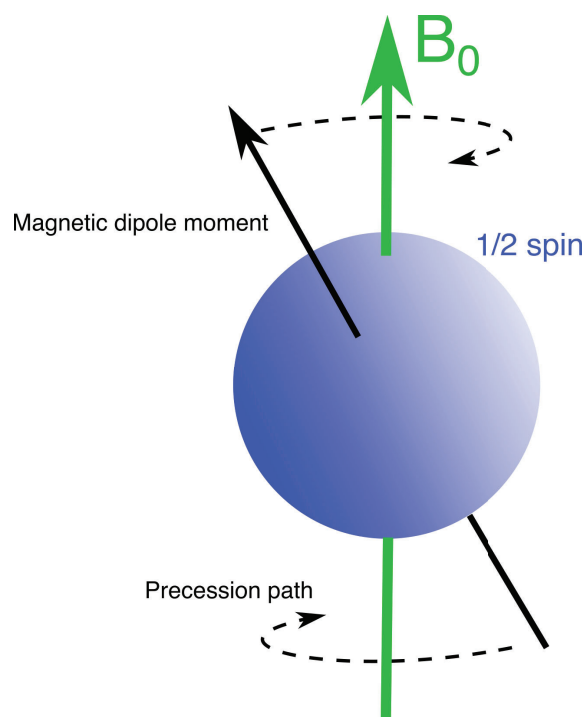


Figure 1.2: Nuclear 1/2 spin precession under an external magnetic field.

This motion is known *precession* and its angular velocity is specific on each nuclei, producing the *Larmor frequency*. The rate of precession defined by the angular velocity is:

$$\vec{\omega}_0 = \gamma \vec{B}_0 \quad (1.4)$$

The speed of the *Larmor frequency* is determined by the gyromagnetic ratio and the

strength of the B_0 . However, the precession direction is only determined by γ and can be clockwise or anticlockwise. The NMR signal happens only when the irradiated frequency matches the resonance frequency of the nuclei and therefore its spin state changes because of the energy absorption. This energy ($\Delta\vec{E}$) is given by the equation (1.5):

$$\Delta\vec{E} = h\vec{\nu} = \frac{h\gamma\vec{B}_0}{2\pi} \quad (1.5)$$

where h is the Planck's constant, 6.626×10^{-34} Js.

Only energy at this frequency stimulates transitions between the spin up and spin down energetic levels. This quantized energy absorption is known as resonance absorption and the frequency of energy is known as the resonant frequency[11].

1.4 Spin relaxation

The irradiation of the radiofrequency pulse perturbs the sample at the thermal equilibrium. Just after the pulse excitation, the bulk magnetization vector is tilted away from the thermal equilibrium pointing along the B_0 field axis, +z direction, ending in a spin population difference in the energetic states. While there is still magnetization in the transverse plane, the spins will precess around the axis of the external magnetic field. The spin relaxation is dependent on two relaxation times: T_1 or longitudinal relaxation time, and T_2 or transverse relaxation time. T_1 describes the transitions between energetic levels to re-establish the Boltzmann distribution at thermal conditions after any perturbation of the equilibrium, or can be understood as the time required to recover 63 % of the polarization at the equilibrium.

T_1 is defined as:

$$M_z(t) = M_z(0)e^{-t/T_1} + M_0(1 - e^{-t/T_1}) \quad (1.6)$$

Where $M_z(t)$ is the magnetization in the z direction at a given time and magnetic field for a spin ensemble, $M_z(0)$ represents any remnant longitudinal magnetization that still presents at time $t = 0$, M_0 is the equilibrium magnetization, and T_1 is the longitudinal relaxation time constant.

T_2 describes the loss of coherence in the spins ensemble precessing around the external magnetic field, or the loss of signal due to dephasing in the xy plane. The loss of magnetization in the xy plane is described by the equation 1.7

$$M_{xy}(t) = M_0 e^{-t/T_2} \quad (1.7)$$

Where M_{xy} is the magnetization in the plane xy at a given time, and T_2 is the transversal relaxation time constant.

The evolution of magnetization in all 3 axis can be described by the Bloch equations, introduced by Felix Bloch in 1946[1]. These set of equations describes the time evolution of magnetization along an axis (represented in Fig. 1.4) and are used to predict the macroscopic change of magnetization along the time:

$$\begin{aligned} \frac{dM_x(t)}{dt} &= \gamma(B_0 M_y(t) - B_1 M_z(t) \sin(\omega t)) - \frac{M_x(t)}{T_2} \\ \frac{dM_y(t)}{dt} &= \gamma(B_0 M_x(t) - B_1 M_z(t) \cos(\omega t)) - \frac{M_y(t)}{T_2} \\ \frac{dM_z(t)}{dt} &= \gamma(B_1 M_x(t) \sin(\omega t) - B_1 M_y(t) \cos(\omega t)) - \frac{M_z(t) - M_0}{T_1} \end{aligned} \quad (1.8)$$

Where M_0 is the thermal equilibrium magnetization, B_0 is the external magnetic field along the z-axis, B_1 is the radiofrequency field amplitude perpendicular to the B_0 with the corresponding coordinates, and T_1 and T_2 are the relaxation time constant.

T_2 is defined as a time constant for the decay of transverse magnetization in the xy plane from interaction of nuclear spins. However, the transverse magnetization usually decays much faster than expected. This effect is called T_2^* , considered as the effective T_2 and results from inhomogeneities in the external magnetic field B_0 producing a coherent dephasing of spins. This lack of field homogeneity is mainly affected by defects in the magnet from susceptibility-induced field distortions produced by the measured sample. The T_2^* can be rephased doing a spin echo and therefore recover the transverse magnetization. T_2 and T_2^* are correlated by the following formula:

$$\frac{1}{T_2^*} = \frac{1}{T_2} + \frac{1}{T_{2I}} + \frac{1}{T_{2S}} \quad (1.9)$$

Where T_2^* is the effective T_2 , T_2 is the relaxation induced by spin-spin interaction, T_{2I}

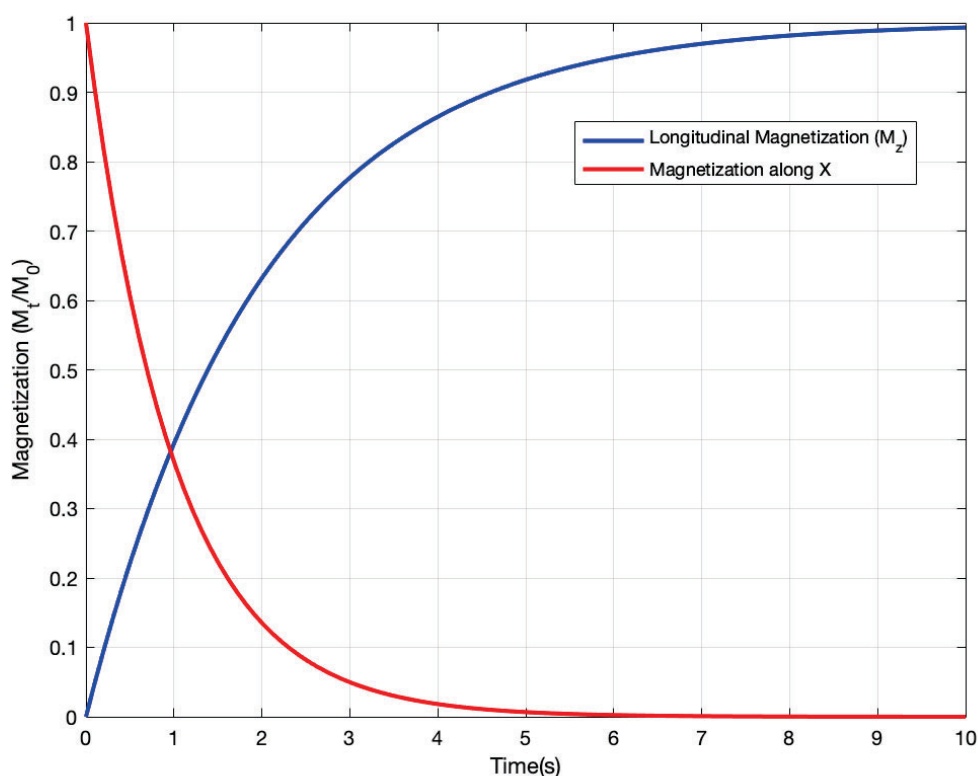


Figure 1.3: Spin magnetization vector evolution over time. Blue line represents the exponential growth of longitudinal magnetization dictated by the time constant T_1 , when 63 % of the polarization is achieved. Red line represents the loss of signal in the xy plane because of the z magnetization recovery and the lost of spin coherences. The example plotted represents when $T_2 = T_1/2$

is the dephasing time by the main B_0 inhomogeneities and T_{2S} is the dephasing time due to the magnetic susceptibility differences.

In hyperpolarization, the lifetime of the excited nuclear spins can vary from a few ms[12] to tens of minutes[13], depending on factors such as B_0 , temperature, ionic strength or the solvent surrounding the sample. These extended lifetimes are crucial for the success of hyperpolarization, making relaxation critical in this particular field. In order to be able to measure a hyperpolarized signal, the spins have to be adiabatically transported as fast as possible because the hyper intense signal decays exponentially with time at a given rate depending on the T_1 .

Nuclear spin relaxation requires a stimulation by a fluctuating field to induce spin quantum state transition or loss of coherence. There are 3 mechanisms able to do this:

dipole-dipole, chemical shift anisotropy, and quadrupolar mechanisms.

1.4.1 Dipole-dipole relaxation

Dipole-dipole relaxation is caused by fluctuations through the space between nuclear spins. It is the most important relaxation mechanism for many spin-1/2 nuclei. Their position in the space can alter the local field experienced by neighboring nuclei. There are 4 major factors establishing the strength of the dipolar interaction: type of spin, distance between them, angle between them and their relative motion[14]. Protons have a strong dipolar interaction with ^{13}C , making them relax faster than without them and viceversa. To extend ^{13}C lifetime, protons are usually replaced by deuterium[15].

1.4.2 Chemical shift anisotropy

Chemical shift anisotropy (CSA) relaxation is caused by the unsymmetrical electron distribution depending on the orientation of the nuclear spin with respect to the molecular structure. This fluctuating field is the stimulus of the CSA relaxation. This generally affects the nuclei with large chemical shift range since they possess the biggest shift anisotropy. CSA relaxation is dependent on the square of the external magnetic field, meaning it has greater significance in higher B_0 :

$$\frac{1}{T_1^{CSA}} \propto \gamma^2 B_0^2 \frac{\tau_C}{1 + \omega_0^2 \tau_C^2} \quad (1.10)$$

Where T_1^{CSA} is the CSA contribution to the T_1 relaxation, γ is the gyromagnetic ratio of the spin, B_0 is the external magnetic field strength, ω is the Larmor frequency of the spin, and τ_C is the correlation time. For example, the $[1-^{13}\text{C}]$ pyruvate T_1 is $\approx 20\%$ larger at 7.0 T than at 9.4 T due to the strong CSA relaxation[16].

1.4.3 Quadrupolar relaxation

Quadrupolar relaxation mechanism is only relevant for those nuclei with $I > 1/2$ and is often the dominant relaxation process for these. Quadrupolar nuclei possess an electric quadrupole moment in addition to a magnetic dipole moment resulting from the charge distribution of the nucleus deviating from the usual spherical symmetry associated to spin- $1/2$. As a result, the magnetic moments of quadrupolar nuclei take less time to return to random orientations (loss of coherence) after being pulsed by the NMR probe. Therefore, these nuclei possess an extremely low T_2 relaxation constant, making the linewidths of these nuclei hundreds or even thousands of hertz wide.

1.5 Atomic fingerprint: Chemical shift

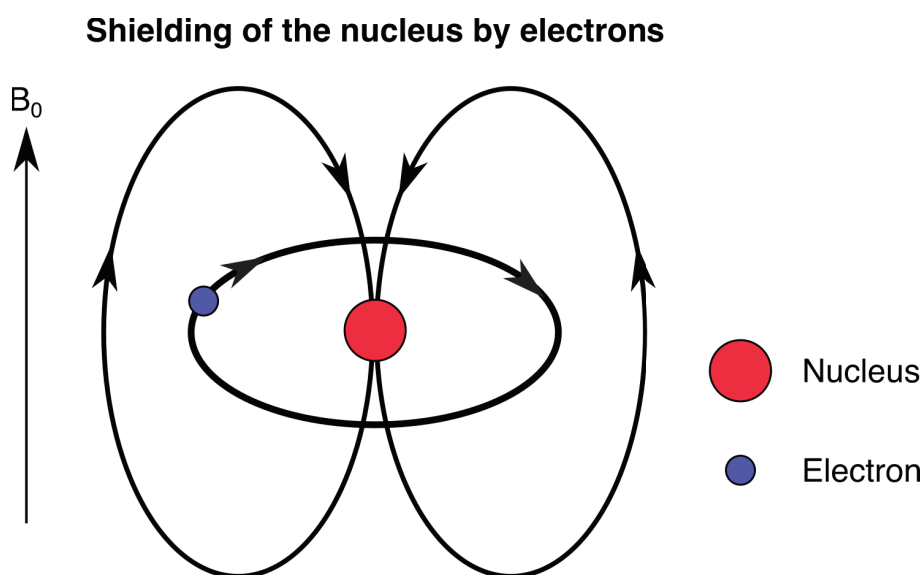


Figure 1.4: Diagram of the hydrogen atom. The transversal arrows moving around the nucleus represent the path that the electron is following, and the longitudinal arrows represent the inherent magnetic field lines of the spin nucleus.

The frequency that a certain nucleus absorbs is dependent on the external magnetic field B_0 and the electronic surroundings of each spin as shown in Fig. 1.4. The combination of both results in the Larmor frequency and can be normalized to obtain a value independent of B_0 strength and relative to a standard, called chemical shift. Because of its different molecular environment, each nucleus perceives a different local magnetic field, and therefore resonates at a different precession speed. This difference in magnetism is known as

chemical shielding and is proportional to B_0 :

$$B_i = B_0(1 - \sigma_i) \quad (1.11)$$

where σ_i is the shielding term for nuclei i . Chemical shielding generates different frequencies for the same nuclei in different molecular environments. However, as the shielding term is very small ($\approx 10^{-4} - 10^{-6}$), frequencies are usually displayed as part per million (ppm). The usual scale to express frequency differences is the ppm scale. The Larmor frequency of the nuclei of interest relative to the reference frequency is:

$$\omega_{i(ppm)} = \frac{(\omega_{i(Hz)} - \omega_{ref})}{\omega_{ref}} \times 10^6 \quad (1.12)$$

Where ω_i is the frequency of the spin of interest and the ω_{ref} is the frequency of a known spin with invariable chemical shift. The frequencies values represented in ppm is well accepted by the community for describing the frequency independently of the B_0 strength. This means that the frequency values of a spin displayed in ppm scale, would have the same value for a measurement carried out in a 1.5 T than in a 30 T magnet.

1.6 Magnetic Resonance Imaging

Magnetic Resonance Imaging (MRI) provides detailed and non-invasive visualization of any substance containing high density of NMR active nuclear spins. ^1H MRI is mainly used to visualize internal structures of living beings thanks to the high proton density in either water, fat or other soft tissues in the body[17]. The main advantage of MRI is the high spatial resolution and 3D spatial data localization, offering good contrast between tissues due to the difference in proton density and their relaxation constants values. The water protons can exhibit different T_1 and T_2 values depending on the tissues they are contained in or localization in the body. I will explain how these two constants contribute to improving the contrast in MRI images in section 1.6.3. The principal drawback of MRI is the lack of sensitivity, being almost 10^3 less sensitive than other imaging techniques such as PET[18].

While ^1H MRI primarily provides detailed images, magnetic resonance spectroscopic imaging (MRSI) goes further by offering qualitative and quantitative information about the molecules present in the measured sample by analyzing the resonance frequencies of specific nuclei within molecules. MRSI is currently the domain of heteronuclear species, mostly ^{13}C and ^{31}P , due to their large chemical shift range and narrow spectral line widths relative to ^1H , despite their low sensitivity. MRSI main advantage is the capability of performing *in situ* measurements involving a combination of spectral and spatial information.

In the past 20 years the sensitivity limitation has become less important thanks to the development of ^{13}C hyperpolarization techniques such as dissolution dynamic nuclear polarization (d-DNP) and para-hydrogen induced polarization (PHIP), boosting the level of nuclear spin polarization thousands of times greater than the thermal one. Although the spatial resolution is limited, high temporal *in vivo* measurements are possible thanks to hyperpolarization[19]. Moreover, since magnetic resonance avoids the use of ionizing sources, MRI is ideal for patients who need to be scanned regularly.

1.6.1 Fundamental theory of MRI

In MRI, the external magnetic field is made spatially dependent through the application of magnetic field gradients[20]. These gradients are small perturbations superimposed on the main magnetic field B_0 , producing a small field variation ($< 1\%$). These perturbations are linear to B_0 :

$$B_i = B_0 + G_t \otimes r_i \quad (1.13)$$

Where B_i is the magnetic field at the location r_i (m), G_t (mT/m) is the total gradient amplitude, mathematically represented as a tensor, and \otimes is the Kronecker product. Magnetic gradients produce linear variations either in x, y or z axis direction. Each one is assigned to specific functions: slice selection (1.6.1.1), frequency encoding (1.6.1.2), and phase encoding (1.6.1.3).

The presence of magnetic field gradients requires an expanded version of the Larmor equation given in 1.1:

$$\omega_i = \gamma(B_0 + G \cdot r_i) \quad (1.14)$$

Where ω_i is the frequency of the nuclei at the position r_i (m), γ is the gyromagnetic ratio of the nuclei, and G (mT/m) is a vector representing the total gradient amplitude in a specific direction. The presence of the gradient makes each nuclei resonate at a unique frequency depending on the position within the gradient field. In imaging, the MRI image is simply a frequency and phase map of the protons generated by unique magnetic fields at each point throughout the image. The displayed image consist of pixels that represent volume elements (voxels) of the object under study. The pixel intensity is proportional to the number of protons contained within the voxel, whose can be also weighted by either T_1 or T_2 relaxation times.

1.6.1.1 Slice selection

The first step to run an MRI experiment is the localization of the radiofrequency excitation to the region of space, which is accomplished through the use of frequency-selective

excitation along with a gradient called slice selection gradient, G_{ss} . The gradient direction determines the slice orientation. The gradient amplitude together with certain radiofrequency pulse characteristics determine the slice thickness and slice position (Fig. 1.5).

A slice selection radiofrequency pulse has two parts associated: the offset of the pulse (central frequency) and the frequency bandwidth (spectral window). When the pulse is emitted in the presence of the slice selection gradient, only a narrow region of the tissue achieves the resonance condition and absorbs the radiofrequency energy.

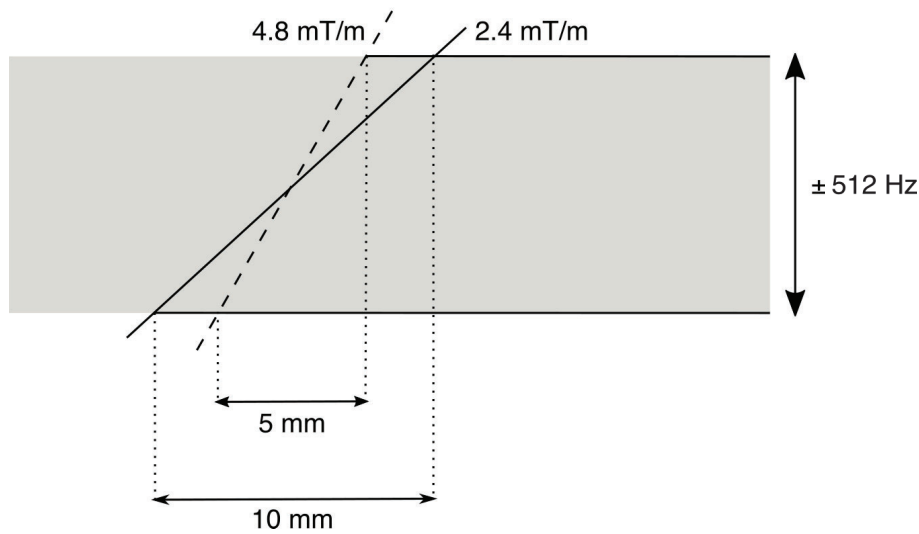


Figure 1.5: The desired slice thickness is determined by the slice selection gradient amplitude for a given range of frequencies. In this example we can achieve a 5 mm thick slice with a 4.8 mT/m gradient, in a 512 Hz frequencies bandwidth. The strongest the gradient, the thinner the slice.

Different slice positions are achieved by changing the central frequency. The slice thickness is determined by the gradient amplitude G_{ss} and the bandwidth of frequencies $\Delta\omega_{ss}$ incorporated into the rf pulse:

$$\Delta\omega = \gamma\Delta(G_{ss} * \tau) \tag{1.15}$$

Usually, $\Delta\omega$ is fixed, so the thickness (τ) is just modified by changing the amplitude of the G_{ss} . Thinner slices require larger G_{ss} .

1.6.1.2 Frequency encoding

In an imaging pulse sequence, the MR signal is always detected in the presence of a gradient known as the readout gradient or frequency encoding gradient G_{FE} , which produces

one of the two visual dimensions of the image (Fig. 1.6). Usually, the sequence uses a

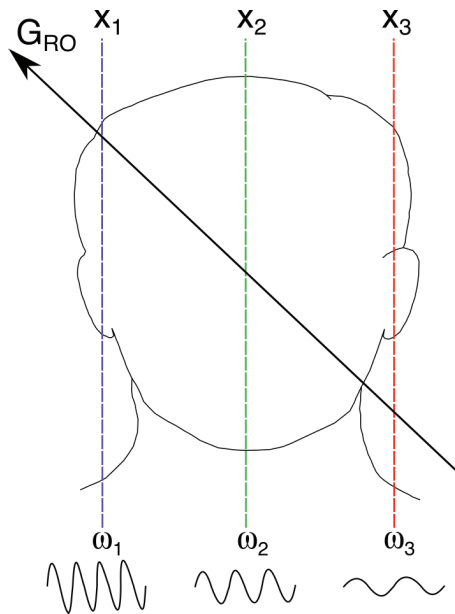


Figure 1.6: Frequency encoding readout process. After the excitation, each proton within the excited slice precesses at the same frequency. During the detection of the echo, a gradient (G_{FE}) is applied, causing a variation in the frequencies for the protons generating the echo signal. The frequency of precession ω_i for each proton depends upon its position x_i , according to the equation 1.16

pulse excitation, such as a 90° slice-selective pulse, to excite a particular region of the object under study. Following excitation, the next magnetization within the slice is oriented perpendicular to the B_0 and will precess with the frequency ω_0 . T_2^* processes induce dephasing of the transverse magnetization. This dephasing can be reversed to form an **echo** signal by applying a 180° rf pulse or a gradient echo pulse.

As the echo is forming, the readout gradient is applied perpendicular to the slice direction. This new gradient field makes the nuclei precess at different frequencies depending on their position in the magnet. Each of these frequencies is superimposed into the echo, and the whole range of frequencies can be calculated with the equation 1.16. The magnitude of the G_{FE} and the frequency that is detected enables the corresponding position of the nuclei to be determined.

$$\Delta\omega_{FE} = \gamma\Delta(G_{FE} * FOV_{FE}) \tag{1.16}$$

Where $\Delta\omega_{FE}$ is the total range of frequencies in the frequency encoding dimension, G_{FE}

is its gradient amplitude and FOV_{FE} is the field of view.

1.6.1.3 Phase encoding

Now we are going to focus on the last and third direction, the phase encoding dimension. The phase encoding dimension is visualized along with the frequency encoding dimension in the MRI image. The phase encoding gradient, G_{PE} , is perpendicular to both G_{SS} and G_{FE} . It differs from the previous gradients because it is the only gradient that changes amplitude during the data acquisition loop of a standard two-dimensional imaging sequence. Any signal amplitude variation detected from an acquisition to the next is assumed to be caused by the influence of G_{PE} during the measurement.

The principle of phase encoding is based on the fact that the proton precession is periodic in nature. Prior to the application of the G_{PE} a proton within a slice precesses at the base frequency ω_0 . In the presence of G_{PE} its precessional frequency increases or decreases according to equation 1.14. Once G_{PE} is turned off, the proton precession returns to its original frequency, but ahead or behind in phase compared to its previous state (Fig. 1.7).

The amount of phase shift induced depends on the magnitude and duration of G_{PE} that the proton experienced and its location. Protons located at different positions in the phase encoding direction experience different amounts of phase shift for the same G_{PE} pulse.

The MRI image information is obtained by repeating the slice excitation and signal detection multiple times, each with a different amplitude of G_{PE} .

1.6.2 Radiofrequency coils

All MR measurements require a transmitter and receiver coil or antenna to broadcast the rf pulses and detect the NMR signal. Although transmitter coils can be any size and shape, the one requirement that must be met is that they generate an effective B_1 field perpendicular to B_0 . Another feature of most transmitter coils is that they can produce uniform rf excitation over a desired area; that is, a volume can be defined within the coil in which all protons experience the same amount of rf energy (B_1 homogeneous region).

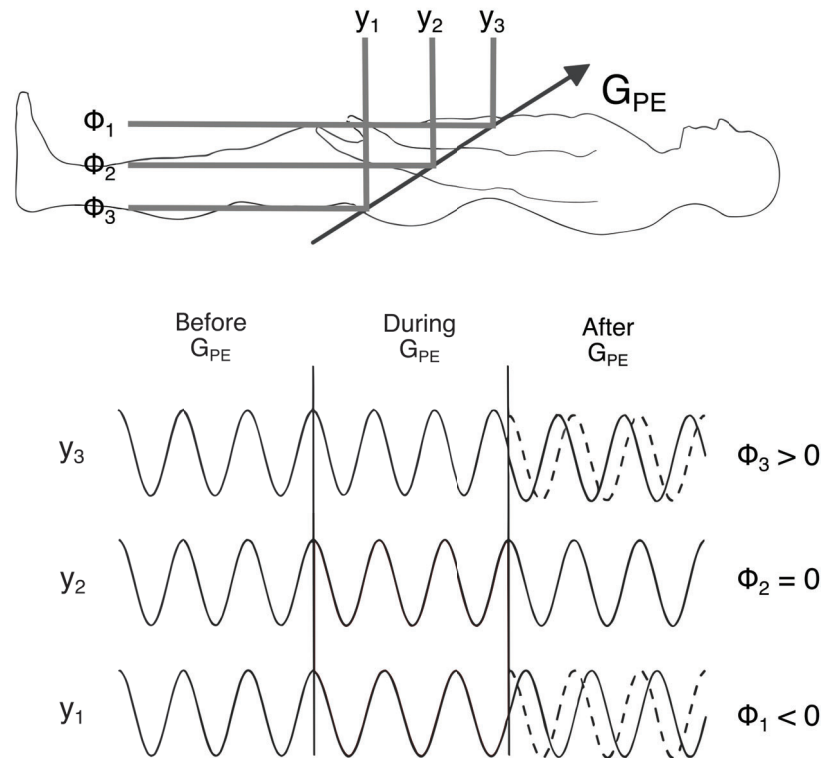


Figure 1.7: Schematic explaining the phase encoding gradient. Applying the G_{PE} in a human, the protons experience a different gradient amplitude depending on the position and the precessional frequency experience a shift. The protons placed in the middle of the gradient do not experience a shift in phase frequency at all (y_2). The protons experiencing a small gradient precess slower and are dephased negatively (y_1). The protons experiencing a big gradient magnitude, precess faster and are dephased positively (y_3)

MR systems use surface coil and either saddle or volumetric bird cage coil designs, which produces uniform rf excitation even though the coil opening is parallel to B_0 . These coils are often adjusted or tuned to the patient to object under study to get the maximum efficiency in rf transmission. The coils can detect a wide variety of nucleus choosing the right frequency position of the spectrum. The most used coil is a dual-tuned coil for ^{13}C and ^1H . In general, to maximise the signal-to-noise ratio (SNR), it is recommended to use a transmit volume coil in combination with a dedicated receive-only surface coil. Volumetric transmit/receive coils should be chosen only when no surface coil is available that covers the entire area to be examined or to obtain images with a homogeneous image brightness. The most commonly used types of coils are as follows:

- **Volumetric RF coils:** Allow the acquisition of a homogeneous signal from an entire

volume (cylindrical shape). In preclinical MRI scanners, the bore diameter can have different dimensions from 30 mm to 72 mm diameter for preclinical scanners.

- **Surface RF coils:** These coils are placed on top or the bottom of the region of interest and provide good SNR close to the surface of the object

1.6.3 MRI sequences

A pulse sequence is the measurement technique by which an MRI image is obtained. It contains the hardware instruction (rf pulses, gradient pulses and timings) necessary to acquire the data in the desired manner.

Comparison and understanding of pulse sequences is facilitated by the use of timing diagrams. Elapsed time during sequence execution is indicated from left to right along the horizontal axis. Each horizontal line corresponds to a different hardware component. In figure 1.8 I have represented a "Pulse-acquire" with gradient echo. The diagram is composed by 5 lines: one representing the radio frequency transmitter (RF excitation pulse), one representing the slice selection gradient or G_z (in red and mentioned in section 1.2.1.1) representing the z axis in the MRI scanner, one representing the phase encoding gradient or G_y (in blue and mentioned in section 1.2.1.2), one representing the frequency encoding gradient or G_x (in yellow and mentioned in section 1.2.1.3), and last the data acquisition line with the echo signal.

A commonly used pulse sequence in MRI is the spin echo sequence because it compensates for the constant field heterogeneities. It has at least two rf pulses, an excitation pulse (90°) and either a refocusing pulse (180°) or a gradient echo to generate the spin echo. A refocusing pulse is required for every echo produced. Spin echo sequences also use gradient pulses of opposite polarity in the readout and slice selection directions to refocus the spins (protons mostly) at the same time as the spin echo. In this specific sequence, a dephasing frequency encoding gradient is applied at the same time as the phase encoding gradient so as to cause the spins to be in phase at the center of the acquisition period. This gradient is negative in sign from that of the frequency encoding gradient turned on during the acquisition of the signal. An echo is produced when the frequency encoding gradient is turned on because this gradient refocuses the loss of spins coherence which occurred from the dephasing gradient. The reversal of the gradient is responsible

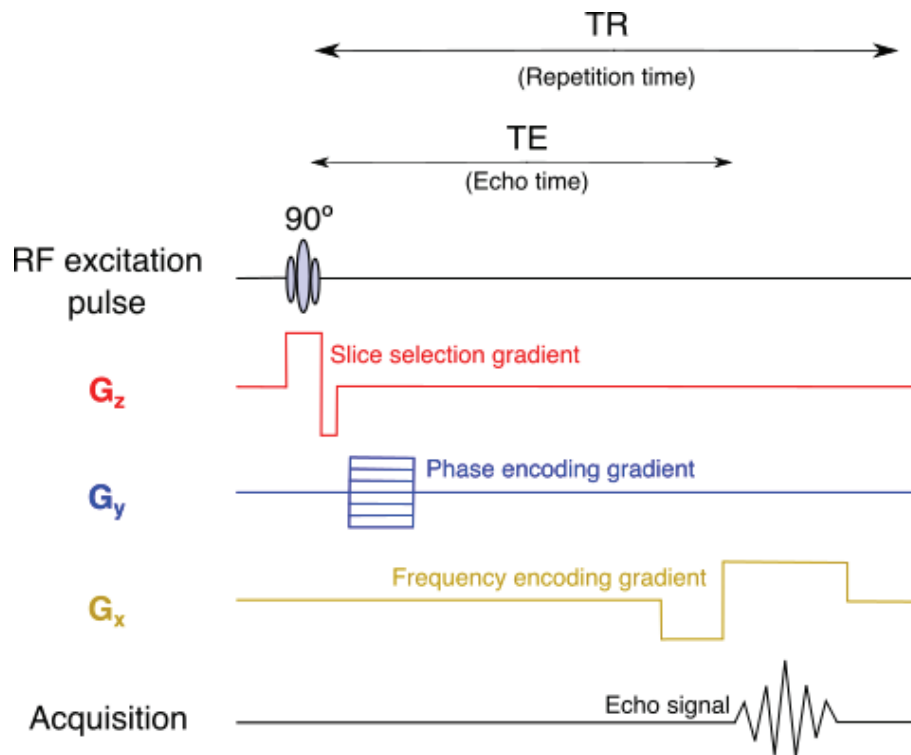
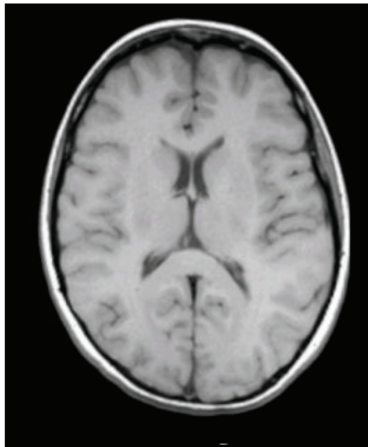
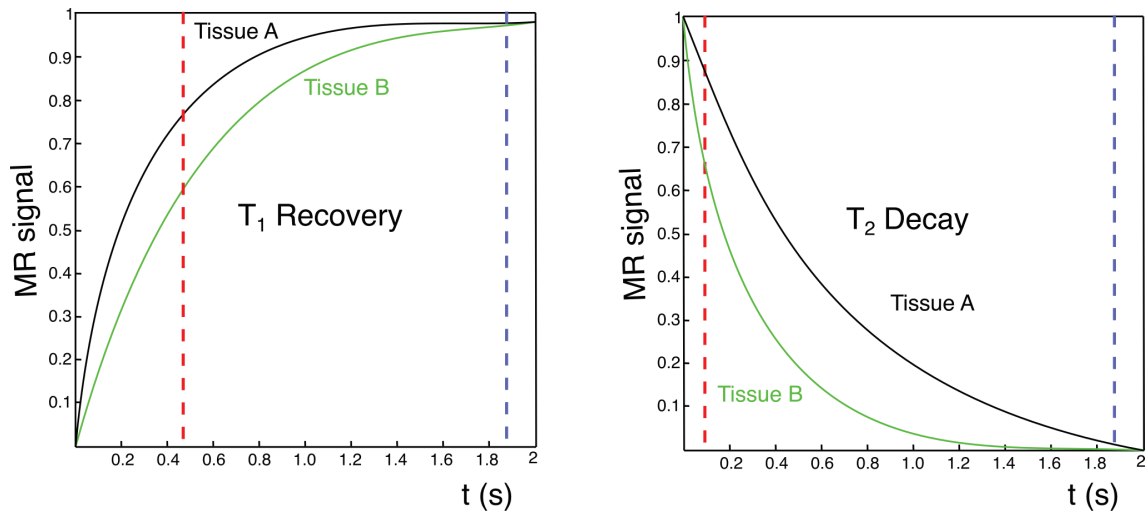


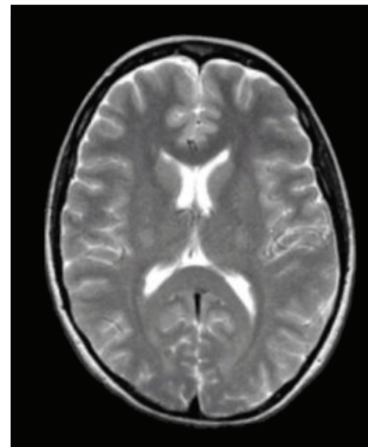
Figure 1.8: Pulse-acquire gradient echo in MRI. The repetition time, TR, is the time between successive excitation pulses for a given slice. The echo time, TE, is the time from the excitation pulse to the echo maximum.

for the echo. In this sequence the echo is produced by the gradient echo, not a 180° pulse. The standard sequences for proton imaging are generally used to produce T_1 -weighted images when acquired with relatively short repetition time (TR) and echo time (TE), with less than 700 ms and 30 ms respectively. In this case the contrast and the brightness of the image are predominantly determined by T_1 values of the protons in the selected region of the tissue. In short a TE sequence there is a little spin dephase in the transverse plane making a low T_2 effect. Having a short TR we increase the effect of the T_1 by giving a short time for the spins to recover from its equilibrium position, then we lose signal from tissues that recover slowly (large T_1).

T_2 weighted images are acquired with relatively long TR and TE (more than 700 ms). In this case the contrast and the brightness of the image are predominantly determined by T_2 . In long TE acquisition, the effect of T_2 predominantly as there is plenty of time for the spins to dephase and the signal will be lost from tissues that dephase fast (short T_2). Furthermore, having enough time for all the spins to recover, the effect of T_1 is going to be negligible. We show these effects in figure 1.9.

T₁ weighted

Short TE and TR

T₂ weighted

Long TE and TR

Figure 1.9: Diagram illustrating the fraction of the FID recorded by the instrument to acquire the respective image measured in T₁ and T₂ weighed

1.6.4 Magnetic Resonance Spectroscopic Imaging

In this thesis I only focus in Chemical Shift Imaging (CSI), a MRSI sequence. CSI is a multiple voxel technique to obtain localized spectroscopic information from multiple areas of the same slice with a single measurement. CSI is the most common method to obtain spatially localised NMR spectra also called magnetic resonance spectroscopic imaging (MRSI). CSI are analogous to standard imaging techniques for using phase-encoding gradient in both dimensions of the spatial localization. In these experiments we obtain molecular information through their Larmor resonances. It would not make

sense to use frequency encoding dimension to get localized data because the Larmor frequencies would be affected positionally by the gradient. Each localized spectrum (Fig. 1.10 b)) in the matrix is found in a voxel (volumetric pixel) and we can localize the information overlapping the resulting CSI matrix with a proton image (Fig. 1.10 a)).

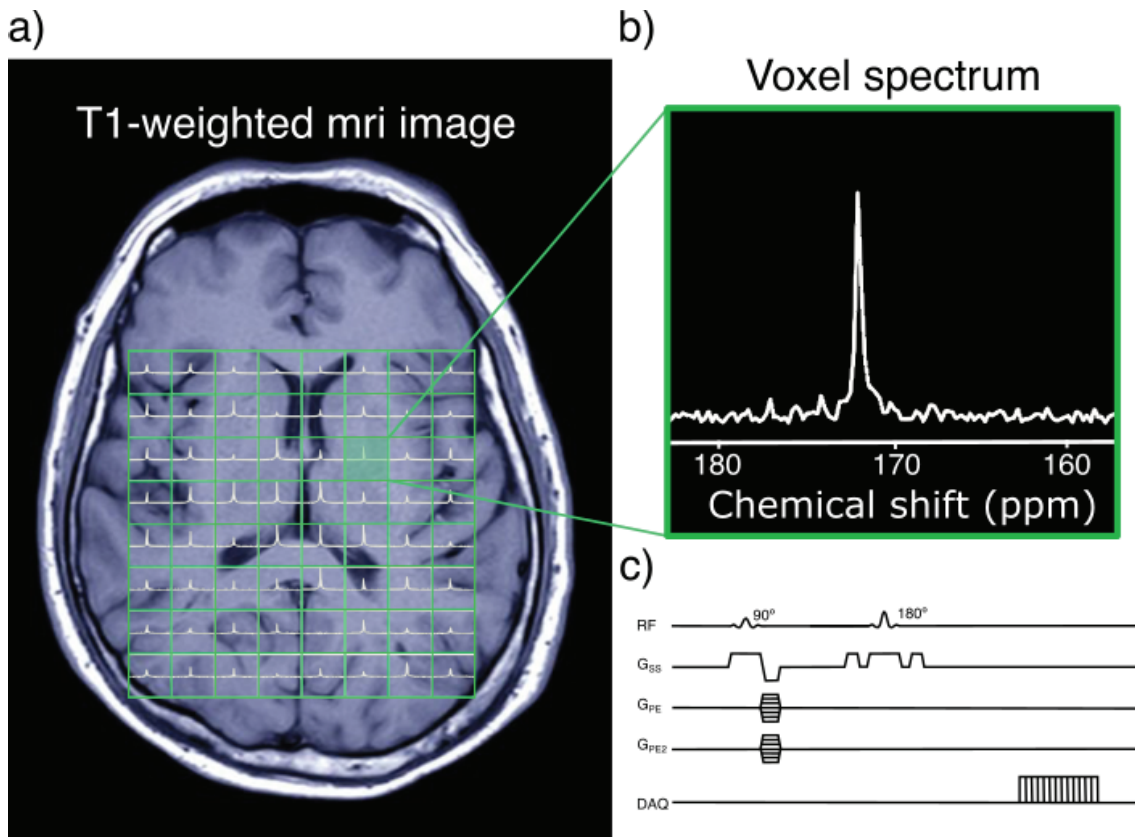


Figure 1.10: Representation of a CSI experiment. a) T₁ weighted MRI image of a human brain, with a 8x8 CSI matrix overlapping with the corresponding ¹³C spectra in each voxel. b) Zoom of one of the voxels contained in the CSI matrix. In the spectrum we can see the [1-¹³C]pyruvate signal at 172 ppm. c) Pulse sequence of the 2D-CSI experiment showing the radiofrequency pulses, all 3 gradients and the acquisition diagram.

1.7 Hyperpolarization-enhanced MRI and MRSI

Hyperpolarization has emerged as a revolutionary technique in the last 20 years pushing the boundaries of NMR sensitivity and opening new avenues for many research fields. Some of these fields include molecular imaging in medicine[21], elucidating molecular structures[22], dynamics[23], biomolecular interactions[24], drug discovery[25], and reaction monitoring[26]. Unlike conventional NMR, hyperpolarization techniques enhance the polarization of nuclear spins to levels far exceeding those achievable under thermal equilibrium conditions. This remarkable enhancement of nuclear polarization translates directly into more intense NMR signals.

Hyperpolarization methods leverage a variety of physical principles to produce highly polarized nuclear spins. These techniques allow researchers to observe NMR signals that were once too weak to be detected, enabling investigating previously inaccessible answers for chemistry, physics, and biology[27, 28]. Hyperpolarization is gaining significant attention due to its potential to revolutionize fields such as molecular imaging for medical studies.

In this thesis, I will delve into the underlying principles of the two hyperpolarization techniques most used for metabolic imaging, more specifically Dynamic Nuclear Polarization (DNP) and Para-hydrogen Induced Polarization (PHIP). I will discuss also how can they tandem a proper synergy with organs-on-chip for the future of molecular imaging in personalized medicine. These techniques are at the core of my PhD work.

1.7.1 Comparison between hyperpolarized and thermal NMR

The polarization of nuclear spins at room temperature is low even in high magnetic fields, due to the weak interaction of nuclear spins with magnetic fields:

$$p_{thermal} = \tanh\left(\frac{B_0 \hbar |\gamma|}{2k_B T}\right) \quad (1.17)$$

Where B_0 is the external magnetic field (T), \hbar is the reduced Planck constant, γ is the gyromagnetic ratio of the spin under study, k_B is the Boltzmann constant, and T is temperature (K). In figure 1.11 are represented the polarisation level of 3 spins 1/2 (electron, proton and carbon-13) as a function of T/B_0 .

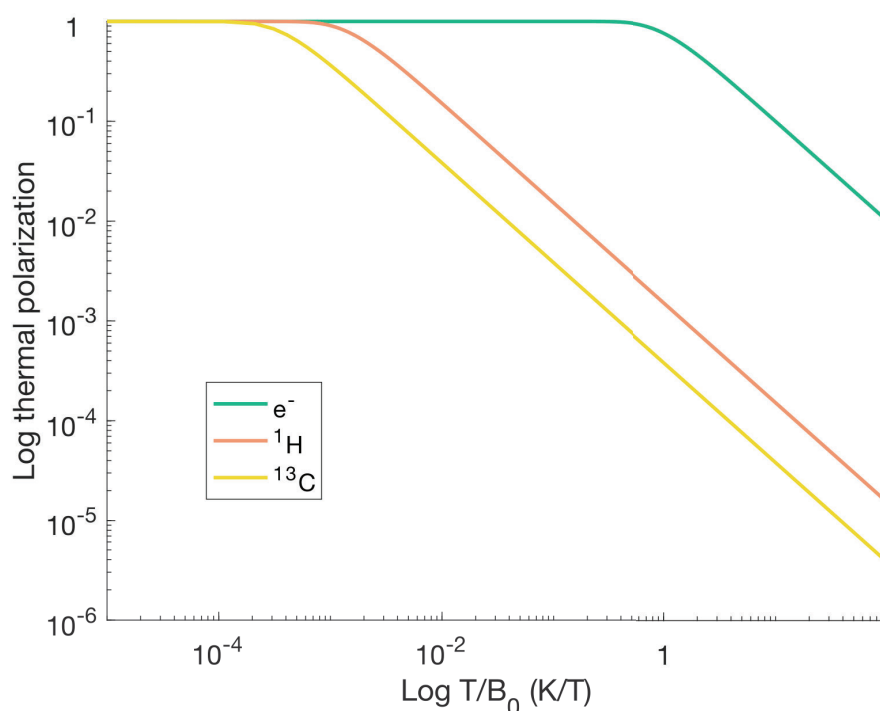


Figure 1.11: Polarization of the spins ensemble for electron (green), proton (red) and ^{13}C carbon (yellow) as a function of T/B_0 .

The inherently low NMR sensitivity encouraged the scientific community to look for alternatives or new approaches to enhance the NMR signal avoiding long acquisition times or many averages or scans (accumulation of data during an acquisition). DNP, for example, can strongly polarize nuclear spins for $>10,000$ times in a temporal window of less than 1 hour[9, 29]. The main motivation for preparing a spin system in a hyperpolarized state is to enhance the signal-to-noise-ratio (SNR) in spectroscopic or imaging applications. The aim is to achieve stronger signals in magnetic resonance experiments compared to those attainable under thermal equilibrium conditions. For an ensemble of $1/2$ spin nuclei we consider hyperpolarization when the NMR signal is doubled compared to thermal equilibrium[30]. In acquisitions limited by SNR, this reduction would shorten the experiment duration by a factor of four[31]. In a hyperpolarized experiments, a single scan yields thousands more SNR compared to a thermal acquisition with hundreds of averages.

The SNR is defined in NMR as:

$$SNR \propto n\gamma_e T^{-1} \sqrt{\gamma_d^3 B_0^3 NS} \quad (1.18)$$

Where n is the nuclei in resonance, γ_e is the gyromagnetic ratio of the excited nuclei, T is the temperature of the sample (K), γ_d is the gyromagnetic ratio of the detected nuclei, B_0 is the applied magnetic field strength (T) and NS is the number of scans or averages. There are only 3 ways of improving the SNR without changing the $1/2$ nuclear spin at thermal equilibrium state: increasing the external magnetic field strength (increases by a factor of $B_0^{3/2}$ (eq. 1.18)), decreasing the temperature (inversely proportional) or increasing the number of averages (increases by a factor of $NS^{1/2}$ (eq. 1.18)). The magnetic field strength is limited by many factors such as hardware limitations, safety and price, being expensive to manufacture, install, and maintain. The initial capital investment for ultra-high field instruments can be prohibitive for many research institutions and companies. An understandable comparison would be to compare the increase in SNR of a spin $1/2$ at 1 T and 30 T. Considering the same nuclei, the same acquisition temperature and the same number of averages, we would obtain a signal increase of 164 times comparing a 10 \$ magnet (1 T) with a 10,000,000 \$ magnet (30 T).

1.7.2 Hyperpolarization techniques

Most of the hyperpolarization techniques rely on a polarization source that can act as a reservoir of low entropy with which the nuclear spins can exchange energy at lower temperatures. These sources are replenished directly by establishing thermal equilibrium characterized by Boltzmann statistics¹ under the experimental conditions, by thermally induced or photoinduced processes in molecular species or materials[32].

For example in dissolution Dynamic Nuclear Polarization (dDNP), the polarization source is free electrons in a radical molecule². The electrons are much more polarizable than nuclear spins (by a factor of 10^3 - 10^5) under the same magnetic field strength. They can reach the polarization unity at relatively low temperatures (tens of kelvin degrees) and high magnetic field (described in figure 1.11). This polarization can be then transferred to the target spin through a specific microwave frequency. Other techniques such as parahydrogen induced polarization (PHIP), rely on preserving the population on an NMR invisible spin state using parahydrogen gas. PHIP breaks the symmetry of the

¹The Boltzmann statistics describes the number of nuclei in each spin state depending on the temperature and the difference of energy between levels (eq. 1.2).

²Molecule containing one or more unpaired electrons in valency shell or outer orbit

singlet state through a chemical reaction, triggering the corresponding cascade to equilibrium, thus producing the hyperpolarized signal. I will discuss this topic in more detail in section 1.7.2.4.

1.7.2.1 Brute Force

Brute force hyperpolarization takes a simple and remarkably effective approach, leveraging extreme conditions to achieve relatively high polarization levels compared to room temperature equilibrium[33].

The principle is to subject the sample to very low temperature (helium liquid temperatures $\approx 1 - 4$ K), and high external magnetic fields (more than 1 T) perturbing the thermal equilibrium and inducing a difference in the spin populations following the Boltzmann distribution (eq 1.2, page 32). This alteration from the steady-state leads to an overpopulation of specific nuclear spin states, resulting in significantly enhanced NMR signals. A 1% of ^1H polarization can be reached under these conditions and then transfer the polarization to the ^{13}C through thermal mixing[34]. This method has well demonstrated a >1500-fold enhancement in ^{13}C signal for key small-molecule metabolites such as [$1\text{-}^{13}\text{C}$]pyruvic acid[35], [$1\text{-}^{13}\text{C}$]lactate[36], and [$1\text{-}^{13}\text{C}$]acetate[37]. This concept challenges the conventional NMR paradigm that relies on the Boltzmann distribution and explores a novel path to amplify nuclear polarization without the need for complex polarizing agents or sophisticated equipment[30].

1.7.2.2 Spin Exchange Optical Pumping (SEOP)

The Spin Exchange Optical Pumping (SEOP) technique for generating spin-polarized gases such as ^3He and ^{129}Xe is fundamentally straightforward and cost-effective to implement in experiments, yet still provides excellent performance[38]. The basic concept consists in a hot vapor of alkali-metal (usually Rubidium) atoms that are optically irradiated with light to polarize the unpaired electron spins. A noble gas (typically ^3He) is passed through the vapor and collides with the alkali-metal atoms enabling polarization transfer to the noble gas nuclei.

This hyperpolarization method is fast compared to others, enabling polarization times in the seconds-minutes time scale reaching polarization levels of 50 % [39]. Although this

technique has a limited application to only noble gas atoms (^{129}Xe [40] and ^3He [41]), some SEOP-hyperpolarized MRI clinical studies have been performed[42]. This remarkable gain in polarization enhancing the MRI signals is raising potential to improve sensitivity and contrast in pulmonary imaging[43].

1.7.2.3 Dissolution Dynamic Nuclear Polarization (dDNP)

Dynamic Nuclear Polarization (DNP) covers a range of subtechniques such as dissolution DNP (the one this thesis will be focused on), solid-state DNP and Overhauser DNP³.

Dissolution DNP (dDNP) is a hyperpolarization technique based in the crosspolarization of an electron from a free radical molecule to a nuclear spin through a microwave frequency irradiation (process represented in figure 1.12).

We have to fulfill a number of specific conditions to hyperpolarize a sample with dDNP:

³Overhauser-DNP operates at room temperature and is based on the Overhauser crosspolarisation between the free electrons from the free radical molecule and the nuclei of interest in the sample.

Requirement	Definition	Function	Examples
Magnetically active nuclear spins ($I \neq 0$)	These are the nuclei that will be hyperpolarized and give NMR signal	Information of the system	^1H , ^{13}C , ^{15}N
Low temperature	The sample has to be inside a cryostat to reach liquid helium temperatures	Reach higher polarization levels	1.4 K
High magnetic fields	The cryostat has to be surrounded by a superconductive magnet	Enable the difference of spin states	> 3.35 T
Free radical molecules	The sample has to be mixed with molecules containing unpaired electrons	Transfer the polarization from the electron to the spin of interest	TEMPO, OX63, BDPA, UV-induced radicals
Paramagnetic atom/molecule	Atoms and molecules with one or more unpaired electrons in the outermost orbital	Reduce the T_1 of the free radical electron	Gd-DOTA, Gd^{+3}
Glassing agent (not needed for PA)	Chemical solvent that mixed with the sample make it transparent to MW once frozen	Prevent opaque solidification of the sample which could interfere with MW.	Glycerol, DMSO
Microwave frequency irradiation	Radio-frequency radiation in the electromagnetic spectrum (900–2450 MHz).	Source of energy to transfer efficiently the polarization from the free electron to the spin of interest	microwave irradiator

Table 1.1: Variables in a DNP experiment classified by requirement, definition, function and examples.

The enhancement of the NMR signal caused by dDNP was first described by Jan H. Ardenkjær-Larsen et.al in 2003 in Malmö, and they reached an increase in the SNR in >10,000 times in a ^{13}C signal[9]. Theoretically the nuclear spin polarization can be enhanced by a factor up to γ_e/γ_n , where the $\gamma_e = 1.76 \times 10^{11} \text{ rad} \cdot \text{s}^{-1} \cdot \text{T}^{-1}$ and the γ_n is the gyromagnetic ratio of the nuclear spin under study.

DNP can fully polarize until unity the electrons at a T/B_0 ratio < 1 , or in other words, at relatively high magnetic field (> 1 T) and liquid helium temperature or lower (< 4 K). This extremely high electron polarization can be then transferred to nearby nuclear spins

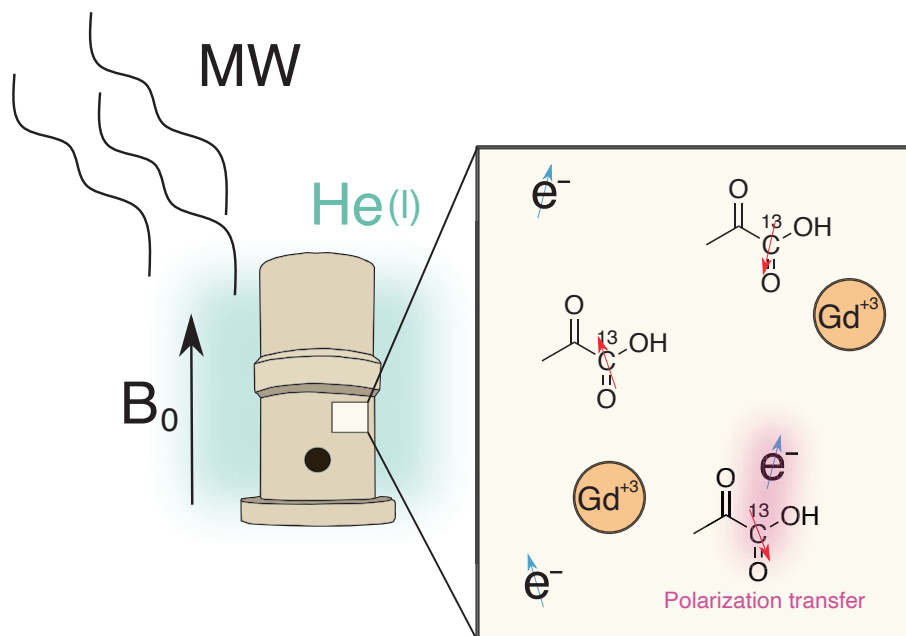


Figure 1.12: Schematic representation of the sample cup introduced inside the polarizer under external magnetic field and surrounded by liquid helium. The sample cup (represented in the figure surrounded by liquid helium) contains the ^{13}C -labelled compound (in this case $[1-^{13}\text{C}]$ pyruvate), the Gd-DOTA and the free radical molecule with an unpaired electron.

by irradiating the sample with microwave-frequency.

The source of free electron are radical molecules with an unpaired electron and soluble in the sample to reach homogeneity. Polarization transfer is only efficient when homogeneous dispersion is achieved resulting in a "glass-like" appearance upon freezing, characterized by transparency rather than opacity, and thereby facilitating microwave penetration through the frozen solution.. This method benefits from the high electron polarization and its short T_1 . Even though the electron T_1 is short, the sample is also prepared with a small amount of a paramagnetic compound, which reduces the electron T_1 and enhances the yield of the polarization. This spike enables reaching higher levels of polarization in short build up time curves. After ensuring homogeneity within the sample, it is irradiated with micro-frequency waves to induce the polarization transfer from the free radical electrons to the nuclear spins under study. The signal increase is often tracked every 5 minutes by acquiring a small flip angle (5°) and plotted over time making the build up curve (Fig.1.13):

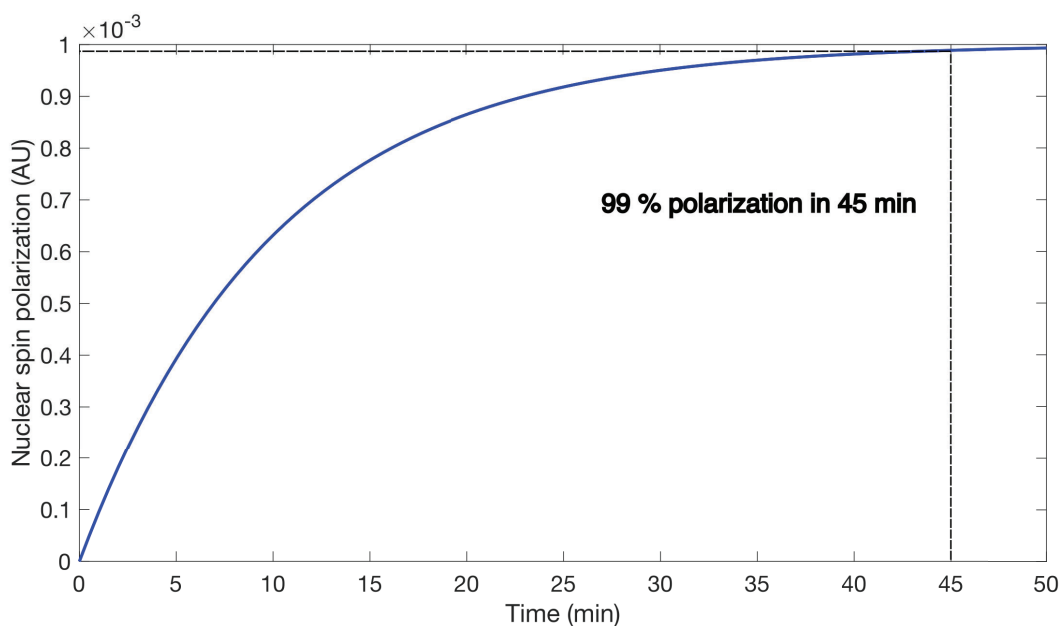


Figure 1.13: Build-up function showing the evolution of the ensemble spin polarization over time inside the polarizer when the microwave source is irradiating the sample.

The depolarized electrons then rapidly repolarize due to the short T_1 , whereas the nuclear spins retain nonequilibrium polarization. This nonequilibrium polarization diffuses through the sample, and after some time (typically tens of minutes), the nuclear spins in the sample are sufficiently polarized (polarization level values between 5-60 %). At this point the sample is rapidly dissolved with a pressurized hot solvent, and ejected from the cryostat.

The most used commercial apparatus for preclinical research during the past 15 years is the Hypersense from Oxford Instruments. The machine is composed by a liquid helium cryostat operated under vacuum at lower pressure reaching 1.4 K in a high-field magnet of 3.35 T, with a microwave source integrated with the corresponding mechanisms to make it automated and user-friendly.

1.7.2.4 Para-Hydrogen Induced Polarization (PHIP)

Para-Hydrogen Induced Polarization (PHIP) is a hyperpolarization technique which takes advantage of the singlet state spin population of the molecular hydrogen to enhance the NMR signal of some 1/2 spin nuclei, such as ^{13}C , ^{15}N and the ^1H themselves. Molecular hydrogen is composed by two atomic hydrogens with spin number 1/2, that are magnet-

ically equivalent. The molecular hydrogen can then exist as two possible nuclear spin isomers: orthohydrogen ($I = 1$) and parahydrogen ($I = 0$). Orthohydrogen is also called "triplet state", because the angular momentum projection along the z-axis can take three different values: $m_I = -1, 0, +1$. On the other hand parahydrogen (p-H₂) is called the singlet isomer ($m_I = 0$) and it is not magnetically active because of its molecular symmetry, making it invisible in conventional NMR.

These four states can be written as a linear combination of the Zeeman basis states⁴:

$$\begin{aligned}
 \text{Singlet State } |S_0\rangle &= \frac{(|\alpha\beta - \beta\alpha\rangle)}{\sqrt{2}} \\
 |T_+\rangle &= \frac{(|\alpha\alpha\rangle)}{\sqrt{2}} \\
 \text{Triplet State } |T_0\rangle &= \frac{(|\alpha\beta + \beta\alpha\rangle)}{\sqrt{2}} \\
 |T_-\rangle &= \frac{(|\beta\beta\rangle)}{\sqrt{2}}
 \end{aligned} \tag{1.19}$$

All four states are equally populated at room temperature resulting in a mixture of 25 % each. However, the para-state is lower in energy and therefore thermodynamically more stable state. Parahydrogen can be obtained flowing H₂ gas over a Fe₂O₄ catalyst at extremely low temperatures. The enrichment is about 50 % at 77 K and increases to 100 % at temperatures below 25 K. This process must be done carefully because the H₂ liquifies at temperatures below 20 K, and the working pressures could become dangerous and the process would be unsuccessful.

In PHIP there is just one (ALTADENA) or two (PASADENA) populated quantum states. Once relaxation begins, quantum transitions occurs towards equilibrium producing large NMR signals. The requirement is to break the symmetry of the hydrogen molecule, and have different chemical shifts for each hydrogen nuclei. This happens when parahydrogen is added to another molecule through a process called hydrogenation reaction. These protons end up in chemically different positions in the product making them magnetically different. Thanks to the original para-enrichment only the para-spin state is populated. As mentioned before, hyperpolarization occurs due to the big population dif-

⁴Zeeman basis states corresponds to the two possible states of a 1/2 spin system under an external magnetic field, α and β . In the hydrogen molecule, there are two bonded spin 1/2, so 4 Zeeman eigenbasis states are possible

ference between quantum states producing non-steady states[44].

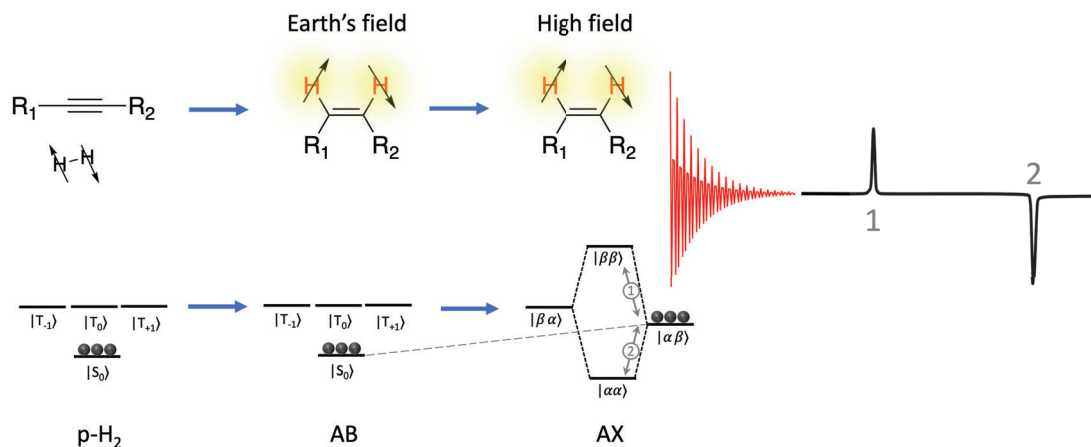


Figure 1.14: Diagram showing a para-hydrogen hydrogenation reaction and the corresponding quantum states in each step of the procedure. In this case the figure represents an ALTADENA (Adiabatic Longitudinal Transport After Dissociation Engenders Net Alignment) reaction. The process starts with an alkyne compound and its hydrogenated with parahydrogen at earth's field, keeping the all the population in the same state. After measuring the sample in a high field, we would detect two peaks with different phase corresponding to the spins precession of transitions 1 and 2.

An appropriate example of this procedure would be the PHIP-ALTADENA experiment showed in Figure 1.14. An alkyne substrate is hydrogenated with p-H₂ at low magnetic field (earth's field), and the AB (A being a spin 1/2 and B another spin 1/2) system matches the condition $^{13}J_{AB} \gg \Delta\omega$ ⁵. Here the three triplet quantum states are degenerated⁶ ones from the triplet state and the only populated one, the singlet state. After increasing the magnetic field, the condition $^{13}J_{AB} \ll \Delta\omega$ is fulfilled and the eigenbasis (Fig. 1.14, AB system) becomes the Zeeman basis (Fig. 1.14, AX system). Through this field cycling we have an evolution from the singlet-triplet states to the Zeeman states. After applying a 90° pulse we can observe the two transitions showing two antiphased peaks in the spectrum of the Fig. 1.14.

⁵ J_{AB} is the J coupling at 3 chemical bonds between the spin A and the spin B. $\Delta\omega$ is the difference in Larmor frequency at a specific magnetic field strength.

⁶In quantum mechanics, two or more different measurable states of a quantum system are degenerated if they give the same energetic value upon measurement.

1.7.2.5 Signal Amplification by Reversible Exchange (SABRE)

Another approach to enhance the signal using the singlet state of molecular hydrogen, is the Signal Amplification By Reversible Exchange (SABRE), a non-hydrogenative PHIP variant. This technique proves that the polarization transfer from parahydrogen to the substrate of interest does not require incorporation of p-H₂-derived protons into the molecule. In this case, the target molecule becomes hyperpolarized but remains chemically unaltered[45], because the polarization is therefore transferred to the target molecule using an iridium polarization transfer catalyst (PTC). In this process the polarization is transferred through a spin-spin coupling network in the temporary association of the para-hydrogen and the target molecule in the Iridium catalyst. During the SABRE process, the PTC establishes scalar couplings between p-H₂ and the target ligand. It is considered a continuous hyperpolarization technique because that p-H₂ and the target molecule are in chemical exchange on and off the metal center, without altering any of the reagents.

The polarization transfer happens when both molecules are bonded to the catalyst center, and they are placed in a specific magnetic field or using coherence transfer at high field. Under the right circumstances (temperature, magnetic field, solvent...) the couplings between the p-H₂ and the nuclear spin under study in the target molecule convert the hydrogen singlet order to flow into magnetization on the target ligand, including direct transfer to the heteronuclei mentioned before. This flow of order is achieved by level anti-crossing at micro-Tesla field called Amplification by reversible exchange in shield enabling alignment transfer to heteronuclei (SABRE-SHEATH) or at high field in rotating frames created by very weak radiofrequency irradiation. The repetition of the binding and dissociation steps allows the build-up of hyperpolarized target molecule in the sample if there is still some hydrogen in the singlet state left.

1.7.3 Hyperpolarization for metabolic analysis

Hyperpolarized ¹³C MRI is becoming one of the most powerful molecular imaging strategies that allows safe, nonradioactive, real-time, and pathway-specific investigation of physiologic processes that were previously inaccessible to imaging[46]. To extract information from the metabolic pathways, we have to consider which probe we want to

polarize, which usually are biomolecules modified only by the ^{13}C enrichment. The selection of the labelled compound has to take into account two factors:

1. The labelled carbon atom requires a long T_1 , to enable tracking the metabolic conversion for longer and survive transport.
2. The chemical shift difference between the probe and its product, at the labelled position, has to be different enough at the observed B_0 to integrate them independently.

Other variables for biocompatibility to take into account are water solubility and if it is feasible to be injected at physiological pH values.

Some of the protocols for hyperpolarized ^{13}C labelled metabolites have already been used for *in vivo* investigations of metabolism relevant to human diseases. A few examples are [2- ^{13}C]pyruvate for probing mitochondrial metabolism[47] in eukariotic cells, [1,4- $^{13}\text{C}_2$]fumarate for assessing tissue necrosis[48], [^{13}C -bicarbonate for measuring pH[49], [1- ^{13}C]dehydroascorbate (DHA) for interrogating redox capacity[50], [2- ^{13}C]dihydroxyacetone (DHAc) to investigate acute changes in glucose metabolism in liver and kidneys[21], and ^{13}C urea for imaging perfusion[51] and extracellular diffusion[52].

Researchers have used these probes to investigate metabolic and physiological processes associated with a wide variety of neoplastic, inflammatory processes, and metabolic diseases[46]. However, the most widely used hyperpolarization probe so far has been [1- ^{13}C]pyruvate for a considerable number of reasons, some of which are:

1. It is the molecule that has achieved the highest polarization level for its carbon atom, reaching 50 % in 5 T clinical polarizers[53].
2. The C1 of the [1- ^{13}C] pyruvate has a reasonable long T_1 (approximately 77 seconds in a 80 mM dissolution at pH 7 at 1.5 T), therefore enabling *in vivo* studies with high SNR[54].
3. The [1- ^{13}C]pyruvate is also a highly biologically relevant probe, as pyruvate is involved in multiple metabolic pathways such as glycolysis, tricarboxylic acid (TCA) cycle, and amino acid biosynthesis.

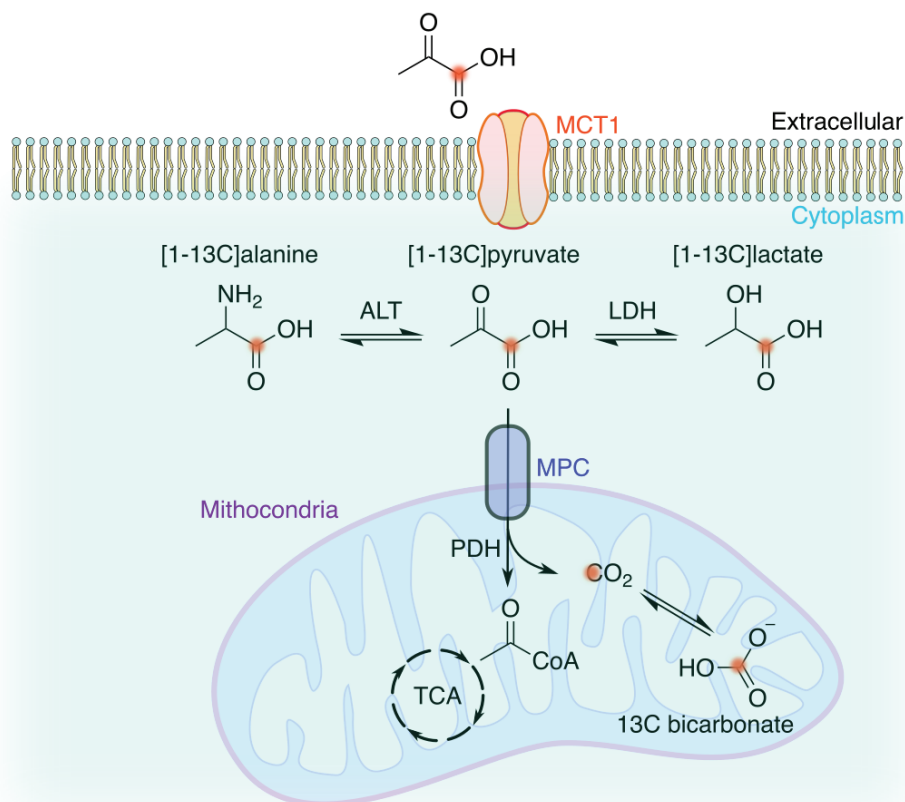


Figure 1.15: Schematic diagram of the pyruvate metabolic pathways. $[1-^{13}\text{C}]$ pyruvate is taken up into the cells through the MCT1 transporter and metabolized in the cytosol into $[1-^{13}\text{C}]$ lactate and $[1-^{13}\text{C}]$ alanine by the enzymes lactate dehydrogenase (LDH) and the alanine transaminase (ALT), respectively. $[1-^{13}\text{C}]$ pyruvate is also transported into the mitochondria through the MPC transporter and metabolized into ^{13}C CO_2 and Acetyl CoA by the enzyme pyruvate dehydrogenase (PDH). In this case CO_2 is rapidly converted to ^{13}C bicarbonate and they reach a chemical equilibrium. MCT1 = monocarboxylate transporter 1, MPC = mitochondrial pyruvate carrier, TCA = tricarboxylic acid cycle. Red circle = position of the ^{13}C hyperpolarized atom

4. Once hyperpolarized $[1-^{13}\text{C}]$ pyruvate has been administered to living organisms, it is rapidly taken up by the cells containing the corresponding transporters (MCT1 and MPC)
5. The $[1-^{13}\text{C}]$ pyruvate is metabolized in seconds by the corresponding enzymes: into $[1-^{13}\text{C}]$ lactate by lactate dehydrogenase (LDH), and alanine transaminase (ALT), both placed in the cytosol⁷.

⁷The cytosol is a semi-fluid substance filling the interior of the cell and embedding the other organelles and subcellular compartments[55]

6. After [1-¹³C]pyruvate has entered the mitochondria by a subgroup of the mitochondrial pyruvate carrier (MCT) family, its converted by the enzyme pyruvate dehydrogenase (PDH) into ¹³CO₂ and acetyl-coenzyme A (Acetyl-CoA) (although the Acetyl-CoA has not the labelled ¹³C).

The production of ¹³CO₂ is the direct readout of PDH activity and flux towards the TCA cycle (Fig. 1.15). [1-¹³C]pyruvate has been widely used to interrogate metabolism in a variety of diseases such as cancer[56], ischemia[57], liver disease[58], and inflammation[59] in preclinical models. Pyruvate was translated to clinical metabolic studies in 2014[60] and has been demonstrated to be safe and feasible[61].

1.7.3.1 Liver disease

Chronic diffuse liver diseases, such as non-alcoholic fatty liver disease (NAFLD) and cirrhosis, are becoming global health concerns and require early diagnosis and proper management[62]. Likewise, liver cancer is the fourth leading cause of cancer-related death in the world[63, 64]. Hepatic metabolism is tightly controlled by a variety of factors and it changes under different liver pathological conditions[65]. Recent studies indicate a strong potential for HP ¹³C MRI in the diagnosis and monitoring in both diffuse liver diseases[66] and liver malignancies[67, 21]. These studies are mainly focused on detection and diagnosis, assessment of disease progression, and prediction of therapeutic responses. The liver is an essential metabolic organ in the body, responsible for the metabolism of carbohydrates, lipids and proteins[68], therefore having pyruvate as a key branch point of multiple metabolic pathways.

As explained in section 1.15 (page 62) Hyperpolarized [1-¹³C]pyruvate is rapidly (order of seconds) taken by cells and converted into different products. HP [1-¹³C]pyruvate is to date the only probe available for human examinations and thus widely used for clinical studies[67]. It has been predominantly used to interrogate metabolism associated with early and precise liver disease diagnosis and disease progression evaluation[69]. For example, the activity of ALT is usually elevated in patients with liver injury, which can lead to the increase of [1-¹³C]alanine[70]. Abnormal glucose and lipid metabolism also often occurs in NAFLD patients[71]. In addition, metabolic reprogramming in hepatocellular carcinoma (HCC), especially the increased lactate production[72], can be identified by

HP ^{13}C MRI.

Compared to current imaging methods, HP ^{13}C MRI provides unique metabolic information about pathway-specific alterations without using ionizing radiation. This additional metabolic information opens up possible novel diagnostic and therapeutic opportunities.

Anareobic metabolism

Hyperpolarized $[1-^{13}\text{C}]$ pyruvate is widely studied for being the first clinical probe ever tested, its high polarization levels and long T_1 , and its versatility for diagnosis of different diseases[73]. It is used to interrogate metabolism associated to liver disease diagnosis and evaluation under treatment. Generally a common altered feature in metabolism is the over regulated glucose uptake and corresponding fermentation to lactate(Fig. 1.16, orange section)[74]. This phenomenon is also observed in the presence of healthy mitochondria and in the presence of cancerous cells is called Warburg effect[75]. The strategy is different when the liver disease is induced by diet or alcohol, and the pyruvate-alanine conversion becomes also informative of the disease stage[58]. The kinetic rate of apparent lactate conversion metabolism is also estimated, providing information about cofactors and enzymes associated with its conversion such as, NAD^+ , NADH_2 and LDH activity on a specific organ or tissue(Fig. 1.16, orange section).

Aerobic metabolism

Quantifying the bicarbonate release when pyruvate is converted to Acetyl-CoA, provides information about aerobic oxidation activity(Fig. 1.16, blue section)[76]. The appearance of HP $[^{13}\text{C}]$ bicarbonate could arise from pyruvate metabolism in multiple alternative pathways[77, 78]. The most common one is the pyruvate decarboxylation through PDH. To directly track the TCA cycle, the second carbon of the pyruvate must be labelled. Otherwise we would only follow the conversion from $[1-^{13}\text{C}]$ pyruvate to ^{13}C bicarbonate.

Urea cycle

The urea cycle, located exclusively in the liver, is the metabolic pathway responsible of removing ammonia from aminoacid degradation and converting it to urea as a waste molecule (Fig. 1.16, pink section). Carbamoylphosphate synthetase (CPS1), and or-

nithine transcarbamyase (OTC) are two enzymes responsible of this transformation found in the mytocondria, and its been proved that liver diseases such as NASH maked dysfunctional the mitochondria[79]. This mitochondrial injury leads to modification of the OCT and CPS1 genes, reducing their expression and funcion, resulting in accumulation of ammonia[80].

We tracked these 3 pathways using NMR to address a currently unmet clinical need for noninvasive diagnosis and treatment monitoring of liver diseases such as nNAFLD or non-alcoholic steatohepatitis (NASH), an illness of growing concern worldwide.

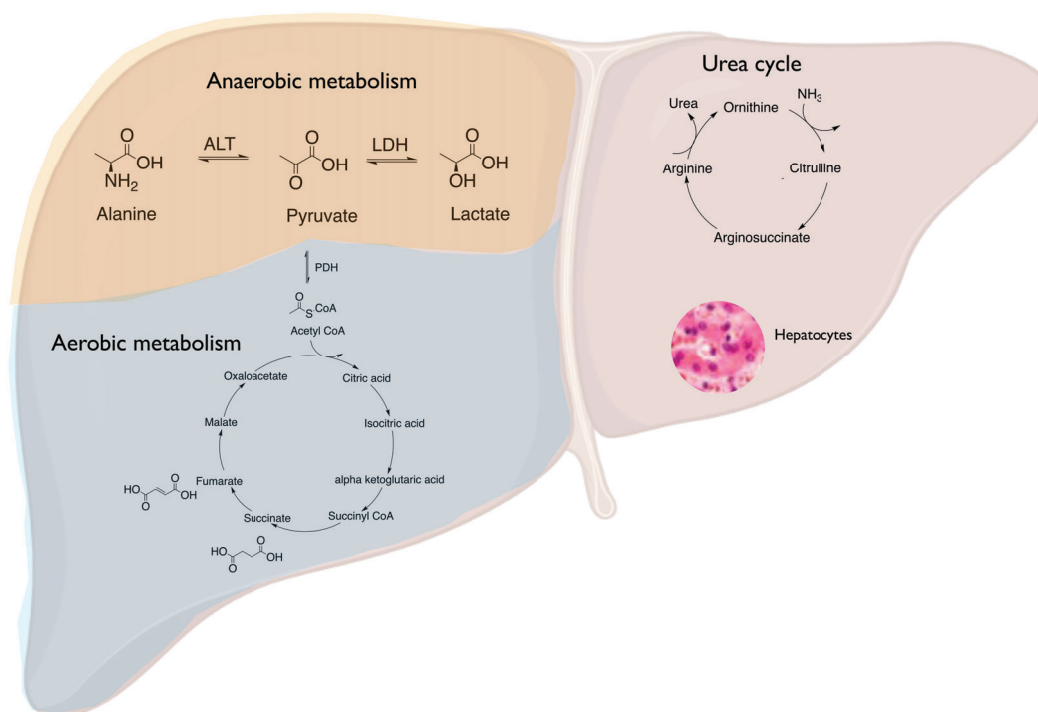


Figure 1.16: Metabolic pathways found in the liver and disregulated by liver disease. In the aerobic and anaerobic metabolism we find key metabolic reactions relevant for the tracing of [1-¹³C]pyruvate. In the urea cycle we can relate liver disease with overproduction of ammonia released to the blood. Although the reactions are depicted in different parts of the organ for visualization, all three reactions occur throughout the liver.

1.7.3.2 *In vitro* ¹³C hyperpolarized MR studies

Hyperpolarized MR has gone far beyond only clinical and preclinical models to study metabolic activity. During the past decades, researches have been putting effort in devel-

oping new *in vitro* cell models trying to mimic *in vivo* behaviour for different purposes such as personalized medicine, or avoiding animal testing[81].

1.8 Microfluidics and organ-on-a-chip devices

Microfluidics devices, often referred as microfluidic chips or lab-on-a-chip systems, are miniaturized platforms that manipulate and control small volumes of fluids, typically on the microliter (our case) to picoliter scale[82]. These devices are designed to perform various chemical, biological, and physical processes with high precision and control[83]. Organ-on-a-chip (OoC) term remarks the convergence between tissue engineering and microfluidics. This approach refers to miniature, interconnected systems of microchannels, chambers, and other microstructures designed to mimic the physiological environment of human organs or tissues[84]. These devices are typically constructed at the microscale, often using microfabrication techniques such as photolithography[85, 86].

Microfluidic devices are expected to offer effective solutions to persisting problems in drug development and personalized disease treatments. One big advantage is the capability of allowing experimental analysis with tiny amounts of sample, saving cost and enhancing the throughput[87]. Only some of the hyperpolarisation techniques have been combined with microfluidic systems. Microfluidic systems can be manufactured from a variety of materials, such as glass, rigid polymers like polycarbonate and poly(methyl methacrylate), and flexible and rubbery polymers, usually polydimethylsiloxane (PDMS). PDMS-based soft lithography[88, 89] presents an attractive approach for creating highly integrated microfluidic devices equipped with all sort of gadgets like vales, traps, channels, etc[90, 91]. PDMS stands out as a low cost and high-versatile biocompatible elastomer optically transparents and gas permeable. These properties make this material feasible for the cultivation of biological systems within controlled environments[92]. Furthermore, PDMS membranes can be bonded easily to hard materials such as glass and glassy polymers to incorporate both active and passive functional components[93].

1.8.1 Scaffolds for 3D-structure cell models

Tissue engineering represents a new research field combining biology, engineering, and medicine[94]. Within this field, a specialized branch is dedicated to the development

and fabrication of innovative biomaterials capable of hosting individual cells[95] or cell aggregates[96] to form functional biological *in vitro* tissues. Currently, three-dimensional and porous structures are designed and fabricated to support and guide the growth of cells or tissues, mainly composed by biomaterials. These structures are called scaffolds. The combination of the scaffold and the biologic model are aiming to mimic real tissues being a closer representation of organ structures. A reasonable motivation is to avoid animal testing and looking forward personalized medicine using *in vitro* models derived from the patient tissues. These biomaterials are mainly categorized by the fabrication methodology: hydrogels and cryogels. In this thesis I am going to focus in the cryogels, since its the model mainly used for all the projects described. Cryogels are synthesized from

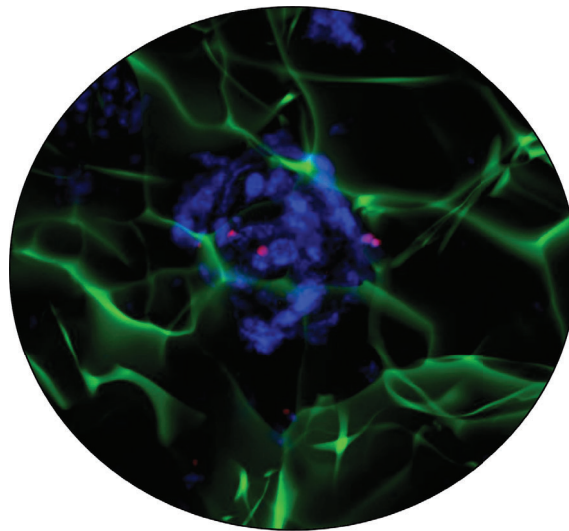


Figure 1.17: Confocal image of HepG2 cell cluster inside the cryogel. Nuclei in blue (Hoechst 33342), apoptotic cells⁹ in red (propidium iodide) and scaffold fibers in green (fluorescein). Microscope image done by Alba Herrero.

a wide variety of natural and synthetic materials, including polymers, gelatin, alginate, and collagen[97]. All the experiments performed in this thesis were carried out using carboxymethylcellulose (CMC) based scaffolds making interlinked networks, producing the corresponding cavities. For the biological model, cell suspension are seeded on top of each scaffold and the cells get encapsulated physically in the cavities. Keeping the seeded scaffolds in the incubator at appropriate temperature and CO₂ %, and changing the media regularly the start to aggregate themselves forming this 3D cell structures showed in Fig. 1.17.

HYPOTHESES AND OBJECTIVES

The overall objectives of this PhD thesis are:

1. To investigate the role of ammonia in liver diseases and develop a protocol to detect and quantify ammonia levels accurately in plasma using ^1H NMR. With this quantification we envisage to discern different stages of liver disease regarding the ammonia quantification.
2. Evaluate all the possible variables that could affect to a hyperpolarized-NMR/MRI measurement using microfluidics as acquisition platform. This evaluation includes measurement paths and materials used for the setup.
3. The development and optimization of a methodology for assuring contrast agent perfusion in biologic porous materials (carboxymethylcellulose based scaffolds) using magnetic resonance imaging with a 3T preclinical scanner.
4. The development of the whole setup for measuring real-time metabolism of biologic in vitro models using hyperpolarized NMR and MRI in microfluidic platforms.

LIVER FIBROSIS STAGING IN LIVER DISEASE BY AMMONIUM QUANTIFICATION IN PLASMA USING ^1H NMR

This was the first project that I developed completely from the beginning, working from the idea, passing through planning and execution, and finally writing the manuscript and publication. I developed and planned the first approach, and checked experimentally the feasibility of the project with Dr. Irene Marco's guidance and suggestions. After some discussion with clinical partners, we agreed to collaborate with a research group at IDIBAPS (Institut d'investigacions biomèdiques Agust Pi i Sunyer) and Hospital Clinic de Barcelona, to subadministrate us the clinical samples we needed to proof the proposed hypothesis. I went through all the experimental process with the plasma samples and subsequently performed all the data analysis. We published this project in NMR in biomedicine[98].

3.1 INTRODUCTION

As explained in the introductory chapter 1, the urea cycle, located exclusively in the liver, is the metabolic pathway responsible of removing ammonia from aminoacid degradation and convert it to urea as a waste molecule. This pathway can be disrupted or damaged by diseases affecting the liver, such as alcohol-related liver disease (ArLD) and nonalcoholic fatty liver disease (NAFLD). These two diseases are currently the two most frequent causes of liver disease in the Western world, accounting for the vast majority of liver-

related deaths, most of the liver transplants in Europe and North America, and associated costs[99, 100]. ArLD and NAFLD progress in stages from minor fat accumulation within hepatocytes (steatosis), to liver inflammation (named alcoholic steatohepatitis [ASH] and nonalcoholic steatohepatitis [NASH] in ArLD and NAFLD, respectively). The stage of the pathology can reach ultimately cirrhosis and cancer, the most advanced stages of the disease when liver transplantation is required. The progression of the disease to ASH and NASH leads to the activation of hepatic stellate cells that trigger fibrogenesis pathways and cause collagen deposition in the liver[101]. Liver fibrosis is the most driving force of chronic liver disease progression and one of the most reliable markers of prognosis[102, 103]. The current gold standard for chronic liver disease diagnosis is liver biopsy, an invasive technique that may pose detrimental side effects[104]. There is a major interest in developing noninvasive and clinically acceptable methods to assess the presence of liver fibrosis in patients with ArLD and NAFLD, of which transient elastography and serological tests have been the most promising[105, 106]. However, the clinical need for an alternative to biopsy for accurate, sensitive, and noninvasive liver fibrosis diagnosis and staging in patients with ArLD and NAFLD remains unmet.

In this chapter of the thesis, I investigated and developed a method to quantify endogenous ammonium in blood plasma and showed it to be a sensitive biomarker of liver disease. We published most of the work compiled here in a peer-reviewed international journal[98]

The ammonium cation (NH_4^+) is an essential biomolecule in blood derived from the breakdown of nucleic acids and amino acids: the two processes used by vertebrates to fulfill their nitrogen demand[107]. Ammonium homeostasis is governed systemically by the interplay of multiple organs including the liver, the gastrointestinal system, the muscles, the kidneys, and the brain[108].

The physiological concentration of (NH_4^+) in blood at equilibrium is about $40 \mu\text{M}$ in healthy subjects but may be significantly altered due to pathological conditions. For example, liver dysfunction may disrupt the metabolism of (NH_4^+) into urea and lead to a life-threatening increase of ammonium in blood[109]. High blood (NH_4^+) concentration (above $50 \mu\text{M}$) is associated with endstage liver disease, hepatic encephalopathy, neutrophil dysfunction, muscle breakdown, and cancer, although its origin remains

elusive[110, 111, 112]. In recent research, high levels of (NH_4^+) have also been found in patients with NASH[80]. Therefore, (NH_4^+) levels could be a valuable biomarker of liver impairment that together with other assays could shine light on its cause. Yet, a robust and reliable method to quantify blood ammonium concentrations for samples from healthy and diseased patients is not available. Current plasma ammonia quantification methods include titration, colorimetry or fluorometry, electrode-based, and enzymatic processes[109]. These methods suffer from significant limitations, namely (i) sample contamination (e.g. with volatile bases during titration), (ii) interference from other compounds normally present in blood[113], (iii) suboptimal environmental conditions for the proper activity of the enzymes involved in the measurement (e.g. low pH and the presence of inhibitors in severe liver disease),[114] and (iv) method calibration using samples of healthy subjects. The latter is critical in a clinical setting, as healthy individuals represent a relatively homogenous sample pool with wellknown basal conditions, while samples from patients with various stages of liver disease present heterogeneous conditions that may affect the (NH_4^+) readout (e.g. blood pH or lipids concentration). Furthermore, certain biochemical processes such as deamination in patients with elevated gamma glutamyl transferase (GGT) activity and as a consequence of haemolysis can alter blood (NH_4^+) concentrations postextraction, confounding quantification[115].

Proton nuclear magnetic resonance ($^1\text{H-NMR}$) is a reliable quantitative analytical tool for small molecules that potentially provides the sensitivity and specificity needed to measure endogenous ammonia in blood. While the characteristic equi-intense triplet of (NH_4^+) has been detected by $^1\text{H-NMR}$ in a wide range of systems (e.g. electrochemical and photochemical N_2 reduction, electrocatalytic N_2 reduction, and chemical reaction solution),[116, 117] measurement of endogenous (NH_4^+) levels has remained elusive in solutions of biological origin. To detect and quantify ammonium accurately in plasma using NMR, I have developed a tightly controlled protocol to process the samples containing the analyte. The study systematically assesses factors influencing accurate (NH_4^+) quantification of ammonia in plasma samples by NMR including solvent deuteration, pH, and NMR acquisition parameters, to determine the limit of detection (LOD) and limit of quantification (LOQ). The protocol established enables reproducible quantification of ammonium in plasma for concentrations above $3 \mu\text{M}$. The potential for clinical application

of this method is assessed by comparing the correlations between ammonium concentrations and other commonly used clinical biomarkers of liver disease. These comparisons showed that the strong correlation between ammonium concentration determined by ^1H -NMR readout and disease progression is likely to be a better diagnostic marker of liver disease stage than current blood hepatic biomarkers, regardless of disease etiology.

In summary, the data demonstrate that ammonium can be accurately and consistently measured in human blood plasma using a simple protocol. Validation in studies of samples from larger cohorts would simplify the way liver pathologies are diagnosed by reducing the need for biopsies and their associated risks.

3.2 MATERIALS & METHODS

All chemicals were purchased from Sigma-Aldrich (Haverhill, UK) unless stated otherwise.

The first aim of this project was to find the best strategy and figure out which were the best conditions to quantify ammonia using ^1H NMR spectroscopy unequivocally from an aqueous solution. We first tested how ammonia behaved in water changing the pH in each sample. Aqueous solutions were prepared by dissolving ammonium chloride (NH_4Cl , 107.0 mg) in H_2O (200 ml). This solution was acidified to pH 5.5 using 1 M HCl in water. A 1 ml aliquot was extracted, and the remaining solution was further acidified with HCl until pH 4.5. The same procedure was repeated for pHs of 4.0, 3.5, 3.0, 2.5, 2.0, 1.5, and 1.0. These samples were then measured in a 500 MHz spectrometer, processed and analysed.

Aqueous solutions were again prepared by dissolving ammonium chloride (NH_4Cl , 107.0 mg) in H_2O (200 ml). Two 25 ml aliquotes were extracted and the solutions were further acidified with HCl until pHs 1 and 3 respectively. Two 5 ml-aliquotes were extracted and the solutions were basified with NaOH 1 M solution until pHs 5 and 7 respectively. These 4 aliquotes were snap-frozen in liquid nitrogen and freeze-dried overnight. Dimethylsulfoxide (DMSO) solutions were prepared by mixing 1 ml of DMSO with trifluoroacetic acid (TFA) added to give TFA concentrations of 0.15, 0.75, 1.3, and 2.6 M; 1 ml of each solution was used to dissolve NH_4Cl (5.0 mg) in each vial. All samples were diluted with 100 ml of DMSO-d_6 . The displacement of the water/TFA chemical shift in

the $^1\text{H-NMR}$ indicated the pH changes upon addition of TFA.

3.2.1 Calibration curve of ammonium chloride in DMSO- d_6

A stock solution of 1 M NH_4Cl in DMSO (268.3 mg in 5 ml) was prepared and diluted with DMSO to give final NH_4^+ concentrations of 26.9, 16.8, 6.7, 3.4, and 0.3 μM . All samples were acidified with 2.6 M of TFA.

3.2.2 Human plasma obtention

This study was a collaboration with Institut d'investigacions biomèdiques Agust Pi i Sunyer (IDIBAPS) and Hospital Clínic de Barcelona. They contributed with the clinical experience and the ethical approvals to work with clinical samples, plasma in this case. They got a written informed consent was obtained from all subjects prior to participation. The experimental protocol was approved by the research and ethics committees of the hospitals where the study was carried out, in accordance with the Declaration of Helsinki (project number HCB/2015/0653). Plasma samples were collected from five healthy subjects, 10 patients with NAFLD, and 10 patients with ArLD (aged 26–73 years). Patients were classified based on the stage of liver fibrosis observed in the liver biopsy into either nonsignificant/early-stage fibrosis (F0-F1 stages) or significant/advanced-stage liver fibrosis (F2-F4 stages) based on the Metavir scale[118]. For both NAFLD and ArLD groups, five patients had early-stage fibrosis and five patients presented advanced fibrosis. Blood samples were obtained from the antecubital vein after a minimum of 10 min of rest. The blood was centrifugated in a refrigerated centrifuge for 10 min at 3500 rpm. Plasma aliquots were stored at 193 K.

3.2.3 Human plasma clinical biomarkers

Routine liver function tests, biochemistry, hematology, and coagulation assessments were performed on all samples from patients with NAFLD by our partner at IDIBAPS.

3.2.4 Human plasma sample preparation for ammonium assay by $^1\text{H-NMR}$

Each plasma sample (0.4–0.6 ml) was transferred into a 2-ml conical flask and treated with TFA (200 μl) to acidify the solution. The sample was snap-frozen in liquid nitrogen

and lyophilized for at least 8 h. The residue was dissolved in a solution containing TFA (200 μ l), DMSO (300 μ l) and DMSO- d_6 (300 μ l), and centrifuged (10,000 rpm, 5 min). The liquid phase was removed from the conical flask and the whole sample (800 μ l) was transferred into a 5-mm OD NMR tube. and ArLD.

3.2.5 Ammonium quantification by $^1\text{H-NMR}$

NMR spectra of ammonium in aqueous solutions were acquired at 300 K using a 14.1-T Bruker Avance-II spectrometer. Subsequent NMR experiments in DMSO were performed at 298 K and 9.4 T in a Bruker Avance-III HD spectrometer equipped with a cryoprobe and TopSpin 2.1 software. For ^1H chemical shifts reference and ammonium quantification, 10 μ l of a standard of sodium trimethylsilylpropanesulfonate (DSS; Cortecnet, Paris, France) in water were added to each sample tube ($\delta_{\text{DSS}} = 0.000$ ppm; final DSS concentration = 0.14 mM). The longitudinal relaxation time constant T_1 of both DSS and NH_4^+ in DMSO was measured in triplicate using an inversion recovery pulse sequence. Because DSS had the longest T_1 ($T_{1,\text{DSS}} = 1.6 \pm 0.1$ s; $T_{1,\text{NH}_4} = 0.5 \pm 0.1$ s), the relaxation delay time (d_1) of subsequent quantitative NMR experiments was set to more than five times $T_{1,\text{DSS}}$. The acquisition parameters for all $^1\text{H-NMR}$ measurements were an acquisition time of 2.5 s; 64×10^3 data points; 90° flip angle; $d_1 = 15$ s; and 128 scans. Solvent suppression experiments were performed with a 1D NOESY presaturation pulse sequence with the above acquisition parameters and the offset presaturation frequency at 4.71 ppm.

3.2.6 Ammonium chloride standards quantification by $^1\text{H-NMR}$

Next, 2.2 mg of ammonium chloride were dissolved into 10 ml of water to obtain a stock solution of 4.1 mM. Then, 10 μ l of this stock solution were diluted with 5 ml of water to obtain a standard 80 μ M solution. Two replicates with 300 μ l of this solution were transferred into conical flasks, and then 100 μ l of TFA were added into each aliquote. Both samples were lyophilized overnight. The samples were redissolved with 600 μ l of a solution containing TFA, DMSO, and DMSO- d_6 (2:3:3) immediately prior to $^1\text{H-NMR}$ acquisition and the corresponding quantifications of the ammonium concentration. The error associated with each value was calculated with propagation of uncertainty.

3.2.7 Data analysis

Data were processed using MestReNova software (Mestrelab Research, v. 14.2.0). NMR signals were zero-filled from 16 K to 64 K, Fourier transformed, and then baseline-corrected using a third-order polynomial fit. The signal-to-noise ratio (SNR) of the ammonium signal was calculated as the ratio of the amplitude of each of the ammonium peaks divided by the root-mean-square deviation of the noise. The full width at half maximum (FWHM) value for each peak of the ammonium triplet was determined by measuring the width of the peak at half of its maximum intensity. SNR and FWHM are reported as the mean \pm standard deviation of the three ammonium peaks. Ammonium concentration in micromoles per liter (μM) was quantified using the formula:

$$[\text{NH}_4^+](\mu\text{M}) = \frac{N_{\text{DSS}}I_{\text{NH}_4^+} + H_{\text{DSS}}10^6}{I_{\text{DSS}}H_{\text{NH}_4^+}V_{\text{plasma}}}$$

Where n_{DSS} is the number of moles of the DSS standard, $I_{\text{NH}_4^+}$ is the integral of the ammonium peak, I_{DSS} is the integral of the DSS peak, H_{DSS} is the number of protons per DSS molecule (9) that give rise to the integrated DSS peak, $H_{\text{NH}_4^+}$ is the number of protons that give rise to the integrated ammonium triplet (4), V_{plasma} is entered as the total volume of the initial plasma sample in liters, and 10^6 is a term to go from molar to micromolar. As suggested by Sun et al.[119], the LOD, defined as the lowest analyte concentration likely to be reliably distinguished from the noise, was set at $\text{SNR} = 3$. The LOQ, where the lowest concentration of an analyte can be reliably assayed, was set at $\text{SNR} = 10$ [119].

3.2.8 Statistical analysis

Continuous variables in blood biomarkers were analysed using ANOVA test; when significant ($P < 0.1$), post-hoc tests were performed among groups using the Mann–Whitney test. Spearman nonparametric correlation test with two-tailed p-value was used to evaluate the link between ammonium and the other measured blood parameters. All the analyses were performed using GraphPad Software (San Diego, CA, USA).

3.3 RESULTS & DISCUSSION

3.3.1 Ammonium quantification

We investigated the effect of pH and two solvents (9:1 water/deuterium oxide [D₂O] and 1:1 dimethyl sulfoxide [DMSO]/DMSO-d₆) on the detection of the ammonium ¹H-NMR signal and on quantification in solutions of 10 mM ammonium. The ammonium ion contains one nitrogen atom and four chemically equivalent hydrogens with a heteronuclear J-coupling, J_{NH}, of 52.4 Hz. The pK_a of the NH₃/NH₄⁺ pair is 9.2. Therefore NH₄⁺ is the dominant form in the acidic solutions (pH < 6) examined. The characteristic equi-intense triplet with the J_{NH} splitting of the ¹H atoms of ammonium was centered at 7.00 ppm in water (Fig.3.1A) and at 7.25 ppm in DMSO (Fig.3.2A).

In the aqueous solution, the addition of 10% D₂O for locking caused a splitting of the ammonium signal into a lower-intensity triplet with the same J_{NH} splitting (Fig.3.1A) centered at 7.00 ppm. The chemical shift of the ammonium triplet was independent of sample pH, but peaks narrowed, and the SNR was highest in acidic conditions, with an upper threshold at pH 2 or less (Fig.3.1B). Ammonium quantification was accurate within 95% for pH values below pH 2. The ammonium signal was undetectable for solutions above pH 3.5 (Fig.3.1A).

Because the protons in the ammonium ion are in rapid exchange with the protons in the solvent, presaturation of the water peak caused a decrease in the ammonium signal by a factor of 100 (Table 3.2). Consequently, ammonium quantification was underestimated by more than 25-fold when water presaturation was applied (Table 5.1). Without presaturation the large water peak poses a dynamic range problem for the detection of submolar concentrations of ammonium, causing baseline distortion and decreased ammonium SNR. Aqueous solvents are not, therefore, suitable for ammonium measurement.

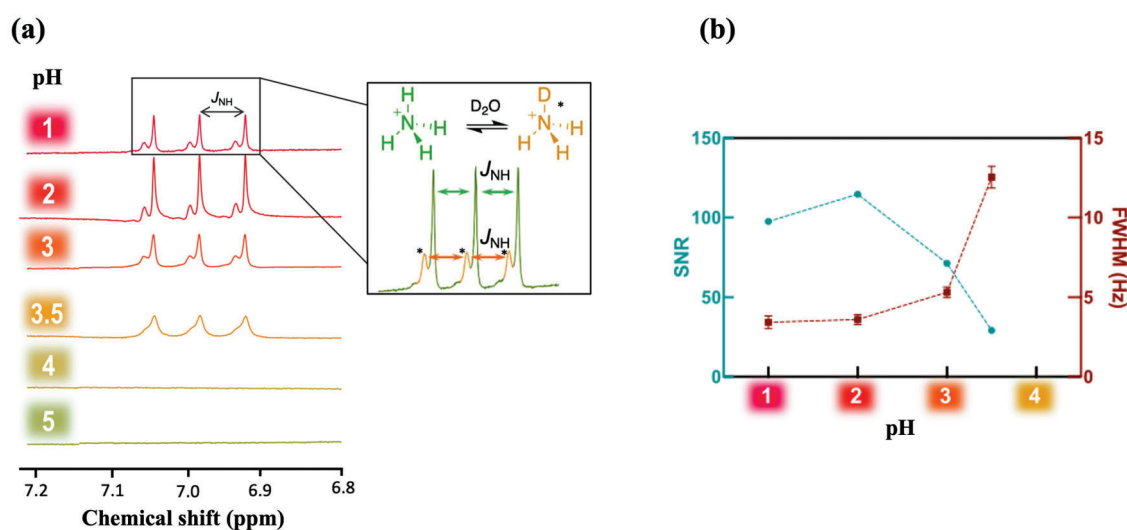


Figure 3.1: Nuclear magnetic resonance (NMR) spectra dataset of 10 mM ammonium chloride in aqueous solution (9:1 $\text{H}_2\text{O}/\text{D}_2\text{O}$). (A) ^1H NMR spectra as a function of pH (chemical shifts and signal intensity referenced to the disodium trimethylsilyl propanesulfonate (DSS) peak). The concentration of ammonium in the solution at pH 1 was about 10 lower than in the other solutions caused by the dilution of the sample during acidification, which accounts for the signal drop. NMR acquisition parameters: 32 scans; 15 s relaxation delay time; $8.5 \mu\text{s}$ pulse width. (B) Signal-to-noise ratio (SNR) (green circles) and full width at half maximum (FWHM) (red squares) of the ammonium signal as a function of pH shown in (A). Ammonium was undetectable at pH > 3.5

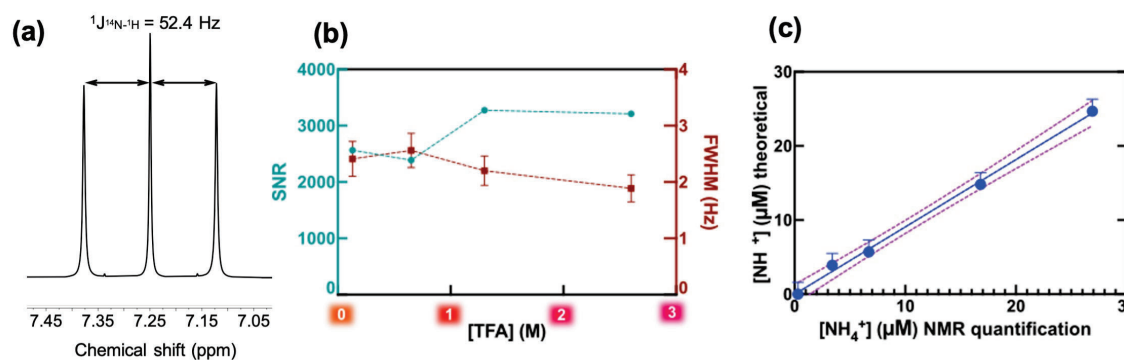


Figure 3.2: Nuclear magnetic resonance (NMR) spectra dataset of 10 mM ammonium chloride in aqueous solution (9:1 $\text{H}_2\text{O}/\text{D}_2\text{O}$). (A) Ammonium chloride in dimethyl sulfoxide and deuterated dimethyl sulfoxide (1:1 $\text{DMSO}/\text{DMSO-d}_6$). (A) Proton nuclear magnetic resonance (^1H -NMR) spectrum (chemical shifts referenced to the DSS peak). NMR acquisition parameters: 32 scans; 15 s relaxation delay time; $8.5 \mu\text{s}$ pulse width. (B) Signal-to-noise ratio (SNR) and full width at half maximum (FWHM) as a function of final trifluoroacetic acid (TFA) concentration. Although pH measurement in organic solvents is problematic, the acidity increases with TFA concentration. (C) $[\text{NH}_4^+]$ calibration curve with 2.6 M TFA added to the DMSO solution. DSS, sodium trimethylsilylpropanesulfonate

pH	$^1\text{H-NMR}[\text{NH}_4^+]$ (M)	Presaturation $[\text{NH}_4^+]$ (M)
5.51	-	-
4.86	-	-
4.44	-	-
4.02	-	-
3.52	0.010	0.0001
3.03	0.010	0.0003
2.48	0.010	0.0003
2.08	0.012	0.0005
1.51	0.010	0.0004
1.00	0.010	-

Table 3.1: Presaturation effect in ammonium NMR quantification in water/D₂O samples. The experiments were done using a 14 T Bruker 600 UltraShield TM. The pulse sequence applied was presaturation using noesypr1d with the following NMR parameters: acquisition time of 2.5 s, 64 K data points, 90° flip angle, $d_1 = 15$ s, 128 scans, and $\text{O}1d$ of 7.71 ppm.

An organic solvent (DMSO/DMSO- d_6) was therefore used to dissolve ammonium chloride and its suitability for the detection and quantification of ammonium was determined. To avoid the problem of determining pH in organic solvents, the samples in DMSO were acidified with TFA, which has no proton signal, at final TFA concentrations of 0.13–2.6 M. The SNR of the NH_4^+ signal was highest at TFA concentrations of more than 1.3 M (Fig. 3.2B).

The calibration curve of ammonium chloride in DMSO/DMSO- d_6 (0.3–27 μM NH_4Cl and 2.6 M TFA) using $^1\text{H-NMR}$ without presaturation was linear with a root mean square error (RMSE) of 1.6 (Fig. 3.2C), a LOD of 3 μM , and a LOQ of 5 μM . To measure ammonium in aqueous biological samples with a large initial water content, a lyophilization procedure that preserved the amount of ammonium present was required. To confirm that the concentration of ammonium was not affected by the lyophilization process, 4 samples containing 15 mg of NH_4Cl at pH 1, 3, 5 and 7 were lyophilized overnight and the samples were weighed the following day. The corresponding measurements are plotted in the Fig.3.3.

I prepared two standard solutions of ammonium chloride in water to a final concentration of 40 μM and were treated by same procedure as the biological samples. The ammonium chloride samples were lyophilized, redissolved in a solution of DMSO and TFA, and their $^1\text{H-NMR}$ signal measured. The corresponding ammonium quantifications

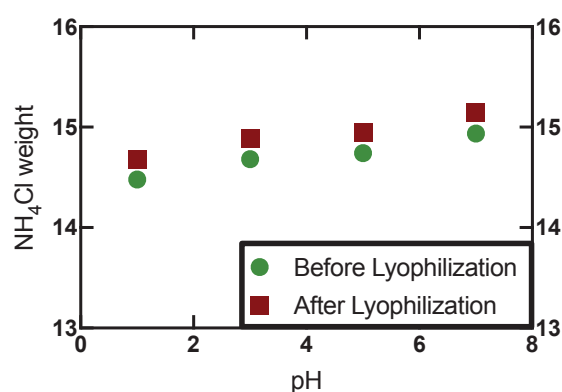


Figure 3.3: Ammonium chloride weight before and after the lyophilization process as a function of the pH.

by $^1\text{H-NMR}$ after the lyophilization step were 40.2 ± 0.2 and $40.5 \pm 0.2 \mu\text{M}$, respectively. The concentration of ammonium was not determined by NMR before the lyophilization step because the sample was in aqueous solution. As explained above, the partial deuteration, water signal overlap, and presaturation effects may result in unreliable measurements of ammonium concentrations.

3.3.2 Ammonium quantification in human plasma

In the optimized protocol, each plasma sample was transferred into a 2-ml conical flask and treated with $200 \mu\text{l}$ of TFA to acidify the solution. The sample was snap-frozen in liquid nitrogen and lyophilized for at least 8 h. The resulting powder was redissolved in 0.8 ml of a solution containing TFA, DMSO, and DMSO- d_6 (2:3:3) (Fig. 3.4). Adding TFA to the samples before the lyophilization step was essential to detect an ammonium signal at the end of the process.

The resulting ammonium concentrations obtained from the samples extracted from healthy subjects (control group) and subjects with initial and advanced stages of either ArLD or NAFLD are shown in Figure 3.5. Figure 3.6 displays a representative ^1H -spectrum used for the ammonium quantification. The plasma ammonium concentration of healthy subjects was $41.76 \pm 1.64 \mu\text{M}$. Plasma ammonium concentrations of patients with initial stages of liver disease were not significantly different than those of control samples, regardless of etiology ($p = 0.085$ for control vs. alcoholic, and $p = 0.13$ for

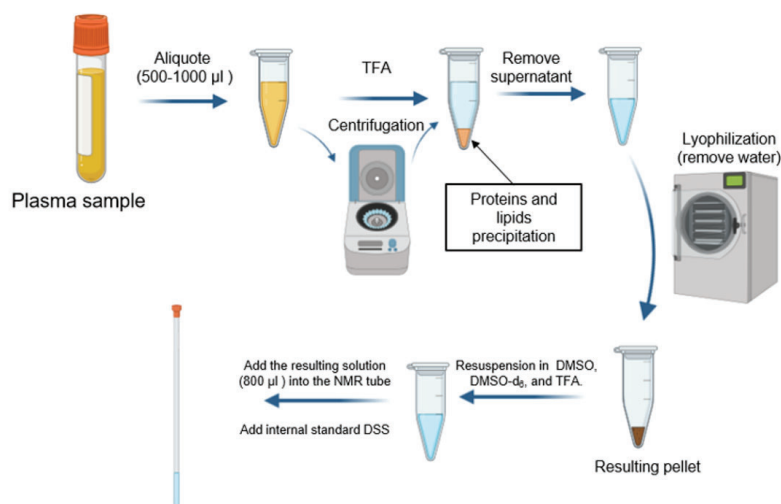


Figure 3.4: Plasma treatment protocol to measure ammonia concentration with ^1H NMR from an aqueous solution (plasma) to an organic solution with DMSO and TFA.

control vs. nonalcoholic). Plasma ammonia concentration of patients with advanced stages of disease was approximately five times higher than the controls ($p < 0.0001$ for both) (Table 3.2). There was no significant difference between groups with alcoholic and nonalcoholic initial stages of the disease.

3.3.3 Correlation between ammonium concentration and clinical biomarkers of fatty liver disease

No statistically significant difference was found for any of the blood parameters assessed between initial and advanced NAFLD (Table 3.2) other than for ammonium. By contrast, there were statistically significant differences between initial and advanced stages of ArLD in the ratio between aspartate transaminase and alanine aminotransferase (AST/ALT ratio), platelets, prothrombin time, and international normalized ratio (INR) (3.2).

There was a significant negative correlation between platelets and plasma ammonia concentration in patients with ArLD but not in patients with NAFLD (Figure 3.7). We found a significant positive correlation between INR and ammonia concentration ($p = 0.054$) in ArLD patients. The ArLD data were clustered in two nonoverlapping groups for the initial and advanced stage of the disease (blue and red circles, respectively; Figure 3.7B).

Clinical data of patients with different stages of liver disease						
Variable	IS-NAFLD Avarage	AS-NAFLD Avarage	p-value	IS-ArLD Avarage	AS-ArLD Avarage	p-value
Age	41.8±13.3	54.6±16.4	0.21	56.4±12.42	59±15.12	0.74
C-reactive protein (mg/dL)	1.2±0.9	1.8±2.8	0.59	0.2±0.4	0.08±0.2	1.0
Creatine (mg/dL)	0.68±0.13	0.70±0.08	0.73	0.85±0.14	0.75±0.12	0.24
Glucose (mg/dL)	96.4±16.8	107.4±23.7	0.45	104.0±18.0	75.6±29	0.24
HbA1c (%)	5.62±0.40	5.87±0.64	0.60	5.16±0.60	5.18±0.77	0.98
AST (UI/L)	30.0±12.9	65.8±62.7	0.3	49.4±24.8	74.6±43.2	0.42
ALT (UI/L)	48.8±29.7	42.4±11.0	1.0	48.0±24.2	41.6±22.8	1.0
AST/ALT	0.7±0.2	1.4±1.1	0.17	1.1±0.4	1.8±0.5	0.031
GGT (UI/L)	27.0±12.8	104.8±124.1	0.17	355.2±481.2	239.0±236.2	1.0
BILI total (mg/dL)	0.6±0.1	1.3±1.8	0.94	1.4±1.4	1.4±0.5	0.33
BILI direct (mg/dL)	0.22±0.04	0.88±1.52	0.88	0.72±1.06	0.56±0.31	0.3
Alkaline phosphatase (UI/L)	76.8±15.8	128.8±80.7	0.17	105.8±58.4	126.2±32.5	0.23
Total protein (mg/dL)	73.2±3.1	72.6±3.9	0.89	66.0±5.2	73.2±7.1	0.056
Albumin (g/L)	43.4±2.7	51.0±3.5	0.41	41.8±4.9	41.6±3.7	0.68
Sodium (mEq/L)	141.4±2.7	413.0±2.0	0.34	104.0±2.1	141.4±0.3	0.17
Postassium (mEq/L)	4.6±0.6	4.6±0.8f	0.98	3.9±0.3	4.12±0.3	0.51
Leukocytes	7842±1871	6568±1118	0.25	6352±1058	4552±1546	0.15

Hemoglobin (g/L)	141.8±19.8	146.2±29.6	0.46	137.6±30.5	134.6±15.2	0.80
MCV	90.1±7.1	101.4±9.4	0.06	99.6±12.3	99.7±5.3	0.55
Number of Platelets	286,800±98,519	226,800±89,340	0.34	173,800±21,913	90,6000±24,203	0.0079
Prothrombin time (%)	94.0±8.5	86.0±18.7	0.68	93.8±8.8	73±15.5	0.047
INR	0.98±0.08	1.08±0.19	0.53	1.02±0.08	1.22±0.13	0.047
MELD	6.2±0.4	8.2±4.3	0.72	7.6±2.1	9.4±2.1	0.32
CHILD PUG	5.00±0.01	6.20±2.68	0.99	5.60±1.34	5.60±0.89	0.99
Total chloesterol (mg/dL)	173.4±62.4	203.8±24.7	0.46	250.8±126.9	168.8±29.1	0.15
Triglycerides (mg/dL)	154.0±120.4	119.2±31.5	1.0	270.6±286.6	235.2±326.0	1.0
Ammonium (μM)	90.1±19.1	220.9±40.2	0.0005	86.8±23.4	139.9±30.8	<0.0001

Table 3.2: Clinical and laboratorial data of patients with different stages of nonalcoholic fatty liver disease (NAFLD) or alcohol-related liver disease (ArLD). Biochemical values were obtained using standard blood analysis from a cohort of patients with either initial or advanced stages of NAFLD and another cohort of patients with ArLD (n = 5 patients per group). Significant differences in the biochemical values between initial and advanced stages of NAFLD or ArLD are highlighted in bold ($p \leq 0.05$ calculated using nonparametric T-test)

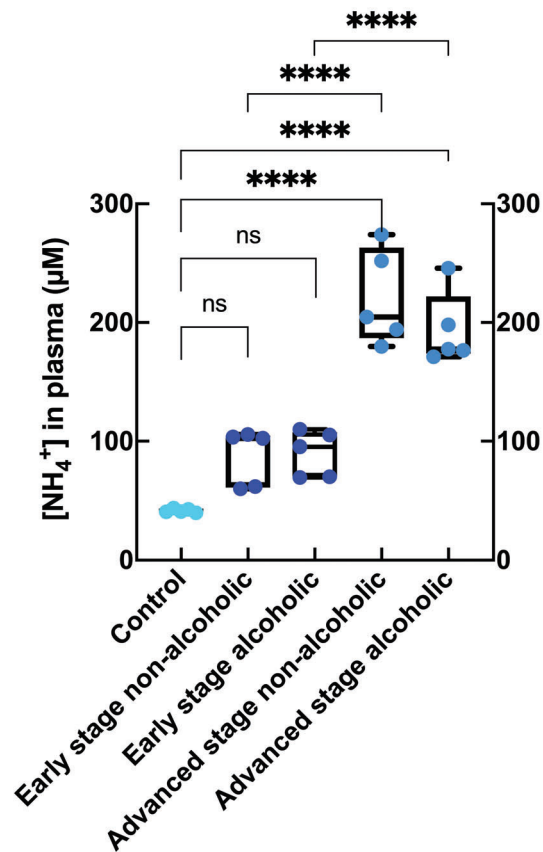


Figure 3.5: Concentration of ammonium present in plasma from healthy subjects (control; $n = 5$), initial and advanced stages of alcohol related fatty liver disease ($n = 5$ for each group), and initial and advanced stages of nonalcoholic fatty liver disease ($n = 5$ for each group); **, $p < 0.01$; ***, $p < 0.001$; ****, $p < 0.0001$. Each blue shade represent different subject groups

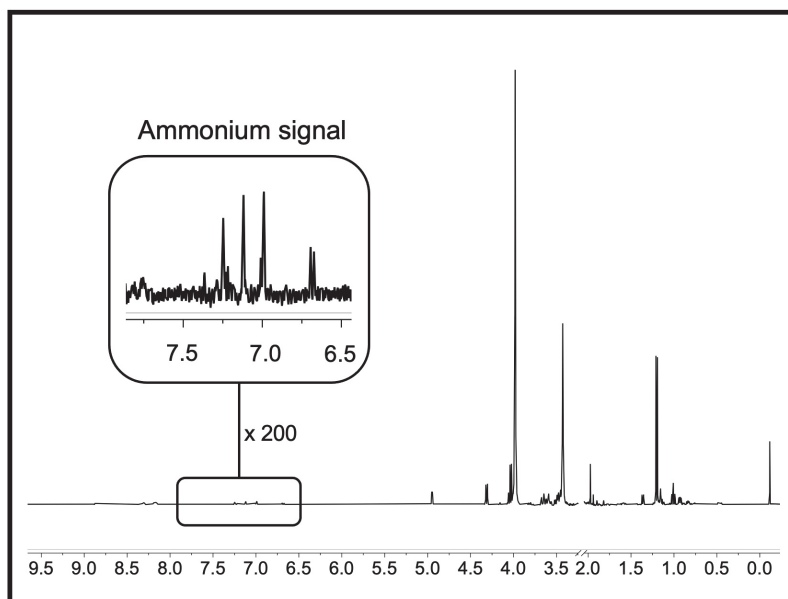


Figure 3.6: Representative proton nuclear magnetic resonance ($^1\text{H-NMR}$) spectrum of blood plasma from an advanced-stage nonalcoholic fatty liver disease patient after lyophilization and dissolving in dimethyl sulfoxide (1:1 DMSO/DMSO- d_6). Chemical shifts are referenced to DSS. NMR acquisition parameters: 128 scans; 15 s relaxation delay time; $8.5 \mu\text{s}$ rf pulse width. DSS, sodium trimethylsilylpropanesulfonate

Blood endogenous ammonium concentrations above $100 \mu\text{M}$ are strongly associated with severe liver diseases, such as hepatic encephalopathy, NASH, and hepatitis C[80]. However, accurate quantification methods capable of detecting upregulated ammonium concentrations in blood at treatable stages of the disease have not been developed for clinical use. We have developed a robust protocol capable of quantifying ammonium in plasma by $^1\text{H-NMR}$ that is also applicable to other biological fluids. The protocol could readily be adopted as a diagnostic screening tool for diseases where ammonia is a biomarker, particularly for liver fibrosis in patients with NAFLD and ArLD, provided that larger cohort studies validate the data presented.

Ammonium is well suited for analysis by $^1\text{H-NMR}$. NH_4^+ exhibits heteronuclear scalar spin–spin couplings, which are rarely observed because of quadrupolar line broadening.[120] When the ^{14}N atom is coordinated symmetrically giving a tetrahedral conformation, ^{14}N loses its quadrupolar electric moment that results in coupling with the hydrogen atoms[121] and the signal then corresponds to a triplet with equivalent intensities. However, ammonium quantification is challenging because it is affected by several variables. The present study critically assesses factors influencing accurate NH_4^+ quantification, including sol-

vent deuteration, pH, and pulse sequence.

The choice of solvent substantially affects ammonium quantification, and aqueous and organic solvents were examined. In metabolomic and small-molecule studies by $^1\text{H-NMR}$, D_2O is generally used as a solvent. However, this solvent cannot be used for $^1\text{H-NMR}$ quantification of molecules like ammonium that have labile protons that can exchange with the ^2H atoms of the solvent molecules, causing partial or total signal suppression of the signal, depending on the $^2\text{H}/^1\text{H}$ ratio in the solution. Figure 3.1 shows the effect of 10% D_2O in solution on the $^1\text{H-NMR}$ spectrum, splitting the ammonium signal into a triplet from mono-deuterated ammonium. The shift in center frequency of the multiplet is due to an isotopic effect caused by the deuterium atom, and the apparent increase in line width is attributed to the $^2J_{\text{HD}}$ coupling (Figure 3.1A). To shift the ammonium/ammonia equilibrium to the cation form for accurate detection, acidification of the samples was required. This ensured sufficient protonation of ammonia, thereby excluding confounded quantitation of NH_4^+ .

At the 10 mM ammonium concentration used to set up this protocol, ammonium quantification was accurate for pH values between 0 and 3. However, as SNR and FWHM increased as pH decreased, the quantification of solutions with low ammonium concentrations would benefit from the higher SNR obtained at the lowest accessible pH. The changes in SNR and FWHM can be explained by the dissociation of the ^1H atoms of ammonium. In solution, each of the four ^1H atoms have the same dissociation probability. The dissociation rate constant k_d is highly affected by pH, decreasing as pH acidifies[121]. At low exchange rates ($k_d \ll J_{\text{NH}}$), spectral lines are sharper, resulting in improved SNR. The analysis of biological samples by $^1\text{H-NMR}$ is often performed in nonacidic pHs with D_2O as the choice of solvent, which probably explains why ammonium present in biofluids has not been previously detected by $^1\text{H-NMR}$. We also observed that water presaturation pulse sequences led to a dramatic decrease of the ammonium signal caused by the proton exchange between ammonium and water. To presaturate the water peak, radiofrequency irradiation is applied to water protons that are continuously exchanging with ammonia, resulting in peak suppression for both molecules.

The protocol was therefore optimized using DMSO as a solvent. Because accurate pH determination relies on using a protic solvent, samples were acidified with TFA, the acid

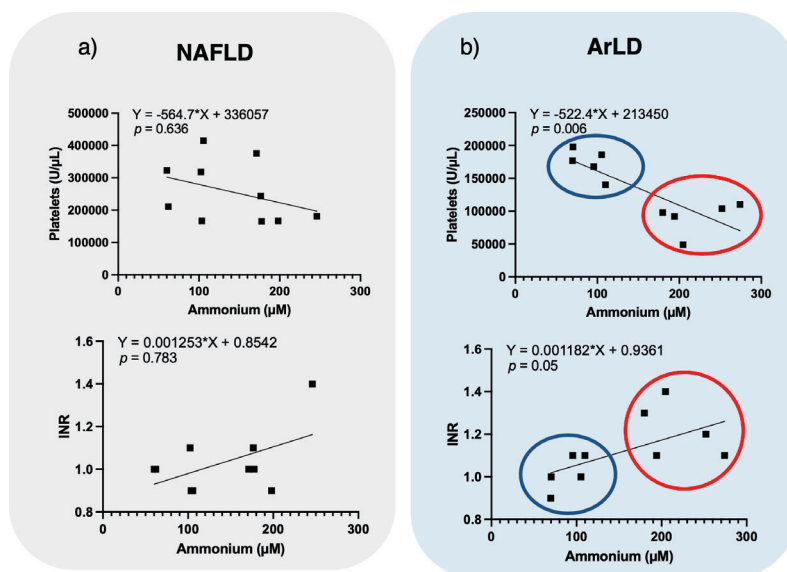


Figure 3.7: Nonparametric Spearman correlations between platelets and ammonium concentration (top) and international normalized ratio (INR) and ammonium concentration (bottom) for patients with liver disease from either (A) Nonalcoholic fatty liver disease (NAFLD; $n = 10$) or (B) Alcohol-related liver disease (ArLD; $n = 10$). The blue and red circles show the two data groups corresponding to initial and advanced stages of alcoholic fatty liver disease

being chosen because it has a proton-free counterion and therefore gives no ^1H NMR signal. Acidification also assisted the precipitation of the proteins and lipids of the sample. After acidification, the solution was centrifuged and the supernatant was pipetted off for the next stage of the process. A 200- μL volume of the TFA was sufficient to accurately quantify ammonium concentration in plasma with a RMSE of 1.6 μM , a LOD of 3 μM , and LOQ of 5 μM . The protocol therefore enables precise and reproducible quantification of ammonium concentration far beyond the typical range found in human plasma (from 40 μM in healthy subjects to more than 100 μM in pathological cases). Quantification also confirmed that the yield of the lyophilization procedure was 100%, that is, it did not result in losses of ammonium, and that the addition of TFA to the sample does not interfere with the internal standard for quantification.

Plasma samples from healthy controls and four patient groups were processed using the above protocol to quantify the ammonium concentration. Plasma contains approximately 92% water and 8% solids[122]. Using a well-known protocol for protein and macromolecules precipitation, TFA was added to plasma samples to obtain a nearly

solids-free solution after supernatant removal[123]. The early-stage ArLD and NAFLD disease groups showed some differences in ammonium levels of around 50 μM variation, where the mean concentration was higher than for the control group. However, this difference between control and early-stage groups was not statistically significant. The variation of 50 μM may be due to differences in disease severity within the patient group in the initial stage of classification. By contrast, a striking and statistically significant increase in ammonium concentration was observed for each of the two liver disease groups compared with both initial-stage and control subjects.

An interesting finding of this study is that ammonium concentration is strongly correlated with platelet levels ($p = 0.075$) and with INR, especially for the ArLD group. At advanced stages of chronic liver disease such as liver cirrhosis, patients may develop portal hypertension, which in turn leads to the development of clinical decompensations of cirrhosis. In this case, spleen size may increase, and peripheral blood platelet levels may decrease, as thrombopenia is a marker of portal hypertension in patients with cirrhosis. Also, coagulation tests such as INR are frequently used to stage the platelet synthesis capacity of the liver, which may be impaired by disease and used in liver function scores. The coagulation tests are also used for staging standardized numbers such as model for endstage liver disease (MELD) or Child–Pugh scores (Fig.3.8).

The correlation between the ammonia levels and platelet counts and INR levels in patients with ArLD may therefore be reflecting a correlation with ammonium levels and more advanced stages of liver disease, such as the appearance of portal hypertension or the impairment of liver synthesis capacity.

Although a limitation of this study is the small cohort assayed, it is striking that the ammonium assay protocol is capable of clearly discriminating the samples corresponding to healthy and early-stage–diseased subjects from those of patients with advanced stages of the disease. Taken together, these data support the notion that there is a direct correlation between blood ammonium concentration and the disease stage of patients with ArLD and NAFLD, and that when validated by larger sets of samples may have clinical application.

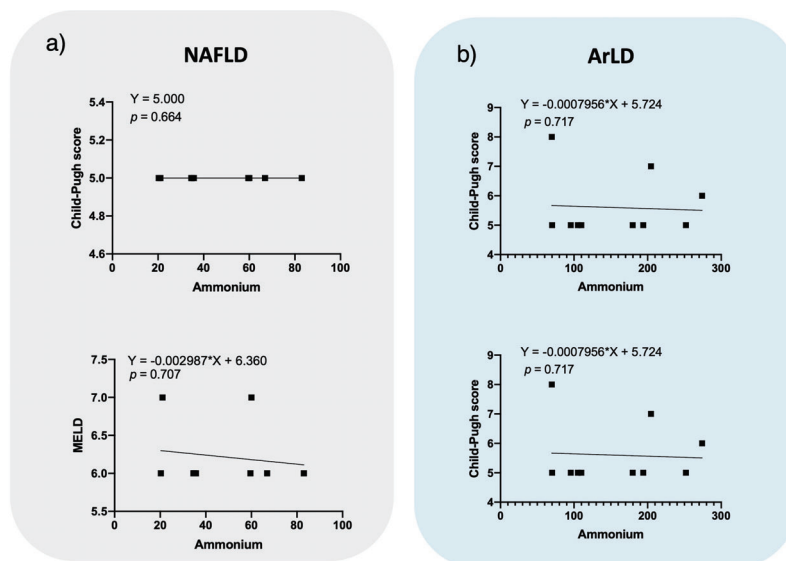


Figure 3.8: Graphical representation of non-parametric Spearman correlation between Child-Pugh score and ammonium (top) and MELD (model for end-stage liver disease) and ammonium (bottom) for patients with fatty liver disease from either (a) non-alcoholic (n = 10) or (b) alcoholic etiology (n=10).

3.4 CONCLUSIONS

I have developed a robust, reliable, and biopsy-free protocol to quantify ammonium in biological fluids with a wide dynamic concentrations range, relative to other methods currently available. To demonstrate potential applications within medical diagnostics and disease staging, I quantified the ammonium concentration in blood plasma samples of patients suffering from a steatohepatic liver condition. I then demonstrated that the method can be used to discern between some stages of the disease retrospectively. Unfortunately, this methodology requires large plasma sample volumes (> 1 mL), more than 24 hours to finish all the steps, and expensive equipment (high field NMR spectrometers). These limitations with the high expertise required may hinder this methodology for a future application in hospitals or clinical centers[124].

Prospective studies with a larger cohort of patients should validate the clinical applicability and, in future, with some optimizations, the protocol could be used in a clinical setting either for population screening or to assess treatment efficacy.

LEVERAGING MAGNETIC RESONANCE IMAGING TO STUDY BIOCOMATIBLE SCAFFOLDS DIFFUSION AND PER- FUSION FOR LAB-ON-A-CHIP SYSTEMS

This is one of the last projects I worked on during my doctoral thesis, together with my two colleagues, mentors and friends, Alex and David. It was already loaded to ChemRxiv. We wanted to use 3D cell in biomaterial scaffolds already described in the introduction(1.8.1). The cells are embedded by a porous material making some resistance to perfusion and flow. In this case, it was crucial for fluid perfusion through the scaffold to facilitate the cells interaction with the hyperpolarized NMR contrast agent. The main purpose of this project was to assess the perfusion and the diffusion of various scaffold material compositions and evaluate the effectiveness and the robustness of the process. My contribution was a portion of the intellectual design, the major part of the experimental design and execution, and completed the manuscript writing with my two colleagues and our supervisor Dr. Irene Marco-Rius.

4.1 INTRODUCTION

Developing 3D cell culture models is currently receiving high interest in the tissue engineering field. The novel applications of these *in vitro* models, besides avoiding animal testing and aiming for personalised and regenerative medicine, are raising the interest

of biomedical engineers and biotechnologists[125]. They can be customised taking into account different factors such as cells or tissue type, size and shape[125]. Novel bio-engineering research lines now focus on developing approaches to promote cell adhesion, proliferation and differentiation in a physiologically relevant environment[126, 96, 127]. Hence, hydrogels and cryogels emerged as the leading candidates for cellular scaffolds due to their biocompatibility and physical properties[128, 129].

Hydrogels are mainly used as a support material for cellular proliferation since they mimic the extracellular matrix (ECM) properties. This approach makes it possible to surround cells or any biological system within a suitable environment. Encapsulating cells within hydrogels confers several beneficial properties, including high water content and mechanical adjustability to generate specific architectures[130, 131]. The hydrogel fabrication process involves the formation of stable polymeric network matrices, typically incorporating nanofiber materials such as collagen, fibronectin and laminin[132]. The application of the hydrogel fabrication for producing 3D structures with high mechanical and structural stability is becoming establishing as an advantageous tool in the field of scaffold generation. However, producing big pores in a reproducible way remains still a challenge[133, 134, 128, 135, 136]. The pore size has a constraining effect on different essential aspects for the complete functionality of the model. Consequently, the pore sizes will have a direct impact on the elimination of waste products, the appropriate oxygen diffusion, nutrient delivery and vessel formation in tissues[136, 137, 138, 139]. Small porous size also hampers vessel formation, a fundamental factor to engineer fully functional tissues[138, 139]. Moreover, these limitations hamper the possibility of injecting external solutions or substances into cells, such as drugs or contrast agents for imaging.

In contrast, cryogels have risen as a promising alternative to hydrogels, adeptly addressing several of their drawbacks and limitations. Cryogels have characteristic big microporous sizes with sponge-like appearance and high pore interconnectivity and water content[140, 141]. Furthermore, this highly intertwined net-like pore structure allows high liquid diffusion, overcoming hydrogel limitations[130]. These features make them particularly attractive to techniques requiring fast liquid perfusion inside scaffolds for real-time metabolism tracking or drug-based solution infusion studies. Furthermore, it is possible to synthesise cryogels from natural and synthetic materials, including polymers,

gelatin, alginate, and collagen[97]. Functionalisation with bioactive molecules, such as growth factors[142], peptides[143], and extracellular matrix components[144], is also an attractive feature of these scaffolds. Another interesting characteristic is that they can be functionalised with bioactive molecules, such as growth factors[142], peptides[143], and extracellular matrix components[144]. This versatility makes it possible to choose materials that match the properties of the corresponding target tissue. All the experiments performed in this work were carried out using carboxymethylcellulose (CMC) based scaffolds making interlinked networks (reaction showed in Fig. 4.1), producing the corresponding cavities. This hollows confer a specific porosity to the material.

Carbodiimide crosslinker mechanism through caroxylic position activation

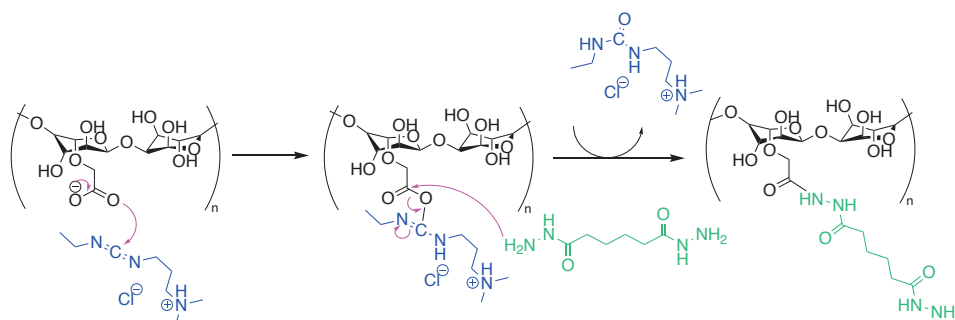


Figure 4.1: Mechanism of the chemical reaction between carboxymethylcellulose polymer and N-(3-Dimethylaminopropyl)-N'-ethylcarbodiimide hydrochloride (EDC). In the first step the carbonyl is activated to make it more electrophile with the EDC as a coupling agent. In the next step there is a nucleophile addition of the adipic acid dihydrazide (AAD) to the CMC carbonyl forming the resulting coupling as an amide bond .

Nowadays, many techniques are available to analyse pore size and distribution. The most frequently used strategies are gravimetry[145], mercury intrusion porosimetry (MIP)[146], confocal laser scanning microscopy (CLSM)[145], computed tomography (CT)[147] and computed micro tomography (CMT)[148, 149], among others. Computed microtomography (CMT) stands out for its precise and non-destructive 3D evaluation of open and closed porosities[148, 149, 150]. Tomography is a method by which you can obtain an object's 3D image that corresponds to its internal structure[150]. Computed tomography (CT) is considered a high-resolution technique with a pixel size typically between 1-50 μm , al-

lowing investigation of microstructure samples using X-rays[148]. Approaches such as gravimetry[145], mercury intrusion porosimetry (MIP)[146] or confocal laser scanning microscopy (CLSM)[145] are also commonly used. However, these techniques only enable us to examine microstructures, lacking the capability to assess and evaluate perfusion efficiency through a porous material.

Yet, in the biomaterials research field, studying liquid diffusion and perfusion is of paramount importance. Understanding how fluids flow within biomaterials is crucial for optimising the design of tissue-engineered constructs and drug delivery systems. For example, confocal fluorescence microscopy is a powerful tool for studying the perfusion within biomaterials[151, 152, 153]. This optical imaging technique is usually coupled with fluorescence techniques, making a suitable synergy to gain insight into the diffusive properties of the material. So far, researchers have explored capillary network formation in tissue-engineered scaffolds[151], drug release kinetics from implantable devices[152], and the behaviour of nanoparticles within porous matrices[153]. Nevertheless, confocal microscopy is primarily designed for imaging surfaces and struggles to penetrate deep into materials, making it less effective for three-dimensional analysis. It is also relatively slow to capture images, making it challenging to measure fast perfusion. Also, while the technique usually offers good lateral resolution, the vertical axis may be less precise, affecting fine details within porous structures[154]. Moreover, the size and structure of the fluorescent particles used have a pivotal role in diffusion rate constants, also influencing the chemical and structural properties of the object under study[155]. The size of the fluorescent particles is another factor to take into account. This property may also influence the structural and chemical properties of the object under study. Diffusion depends on the size of the molecule. Therefore, a diffusion study on small molecules would be totally unfeasible with such large molecules[155]. Besides, multiple measurements make the fluorophore lose its fluorescence activity due to light-induced damage (i.e. photobleaching)[156, 157].

Magnetic resonance imaging (MRI) has been used in modern medicine to accurately and non-invasively characterise the properties of multiple biological materials[158, 159, 160, 161, 162]. For example, researchers used a Fast Spin Echo (FSE) sequence in a clinical 3 T scanner to assess cortical bone microstructures[158, 159, 160]. In this study they

demonstrated that free water in microscopic pores of cortical bone can be imaged with a FSE sequence, characterising then the pore size and strongly correlating the results with μ CT images.[159, 160, 163]. Researchers have also used MRI in relaxometry to provide information on the pore structure materials. The water longitudinal and transverse relaxation time constants (T_1 and T_2 , respectively) increase in proportion to the surface-to-volume ratio of the pore space. The smaller the pore, the shorter the relaxation time due to the high probability of interaction with the surface[161, 162]. MRI provides key information on the pore sizes and relationships between structure and fluid flow properties in porous media[164]. A pivotal advancement in MRI technology is the use of contrast agents, which enhance the visibility of specific tissues or structures[165, 166]. This progress aids an accurate characterisation and quantification of various physiological processes[165, 166]. Among these contrast agents, deuterium oxide (D_2O), also known as heavy water, emerged as a compelling choice for investigating diffusion[167] and perfusion[168]. D_2O and water have similar physical and chemical properties except for the nuclear mass (D_2O has one neutron) and the spin number ($I_H = 1/2$ and $I_D = 1$). Hence, at high magnetic fields, deuterium is practically invisible when measuring the proton frequency range. A few perfusion pre-clinical studies used D_2O as a tracer[168]. This contrast-enhanced strategy with D_2O allows monitoring the signal attenuation of 1H in MRI when administering D_2O as an indirect measurement[169]. For example, this approach was used to guide endovascular neurointervention, potentially improving the precision treatment of various diseases[169].

In this work, I use MRI and D_2O (Fig. 4.2) to accurately and non-invasively measure the passive diffusion and active perfusion properties of two biocompatible materials, CMC-based and PEGDA-based scaffolds. The work aims to aid the advance of biotechnology, bioengineering and ultimately, personalised medicine (amongst others) since cell scaffolding employs these biomaterials to generate 3D biologic environments. We used D_2O as a contrast agent to detect the decay in the proton signal due to the reduction of proton density from the original water contained within the scaffolds. Since there is an absence of chemical reactivity among the reagents, I can measure the scaffold properties non-destructively and even reuse them. We successfully show the applicability and practicality of this strategy to study the passive diffusion (Fig. 4.2A, left) of scaffolds

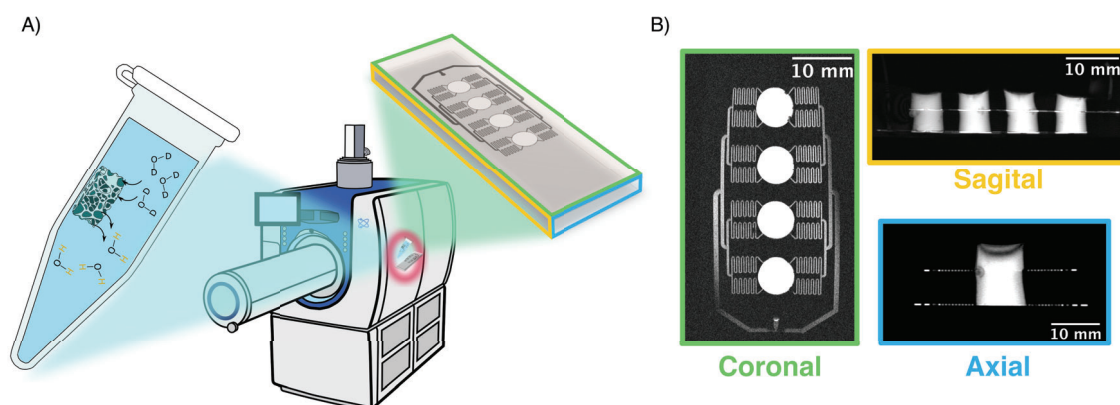


Figure 4.2: Diffusion (Eppendorf) and perfusion (4-well microfluidic chip) of biocompatible scaffolds using a pre-clinical 3T MRI scanner. A) Schematic illustration of the experimental setup consisting of the scaffold under study (hydrogel or cryogel), heavy water, a 0.5 mL Eppendorf, a 4-well microfluidic platform, and a 3 T MRI scanner. For diffusion studies, I submerged the scaffolds (origin of the water proton signal) into the Eppendorf containing deuterium oxide (absence of signal). For perfusion studies, I enclosed the scaffolds into the microfluidic chip wells and injected deuterium oxide from the microfluidic features of this. B) Proton MRI coronal (green), sagittal (orange), and axial (blue) plane images of the 4-well microfluidic device filled with water using a T_1 -FLASH MRI sequence. Acquisition parameters of the MRI images: acquisition time 9.0 ms, repetition time 425.0 ms, 60° flip angle, 1024 acquisition points, 16 averages, 192x128 image size

contained in an enclosed environment with D_2O and active perfusion (Fig. 4.2A, right) of these using custom microfluidic systems (Fig. 4.2B). Furthermore, both studies demonstrated highly effective and reproducible within this easy-to-handle system setup. With these results, I expect to open a new prospective approach for diffusion and perfusion studies using MRI technology.

4.2 MATERIALS & METHODS

4.2.1 1% CMC cryogel fabrication

We dissolved a prepolymer solution containing 1 % 90 kD Carboxymethylcellulose in MilliQ water under magnetic stirring for 1 h at $45^\circ C$. We prepared the crosslinking reagents as 0.5 M MES hydrate buffer adjusted at pH 5.5 with NaOH, 5 % Adipic Acid Dihydrazide in MilliQ water, and $1 \mu g/\mu l$ N-(3-Dimethylaminopropyl)-N'-ethylcarbodiimide hydrochloride dissolved in MilliQ water. Next, I mixed 1 ml of the prepolymer,

50 mM of MES buffer, 1.83 mM of ADH, and 18.9 μM of EDC. Shaking was critical to avoid early crosslinking before freezing the sample. We filled polydimethylsiloxane (PDMS) circular moulds (chambers measuring 2 mm in height and 10 mm in diameter, enclosed between two squared 24x24 mm cover glasses) with the final prepolymer solution. Then, I stored the samples at -20°C for 24 hours. Finally, I thawed the resulting cryogels at room temperature and sterilised them by autoclave.

4.2.2 10% PEGDA hydrogel fabrication

We dissolved a prepolymer solution containing 10 % PEGDA (Poly(ethylene glycol) diacrylate (PEGDA), M_n 575 g/mol) and 1 % Irgacure D-2959 (2-Hydroxy-4'-(2-hydroxyethoxy)-2-methylprop-iophenone, all w/v) in Phosphate Buffer saline (PBS) at 65°C for 1 h, filtered and crosslinked under UV light using a MJBA mask aligner (SUSS MicroTech) (power density of 25 mW cm^{-2}). We obtained disc-like samples of 10 mm in diameter by exposing the prepolymer solutions for 500 s. After UV exposure, we washed with PBS unreacted prepolymer solution and I left the resulting samples to reach equilibrium swelling for 24 h at 4°C . Before MRI measurement, I punched hydrogels to the desired final diameter (5 mm).

4.2.3 Microfluidic chips fabrication

We fabricated the molds with microfluidic channels and features using standard photolithography methods using silicon wafers (4" n-type <111>, MicroChemicals GmbH), photoresist (SU-8 2100, KAYAKU Advanced Materials, Inc.) and UV light [170, 171]. We finally silanised the wafer by vapour exposure of $^1\text{H}, ^1\text{H}, ^2\text{H}, ^2\text{H}$ -perfluorooctyl-trichlorosilane (PFOTS, 97%, Merck). Then, we used standard soft lithography with polydimethylsiloxane (PDMS) to produce the microfluidic devices from the patterned SU-8 molds. We prepared the PDMS prepolymer (Sylgard 184, Ellsworth Adhesives) in a 10:1 ratio (elastomer base: curing agent, w/w). Our chips consisted of two PDMS layers with the microfluidic channels serving two functions: 1) distributing the liquid (in the lower 5-mm thick layer) through four distinct channels that collectively distribute the sample into each well, and 2) removing excess liquid during injection (in the top 5-mm thick layer, unused in the results shown in this work). We punched the chambers (i.e. well) and inlet and

outlet ports in the corresponding PDMS layers using 6 mm and 1.2 mm biopsy punches, respectively. We activated and bonded together the two PDMS layers and a glass slide (75 x 25 mm Corning) using O₂ plasma (PDC-002, Harrick Plasma).

4.2.4 Custom nylon mesh fabrication

A postdoctoral researcher (Dr. Alejandro Portela Otaño) modified a nylon mesh with a pore size of 100µm (Lythe Official, Whitby YO21 3RT, UK) by adding a frame of a biocompatible 3D printing resin (SolusArt v3.0, Gesswein, USA) following a customised fabrication process using a Digital Light Processing 3D printer (DLP, Microlay, Versus 385nm, Spain). We cut a sheet of the nylon mesh with the size of the 3D printer build platform and taped it with special double-side adhesive tape (No.99786, 3M, USA) of 1 cm width and 0.3 mm thickness on the four edges of the Building Platform. We cured the 3D resin layer by layer following the CAD design of a ring of 6 mm outer diameter and 5.5 mm internal diameter, resulting in an embedded nylon mesh inside a rigid ring-shaped frame formed by the cured 3D resin. We show a schematic of the fabrication process and the mesh itself in Fig. 6.2A and Fig. 6.2B, respectively.

4.2.5 Magnetic Resonance Imaging for Diffusion and Perfusion Studies

We obtained the MRI images using a dual-tuned ¹H-¹³C volume coil (42 mm inner diameter, Bruker) inside a horizontal 3T MRI scanner (BioSpec 105 mm bore diameter, Bruker®). We corrected magnetic field inhomogeneities with a shimming protocol applied to a water-filled Eppendorf prior to imaging. We used ParaVision 360 version 3.4 to acquire the images in the 3T MRI scanner. We acquired the magnetic resonance proton images using a T₁ FLASH sequence with the following acquisition parameters: echo time 9.0 ms, repetition time 425.0 ms, 60° flip angle, 4 averages, 192x128 image pixel size, 10x40 field of view, 20 mm thickness, 1 slice, 2 dummy scans of 849.787 ms, acquired with linear encoding, a bandwidth of 13888.9 Hz, a working frequency of 127.64 MHz and a working chemical shift of 4.7 ppm.

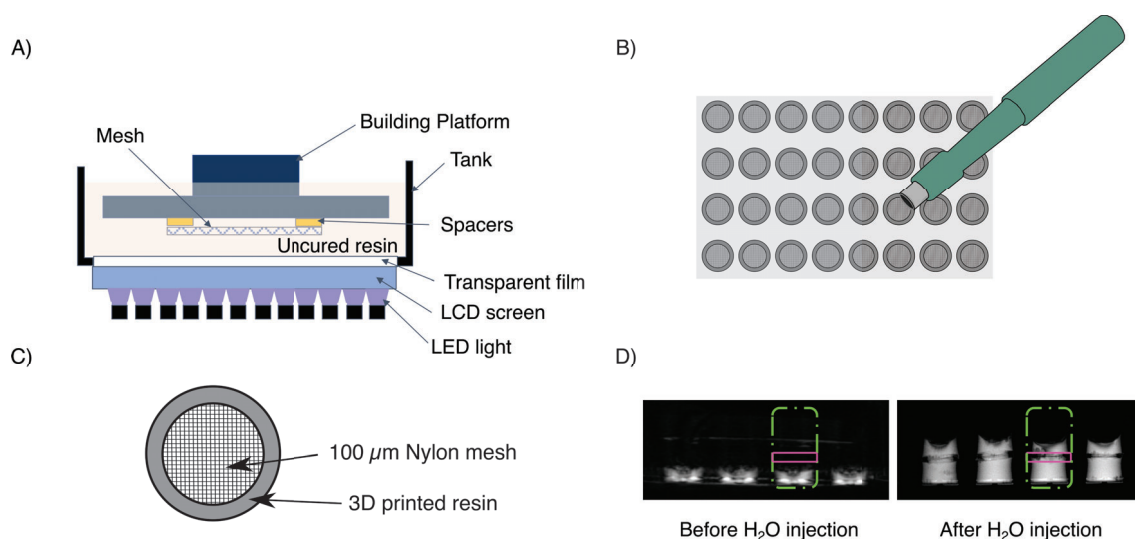


Figure 4.3: Custom nylon mesh used to allow perfusion studies in a microfluidic chip. A) Schematic representation of the nylon mesh fabrication setup, placing it with adhesive spacers on the building platform of a DLP 3D printer. B) Schematic image of the punching procedure to obtain individual meshes with a 5 mm i.d. biopsy punch. C) Schematic image of the nylon mesh used. D) T₁-FLASH sagittal images of the 4-well chip used containing the scaffolds at the bottom (water signal from the scaffold) before (top) and after (bottom) injecting water. We highlighted the well region with dashed green lines and the one with meshes in pink.

4.2.6 Data Processing and Analysis

We used Bruker's inbuilt acquisition software (ParaVision 360, version 3.4) to process all the proton MRI images acquired and obtain the subsequent DICOM files. From the DICOM images, I defined all the regions of interest (ROI) required (i.e. scaffold and container region) using ImageJ (version 2.14.0) and generated binary masks from them. At this point, we processed all the data using custom-made Python scripts (version 3.10.9) to extract pixel intensity values and compute region averages or sums from individual ROIs. The postdoctoral researcher from the group, Dr. David Gomez-Cabeza wrote these scripts.

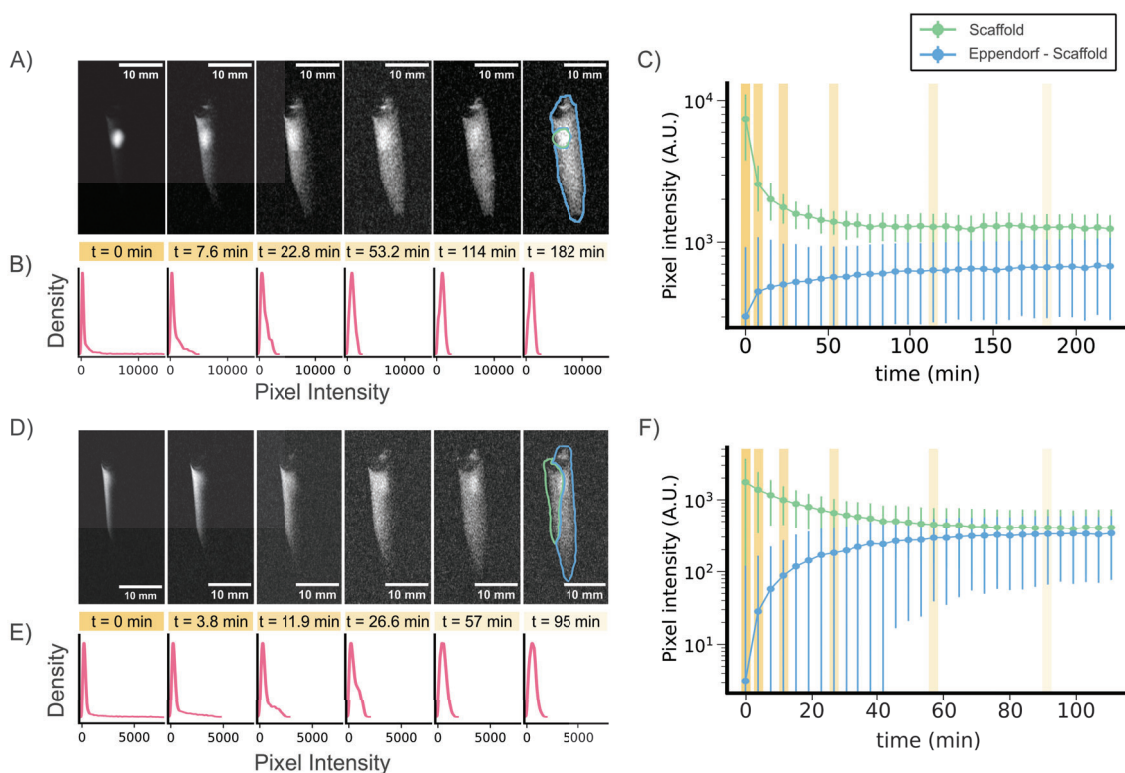


Figure 4.4: Diffusion studies of commonly used biocompatible scaffolds using MRI. Sagittal proton images at different times of an Eppendorf containing D_2O and a water-saturated PEGDA hydrogel (A) or CMC cryogel (D). For each image shown, I display a kernel density estimation of the pixel intensity inside the container for both the hydrogel (B) and the cryogel (E), indicating a starting point of a distribution with a long right tail (high proton signal located in a small spatial region) evolving to a normal distribution due to the diffusion of water particles in the whole Eppendorf. Plots of the mean pixel intensity for the scaffold region (green) and the rest of the container (blue) for all images acquired every 3 minutes and 48 seconds during 4 hours and 22 minutes for the PEGDA hydrogel (C) and 1 hour and 54 minutes for the CMC cryogel (F).

4.3 RESULTS & DISCUSSION

4.3.1 Study of passive diffusion properties of bio-compatible scaffolds using MRI and D_2O as a contrast agent

Firstly, I used MRI to test the passive diffusion of water in both a PEGDA hydrogel and a CMC cryogel. We filled 0.5 mL Eppendorfs with deuterium oxide (D_2O) and introduced the scaffold under study in them. Immediately after insertion of the scaffolds, I started the proton MRI imaging sequence to acquire a frame every 3 minutes and 48 seconds for about 4.4 hours for the hydrogel (Fig. 6.3A) and 1.9 hours for the cryogel (Fig. 6.3D).

We then manually defined the scaffold and the Eppendorfs regions of interest (ROIs).

We doubtlessly observed the passive diffusion of water from a scaffold into an enclosed environment with proton MRI imaging and using contrast agents (i.e. D_2O). Analysing the distribution of pixel intensities inside the container used, I observed that both the hydrogel (Fig. 6.3B) and the cryogel (Fig. 6.3E) showed a particle exchange with the surrounding media following Fick's laws of passive diffusion. First, the proton signal intensity came only from the scaffold, making for a small region of the ROI to have high pixel intensities. Hence, most pixels had signals close to the machine's background noise. The first kernel density estimates of Fig. 6.3B and Fig. 6.3E show this phenomenon for both scaffolds. The highest probability region is located around the background noise value, with the distribution having a long right tail, representing the few scaffold ROI pixels with high intensity. As time progressed, the passive diffusion observed in both cases distributed uniformly the water protons across the entire container. Consequently, the kernel density estimates evolved towards Gaussian distributions, now centred at the mean pixel intensity instead of in the background ones.

The scaffolds analysed in this study showed different diffusion constant rates and homogeneous particle exchange efficiency, highlighting the CMC cryogel as the best candidate for a fast and thorough diffusion. As shown in Fig. 6.3C, the PEGDA hydrogel exhibited a fast particle exchange at the beginning of the analysis, potentially from the water particles surrounding the scaffold on their immediate surface. Yet, the water contained in the core of the scaffold took a longer time to diffuse. The system seemed to stabilise after 2 hours and 40 minutes. However, the proton images still have higher pixel intensity in the scaffold ROI (Fig. 6.3A). On the other hand, the CMC cryogel showed a more uniform diffusion for its enclosed water, with the system stabilising after 1 hour and 20 minutes, as shown in Fig. 6.3F. Furthermore, the pixel intensities in the proton images (Fig. 6.3D) were more uniformly distributed by the end of the experiment, suggesting full diffusion of all the water contained in the scaffold. Hence, with these experiments, I showed the usefulness of MRI to characterise inherent properties of bio-materials (i.e. diffusion characteristics) with a high enough resolution to determine differences between scaffolds types.

4.3.2 Study of the perfusion properties of bio-compatible scaffolds using custom-designed microfluidic systems

In specific scientific scenarios, rapid perfusion within the scaffold is mandatory (in the range of a few seconds) to prevent deterioration of the injecting reagent. For example, in Hyperpolarised Magnetic Resonance (HP-MR), the contrast agent normally has a lifetime of about 1-2 minutes, requiring swift delivery[31]. Another clear example would be to ensure a complete wash of a drug previously administered to the cells for therapy studies[172]. For this reason, I studied scaffold perfusion using microfluidic chips containing wells where I placed the scaffolds. To enforce perfusion and retain the scaffolds inside these wells, my lab colleague Alejandro Portela developed 3D-printed mesh structures (Fig. 6.2 c). To avoid the formation of air bubbles in the microfluidic channels, I previously filled this with D₂O. Fig. 4.5A shows the procedure schematic, where a scaffold is inserted into a chip well, and the mesh is added on top to allow fluid flow perfusion into scaffolds. Also, note that any flow rate reported indicates the one used for the injection, which gets distributed across the 4 parallel channels, making the speed observed in the well be one-quarter of the original one.

4.3.3 Perfusion assessment of CMC scaffolds in a 4-well microfluidic device

4.3.3.1 Fast perfusion evaluation of 10 % PEGDA hydrogels

Our strategy to study the perfusion properties of scaffolds spotlighted issues on removing water from the core of PEGDA hydrogels when performing manual D₂O injections (\approx 10-50 mL/min). Furthermore, the customised meshes fulfilled their purpose by effectively hindering the scaffolds at the bottom of the wells, forcing the injected solution to pass through them. When perfusing the contrast agent through the PEGDA hydrogel scaffolds, I clearly observed, in a consistent manner, a reminiscent water proton signal located in the scaffold region. We can observe this phenomenon in Fig. 4.5B, where even after the D₂O injection, there is still some pink colour (water proton signal) at the bottom of the chip's wells. By representing the horizontal pixel sum of each well, as shown in Fig. 4.5C, we can more evidently observe the presence of water signal after the perfusion test, represented by spikes of signal at the bottom of the well in all tests performed. Hence,

with these results, I demonstrated that this type of commonly used scaffold (i.e. 10 % PEGDA hydrogels) would be inefficient for fast perfusion requirements, such as when using HP-MR substrates or when we want to rapidly remove administered drugs to seeded cells.

It is a step-by-step guide detailing the preparation of the microfluidic device and the precise sequence for introducing its components. In the final step, a thorough examination is performed to assess the impact of the mesh on the D₂O perfusion within the scaffold.

Purple represents water proton signal before manual injection of D₂O, and pink after it. Red represents water proton signal before manual injection of D₂O, and cyan after it.

4.3.3.2 Perfusion evaluation of 1 % CMC cryogel scaffolds

Thanks to magnetic resonance imaging (MRI), we reliably and reproducibly detected complete perfusion of the contrast agent (i.e. deuterium oxide) testing 1 % CMC cryogel scaffolds, again performing manual injections into the microfluidic chip, with varying flow rates from 10 to 50 mL/min. Compared to the experiments performed with the PEGDA hydrogel, when using a 1 % CMC cryogel, all the D₂O injected perfused, removing all the water from the scaffold and placing this at the top of the well. We can observe this process in the proton images from Fig. 4.5D and confirm the absence of proton signal after injection by looking at the horizontal pixel sum of each well shown in Fig. 4.5E. Despite having four replicates per experiment thanks to having four independent wells in the chip, I repeated this experiment three times to ensure the perfusion efficiency of the cryogel tested. As I indicate in Fig. 4.5F, the results were consistent at each trial, with each replicate showing that for each well, all the water proton signal was displaced out of the scaffold into the top of the well after the injection of D₂O.

Furthermore, MRI allowed us to determine that the perfusion properties of the 1 % CMC cryogel were consistent in a wide range of flow rates. We substituted the hardly reproducible manual injection with a controlled one, leveraging an automatic syringe pump to perfuse the deuterium peroxide. We selected a range of flow rates to represent common ones used for continuous media recirculation in microfluidic devices[173], going up to the maximum allowed by our pump. As previously done, I placed a single scaffold in each well of the microfluidic chip used and injected D₂O at different flow rates (i.e. 0.1, 0.5,

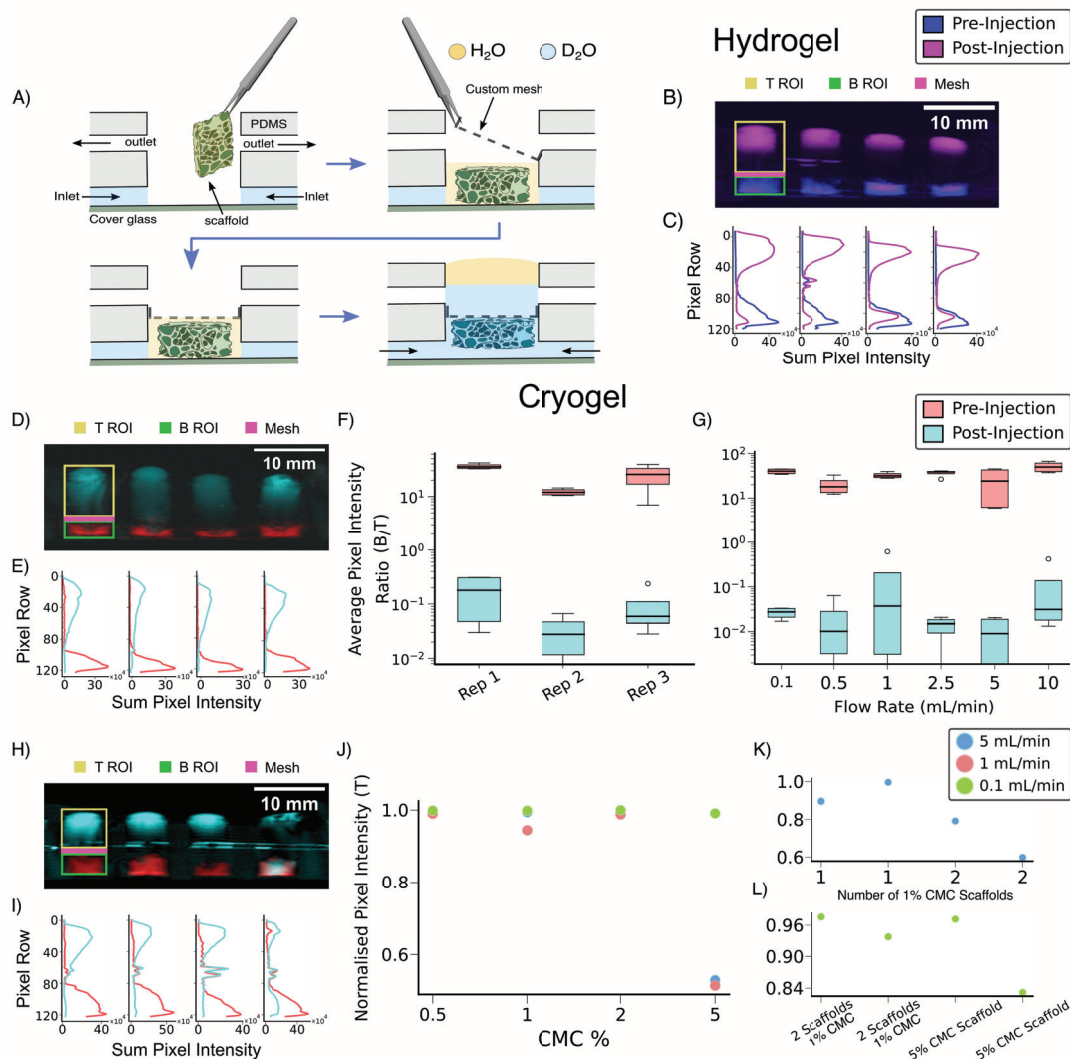


Figure 4.5: Perfusion studies of hydrogels and cryogels using MRI. A) Protocol conducted to execute all perfusion experiments with scaffolds using a 4-well microfluidic chip and a custom mesh to keep them in place. B) Sagittal proton MRI image composite of the 4-well chip containing a 10% PEGDA hydrogel in each well. C) Horizontal pixel sum of each well ROI from panel B. D) Sagittal proton MRI image composite of the 4-well chip containing a 1% CMC cryogel in each well. E) Horizontal pixel sum of each well ROI from panel D. F) Average pixel intensity of the four wells scaffold region (B ROI) over the rest of the well (T ROI) for three replicates of an experiment with a single 1% CMC cryogel per well. G) Pixel average of the four wells B ROI over T ROI for experiments with a single 1% CMC cryogel per well injecting the D₂O at different flow rates (0.1, 0.5, 1, 2.5, 5 and 10 mL/min). H) Sagittal proton MRI image composite of the 4-well chip containing a 0.5%, 1%, 2% or 5% CMC cryogel in each well (from left to right). I) Horizontal pixel sum of each well ROI from panel H. J) Well region without scaffold (T ROI) pixel intensity normalised by the total one (T ROI + B ROI) for three experiments containing a 0.5%, 1%, 2% or 5% CMC cryogel in each well injecting D₂O at different flow rates (0.1, 1 and 5 mL/min). K) Normalised T ROI for an experiment containing one or two 1% CMC cryogels in each well injecting D₂O at 5 mL/min. L) Normalised T ROI pixel intensity for an experiment containing two 1% or one 5% CMC cryogels in each well injecting D₂O at 0.1 mL/min.

1, 2.5, 5, and 10 mL/min) for each experiment. As represented in Fig. 4.5G, in all cases, the water proton signal was removed from the scaffold region and pushed to the top of the well. Also, the low variability in the box plots for the post-injection indicates that the water proton signal was displaced to the top of the well (T ROI) for all the wells in every experiment. Hence, with these results, I again validated the utility of MRI for studying perfusion and also demonstrated the advantage of the cryogel used for fast, efficient and consistent perfusion of media at a wide range of flow rates.

D₂O perfused properly through the 1 % CMC scaffold when I swiftly injected the deuterated water manually. We placed the 4-well microfluidic chip with the corresponding connections in the MRI scanner bed, setting the centre of the device in the most homogeneous region of the MRI scanner. We first flowed D₂O through the inlet channels, filling half of the well. We then removed all the D₂O of the cavities and put a scaffold submerged in water with tweezers. Later, I placed the mesh on the top of the scaffold. The chip then contained one scaffold with the corresponding mesh at the top surrounded by water in each well. We injected the solution from the bottom and perfused D₂O through the tubing and the channels to avoid the production of bubbles during the injection. After moving the chip inside the MRI scanner, I acquired a T₁-FLASH sequence to image all three planes of the chip to verify I placed it properly and check the absence of bubbles..

I took the chip out of the MRI scanner to make the manual injection, avoided any potential overflow of the solution out of the wells. We quickly injected the D₂O, pushing the syringe manually taking around three seconds to fill all the wells contained in the microfluidic device. The total volume injected manually with the syringe was $\approx 600 \mu\text{L}$ at around 12 mL/min of flow rate. In reality, the flow is distributed across 4 channels at the same time, so the speed at which it is delivered is one-quarter for each well, so 3 ml/min. We carried out three replicates of the experiment to assess the reproducibility of the experimental approach.

The customised meshes fulfilled their purpose by effectively hindering the scaffolds at the bottom of the wells, forcing the injected solution to pass through them. With this methodology, I successfully achieved to perfuse a dissolution into the scaffold in less than 5 seconds. This fact allows us to confidently inject any dissolution that requires rapid execution.

4.3.3.3 Controlled perfusion evaluation of scaffolds using a syringe pump

In this approach, I injected the external solution in a controlled manner using a syringe pump, testing how the injection flow rates affect the perfusion inside the scaffold. In this case, I substituted the hardly reproducible manual injection by a reliable and controlled way using an automatic syringe pump. We connected the syringe to the microfluidic chip through a 3 mm OD PTFE tubing using a luer connector. We tested six different flow rates: 10 mL/min, 5 mL/min, 2.5 mL/min, 1 mL/min, 0.5 mL/min and 0.1 mL/min. Also pointing out that the real flow that the scaffolds see is one fourth of the corresponding one. We effectively pushed out the water solution from the scaffold at all tested flow rates. In Fig. 4.6 I show a schematic example of the setup was performed simulating the flow of the experiment.

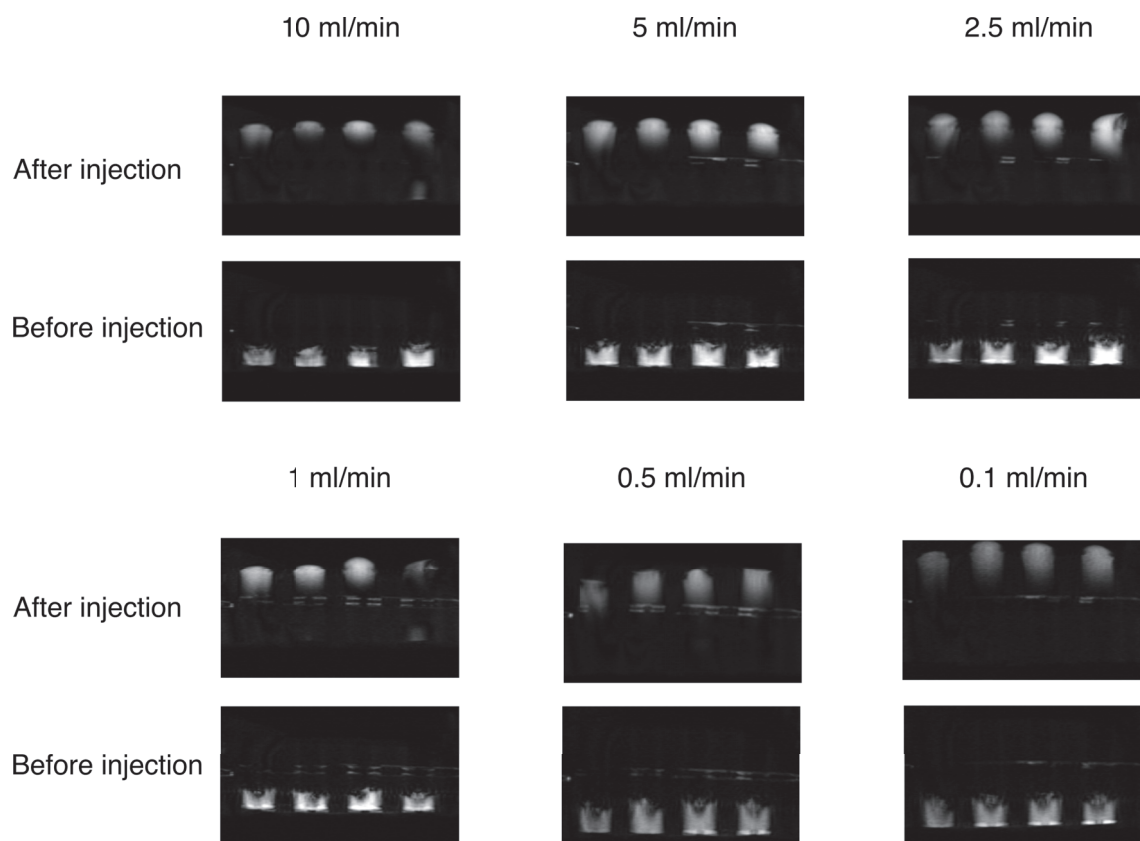


Figure 4.6: Sagittal MRI images from the microfluidic device before and after the D_2O injection with different flow rates. We tested 6 different flow rate (10 mL/min, 5.0 mL/min, 2.5 mL/min, 1.0 mL/min, 0.5 mL/min, 0.1 mL/min) and for each flow rate we show the MRI imatge before and after the D_2O injection trough the bottom of the microfluidic device

4.3.3.4 Controlled perfusion evaluation of variable % of CMC cryogel scaffolds

With this new approach to assessing scaffold perfusion, I determined that denser cryogels have more problems letting liquid inside, particularly at high flow rates. To further validate the capabilities of MRI to study perfusion, I tested cryogels with a different carboxymethylcellulose (CMC) % (w/w), modifying their stiffness, density and porosity. Concretely, I made and tested cryogels with 0.5, 1, 2 and 5 % of CMC. The initial tests, done at a flow rate of 1 mL/min, indicated perfusion issues only with the 5 % CMC cryogel. We shown these issues in Fig. 4.5H, where there is still water proton signal at the bottom of the well (B ROI) after injecting D₂O, where the scaffold's percentage of CMC is in increasing order, from left to right. Again, the horizontal pixel sum (Fig. 4.5I) clearly evidenced this fact, showing signal peak in the bottom region after injection of the contrast agent. We indicate the results for three different flow rates in Fig. 4.5J, where the 5 % CMC cryogel only fully ejected its contained water at the lowest flow rate (i.e. 0.1 mL/min). We hypothesised that this phenomenon happened due to higher porous resistance at high flow rates in a much denser, stiffer and less porous scaffold. This lower perfusivity also happened if I stacked two 1 % CMC cryogels in one same well, as shown in Fig. 4.5K, indicating that the scaffold disposition and fluid resistance also plays an important role. We back up this assumption by also reducing the flow rate in this case to 0.1 mL/min, where again there is a significant increase in perfusion efficacy as indicated in Fig. 4.5L. Hence, thanks to MRI and contrast agents I determined the perfusion efficiency of scaffolds of different stiffness, densities and porosities uncovering some fluidic issues potentially caused by high resistances.

We modified the fabrication of the CMC scaffolds, adapting the % (w/w) of the carboxymethylcellulose to modify the stiffness, density, and porosity of the biomaterial and test how this could possibly affect its perfusion.

We then connected the syringe pump with the microfluidic device the same way I did in the previous experiment. In this case, I tested the perfusion with three different flow rates: 5 mL/min, 1 mL/min, and 0.1 mL/min 4.7. In the first two experiments using 5 and 1 mL/min respectively, the perfusion was almost completed in 0.5, 1 and 2 % CMC scaffolds. However, in the 5 %, I got some of the water signal still in the bottom of the

well, where I placed the scaffold. In the last experiment at 0.1 mL/min, all the water contained and surrounding the scaffold was pushed up of the well, having no protons in the bottom part of the wells.

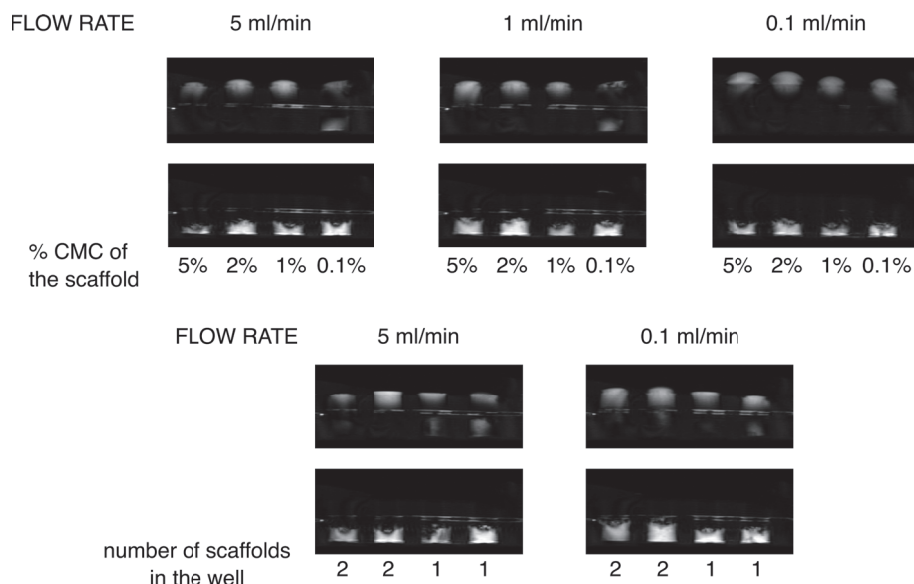


Figure 4.7: Sagittal MRI images from the microfluidic device before and after the D_2O injection with different flow rates, different % of CMC in the scaffolds and different number of scaffolds in the well. In the top row we tested the perfusion with 3 different flow rates and 4 different CMC scaffolds compositions. In the bottom row we tested the perfusion at two different flow rates with different number of scaffolds at 1 % CMC.

4.4 CONCLUSIONS

In this work, I show how magnetic resonance imaging combined with D_2O as contrast agent is an advantageous tool to investigate the physical properties of materials. In particular, I used this approach to examine the diffusion and perfusion properties of porous bio-compatible materials (i.e. scaffolds) commonly used to develop 3D cell culture models. Thanks to the deuterium's different spin number compared to the hydrogen one, I submerged water-filled scaffolds into an enclosed container filled with deuterium oxide (D_2O). Hence, I imaged, over time, the diffusion of water molecules enclosed in scaffolds into the surrounding environment. Furthermore, thanks to microfluidics and custom-made meshes, I studied the perfusion properties of such materials, highlighting the importance of the scaffold stiffness, density and porosity type. Therefore, I show a novel methodology to effectively study diffusion and perfusion in a fast, easy, low-cost and reproducible

way.

POLARIZATION LOSSES RESULTING FROM THE NONADIABATIC PASSAGE OF HYPERPOLARIZED SOLUTIONS THROUGH METALLIC COMPONENTS

This project came out from an initial idea discussed with my supervisor and colleagues from the IDIBAPS research center. The main objective was to ensure that the hyperpolarized contrast agent remained unperturbed in its polarization throughout injection via a cannula inserted into the animals under study in the MRI scanner. I had the privilege to collaborate on this project with one of my mentors and close friends, Dr James Eills. My role in the project was both partial planning and designing of the experiments, half of the experimental work and designing certain figures of the manuscript. This project was eventually published in Journal of Magnetic Resonance[174].

5.1 INTRODUCTION

Hyperpolarization has opened the door to many applications such as *in vivo* metabolic imaging[175, 48, 21, 176, 177], the elucidation of biomolecular structures[178, 179, 180, 181], investigations of polymers and viscous liquids[182, 183] plus heterogeneous and homogeneous hydrogenation reaction mechanisms[184, 185, 186, 187], and many more. Central to most of these applications is that the nuclear spin polarization survives move-

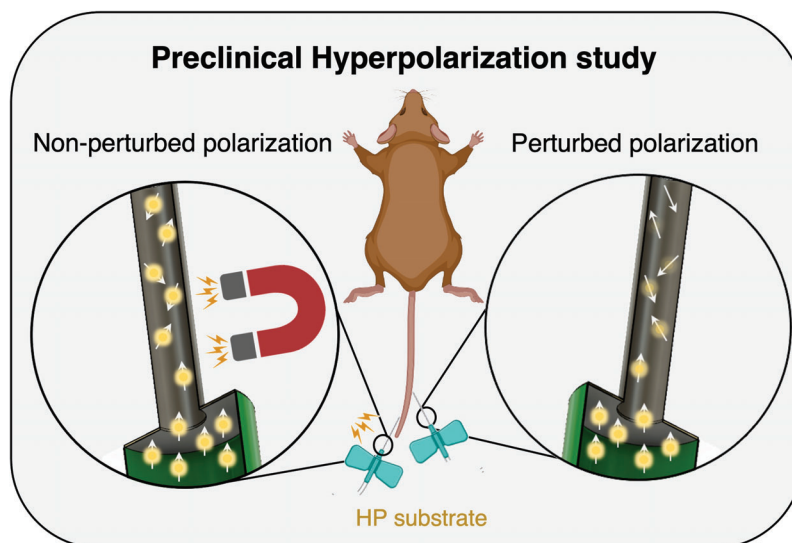


Figure 5.1: Graphical representation of the third chapter purpose. In this picture I represented the injection of hyperpolarized $[1-^{13}\text{C}]$ pyruvate to a mouse through its tail. We represent the injection with the presence of a magnet, preserving the spins polarization when the solution transferred through a needle, and the injection without the presence of the magnet, with the polarization being perturbed by the needle.

ment of the liquid sample, for example during transport across a laboratory, or during sample mixing. That is because the hyperpolarization procedure is often carried out away from the measurement device in a separate instrument[188].

The profile of magnetic field experienced by the sample vs. time determines the survival of nuclear spin polarization during transport. On the one hand, spin relaxation governs how rapidly polarization returns to thermal equilibrium and is generally (although not always) characterized by a decay time constant, T_1 , that is field-dependent. Generally, if the transport time is similar to or longer than T_1 , a significant fraction (more than half) of the starting polarization is lost.

The earth's field is in principle sufficiently strong and homogeneous to satisfy adiabaticity, even at high transport rates such as fluid flow inside capillary tubes[189, 190, 191, 192, 193, 194, 195, 196]. However, in an unshielded laboratory environment there exist additional background fields from magnetic objects, such as NMR magnets or electrical laboratory equipment. In this case, the total magnetic field is much less homogeneous, and may be weak enough so that adiabaticity cannot be fulfilled when the sample is in motion. These points in space are colloquially referred to as a 'zero-field crossings'[197].

This term is helpful, although it may be slightly misleading since it is likely that inhomogeneity in the directionality of the field lines (causing an effective rotation in the B_0 field during transport) is more problematic than going to low field itself. One way to maintain adiabaticity in order to preserve spin polarization is to provide a high magnetic field along the sample transport path by using a magnetic tunnel[197, 191, 198, 199].

This is particularly helpful for solid samples where strong intermolecular dipole-dipole couplings can lead to nonadiabatic transfer effects near Earth's field, because these couplings become the interaction of leading strength[200]. An additional benefit of magnetic tunnels is that T_1 time constants are often slightly longer in elevated field compared to Earth's field[201, 202], especially if the solution contains paramagnetic species such as the radicals used for the DNP process or quadrupolar nuclei, such as ^{14}N [203].

We have observed in experiments with hyperpolarized samples that passage of the sample through stainless steel parts such as syringe needles or through capillary tubing supporting nuts/ferrules can lead to partial or complete loss of the hyperpolarization. We attribute this to the spins experiencing nonadiabatic changes in the B_0 field when passing rapidly through these small-diameter, weakly ferromagnetic parts. In this work I investigate how nuclear spin polarization in liquid samples is affected by passage through stainless steel syringe needles under conditions such as the needle length/diameter, orientation in space with respect to the ambient field, and strength of additional guiding fields. We have carried out experiments with dDNP-polarized $[1-^{13}\text{C}]$ pyruvate detected in a 1.4 T bench-top NMR magnet, and with water polarized in a 1 T permanent magnet, detected in a sub-Earth's-field spectrometer.

5.2 MATERIALS & METHODS

5.2.1 HF Experiments with Hyperpolarized $[1-^{13}\text{C}]$ pyruvate

To hyperpolarize $[1-^{13}\text{C}]$ pyruvate, 24 μL of $[1-^{13}\text{C}]$ pyruvic acid (Merck, Darmstadt, Germany) containing 15 mM trityl radical OX063 (GE Healthcare, Illinois, U.S.A.) and 1.5 mM gadoteric acid (Guerbet, Villepinte, France) was placed into a sample cup and inserted into a HyperSense commercial dissolution-DNP polarizer (Oxford Instruments Ltd., Oxford, U.K.) operating at 3.35 T magnetic field. This sample was cooled to 1.3 K, and irradiated

with 100 mW microwaves at 94.115 GHz for approximately 40 min. The hyperpolarized frozen solid was then rapidly dissolved and flushed out of the polarizer by injecting 5.2 mL of heated phosphate buffered saline supplemented with 1% HEPES, 0.01% EDTA, 0.1% NaCl, and 0.2% NaOH (pH 12). This yielded a 5 mL solution of 80 mM [1-¹³C]pyruvate at pH 7 and around 12.5% ¹³C polarization, which was collected in a plastic falcon tube. The resulting mixture was then further diluted by adding 10 mL MilliQ water, resulting in 15 mL of 27 mM [1-¹³C]pyruvate solution. This dilution was performed to have enough sample to fill all the NMR tubes required for each experiment. The radicals (24 μM in our experiments) were not filtered because (i) the impact on T_1 is small, even at very low fields where the adiabatic condition fails to be met,[204] and (ii) to a large extent, relaxation and nonadiabaticity contributions to polarization loss are decoupled from one another.

The sample was extracted through a plastic capillary (1/16 inch O.D., 1/32 inch I.D., polyether ether ketone) into a 20 mL plastic syringe. At this point after extracting the sample from the polarizer it had not come into close contact with any metallic parts. The sample was then injected into 5 mm O.D. borosilicate NMR tubes through either the same plastic capillary (for control experiments), or a metal syringe needle, as described in the text. The sample injections were performed every T s (for Fig. 5.2 $T = 10$ s, for Fig. 5.2 $T = 12$ s), with 300-400 μL of hyperpolarized solution injected into each tube (a sufficient volume to completely fill the NMR coil to ensure quantitative measurements). After filling, each tube was immediately inserted into a 1.4 T benchtop NMR spectrometer (Pulsar, Oxford Instruments) and a ¹³C NMR spectrum was recorded. The tube was then removed from the NMR magnet and discarded. In this way, the hyperpolarized [1-¹³C]pyruvate solution was kept in the 20 mL plastic syringe, with a small aliquot ejected into a separate NMR tube every 10 – 12 s immediately prior to NMR signal acquisition. The acquisition parameters for all ¹³C NMR measurements were an acquisition time of 3.2 s; 16 k data points; 90° flip-angle excitation pulse (15.5 μs).

Needle	Gauge	Length (in.)	Provider
I	21G	2	BD Microlance
II	20G	0.5	Darwin Microfluidics
III	19G	1	Henke Sass Wolf
IV	18G	1.5	BD Microlance
V	25G	5/8	BD Microlance
VI	25G	0.5	Darwin Microfluidics
VII	27G	3/4	BD Microlance

Table 5.1: Summary of the seven metal syringe needles used in this work. Unless otherwise specified, needle VII was used for experiments.

5.3 RESULTS & DISCUSSION

5.3.1 HF experiments with hyperpolarized [1-¹³C]pyruvate

A concentrated pellet of neat [1-¹³C]pyruvic acid was polarized via dissolution DNP using a HyperSense polarizer (Oxford Instruments, U.K.), and ejected via rapid dissolution. The resulting pH neutral solution contained [1-¹³C]pyruvate at 80 mM concentration and 12% ¹³C polarization. 4 mL of this solution were immediately diluted further with distilled H₂O to bring the total volume up to 20 mL. Then, 400 μ L aliquots of this solution were dispensed sequentially into a series of 5 mm o.d. NMR tubes using either a plastic capillary or a syringe needle to direct the solution into each tube.

These dispensing operations were performed rapidly (one every few seconds), and the tubes were taken every 10 s for signal acquisition. An illustration of the experiment is shown in Fig 5.2(a,b). Initial NMR acquisitions on NMR tubes filled via a PEEK capillary served as control points, since the hyperpolarized solutions did not come into contact with any metal parts. Subsequent NMR tubes were filled using seven different metal syringe needles, as shown in Table 5.1 (in the Materials and Methods) and Fig 5.2(c). The solution was either supplied through the needle in Earth’s field (cyan), with a neodymium N52 bar magnet (1.45 T remanent field) held next to the needle (purple), or with the needle inside a 1 T Halbach magnet (gold). The resulting data are shown in Fig 5.2(e).

We observe that the control spectra (black points) in Fig 5.2 show an exponential decay in amplitude over time, with a time constant of 56 ± 0.4 s. This corresponds to the ¹³C T_1 decay time constant of the solutions in Earth’s field, during the period when the samples were kept outside the NMR magnet prior to measurement. Injection through a

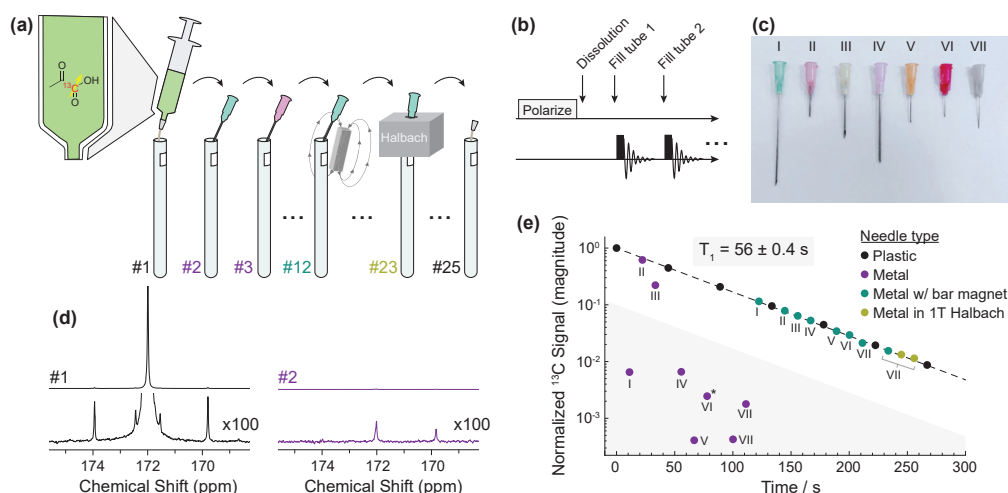


Figure 5.2: (a) Experimental schematic illustrating the methodological progression: initial NMR tube filling via a PEEK capillary for the first acquisition is indicated by #1. Subsequent NMR tubes were filled using individual syringe needles for acquisitions #2-#25, with strategic positioning of an N52 bar magnet for acquisitions #12-#22 or a 1T Halbach magnet for acquisitions #23-#25. (b) Simplified sequence showing the experimental procedure. (c) The 7 syringe needles used for this experiment. (d) A comparison between the ^1H -decoupled ^{13}C NMR spectra of acquisitions #1 (left) and #2 (right) illustrated in (a), showing a significant decrease of the $[1-^{13}\text{C}]$ pyruvate ^{13}C signal when the sample was passed through a syringe needle in #2). The bottom spectra are a vertical zoom $\times 100$ of the corresponding top spectra. The satellite peaks observed are from the natural abundance of pyruvate molecules with an additional ^{13}C nucleus in the C2 or C3 position. (e) Effect of different injection conditions on $[1-^{13}\text{C}]$ pyruvate liquid-state polarization. Data points represent the integrals (absolute value) of the $[1-^{13}\text{C}]$ pyruvate ^{13}C NMR signal of the labelled C1 position, normalized to 1 for the first scan. The dotted line represents an exponential decay function of the form $M(t) = M_0 \exp(-t/T_1)$ fit to the data, and the fitted T_1 value is given in the plot. The grey shaded region represents the area in which the ^{13}C integral is more than $10\times$ lower than predicted from the control experiments. The asterisk denotes a data point with negative amplitude.

syringe needle reduced the magnitude of the NMR signal by at least a factor of 10 in almost all cases, with the exception of needles II and III. In one case (needle VI) the resulting ^{13}C signal was still weakly hyperpolarized but inverted in sign, indicating that (as expected) these signal losses result from nonadiabatic passage through the needle and not an incoherent relaxation process. In contrast, when the N52 permanent magnet was placed adjacent to the needle during injection, and likewise when the needle was placed inside a permanent 1 T Halbach magnet, the polarization was preserved in all cases.

In Fig 5.2(d) a comparison between ^{13}C spectra in the frequency range of the pyruvate C1 site is shown for a sample injected through a plastic capillary and through syringe nee-

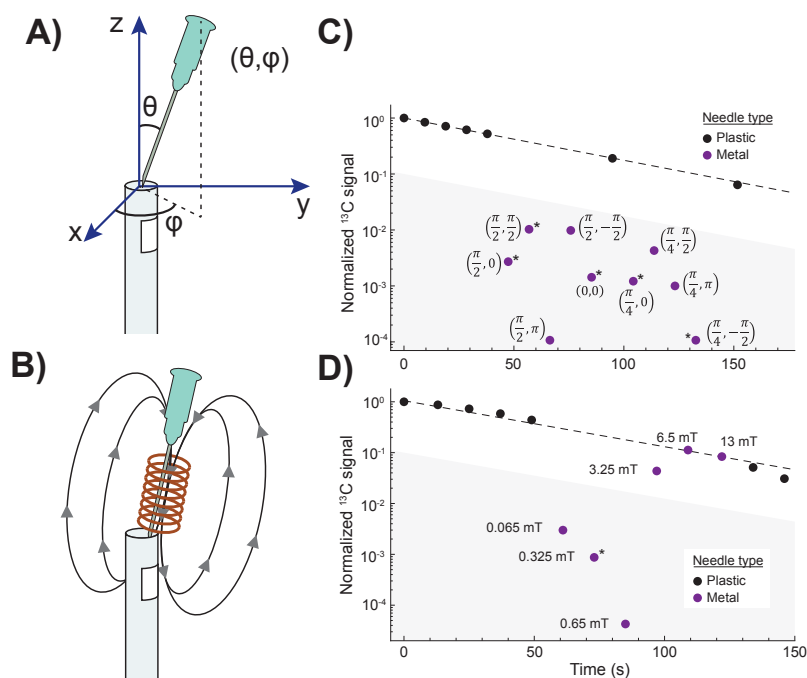


Figure 5.3: (a,c) Effect of the angle of the syringe needle in space on the ^{13}C polarization. Data points represent the integrals (absolute value) of the $[1-^{13}\text{C}]$ pyruvate ^{13}C NMR signal of the labelled C1 position, normalized to 1 for the first scan. Numbers in brackets represent the angle of the needle with respect to the laboratory in spherical coordinates, as represented in part (a). The dotted line represents an exponential decay function fit to the data, and the grey shaded region represents the area in which the ^{13}C integral is more than an order of magnitude lower than predicted from the control experiments. Asterisks indicate data points that have a negative integral. (b,d) Effect of an applied magnetic field on the ^{13}C polarization. The experiment was carried out with the needles always upright in an NMR tube, but with a variable field applied during sample injection using a solenoid coil. The applied fields are written next to the corresponding data points.

dle I. For the solution that passed through the syringe needle, the central peak at 172 ppm is almost completely lost. The additional peaks in the spectrum, which somewhat survive, are ^{13}C satellite peaks from the $[1,2-^{13}\text{C}_2]$ (outer satellites) and $[1,3-^{13}\text{C}_2]$ (inner satellites) pyruvate isotopologs.

To understand whether the alignment of the needle in space (i.e., its alignment in the laboratory magnetic field) affects the adiabaticity of the process, I repeated the hyperpolarized $[1-^{13}\text{C}]$ pyruvate multi-injection experiment using needle VII, with the solution injection into the NMR tubes carried out at different needle orientations in space (Fig. 5.3(a)).

I also performed periodic control experiments, injecting the pyruvate solution through a plastic capillary into the NMR tubes. As before, the NMR tubes were placed in a

1.4 T bench-top NMR spectrometer for ^{13}C signal acquisition, and the integrals of the C1 [$1\text{-}^{13}\text{C}$]pyruvate NMR signals are plotted in Fig. 5.3(c). The orientation of the needle with respect to the axis system of the laboratory is denoted in spherical coordinates as (θ, ϕ) , with θ the polar angle and ϕ the azimuthal angle, next to the corresponding data point. These data indicate that the orientation of the needle in space does not significantly influence the dephasing of the spins, since in all cases a signal reduction by more than a factor of 10 is observed.

We then carried out an experiment to determine what strength of applied magnetic field around the syringe needle would make the injection process adiabatic to preserve the ^{13}C hyperpolarization. The hyperpolarized [$1\text{-}^{13}\text{C}$]pyruvate multi-injection experiment was repeated using needle VII, with a solenoid electromagnet wrapped around the needle to provide a guiding magnetic field (Fig. 5.3(b)). The strength of the guiding field was varied between experiments by changing the current through the coil with a variable DC supply. The ^{13}C NMR signal integrals from the C1 site in [$1\text{-}^{13}\text{C}$]pyruvate are shown in Fig. 5.3(d). The applied field for each injection is shown next to the corresponding data point. We observed that a field of between 3.25 mT and 6.5 mT was required for the solution transport through the needle to be adiabatic.

Periodically, for some experiments in this series, the pyruvate solution was injected through the plastic capillary to obtain reference signals to quantify the polarization loss. In Fig. 5.4 I show a comparison between the ^{13}C spectra for two hyperpolarized [$1\text{-}^{13}\text{C}$]pyruvate samples: one that passed through a plastic capillary and the other that passed through needle VII. For the latter, the central peak from the C1 site is dramatically reduced in amplitude by the nonadiabatic passage through the needle, but the carbon satellite peaks from the 1.1% of molecules with a ^{13}C nucleus in the C2 position remain hyperpolarized. The ^{13}C NMR signal of the C2 carbon (207 ppm) is also mostly unaffected by the needle passage. The chemical shift difference between the two carbon sites is 35.1 ppm and the $^1J_{\text{CC}}$ -coupling is 62 Hz, meaning the J -coupling dominates at low fields, leading to a change in the eigenbasis to the singlet-triplet basis. The $^{13}\text{C}\text{-}^{13}\text{C}$ singlet state is a non-magnetic state that is unaffected by the magnetic field changes experienced during sample transport (i.e., from the needle passage), but is transformed back into an observable magnetic state as the sample is placed in the high-field NMR magnet. Our observation is the

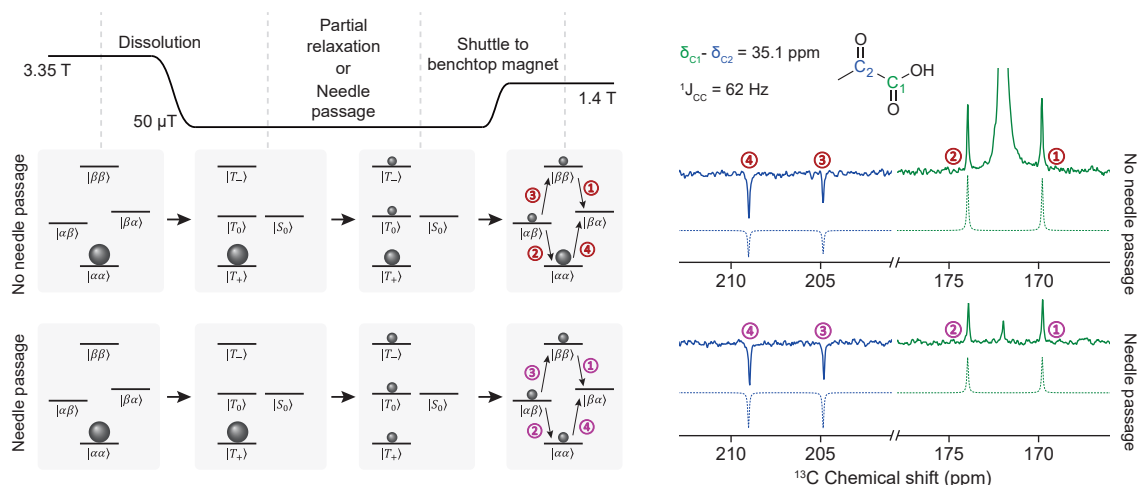


Figure 5.4: Left: Illustration of the ^{13}C spin state populations as they evolve during the course of the experiment. Passage through the needle leads to destruction of overall magnetization, illustrated by the equalization of the triplet state populations in low ($50\ \mu\text{T}$) magnetic field. Without passage through a needle, T_1 relaxation anyway leads to partial redistribution of T_+ population to the other triplet states. The transitions that lead to observable NMR signals are labeled in red/pink. Right: Experimental data showing the ^1H -decoupled ^{13}C NMR signals from two samples acquired 12 s apart, where the first sample was passed through a plastic capillary (top) and the second was passed through a stainless steel syringe needle (bottom). Both spectra were acquired using a 90° flip-angle pulse. Simulated spectra are shown (dashed lines) beneath the experimental spectra. These spectra were simulated by propagating a density operator of initial $\alpha\alpha$ spin order through the experimental process, using a 90° pulse to redistribute the populations evenly within the triplet manifold to mimic passage through the needle, and filtering out coherences generated before the return to high field. In both simulations ^{13}C - ^{13}C dipolar relaxation (which can induce relaxation within the triplet manifold) and relaxation from randomly fluctuating external fields was included. We observe good agreement between simulated peak amplitudes and experiment: this is particularly noticeable for the top spectrum in which peaks 3 and 4 are visibly different in amplitude than peaks 1 and 2.

same effect as reported in Refs. [205, 206, 191, 207], although in our work the samples were not ^{13}C -enriched so I only observe the effect for the 1.1% of molecules with a ^{13}C spin in the C2 position.

To better understand this, we can assume the DNP process generates an excess of population in the $\alpha\alpha$ state which leads to over-population of the T_+ state at low field. For a sample that does not pass through the needle, relaxation leads to partial redistribution of the spin population within the triplet manifold, but a strong singlet-triplet imbalance remains because triplet-to-singlet transitions are nominally forbidden by symmetry rules, and immune to many relaxation mechanisms[208, 209, 206]. For a sample that does pass

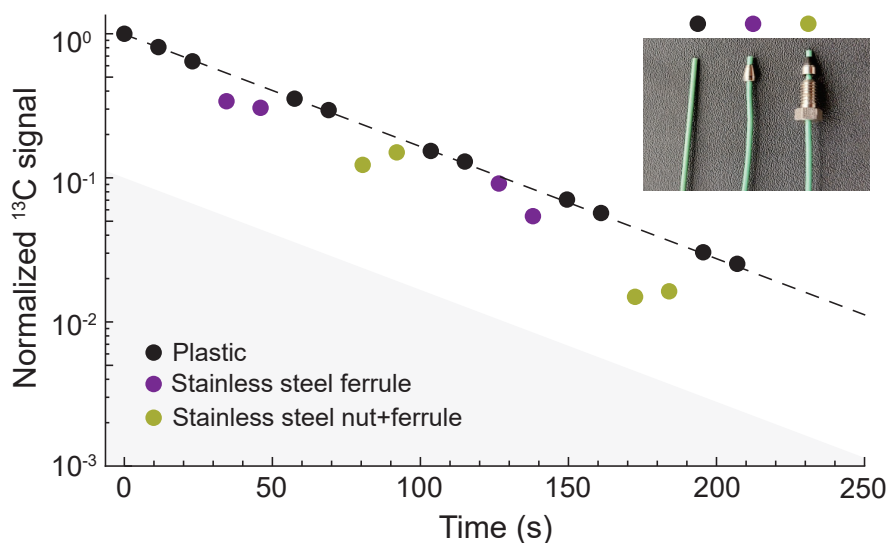


Figure 5.5: Effect of stainless steel ferrules on the ^{13}C polarization. Data points represent the integrals of the $[1-^{13}\text{C}]$ pyruvate ^{13}C NMR signal of the labelled C1 position, normalized to 1 for the first scan. The inset figure shows the capillary tubing, nut, and ferrules used for the injections. The dotted line represents an exponential decay function fit to the data, and the grey shaded region represents the area in which the ^{13}C integral is more than an order of magnitude lower than predicted from the control experiments.

through the syringe needle, this process leads to destruction of magnetization which I model as equalization of the three triplet state populations, but this process cannot induce triplet \leftrightarrow singlet transitions so the S_0 state remains depleted. Upon adiabatic return to high field, both samples exhibit hyperpolarized NMR signals due to the populations arising from the singlet. The spin state populations and eigenbasis changes throughout this process are depicted in Fig. 5.4.

We additionally investigated the magnetization-loss effect for hyperpolarized $[1-^{13}\text{C}]$ pyruvate samples passing through stainless steel ferrules and nuts, which are common components of the connections used in fluidic transport lines. The hyperpolarized sample was collected in a syringe and injected into a series of NMR tubes through one of three capillary tubes, where the tube passes through: (1) no metallic parts (control), (2) a 1/16" ferrule, and (3) a ferrule+nut set (1/16" i.d., 10-32 threads). The capillary in all cases was a 1/16" O.D., 1/32" I.D. polyether ether ketone tube (Part No. 211608, BGB Analytik). The results from this experiment and a diagram showing the three capillaries used are shown in Fig. 5.5. As expected, passage of the sample through the metal components does cause polarization losses, although the effect is significantly weaker than for metal syringe nee-

dles. The typical signal reduction (compared to the control experiment) was $30\pm 10\%$ and $50\pm 20\%$, respectively. Although these polarization losses are relatively minor compared to the near-complete loss observed from passage through metal needles and indeed may go unnoticed, they nonetheless cause some concern. For example, in metabolic tracing applications a minor inconsistency in the NMR signal as introduced by the losses may be comparable to the variation caused by other parameters, leading to false conclusions.

5.3.2 Magnetic field produced by a syringe needle

To better understand the reason why polarization is lost as solutions pass through a syringe needle, I have carried out additional measurements of the magnetic field produced by needle VII.

In Fig. 5.6 I show a 3-axis measurement of the magnetization of needle VII using three uniaxial vector magnetoresistance sensors (PNI Corp. RM3100 module).[210] The syringe needle was placed adjacent to the x -axis sensor, close to the y - and z -axis sensors, and the magnetic field was measured at discrete intervals across one full revolution about the long axis (z). This is illustrated in the schematic in Fig. 5.6(a), and the results are shown in (b). We infer that the needle is magnetized transverse to the long axis due to the large, sinusoidal variation of the x and y field readings with rotation angle, and the field produced outside the needle at a distance of a few mm is on the order of tens of μT .

Information on the internal stray field produced by small metallic components is important to describe the precise mechanism underlying the loss of nuclear spin polarization. Two factors are key: the inhomogeneity of the magnetic field, and rapid motion of the nuclei through the inhomogeneous field profile. We have not observed in any experiment that the magnetization is substantially preserved but reversed in sign, which suggests that the passage cannot be modelled as the spins moving nonadiabatically from the lab field into a homogeneous field within the metal component. This would behave like a 'pulse' on the spins of a given flip-angle, and the projection of the spin magnetization on the new quantization axis (z) may be either positive or negative, producing either an absorptive or emissive NMR signal.

The magnetization destruction effect can be suppressed by applying a magnetic field on the order of 0.1-10 mT around the metallic component to provide a strong-enough

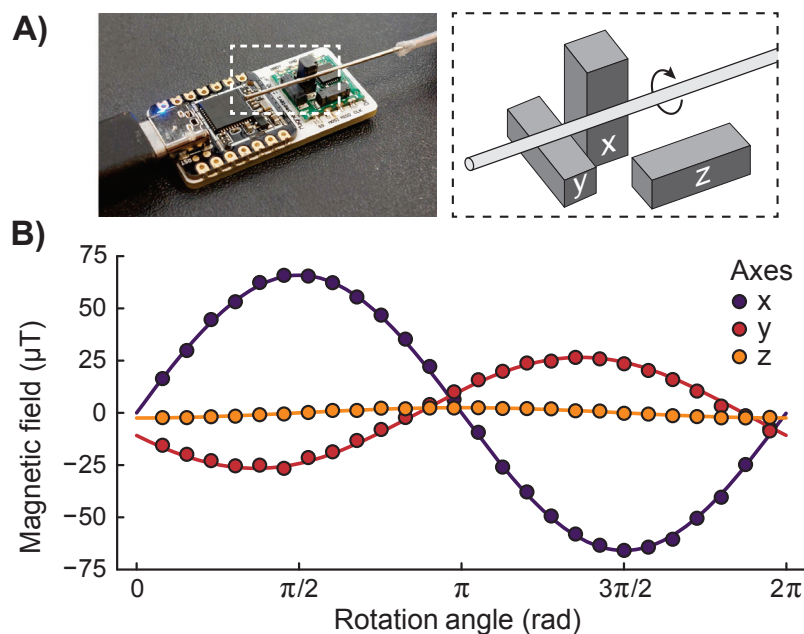


Figure 5.6: Magnetic field outside the needle produced by itself. (a) The experimental setup to measure the magnetic field outside syringe needle VII (27G, 3/4"). (b) The measured field in three axes during a full rotation of the needle. The three vector magnetometer probes are sensitive to fields along their long axes.

field to ensure adiabaticity of the spins during sample passage. The large field range I give (spanning two orders of magnitude) is based on the results obtained in Fig.6.3(d), and is inherently broad since it depends on many experimental factors, such as the internal diameter and remanent magnetization of the needle, the nuclear spin species, and the solution flow rate. This can be done by constructing a magnetic tunnel along the sample transport path[197], and in the case of *in vivo* imaging the intravenous injection can be carried out inside the MRI magnet[21]. From conversations with colleagues and from our own experience, we recognize that it is easy to unintentionally overlook the introduction of metallic parts into sample transport paths without due care. This is especially relevant for components such as nuts and ferrules, which are common in hyperpolarization apparatus for fluidic control, and have been shown to cause a partial loss of hyperpolarization that may go unnoticed.

Although 316 stainless steel is colloquially referred to as nonmagnetic, it can become weakly ferromagnetic during the manufacturing process. This property is not limited to steel; common aluminium alloys also exhibit a small degree of ferromagnetism that can affect NMR measurements[211]. Steel is particularly susceptible to becoming ferromag-

netic if it is cold-worked, which is typically how syringe needles are manufactured[212].

5.4 CONCLUSIONS

In this work I have studied the passage of magnetized solutions through metallic parts, and observed that in many cases the sample magnetization is diminished or lost due to nonadiabaticity of the passage. We have focused on solutions flowing through stainless steel hypodermic needles and capillary tubing supporting stainless steel nuts and ferrules, since these parts are commonplace in hyperpolarization equipment. The transport process can be made adiabatic by application of a magnetic field on the order of 0.1-10 mT around the metallic part, and the magnitude of this field is expected to depend on factors such as nuclear spin species, internal diameter and remanent magnetization of the metallic part, and solution flow rate.

This polarization-loss effect will be familiar to many researchers in the discipline, but commonly goes unnoticed in an applied setting. We hope our work will highlight this pitfall for scientists new to the field, and shed light on the phenomenon. We expect this effect to be especially relevant in the growing area of ultralow- and low-field MRI[213, 214, 215, 216, 217, 218, 219], when hyperpolarized solutions are employed[220, 221]. These studies are typically carried out at between 5 to 60 mT field, meaning that even if the sample transport step is adiabatic, the field of the imaging magnet itself may not be high-enough to ensure adiabaticity of samples passing through syringe needles.

BENCHTOP NMR FOR LAB-ON-A-CHIP

This thesis chapter represents the most substantial project I have undertaken in close collaboration with the companies Oxford Instruments (OI), Multiwave Technologies (MW) and the research centre Institut d'investigacions biomèdiques Agust Pi i Sunyer (IDIBAPS) under Dr. Marco-Rius guidance. I contributed in the experimental development of the microfluidic device, engaging in ongoing discussions with OI and MW to design the optimal coil dimensions and properties for the chip and the necessary features of the spectrometer to effectively accommodate the microfluidic device. I played a pivotal role in sample preparation and development of the hyperpolarization section, both in dDNP and PHIP. In the case of dDNP, I oversaw the daily maintenance of the polarizer and executed the sample preparation and polarization processes. In the para-hydrogen polarisation section, I contributed with the design and development of the complete setup for approximately one year. Subsequently, I also handled sample preparation and polarization for the NMR experiments within the microfluidic device, for all sequences optimization, enzymatic and *in vitro* studies. To finish I performed the corresponding data processing of the experiments mentioned above.

6.1 INTRODUCTION

Benchtop NMR spectrometers (1.4-2 T) emerged as a practical and cheap alternative to high field NMR spectrometers (3-28 T)[222]. The portable spectrometer version is built

around permanent magnets, resulting in a cost-effective, more compact and cryogenic-free, with no need of liquid nitrogen and helium filling. Although their technical capabilities are limited, it is raising as a feasible option to be employed at locations and facilities where there is either a lack of financial support or physical constraints and space limitation[223].

Nowadays, all the commercial producers of benchtop NMR spectrometers are using 5 mm i.d. NMR tube probes, limiting the capacity to host different shape vessels. Furthermore, the sample nature is hindered to mandatory fit in an NMR tube and place it down at the bottom of the tube, where the detection region of the spectrometer coil takes place. These instruments are currently covering a wide variety of disciplines such as material science[224], quantitative NMR for compound purity (assay or potency)[225, 226], food science[227], reaction monitoring processes[228], metabolomics[229], hyperpolarization development towards real-time metabolism tracking[230].

Unlike thermal equilibrium NMR, hyperpolarization techniques enhance the polarization of nuclear spins to levels far exceeding those achievable under thermal equilibrium conditions[9]. This remarkable enhancement of nuclear polarization translates directly into more intense NMR signals[231]. Hyperpolarization emerged as a revolutionary technique in the last 20 years pushing the boundaries of NMR sensitivity and opening new avenues for many research fields[232, 233, 234]. Low field NMR spectrometers lack of sensitivity and resolution compared to high field, two features that do not constraint most of the ^{13}C hyperpolarization experiments. Microfluidics devices, often referred as microfluidic chips or lab-on-a-chip systems, are miniaturized platforms that manipulate and control small volumes of fluids, typically on the microliter to picoliter scale[82]. These devices are designed to perform various chemical, biological, and physical processes with high precision. These devices are typically constructed at the microscale, often using microfabrication techniques such as photolithography[85, 86].

Microfluidic devices are expected to offer effective solutions to persisting problems in drug development and personalized disease treatments. One big advantage is the capability of allowing experimental analysis with tiny amounts of sample, saving cost and enhancing the throughput[87]. Only some of the hyperpolarisation techniques have been combined with microfluidic systems: dDNP[171], PHIP[235], spin exchange optical pump-

ing (SEOP)[236], and chemical induced dynamic nuclear polarisation (CIDNP)[237].

In this study, we have designed and created, a benchtop NMR spectrometer and the

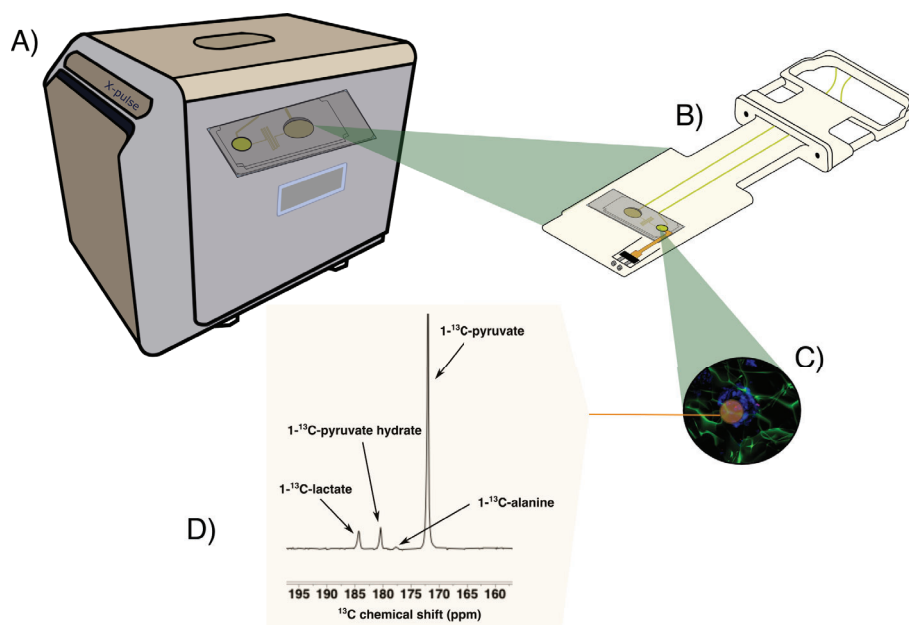


Figure 6.1: Overview of the work presented, including a benchtop NMR spectrometer for the detection of hyperpolarization-enhanced NMR metabolism in 3D tissue engineered cell models. A) NMR spectrometer. B) Chip carrier with the microfluidics chip and the embedded RF coil. C) 3D liver spheroids. (D) Example of metabolic pathway observed upon injected hyperpolarised [1-¹³C]pyruvate.

corresponding microfluidic device optimised to measure real-time metabolism using hyperpolarisation by dDNP. The microfluidic device has incorporated an X-nuclei transmitter/receiver saddle radiofrequency coil to maximise SNR and B_1 homogeneity in the microfluidic well, where the sample under measurement takes place. Furthermore the coil was designed to produce the B_1 field transversal to the B_0 of the permanent magnet, making possible the insertion of the chip completely flat and pointing up, avoiding any potential problem with gravity.

This setup is versatile to test a wide hardware variety such as coil design, size, shape and material. This approach would make also feasible to test different platform shape, size and channels adapting to the user requirements.

I measured ¹³C-pyruvate and fumarate T_1 inside the microfluidic device using the custom made saddle coil to test the efficiency of the system. Then, I moved towards real-time metabolic analysis. In a first approach, I mixed hyperpolarized [1-¹³C]pyruvate with a

lactate dehydrogenase (LDH) and NADH (enzyme co) dissolution, to reduce pyruvate to lactate through an enzymatic reaction. With this conditions I aimed to measure the kinetic constant of the pyruvate to lactate conversion (k_{PL}). Furthermore, I tested cellular metabolism with cells in suspension (HepG2) and measure again the k_{PL} for this cell line. The main aim of this thesis chapter was to proof the efficiency of all the hardware developed (chip, coil and NMR spectrometer) with *in vitro*, real time and non-invasive experiments.

6.2 MATERIALS & METHODS

6.2.1 Development of a benchtop NMR spectrometer for lab-on-a-chip applications

Oxford Instruments modified a 1.4 T commercial benchtop NMR spectrometer (X-Pulse, Oxford Instruments) to allow for planar microfluidic chips to be inserted into the spectrometer between the parallel magnets producing the B_0 magnetic field. For this purpose, they 3D printed a carrier from a photopolymer resin (Formlabs White V4 Resin) to accommodate the chip outside the spectrometer prior to the NMR experiment, and connect the corresponding capacitors to the saddle coil embeded in the microfluidic device for the measurement.

6.2.2 Microfluidic chip device

A microfluidic chip 6.2 was designed and fabricated specially for this NMR spectrometer with the following requirements: i) an experimental sample well to be placed in the homogeneous B_0 region of the spectrometer, ii) a reliable method to control the flow rate upon the injection of a hyperpolarized substrate, iii) a constant delivery and renewal method of the cell media, iv) and a place integrate a transmit/receive radiofrequency coil for for ^1H and ^{13}C nuclei. The microfluidic chip was composed by a glass substrate and a single layer of polydimethylsiloxane (PDMS, Sylgard 184, Dow Corning, USA) and fabricated following a standard replica molding protocol. The chip was designed to measure 75x38x12 mm and approximately 20.25 g on average. There is one inlet channel supplying the liquid to the well through a membrane pump and a serpentine channel, two inlets facing directly to the well from the bottom, and one outlet in the middle height of

the well. The sample well was designed to be sealed on the top by a removable round cover glass, enabling access to the cell chamber and giving the option to seal the system once the cells or engineered tissue have been inserted.

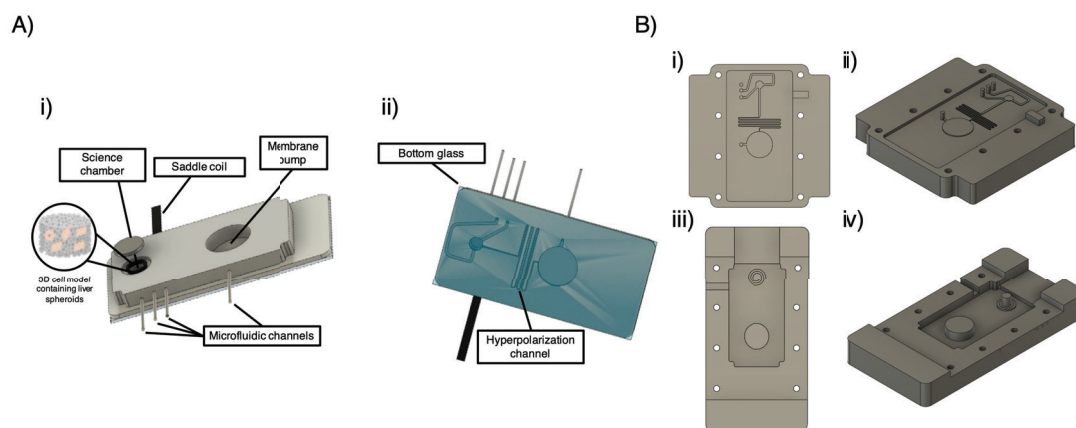


Figure 6.2: Microfluidic device and its corresponding fabrication mold. A) PDMS (Polydimethylsiloxane) microfluidic chip i) The microfluidic device from a tilted top view pointing out its features and characteristics, such as the membrane pump, the microfluidic channels, the saddle coil embedded in the chip and surrounding the sample well, the science chamber (well) and the expected engineered 3D cell model inserted in the well. ii) The microfluidic device from a bottom view pointing the hyperpolarization channel and the bottom glass. B) PMMA (polymethyl methacrylate) mold to fabricate the microfluidic device. i) top view of the mold to replicate the bottom side of the chip. ii) lateral view of the mold to replicate the bottom side of the chip. iii) top view of the mold to replicate the top side of the chip. iv) lateral view of the mold to replicate the top side of the chip.

6.2.3 Coil embedded in the microfluidic chip

The design was optimized numerically with CST microwave studio (Finite Element Solver). A scaffold (height 2 mm and diameter 5 mm) was placed inside the cylindrical saddle coil (relative permittivity 80 and conductivity 1.2 S.m^{-1}) to load the probe. Several parameters such as the number of turns, the height and the diameter of the coils were optimized to reach the highest average B_1 amplitude in the scaffold. The copper traces are $35 \mu\text{m}$ thick and placed on $200\text{-}\mu\text{m}$ -thick polyimide substrate to represent accurately to the final prototype that would be produced on flexible substrate. For each case the coil was tuned and matched to 15 MHz and B_1 field normalized to 1 W of input power.

6.2.4 HP fumarate using PHIP

All the chemicals were purchased from Sigma-Aldrich. I prepared a dissolution of 50 mM disodium[1-¹³C]acetylene dicarboxylate and 100 mM sodium sulfite in D₂O. Then, I added the ruthenium catalyst [RuCp*(CH₃CN)₃]PF₆ and I dissolved it by gentle heating and sonicating, with a final catalyst concentration of 8 mM. We prepared 10 mL of this dissolution to run a approximately 15 experiments ($\approx 700 \mu\text{L}$ per experiment). We decided to prepare small batches of dissolution as it degrades fast (≈ 2 hours). We ran the hydrogenation reaction in a 30 mL of capacity stainless steel reactor set at 100 °C. The p-H₂ (95 % enriched at 20 K) pressure inside the reactor was set at 8.0 bar, and I was bubbling the dissolution for 30 s through peek tubing. To carry out the hydrogenation, a postdoctoral researcher in the group, Dr. James Eills and I built a software-controlled electrovalve circuit to pressurize and depressurize automatically. After 30 s of hydrogenation, the system depressurized automatically and I poured the resulting solution in a test tube placed inside a solenoid coil in a magnetic shield to transfer the polarization from ¹H to ¹³C.

We transformed the proton singlet order into carbon magnetization in the fumarate molecule using a magnetic field sweep setup. The magnetic field sweep was carried out in magnetic shield (3 layers mumetal,ZG-206) through a magnetic field cycle. The power supply provided power as a constant 4.0 V output, as an input to the NMRduino (microcontroller)[238]. The NMRduino output at variable voltage to provide a chosen current to the solenoid coil, to yield the desired magnetic field strength. The coil was initially set at 10 μT , dropped to 0 μT in less than 10 ms, and then increased adiabatically to 2 μT in 4 s. The sample was then removed from the shield and ready for the NMR experiment. The resulting fumarate concentration was 42 mM \pm 2 with a 84 % of chemical yield and 32 % of polarization level.

6.2.5 Hyperpolarized [1-¹³C]pyruvate using dDNP

To hyperpolarize [1-¹³C]pyruvate, 24 μL of [1-¹³C]pyruvic acid (Merck, Darmstadt, Germany) containing 15 mM trityl radical OX063 (GE Healthcare, Illinois, U.S.A.) and 1.5 mM gadoteric acid (Guerbet, Villepinte, France) was placed into a sample cup and inserted into

a HyperSense commercial dissolution-DNP polarizer (Oxford Instruments Ltd., Oxford, U.K.) operating at 3.35 T magnetic field. This sample was cooled to 1.3 K, and irradiated with 100 mW microwaves at 94.115 GHz for approximately 40 min. The hyperpolarized frozen solid was then rapidly dissolved and flushed out of the polarizer by injecting 5.2 mL of heated phosphate buffered saline supplemented with 1% HEPES, 0.01% EDTA, 0.1% NaCl, and 0.2% NaOH (pH 12). This yielded a 5 mL solution of 80 mM [1-¹³C]pyruvate at pH 7 and around 12.5% ¹³C polarization, which was collected in a plastic falcon tube.

6.2.6 Real-time metabolism study of HepG2 cells

All cell culture reagents were obtained from Thermofisher Scientific-Gibco™ unless said otherwise. HepG2 human hepatocarcinoma cells (CliniSciences S.L.) were cultured in Eagle's Minimum Essential Medium (EMEM) (ATCC) supplemented with 10% fetal bovine serum (FBS) and 1% penicilin-streptomycin (P/S) (10^4 U mL⁻¹). Cells were cultured and maintained in 175cm² flasks and incubated at 37°C under 5% CO₂ and the media was changed every 48-72h and passaged once reached 80% confluence. 48h before HP-NMR cell measurement, $5 \cdot 10^6$ cells were seeded in T-75cm² flask. 24h before experiment, cells were treated with 0.1% DMSO. After treatment, the flask was washed with PBS, cells were detached using Trypsin-EDTA 0.25% and centrifuged for 3 min at 200g. Cell viability and number was assessed by trypan blue staining. 10^7 cells were moved in a 1.5mL eppendorf with 120 μL of EMEM next to the polarizer and the BLOC spectrometer in a polystyrene box with water at 37°. We mixed 8 μL of hyperpolarized [1-¹³C]pyruvate sample with the 120 μL of the EMEM containing the cells and the resulting solution was rapidly pipetted into the sample well of the microfluidic device. After closing the well with the round glass the carrier was inserted in the spectrometer as quick as possible (\approx 30-35 s) and start the NMR dynamic acquisition.

We obtained the NMR data using a modified X-Pulse (Oxford Instrument). We corrected magnetic field inhomogeneities with a shimming protocol optimized by Oxford Instruments and some further modifications to a microfluidic device filled with water. We used X-pulse Spinflow software to determine de acquisition parameters and Mestre Nova 15.0.0 version to process the obtained data. We acquired the dynamic acquisitions using a ¹³C array sequence with WALTZ decoupling. The acquisition parameters are the

following: repetition time 5 s, 30° flip angle, 1 averages.

6.2.7 Data analysis

We used a commonly employed simplified mathematical model to describe the reactions done by lactate dehydrogenase and fumarase and fit the kinetic constants of these [239, 240, 241, 242]. The model only considers the conversion of the hyperpolarized substrate (pyruvate or fumarate) to product (lactate or malate) at constant rates of K_{PL} (LDH) or K_{FM} (FH), the reverse reaction with constant rates K_{LP} (LDH) or K_{MF} (FH), and the loss of signal due to the longitudinal relaxation constants (i.e. T_1). The differential equations for the reactions are:

$$\frac{d[\textit{Substrate}]}{dt} = K_{LP/MF}[\textit{Product}] - \left(\frac{1}{T_1^{\textit{Substrate}}} + K_{PL/FM}\right)[\textit{Substrate}] \quad (6.1)$$

$$\frac{d[\textit{Product}]}{dt} = K_{PL/FM}[\textit{Substrate}] - \left(\frac{1}{T_1^{\textit{Product}}} + K_{LP/MF}\right)[\textit{Product}] \quad (6.2)$$

We implemented the code for the parameter fits in the Julia Programming Language, only using the data for the metabolism products. We solved the differential equations numerically using an initial value problem (IVP) solver for stiff problems (CVODE BDF). As a cost function for the optimisation problem, I used the mean squared error (MSE) function defined as:

$$MSE = \frac{1}{N} \sum_{i=1}^N (y_i - \hat{y}_i)^2 \quad (6.3)$$

Where N represents the total number of data points, y_i the experimental data and \hat{y}_i the simulated one. We solved the optimisation problem using a global optimiser (i.e., Differential Evolution) from the Julia package `BlackBoxOptim.jl.`, setting reasonable bounds for all the parameters and allowing the optimisation to run for a maximum of three minutes (convergence of the results for all optimisations happened between 30 seconds and 2 minutes).

6.3 RESULTS & DISCUSSION

6.3.1 Technical development: spectrometer, carrier, chip and RF coil

I constructed a PDMS-based microfluidic chip, featuring channels measuring $200\ \mu\text{m} \times 200\ \mu\text{m}$ that connect to a cylindrical chamber ($5\ \text{mm} \times 5\ \text{mm}$) intended for NMR detection. This setup incorporates a passive membrane pump, designed to transport hyperpolarized solutions. This pump, with a $20\ \text{mm}$ diameter cavity, is topped by an $800\ \mu\text{m}$ PDMS membrane, serving as a damper to diminish pressure surges during hyperpolarized solution injections. The chosen materials ensured no susceptibility artifacts. A saddle RF coil was designed and developed, with a 6-turn structure measuring $5.4\ \text{mm}$ in height and $5.5\ \text{mm}$ in diameter. A scaffold (relative permittivity 80 and conductivity $1.2\ \text{S}\cdot\text{m}^{-1}$) was integrated within the coil to facilitate probe loading. B_1 field amplitude maps depicted the coil's efficiency in the scaffold's vicinity. The scaffold's average amplitude is $1.15\ \text{mT}$ at $15\ \text{MHz}$ for a $1\ \text{W}$ power input, closely matching 75% efficiency of the typical solenoid probe in a standard Pulsar configuration. Within the scaffold volume, the homogeneity displays a relative standard deviation of 20%. Different shimming methods, such as a 3D spatial field mapping analogous to gradient shim, were evaluated. These techniques yielded a linewidth under $0.1\ \text{ppm}$. All this setup is represented in Fig. 6.3

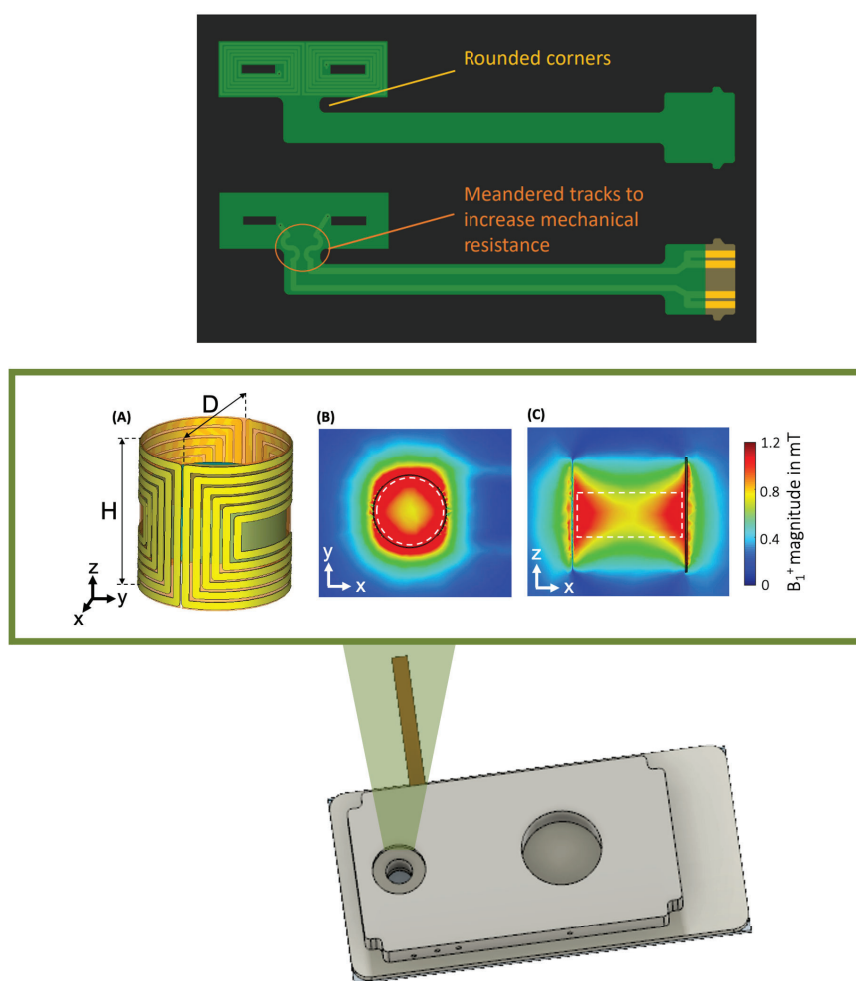


Figure 6.3: Schematic picture of the saddle coil embedded in the microfluidic device. Inside the green box we have from left to right: Schematic representation of the coil turns (6) the height (7 mm) and the diameter (5 mm). Then we have a coronal view of the homogeneity of the B_1 field and a sagittal view of the of the B_1 field.

6.3.2 T_1 measurement of hyperpolarised ^{13}C agents using the customised setup

I carried out experiments to compare the results we are able to get in the BLOC spectrometer compared to the commercial one. We first polarized $[1-^{13}\text{C}]$ pyruvate using dissolution dynamic nuclear polarization (dDNP) and after dissolving it in the buffer I injected the resulting dissolution inside the chip through the membrane pump channel (Fig. 6.7 A). We acquired a ^{13}C spectrum every 4 seconds during 144 seconds. The stacked spectra

of all the measurements is shown in figure 6.7 C). We measured this experiment 3 times. We calculated the longitudinal relaxation constant (T_1) for all 3 acquisitions, integrating the C1 peak of the [1- ^{13}C]pyruvate along the time, and fitting the resulting figure with an exponential decay function (Fig. 6.7 B):

$$y = A + M_0 e^{-t/T_1} \quad (6.4)$$

The resulting T_1 values are 71.4s, 76.8s, and 69.1 respectively. The final T_1 for the carbon 1 in 1- ^{13}C -pyruvate was 72.4 ± 3.9 s. The FWHM value was 13 ± 6 Hz width, between 12 and 11 Hz more than the values I got in the commercial instrument using a 5 mm NMR tubes probe.



Figure 6.4: Schematic representation of the procedure performed to inject the dissolution inside the microfluidic device through the hyperpolarization channel and filling up the well. In this case I blocked two of the channels to have only one inlet and one outlet. The dashed line in the right figure remarks the physical position of the saddle coil.

We then polarized ^{13}C natural abundant fumarate (2 % ^{13}C labelled) using a custom made para-hydrogen induced polarization (PHIP) setup. We injected the dissolution obtained after the acetylenedicarboxylate hydrogenation inside the chip through the membrane pump channel. We acquired a ^{13}C spectrum every 4 seconds during 144 seconds. The stacked spectra of all the measurements is shown in figure 6.7 E). We measured this experiment 3 times. We calculated the longitudinal relaxation constant (T_1) for the 3 acquisitions, with 85.6, 86.3 and 76.5 s respectively (6.7D). The final T_1 for the carbon 1 in fumarate was 82.8 ± 5.4 s. The FWHM value was 5.0 ± 2.1 Hz width.

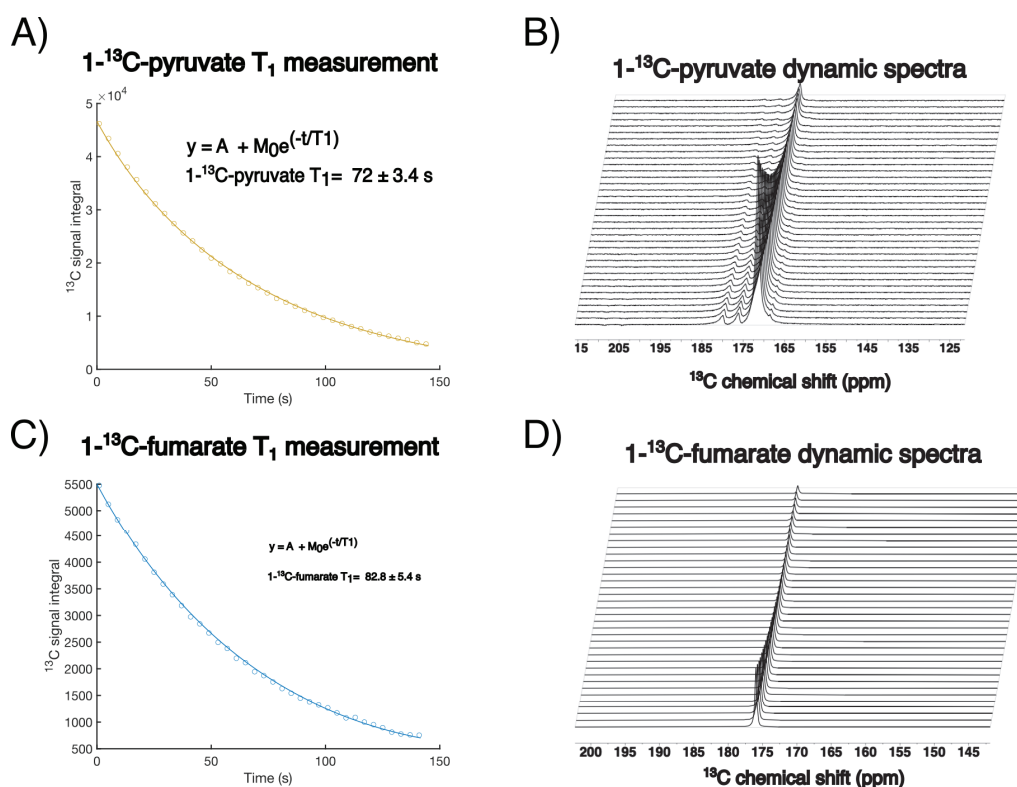


Figure 6.5: Results of the longitudinal relaxation measurements in the BLOC chip with $[1-^{13}\text{C}]$ pyruvate and fumarate. A) Plot showing the exponential decay of the signal due to T_1 relaxation and radiofrequency pulses from $[1-^{13}\text{C}]$ pyruvate. Fitting the function of the equation showed in the figure, I calculated the T_1 with a value of 72 ± 3.4 s. B) stacked spectra of the ^{13}C dynamic measurement of hyperpolarized $[1-^{13}\text{C}]$ pyruvate along time. C) Plot showing the exponential decay of the signal due to T_1 relaxation and radiofrequency pulses from fumarate. Fitting the function of the equation showed in the figure, I calculated the T_1 with a value of 82.8 ± 5.4 s. D) stacked spectra of the ^{13}C dynamic measurement of hyperpolarized fumarate along time.

6.3.3 Real-time metabolism detection using the customised setup

6.3.3.1 LDH kinetics assessment measuring $[1-^{13}\text{C}]$ pyruvate to $[1-^{13}\text{C}]$ lactate

We were able to observe metabolic conversion from $[1-^{13}\text{C}]$ pyruvate to $[1-^{13}\text{C}]$ lactate in either enzymatic solutions and 2D cell cultures using the BLOC setup. First, I performed some preliminary tests mixing hyperpolarized $[1-^{13}\text{C}]$ pyruvate with a solution containing lactate dehydrogenase (LDH) enzymes and NADH as the cofactor of the reduction reaction. The dissolution was placed next to the polarizer to be mixed with the hyperpolarized $[1-^{13}\text{C}]$ pyruvate and rapidly injected through the injection channel of the microfluidic chip (same procedure described in Fig. 6.7A), already placed inside the BLOC spectrom-

eter. We took 18 seconds since the pyruvate solution came out of the hypersense to start the acquisition. We detected conversion from pyruvate to lactate running 35 acquisitions in 50 seconds with 13° of flip angle. The resulting K_{PL} was $7.82 \times 10^{-3} \text{ s}^{-1}$.

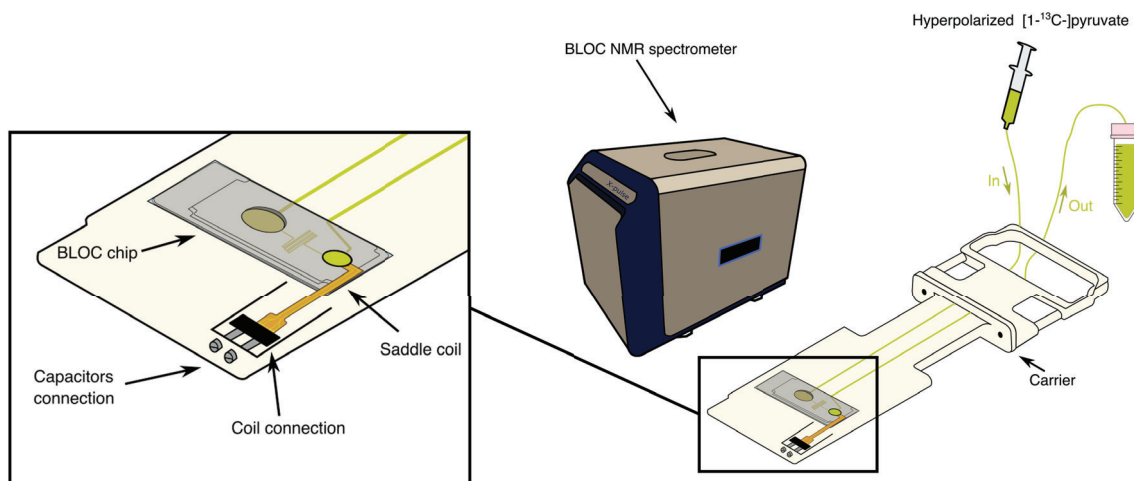


Figure 6.6: Schematic representation of the setup when a hyperpolarized solution is being injected through the channels to the microfluidic device already placed inside the spectrometer.

Pyruvate-Lactate kinetic analysis with LDH and NADH

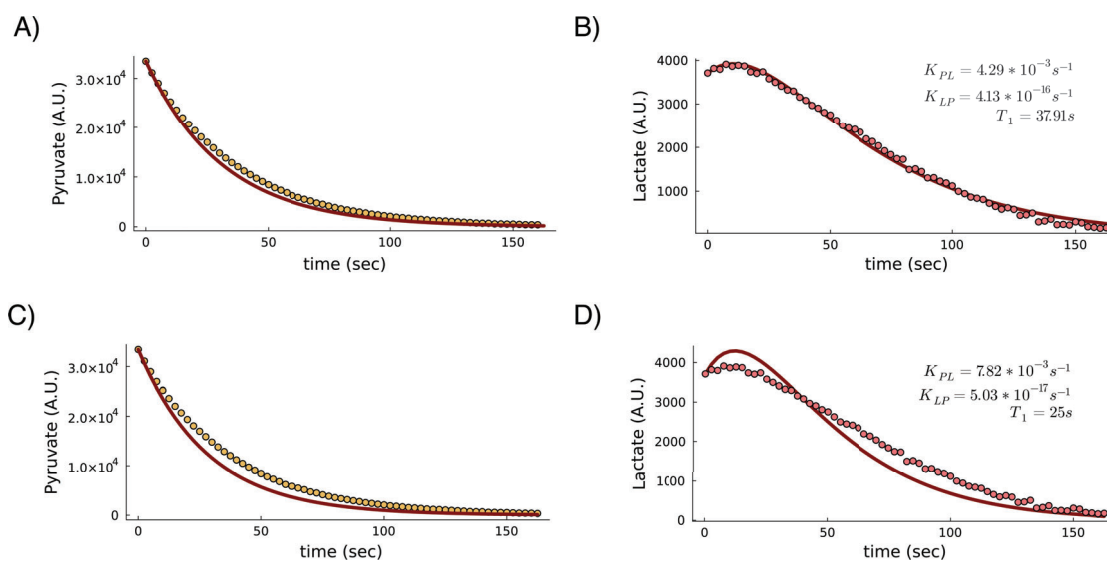


Figure 6.7: Dynamic curves of the real-time metabolism test using $[1-^{13}\text{C}]$ pyruvate, LDH and NADH. A) and B) are fitted with unreasonable (short) T_1 values for lactate (10 seconds). C) and D) are fitted with reasonable T_1 (35 s). K_{PL} represents conversion kinetic constant from pyruvate to lactate, and K_{LP} represents conversion kinetic constant from lactate to pyruvate.

6.3.3.2 Fumarase (FH) kinetics assessment measuring fumarate to L-malate

In this second experiment, I wanted to run the same experiments but using hyperpolarized ^{13}C natural abundance fumarate in presence of fumarase. In this case fumarase converts fumarate to malate without requiring any cofactor. We first prepared a stock solution with 20 μL of fumarase diluted 1:10 with water and then mixing 500 μL of the stock solution with the dissolution coming out from the PHIP setup, containing around 95 mM fumarate in presence of starting material and catalyst. Both dissolutions were mixed and injected in the BLOC chip for the corresponding dynamic measurement (Fig. 6.8).

We used Mestre Nova 15.0.0 version to process the data obtained. We acquired the dynamic data using a ^{13}C array sequence with WALTZ decoupling. The acquisition parameters are the following: repetition time 5 s, 30° flip angle, 1 average.

Fumarate-malate kinetic analysis with fumarase

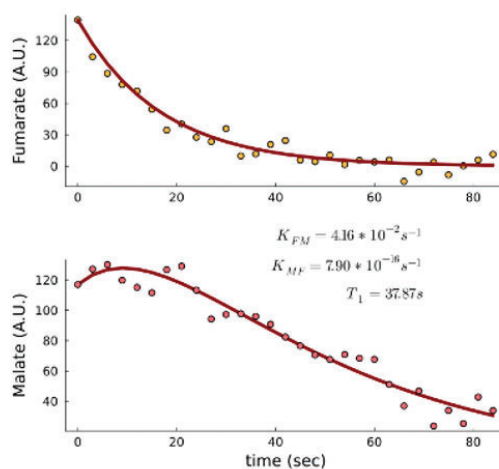


Figure 6.8: Dynamic curve of the real-time metabolism test using $[1-^{13}\text{C}]$ pyruvate, and fumarase within the BLOC chip. K_{FM} represents conversion kinetic constant from fumarate to malate, and K_{MF} represents conversion kinetic constant from malate to fumarate.

6.3.3.3 Kinetic analysis using HepG2 cell lines

The next step was to perform these experiments using 2D cell cultures, in this case with a HepG2 cell line. For each experiment, I used between 7-10 million cells. This procedure was a more tedious as the cells were unable to be injected through the microfluidic channel, the cells would block the channels, nor was there any way to fix them in the well while flowing the hyperpolarized $[1-^{13}\text{C}]$ pyruvate dissolution. The method I employed involved mixing in an Eppendorf tube and promptly transferring it to the microfluidic chip, sealing the well with the cover glass, and rapidly inserting the microfluidic chip inside the BLOC spectrometer (procedure described in Fig. 6.10A). This procedure took between 25-30 seconds each time. We ran this same experiment 3 times. We injected $8\ \mu\text{L}$ of an $80\ \text{mM}$ $[1-^{13}\text{C}]$ pyruvate in $120\ \mu\text{L}$ of cell media containing the HepG2 cells, resulting in a $5\ \text{mM}$ dissolution. We acquired a scan every 5 seconds for 50 seconds with a 30° flip angle and 1.5s of acquisition time. The FWHM of the $[1-^{13}\text{C}]$ pyruvate peak in the first spectrum was of $8 \pm 6.1\ \text{Hz}$ and a signal-to-noise ratio of 86.54. The first experiment had a bigger FWHM value (15.1 Hz) because of the presence of bubbles. In the next two experiments the FWHM were 4.0 and 4.1, without the presence of bubbles. In figure 6.10B), I placed representative stacked spectra of the second experiment carried out. In Fig. 6.10C), I

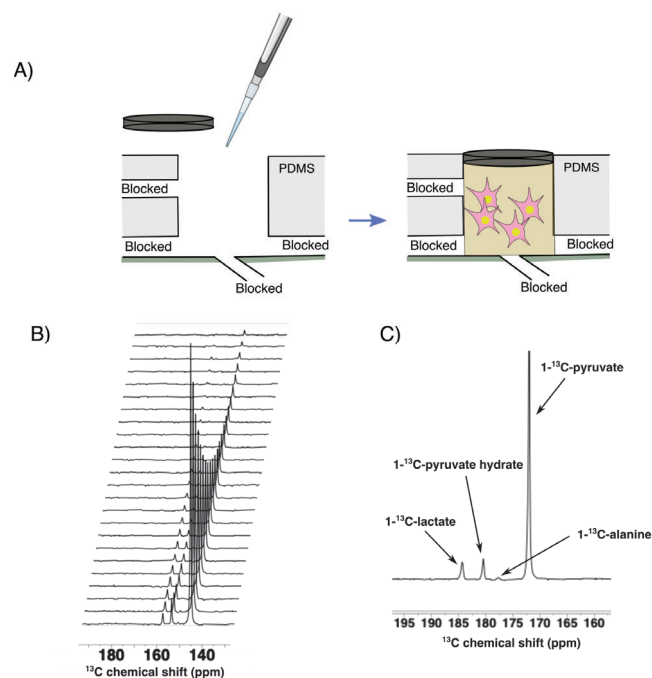


Figure 6.9: *In vitro* metabolic study results with 2D cell culture. A) Schematic representation of the procedure performed to mix the hyperpolarized [$1\text{-}^{13}\text{C}$]pyruvate dissolution with the cells in suspension, and put the resulting dissolution inside the microfluidic device well using an automatic 1 mL pipette. B) ^{13}C stacked spectra of the dynamic acquisition performed with the modified BLOC spectrometer. C) Representative ^{13}C spectrum of the cells in suspension mixed with hyperpolarized [$1\text{-}^{13}\text{C}$]pyruvate after 35 seconds of the mixing. In the picture is explained with arrows all the peaks and the corresponding metabolites.

placed a representative sum-up spectrum, summing up the first eight scans, specifying the metabolites observed.

The K_{PL} values calculated for all three experiments were 3.57×10^{-3} (Fig. 6.10E), 3.08×10^{-3} , and 3.55×10^{-3} . The standard deviation between all three experiments was 2.7×10^{-4} , demonstrating the high reproducibility among all three experiments although the presence of bubbles in one of them.

Pyruvate-Lactate kinetic analysis with HepG2 cells in suspension

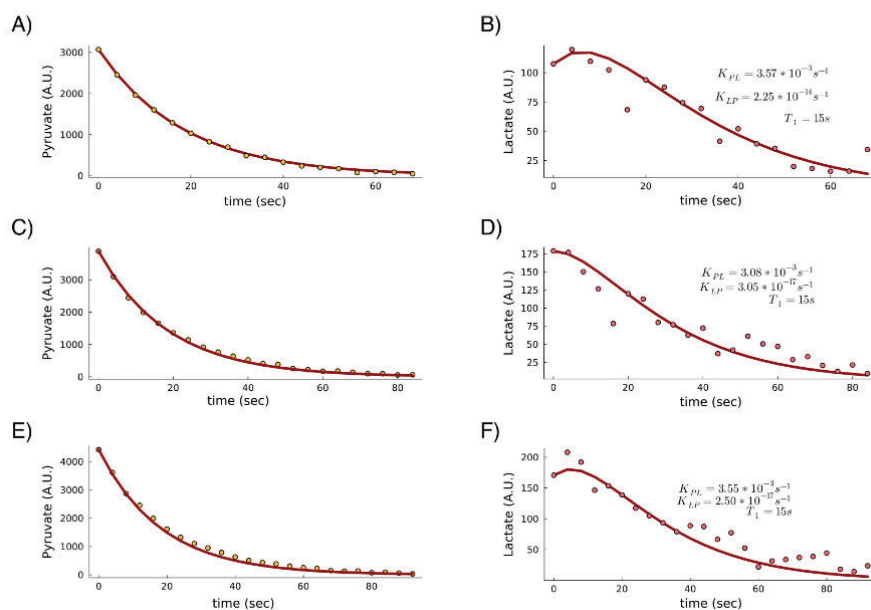


Figure 6.10: Kinetic results with HepG2 cells. A) Fitting of the mono-exponential decay function to the $[1-^{13}\text{C}]$ pyruvate polarization decay due to T_1 , pulses and metabolism for the first replicate. B) Fitting of the kinetic function to the production of $[1-^{13}\text{C}]$ lactate for the first replicate. C) Same as A) for the second replicate. D) Same as B) for the second replicate. E) Same as A) for the third replicate. E) Same as B) for the third replicate.

6.4 CONCLUSIONS

In this chapter, I have evaluated how a modified benchtop NMR spectrometer can fit a cost-effective microfluidic platform to run hyperpolarized-NMR measurements. In this case, I tested a microfluidic chip incorporating an X-nuclei transmitter/receiver saddle radiofrequency coil. I first tested the setup to measure longitudinal relaxation constants of either hyperpolarized $[1-^{13}\text{C}]$ pyruvate using dDNP and hyperpolarized fumarate using PHIP. We then tested real-time metabolism with enzymatic dissolutions and later on with cells in suspension. This study demonstrates the possibility of adapting hardware for user needs in hyperpolarized NMR experiments, either in the spectrometer, the coil and the microfluidic chip. This work aims to span the NMR applications areas such as coil testing, hardware development or even real-time metabolism for drug testing.

HIGH-THROUGHPUT ANALYSIS IN A MULTIWELL MICROFLUIDIC PLAT- FORM FOR HYPERPOLARIZED MRSI

I carried out most of the work captured in this thesis chapter during a doctoral stay I did at UCSF (University of California San Francisco), in the department of Radiology and Biomedical Imaging. I contributed in the chip production once the mold was already designed and fabricated by my colleagues. However, my major contribution was to design and execute the experimental part and the subsequent data processing that involved the application of the microfluidic device in the hyperpolarized MRSI experiments. In this chapter, I first introduce various features of the microfluidic device, including its design, materials, fabrication and functionality. I then move to show a first approach and application of the study performing a parallel detection of the [1-¹³C]-pyruvate oxidation with hydrogen peroxide (H₂O₂) in the multiwell microfluidic device in a MRI scanner, setting different conditions in each chamber. This study was published in Lab on a chip[171]. I conclude the chapter showing a biologic application measuring metabolic activity in 8 wells of the device with all having different conditions.

7.1 INTRODUCTION

Globally, the list of diseases is extensive and keeps growing every passing day, having their own and unique characteristics. Furthermore, the response of the people to these diseases varies significantly from person to person, making impossible to find an efficient

treatment for each disease in every individual. Within this tough situation, personalized medicine is becoming a promising research line and it is aiming to find solutions and answers to the effect of a disease in each individual. Personalized medicine is a broad and rapidly advancing field of healthcare that is informed by each person's unique clinical, genetic, genomics and environmental information[243]. Personalized medicine is used to understand the disease at molecular level to enhance preventive healthcare strategies. The research field is aiming to optimize medical care and outcomes for each person, resulting in an unprecedented customization of patient care[244].

During the past century, the animal testing proved to be highly robust in the experimental evaluation of treatment modalities and pharmaceutical agents, facilitating rigorous assessments of both, their therapeutic effectiveness and potential adverse effects[245]. Animal models are widely used for sharing many biological similarities with humans, making suitable for studying disease mechanisms and treatment responses. Animal variables are also feasible to control and manipulate, which is also often challenging or impossible in human studies. However, the studies can not always translate accurately to humans due to species differences in genetics and their use in research raises many ethical issues, particularly regarding the welfare and treatment of animals. These two reasons are fundamental for the human being to search new alternatives of early stage drug testing or new therapies development.

The Organ-on-a-chip (OoC) approach is becoming a promising alternative to animal testing for medicine. OoC are basically miniature, interconnected systems of microchannels, chambers, and other microstructures designed to mimic the physiological environment of human organs or tissues[84]. They serve as platforms for conducting experiments and studies related to organ function, drug testing, disease modeling, and tissue engineering[246]. Researchers managed to replicate healthy and diseased states, enabling the study of disease mechanisms and development of potential treatment[247]. OoC are expected to offer effective solutions to persisting problems in drug development and personalized disease treatments.

Detecting and monitoring the biologic activity in OoC is essential to get conclusions from the model and the study. Microscopic imaging stands as an essential and widely adopted approach for the real-time assessment and evaluation of diverse organ-on-a-chip systems.

Microscopic images technique enables the observation of critical parameters such as cell quantity, morphology, gene expression, protein secretions, among others[248]. Although they confer a great synergy with microfluidic devices, they lack of crucial information in biologic models such as metabolism conversation and kinetics.

Reactants and products in chemical reactions are detected with a time resolution of seconds and nanomolar sensitivity using dissolution DNP-MR.[249] A major drawback of the technique, however, is that the preparation of hyperpolarized substrates by dissolution DNP is time-consuming and costly, which limits its ability to generate data. A minimum amount of hyperpolarized sample is produced as an equipment limitation, and usually not more than 3-10 % of the sample is used in the experiment[250]. The development of more efficient methods to fully utilize the polarized samples, like the one proposed here, will shorten experimental time, increase throughput, decrease its associated costs, improve control over experimental variables and reproducibility and, as a result, contribute to expand the applications of DNP-MR.

Commercial MR instrumentation only allow single sample acquisitions or a handful of consecutive samples as the polarization decays. Repeated MR readings have been possible with a single dissolution DNP sample by continuous filling of a volume microcoil[206] or sequential acquisitions by removing, reloading, and introducing a new sample again in a magnetic resonance imaging (MRI) scanner and a high field nuclear magnetic resonance spectrometer[251, 252, 253, 254]. However, consecutive acquisitions are impossible to conduct under the same hyperpolarized substrate conditions (i.e. polarization level, substrate concentration and pH might vary between DNP dissolutions) and may be affected by B_0 distortions (shimming maladjustments), which affect data repeatability and make comparison between sample groups impractical. An alternative strategy to effectively shorten the polarization build-up cycle is simultaneous polarization of multiple samples. Currently *in vivo* DNP-MR experiments are typically limited to four samples, which are dissolved one by one on demand, for [1- ^{13}C]pyruvate injections at 5–20 min intervals[195, 53]. However, despite these advances, the throughput of dissolution DNP remains long and inefficient. A relatively large volume of hyperpolarized sample (4.5 mL) is produced in each polarization process, while only a few hundred microliters are usually consumed, and the remaining sample is discarded.

This project was designed to address the unmet need for technology which enables parallel DNP-MR experiments using a single spectrometer and demonstrate that microfluidics can effectively enhance the throughput of a single dissolution DNP shot and provide a large number of replicates for comparing experimental parameters. I developed a microfluidic multiwell plate containing eight different sample chambers from which spectra can be collected simultaneously upon infusion of a hyperpolarized solution. All 8 chambers can be probed with a single DNP sample using the same MR acquisition, with consistent and uniform polarization conditions between sample chambers. As a demonstration of the technology, DNP-MR spectroscopic images were acquired using commercially available RF coils in a preclinical 3T MRI scanner where I detected, in a first approach, reactants and products generated during pyruvate decarboxylation via hydrogen peroxide (H_2O_2), or in the second approach the conversion from pyruvate to lactate due to LDH activity. In the first approach, I followed the reactant concentration-time profiles of three replicates and five control samples that were tested simultaneously in the device. I then moved towards the biologic application measuring metabolic activity of HepG2 cell line in the same microfluidic device, although in this second case I did not follow time evolution profile, I just measured a single acquisition.

7.2 MATERIALS & METHODS

7.2.0.1 Fabrication of the microfluidic platforms for DNP-MR applications

Molds with microfluidic channels and features were fabricated by standard photolithography methods[170]. Silicon wafers (4" n-type <111>, MicroChemicals GmbH) were dehydrated using a hot plate (200 °C for 30 min) and treated with O_2 plasma (PDC-002, Harrick Plasma) at 22.5 mL min⁻¹ and 30 W for 20 min. Photoresist (SU-8 2100, KAYAKU Advanced Materials, Inc.) was spin-coated in two steps (500 rpm for 10 s with acceleration of 100 rpm s⁻¹ followed by 1600 rpm for 30 s with 300 rpm s⁻¹) to form a SU-8 layer of 200 μm thickness. The wafer was then soft-baked in two steps, firstly at 65 °C for 5 min, and secondly at 95 °C for 40 min. Photoresist was finally exposed to UV-light at 320 mJ cm⁻² (17.5 mW cm⁻² for 18.2 s) using a mask aligner machine (MJB4, Süss MicroTec) and post-baked at 65 °C for 5 min followed by 95 °C

for 14 min. SU-8 structures were developed in SU-8 developer (MicoChemicals GmbH) for 16 min, rinsed with Isopropyl alcohol, and dried with a N₂ gun. The wafers were finally hard-baked at 95 °C for 30 min and silanized by vapor exposure of ¹H,¹H,²H,²H-PerfluorooCtyl-trichlorosilane (PFOTS, 97%, Merck) in a vacuum desiccator for 1 h. PDMS layers of the microfluidic device were fabricated by soft lithography protocols using the patterned SU-8 molds. PDMS prepolymer (Sylgard 184, Ellsworth Adhesives) was prepared in a ratio of 10:1 (elastomer base: curing agent, w/w) and degassed in a vacuum desiccator. The prepolymer was then cast on a Petri dish containing the SU-8 mold, baked at 65 °C for 4 h, and left overnight at room temperature.

PDMS layers obtained included the microfluidic channels for 1) distributing the hyperpolarized sample (lower 5-mm thick layer), 2) suck out the excess of liquid during the injection of the hyperpolarized sample (top 5-mm thick layer). Chambers and ports (inlets and outlets) were punched in the corresponding PDMS layers, using 6 mm and 1.25 mm biopsy punches respectively. The three layer and a glass slide (75 x 25 mm Corning) were activated using O₂ plasma (PDC-002, Harrick Plasma) and bonded together, resulting in a device with final dimensions of 11 mm thickness, 75 mm length, and 38 mm width.

To operate the microfluidic device from outside the MRI scanner, the inlet port of the microfluidic network for injecting the hyperpolarized sample, was connected to a female Luer-to-barb fitting using 114 cm of polytetrafluoroethylene (PTFE) tubing (1/16" outer diameter and 1/32" internal diameter Darwin microfluidics). This allowed the fast administration of hyperpolarized solutions by means of a syringe. Remaining ports (i.e., infusion and withdrawal ports) were connected with the same tubing and closed using tubing clamps.

7.2.0.2 Hyperpolarization of [1-¹³C]pyruvate

A volume of 24 μL of [1-¹³C]pyruvic acid (Sigma Aldrich, Munich, Germany) containing 15 mM trityl radical OX063 (GE healthcare) and 1.5 mM Dotarem (Guerbet, Villepinte, France) were inserted into a commercial dissolution-DNP polarizer (HyperSense, Oxford Instruments Ltd.). This sample was polarized for approximately 55 min using 100 mW microwaves at 94.095 GHz in a magnetic field of 3.35 T, reaching a polarization level of around 15–20%. The hyperpolarized sample was dissolved in 4.5 mL of

heated phosphate buffered saline supplemented with 1 % HEPES, 0.01 % EDTA, 0.1 % NaCl, and 0.2 % NaOH (pH 12), yielding 80 mM [$1\text{-}^{13}\text{C}$]pyruvate at pH 7.

7.2.0.3 Flip angle calibration using a 10 M ^{13}C -Urea sample

The pulse length and pulse power produced by the radio-frequency coil establishes how much magnetization of the nuclear spins in the z axis is tilted towards the xy plane. The MRI scanner performs an adjustment before the acquisition called “Reference Power Adjustment” where it calibrates the amount of power required to pass through the coil to get enough signal depending on the number of nuclear spins contained in the sample. This adjustment is therefore dependent on the spins polarization, so in a non-stable polarization state the scanner will be adjusting until the polarization is lost without determining a value. To overcome this fact I calibrated the pulse length previously to the analysis using a 10 M ^{13}C -Urea sample in water and 1 mM Gd-DOTA in a 1.5 mL eppendorf as a phantom. I did the calibration for 3 values of Reference Power: 19.97 W, 5.00 W, 0.04 W. I obtained MR spectra using a dual-tuned ^1H - ^{13}C volume coil (42 mm inner diameter, Bruker) inside a horizontal 3 T MRI scanner (BioSpec 10⁵ mm bore diameter, Bruker®). Magnetic field inhomogeneities were corrected with a shimming process. Acquisition parameters: Repetition time 300 s, acquisition time 632 ms, offset 160 ppm, 1 average, 2048 acquisition points, bandwidth 100 ppm.

7.2.0.4 MRSI data acquisition of the chemical reaction

MR spectra were obtained from each individual chamber in the microfluidic platform by MR spectroscopic imaging (MRSI) techniques using a dual-tuned ^1H - ^{13}C volume coil (42 mm inner diameter, Bruker) inside a horizontal 3T MRI scanner (BioSpec 105 mm bore diameter, Bruker®). Magnetic field inhomogeneities were corrected with a shimming process applied to a water-filled device prior to the DNP-MRSI assays.

1.6 mL of hyperpolarized sample were injected into the microfluidic platform, which resulted in $125 \pm 5 \mu\text{L}$ delivered in each chamber over a period of 3 seconds. Hyperpolarized ^{13}C MR data was acquired with a chemical shift imaging (CSI) sequence (8 x 8 matrix, field of view of 40 mm x 40 mm, area of 5 mm x 5 mm per voxel, slice thickness of 12 mm, 15° flip angle, echo time of 1.49 ms, T_{acq} of 51.2 ms, and RT of 66.907 ms).

Each point of the data set was acquired every 4 seconds. MR T_2 -weighted images were acquired using 4 scans. The whole matrix of voxels (i.e., 64 spectra) were acquired every 4 s with the first scan at the end of the hyperpolarized solution injection, i.e. at time 0. The transfer time between dissolution and injection was around 12 s.

The thermal equilibrium acquisition was performed on the microfluidic device with 100 μL solution of 8 M [^{13}C]urea (Sigma Aldrich, Munich, Germany) and 10 mM DOTA-Gd in two chambers located in the corners of the chip (Fig. 3A, highlighted in yellow). Those chambers were used to center the offset frequency, perform B_1 calibration, shimming, and signal to noise ratio (SNR). Three chambers were filled with an aqueous solution containing 8.2 M H_2O_2 (Sigma Aldrich, Munich, Germany) and 37 mM NaOH (Fig. 3A, highlighted in red). The three remaining chambers were filled with 35 μL deionized water and 6.4 μL of 0.25 M NaOH solution (Fig. 3A, highlighted in blue). The MR localizer was performed with axial, sagittal, and coronal T_2 -weighted images using a spin echo T_2 TurboRare sequence to assess signal location and accurately program the CSI voxels matrix.

7.2.0.5 MRSI data acquisition of the *in vitro* analysis

HepG2 human hepatocarcinoma cells (CliniSciences S.L.) were cultured in Eagle's Minimum Essential Medium (EMEM) (ATCC) supplemented with 10% fetal bovine serum (FBS) and 1% penicillin-streptomycin (P/S) (10^4 U mL^{-1}). Cells were cultured and maintained in T-175 cm^2 flasks and incubated at 37°C under 5% CO_2 and the media was changed every 48-72h and passaged once reached 80% confluence. 48h before HP-NMR cell measurement, $5 \cdot 10^6$ cells were seeded in T-75 cm^2 flask. 24h before experiment, cells were treated with 0.1% DMSO. After treatment, the flask was washed with PBS, cells were detached using Trypsin-EDTA 0.25% and centrifuged for 3 min at 200g. Cell viability and number was assessed by trypan blue staining. 10^7 cells were.

For the study we prepared 2 cell media dissolution. For the first one, I prepared a solution of glucose (Glu) and glutamine (Gln) at 25 and 4 mM respectively in cell medium. I weighed 45 mg of glucose and 5 mg of glutamine and I dissolved them into 10 mL of cell medium. For the second one, I prepared a solution of NADH at 33 mM weighting 84 mg and dissolving it into 4 mL of cell media. For the lysed cells I used RIPA buffer without

SDS. My colleagues resuspended 10 million cells for each condition requiring cells, total of 55 million cell (on of them just required 5 million). The conditions arrangement for each well is the following:

1. Cell medium with additional Glucose and Glutamined and with alive 10 M HepG2 cells.
2. Cell medium with additional Glucose and Glutamined and with lysed 10 M HepG2 cells.
3. Cell medium with additional NADH with lysed 5 M HepG2 cells.
4. Cell medium with alive 10 M HepG2 cells.
5. NADH cell medium with alive 10 M HepG2 cells.
6. Cell medium with lysed 10 M HepG2 cells.
7. Cell medium (negative control).
8. Cell medium with comercial LDH enzyme extract from rabbit muscle and NADH (positive control).

Five minutes prior to the ^{13}C CSI acquisition, we measured proton images with a T_2 TurboRARE sequence covering the entire microfluidic well filled with water with the following acquisition parameters: 1 avarage, 60 ms of echo time, 12 ms of echo spacing, 8 rare factor, 192x192 pixels image size, 25x45 mm FOV, 20 mm slice thickness, 1.4 ms pulse length and 1.12 W pulse power.

For the region selective ^{13}C acquisition we used a CSI sequence with an 8 by 16 grid and the following acquisition parameters: a 22° flip angle (0.0589 ms pulse length and 5.0 W of power), 0.8 ms of echo time, 321.34 ms of repetition time, 20 mm of slice thickness, 25x45 mm field of view, 1024 points, 100 ppm bandwidth, 170 ppm offset, centric encoding order with compress sensing at 25 %. For display purposes, all voxels concerning one same well were summed, obtaining a 2x4 final display grid. After the CSI acquisition we measure a high-resolution proton image with a T_2 TurboRARE sequence with the same FOV parameters used for the CSI acquisition. The acquisition parameters

were: 8 average, 60 ms of echo time, 12 ms of echo spacing, 8 rare factor, 192x192 pixels image size, 25x45 mm FOV, 20 mm slice thickness, 1.4 ms pulse length and 1.12 W pulse power.

7.2.0.6 MRI data processing

For the first approach (chemical reaction) we used 80 mM solution of [1-¹³C]pyruvate polarised with a dDNP HyperSense (Oxford Instruments). We processed and visualized the resulting CSI data in SIVIC[255]. To determine the MR signal from each chamber, spectra from the voxels containing regions of the same chamber were summed. For the second approach we used 3.2 mM solution of [1-¹³C]pyruvate polarised with a dDNP HyperSense (Oxford Instruments). We processed all data with custom made code written in Matlab by a post-doctoral researcher in the lab, Dr. David Gomez-Cabeza.

7.3 RESULTS & DISCUSSION

7.3.0.1 Flip angle calibration using a 10 M ¹³C-Urea sample

The pulse length and pulse power produced by the radiofrequency coil establishes how much magnetization in the z axis is tilted towards the xy plane of the nuclear spins for the corresponding acquisition. The MRI scanner performs an adjustment previous to the acquisition called “Reference Power Adjustment” where to calibrate the amount of power required to pass through the coil to get enough signal regarding the number of nuclear spins in the sample. This adjustment is also dependent on the spins polarization, so it cannot be performed in a hyperpolarized signal because it would be making the adjustment meanwhile the signal is decaying so the reference power value would be shifting and unstable until the polarization is completely lost.

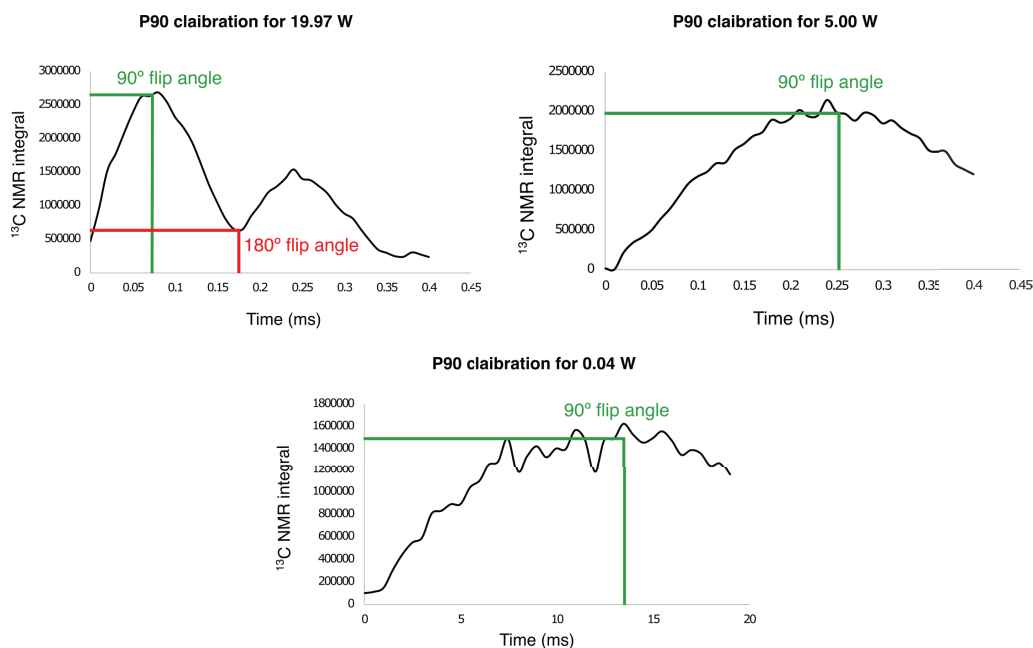


Figure 7.1: Pulse length (P90) calibration using three different power references in a 0.5 mL eppendorf. For the 19.97 W the 90° pulse is 0.08 ms, for the 5.00 W the 90° pulse is 0.25 ms, and for the 0.04 W the 90° pulse is 14 ms. I ran all the measurements with a 10 M ^{13}C Urea sample in water with 1 mM Gd-DOTA doing ^{13}C single pulse measurements. Acquisition parameters: Repetition time 300 s, acquisition time 632 ms, offset 160 ppm, 1 average, 2048 acquisition points, bandwidth 100 ppm.

7.3.0.2 Microfluidic multiwell platform for parallel detection of chemical reactions by magnetic resonance

The microfluidic platform was designed using a CAD software 1) to be MR-compatible (i.e. made of non-magnetic materials), 2) to withstand a wide range of chemical reagents, solvents, and pHs, and 3) to be used in commercially available MRI hardware (i.e. to fit inside a 42-mm inner diameter volumetric RF coil and remain within the boundaries of the homogeneous B_0 region of a preclinical 3 T MRI scanner) for improved usability and ease of implementation. The platform was engineered using microfabrication (photolithography and soft lithography) processes and consisted of a stack of three polydimethylsiloxane (PDMS) layers on a glass substrate (Fig. 7.2A)[256]. The PDMS layers were developed by replica molding using a photoresist-patterned mold and were dedicated to the microfluidic parts: the sample-containing 4×2 array of 6 mm-diameter chambers (of 15 mm center to center spacing, 10 mm height, $\approx 280 \mu\text{L}$ total volume) and the microfluidic channels to distribute the hyperpolarized solution among the chambers.

A network of sinusoidal channels (Fig. 7.2B), acting as fluidic resistances, in the upper PDMS layer split the sample throughout the device and made it possible to deliver the hyperpolarized solution rapidly and simultaneously to all the chambers. Eight distributed microfluidic channels leading to each chamber were designed to deliver the hyperpolarized sample from the top of the chamber to the testing sample, facilitating a rapid delivery of the fluid under 4 s. We integrated two further PDMS layers with microfluidic channels between the top layers to continuously infuse and withdraw solutions into and from the chambers. These channels were grouped in 2 independent sets of 4 chambers that shared inlet and outlet ports (enabling 2 different conditions and 4 replicates when these channels are open). These allow for a myriad of experimental setups in future applications. For example, they can be used for continuous renewal of the solution in the chambers while the device is located inside the MRI scanner. In this work, all experiments were performed with the withdrawal circuits closed in the device shown in Fig. 7.2C).

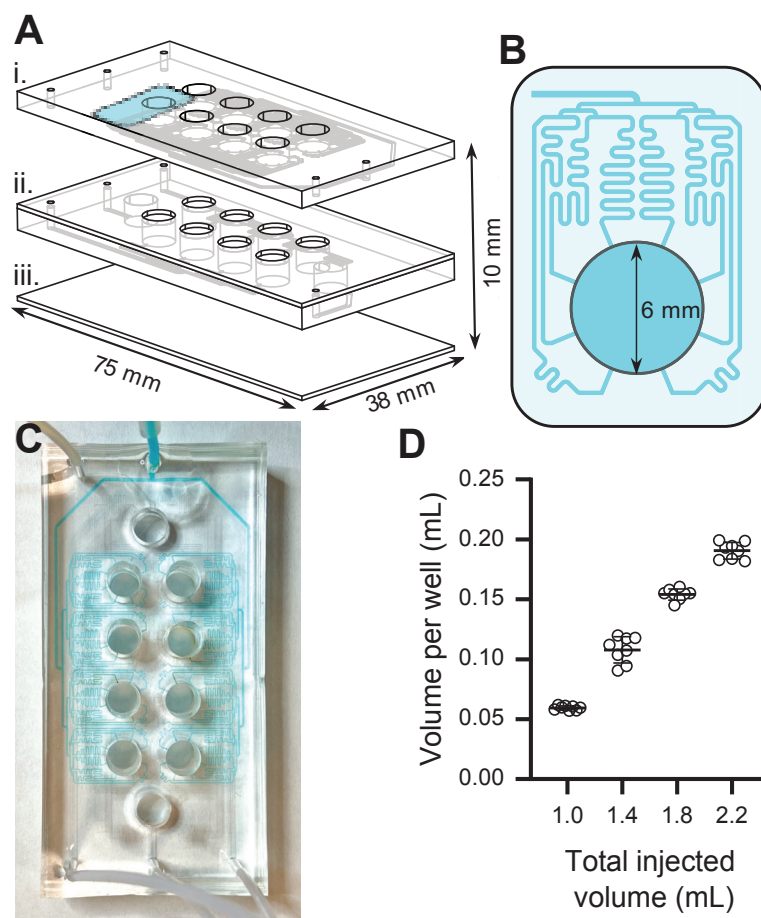


Figure 7.2: 8-well microfluidic plate without medium recirculation for high-throughput DNP-MRSI experiments. (A) Assembling layers of the multiwell plate: i) 4 mm thick PDMS layer for distribution of the hyperpolarized substrate, ii) 5 and 1 mm thick PDMS layers with the detection chambers, and iii) 75 mm x 38 mm glass slide on the bottom of the PDMS chambers as a support. (B) Network of microfluidic channels that injects the polarized sample into one of the chambers. This design is replicated along all the chambers. (C) Photo of the microfluidic device. Microfluidic channels that distribute the polarized sample are filled with blue dye for easy identification. (D) Water volume inside each chamber after injecting 1.0, 1.4, 1.8, and 2.2-mL water into the device (each circle represents a chamber of the microfluidic plate).

To confirm uniform distribution of samples across the chambers, we injected different volumes of water throughout the inlet port and collected and weighed the liquid received in each chamber. For total injected volumes of 1 mL, 1.4 mL, 1.8 mL, and 2.2 mL, the volumes per chamber were $59 \pm 2 \mu\text{L}$, $108 \pm 11 \mu\text{L}$, $154 \pm 5 \mu\text{L}$, and $191 \pm 7 \mu\text{L}$, respectively (Fig. 7.2D). Applying linear regression, the data fit (R-squared of 0.96) the following equation:

$$V_w = \frac{V_t - V_d}{8} \quad (7.1)$$

where V_w is the volume per well, V_t is the total injected volume, and $V-d$ is the dead volume ($576 \pm 69 \mu\text{L}$) mainly due to the long fluidic tubing required for injecting from outside of the MRI scanner.

We confirmed that the injected solutions arrived at each well at the exact same time and with equal volume through the fluidic channels. In order to increase the throughput of HP experiments by a factor of 8 using our microfluidic device, I exploited the potential of MR spectroscopic imaging (MRSI), by which spatial and spectral information can be obtained simultaneously (Fig. 2A). To test the device for HP-MRSI, a solution of 80 mM hyperpolarized $[1-^{13}\text{C}]$ pyruvate was injected through the fluidic channels. The matrix (8×8) and voxel size ($5 \text{ mm} \times 5 \text{ mm}$) was selected to cover all the chambers while maintaining shimming performance (Fig. 2B). Although the voxel size was smaller than the chamber size, I found that multiple voxels per chamber simplified the alignment of the device inside the RF coil. Since no voxel included more than one chamber, analysis was performed by adding the signals from voxels encompassing the same chamber. Fig. 2C shows a representative spectrum from one voxel that contains part of a chamber. The apparent relaxation time constant of $[1-^{13}\text{C}]$ pyruvate was $3.7 \pm 0.7 \text{ s}$, as calculated from the exponential decay of the C1 pyruvate resonance at 176 ppm chemical shift. Although the T_1 of $[1-^{13}\text{C}]$ pyruvate after dDNP is expected to be around 60 s,³⁰ the repeated RF pulses used to obtain the spectroscopic images (i.e., 64 pulses per each scan) caused a much faster ^{13}C polarization loss. The spectral linewidth of the ^{13}C 1 pyruvate peak was 1.8 ppm (53 Hz) at full width at half maximum height. The axial, sagittal, and coronal proton T_2 weighted MR images acquired after the HP ^{13}C -MRSI experiment confirmed that the HP solution had been delivered to all the chambers as expected (Fig. 2B). Contrary to previous studies that increased the throughput either by sequential measurements with the same dissolution sample^[251, 257] or by parallel polarization of 4 samples^[195, 53] our MRSI approach improves repeatability as all tested samples are detected under the same hyperpolarized substrate and shim conditions ($\text{FWHM} = 53 \pm 5 \text{ Hz}$).

Simultaneous detection of eight chemical reaction processes: decarboxylation of hyperpolarized $[1-^{13}\text{C}]$ pyruvate and controls

As mentioned in the introduction, $[1-^{13}\text{C}]$ pyruvate is key metabolite in glycolysis^[258] and a cellular antioxidant agent capable of neutralizing peroxides by decarboxylation^{[259,}

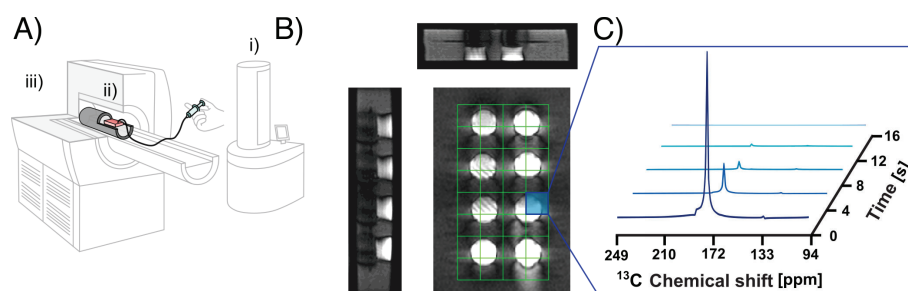


Figure 7.3: High-throughput DNP-MRSI assay. (A) Schematic illustration of the experimental setup consisted of i) polarizer equipment, ii) microfluidic multiwell plate, and iii) magnetic resonance imaging scanner. (B) T_2 -weighted localizer images with axial, sagittal and coronal perspectives. (C) Stacked dynamic spectra of $[1-^{13}\text{C}]$ pyruvic acid of the well highlighted in blue along the experiment. Note that time 0 represents when the MRS data acquisition was initiated. The transfer time between dissolution and injection was 12 s on average, and MRS data acquisition was initiated 25 s after the sample came out from the polarizer. The longitudinal experiment was designed with a CSI sequence as 8×8 voxels matrix, with a FOV of $40 \times 40 \text{ cm}^2$ and a slice thickness of 12 mm, 15° flip angle, echo time = 1.49 ms. $T_{acq} = 51.2$ ms and $RT = 66.907$ ms. Each point of the data set was acquired every 4 seconds.

260]. It is extensively used in dDNP-MR experiments due to its long T_1 relaxation time constant (in excess of 1 minute)³⁰ and high polarization (up to 36 % with SpinLabTM polarizer®)[16], which provide MR signals of both pyruvate and its products. As a proof of concept for detecting fast reactions using our parallelized microfluidic approach, I traced the ^{13}C resonance shifts of the biologically relevant chemical reaction between $[1-^{13}\text{C}]$ pyruvate and H_2O_2 by acquiring spatially localized ^{13}C -MR spectra of the whole device every 4 seconds.

Using the entire chamber capacity of the platform, two chambers of the platform were filled with a $[^{13}\text{C}]$ urea solution for chamber arrangement verification, three with a H_2O_2 solution to initiate the chemical reaction, and three with a sodium hydroxide solution as a negative control of the reaction (Fig. 7.4A). The placement of the microfluidic device and acquisition matrix was validated before to the HP experiment by a proton T_2 -weighted image (Fig. 7.4B) and again after by detecting the thermal signal of the $[^{13}\text{C}]$ urea solution from two opposite corners of the device (Fig. 7.43C). After injection of the hyperpolarized pyruvate solution, the spectra of the chamber regions without H_2O_2 displayed only the pyruvate peak since no reaction had occurred (Fig. 7.4D). In chambers where the reaction took place, the bubbles generated by CO_2 as a side of the reaction were eas-

ily visible, and spectral acquisitions displayed the characteristic multi-peak spectrum of pyruvate decarboxylation¹⁸ (Fig. 7.4E and F), where the following peaks were identified: [$1\text{-}^{13}\text{C}$]pyruvate (176 ppm), [$1\text{-}^{13}\text{C}$]pyruvate hydrate (184 ppm), [$1\text{-}^{13}\text{C}$]2-hydroperoxy-2-hydroxypropanoate (181 ppm), [$1\text{-}^{13}\text{C}$]peroxymonocarbonate (161 ppm), and $^{13}\text{CO}_2$ (125 ppm).

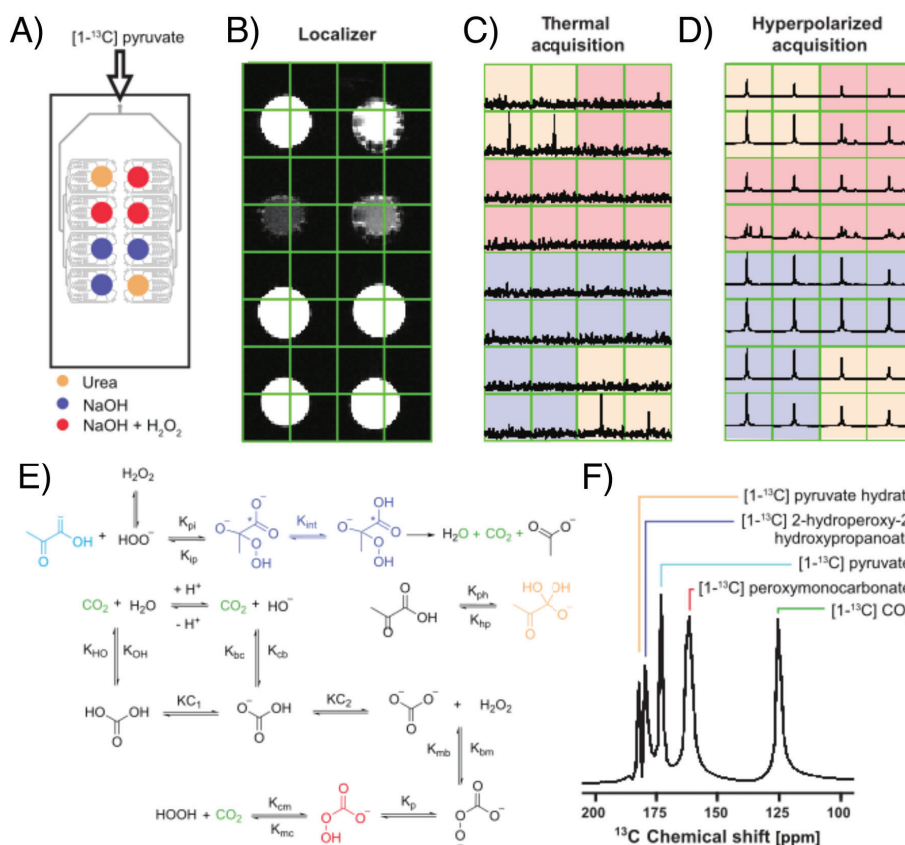


Figure 7.4: (A) Schematic image of the microfluidic device specifying the sample placed in each well. (B) Localizer with a coronal T_2 -weighted image using a spin echo T_2 Turbo-RARE sequence with the corresponding voxels matrix overlapping. (C) Spectroscopic acquisition using a CSI pulse sequence to the microfluidic device at thermal equilibrium. (D) First spectroscopic acquisition point using a CSI pulse sequence to the microfluidic device after the hyperpolarized $[1-^{13}\text{C}]$ pyruvate injection. (E) Scheme of the oxidation reaction between pyruvic acid and H_2O_2 , highlighting all products and intermediates displayed in the spectrum. (F) Representative spectrum of the decarboxylation of $[1-^{13}\text{C}]$ pyruvate reacted with H_2O_2 , showing all the products and intermediate states of the reaction.

Parallel MRSI in the preclinical MRI scanner achieves high throughput at the expense of some spectral resolution. The trade-off in resolution is, however, more than acceptable for hyperpolarized ^{13}C MRSI where the resonances of metabolic products are dispersed over a wide chemical shift range. Additionally, we compared the temporal evolution of the $[1-^{13}\text{C}]$ pyruvate signal between different conditions by averaging the signal intensities from replicated chambers (Fig. 7.5). Dispersion among the three chambers per condition for the pyruvate peak were 23% and 18% at the first acquisition for chambers with and without the chemical reaction, respectively. At the time of the first acquisition (i.e., 25 s

from dissolution), the pyruvate peak intensity from chambers with H₂O₂ was 2.5–3 lower than the signal from chambers containing non-oxidant solutions because of pyruvate's rapid consumption during the reaction (Fig. 7.5A). The pyruvate signal decay was dominated by the RF pulse polarization consumption, with an apparent decay time constant of 3.03 s in chambers with H₂O₂ and 2.96 s in chambers without reactant.

The observation that the relaxation time constant of [1-¹³C]pyruvate was similar (≈ 3 s) among conditions (i.e., chambers with and without H₂O₂) indicates that the resulting decay was exclusively due to the signal exponential decay by T₁ and signal depletion by RF pulsing 64 times/acquisition. This also suggests that practically all the pyruvate had already been converted into the intermediate at the time of the first acquisition. In the chambers with H₂O₂, the signals from reaction subproducts decayed as a result of both the generation of the reactant and the T₁ relaxation time constant of the hyperpolarized carbon nuclei (Fig. 7.5B). While over-crowded peaks in the downfield region (pyruvate, its hydrate and 2-hydroperoxy-2-hydroxypropanoate) could be detected above the noise level (i.e., SNR > 5) for up to 33 s after the injection of hyperpolarized pyruvate, the upfield peaks of the two final products (¹³CO₂ and [1-¹³C]-peroxymonocarbonate) were detectable for over a minute.

The longer observation window for the products is probably attributed to the oxidation reaction, as the ongoing production of the final molecules counteracts the signal decay by T₁. This could account for the slower decay rate of the two generated products (i.e., [1-¹³C]peroxymonocarbonate and ¹³CO₂) respect to the consumed reactant and intermediate compound (i.e., [1-¹³C]pyruvate and [1-¹³C]2-hydroperoxy-2-hydroxypropanoate). Apparent decay rates were $0.28 \pm 0.03 \text{ s}^{-1}$ for [1-¹³C]pyruvate hydrate, $0.50 \pm 0.05 \text{ s}^{-1}$ for [1-¹³C]2-hydroperoxy-2-hydroxypropanoate, $0.15 \pm 0.01 \text{ s}^{-1}$ for [1-¹³C]peroxymonocarbonate, and $0.09 \pm 0.01 \text{ s}^{-1}$ for ¹³CO₂. The time-normalized mass sensitivity is defined as:

$$S_m = \frac{SNR}{m\sqrt{t}} \quad (7.2)$$

where *m* is the amount of substance in mol and *t* is the measurement time in seconds[261]. In systems with small volumes and integrated solenoidal microcoils, which provide strong signals, *S_m* is in the range of thousands ($\approx 1000\text{--}3000$) $\mu\text{mol}^{-1} \text{ s}^{-1/2}$ [262, 263]. In our

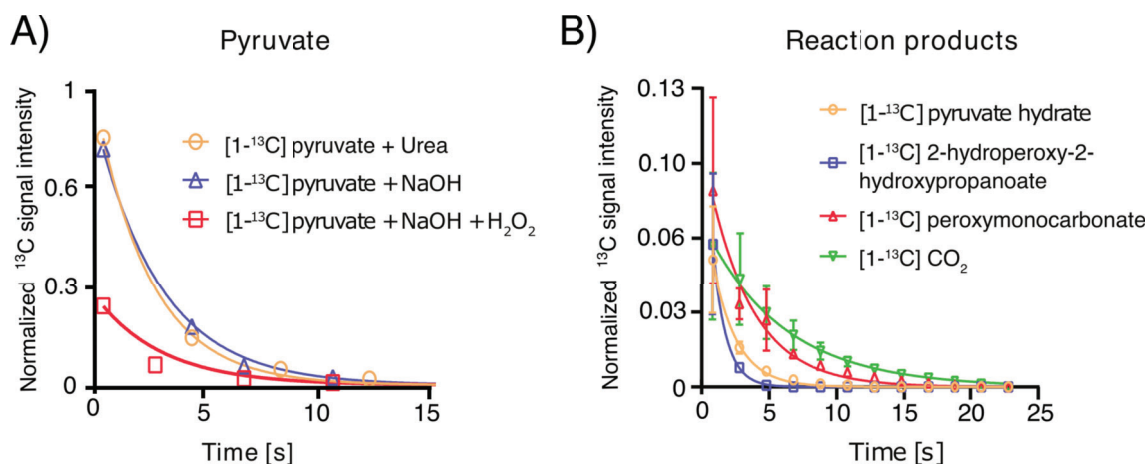


Figure 7.5: Plots of the kinetics study with H_2O_2 (A) Plot showing the temporal evolution of the peak signal intensity, normalized by the signal intensity and volume of $[1-^{13}\text{C}]$ pyruvate, in wells containing ^{13}C urea (orange circle), wells containing H_2O_2 and sodium hydroxide solution (red square) and wells containing water and sodium hydroxide solution (blue triangle). (B) Plot showing the temporal evolution of the normalized peak signal intensity of $[1-^{13}\text{C}]$ pyruvate hydrate (orange circle), $[1-^{13}\text{C}]$ 2-hydroperoxy-2-hydroxypropanoate (blue square), $[1-^{13}\text{C}]$ peroxymonocarbonate (red triangle), and $^{13}\text{CO}_2$ (inverted green triangle) over time in wells containing H_2O_2 and sodium hydroxide solution. Normalized peak signal intensity of $[1-^{13}\text{C}]$ pyruvate (dashed line) in well containing only sodium hydroxide is included in dashed line as a reference. The signal intensity displayed in each of the four voxels corresponding to a well were summed up and each well corresponds to a replicate.

experiment, the SNR and S_m of one single scan ($t = 4$ s) for pyruvate detection were 4229 and $352 \mu\text{mol}^1 \text{s}^{-1/2}$, respectively. This SNR is 56 times higher than the SNR obtained from a thermal polarization measurement with 65 h of averaging time with the same experimental setup and acquisition parameters.

The concentrations of all the species in the reaction were quantified considering a uniform ^{13}C polarization decay (i.e., decay of the pyruvate signal in the well without H_2O_2) among all the species. Although the T_1 values of the products are likely to be slightly different, this simplification enables to determine, approximately, their concentration when T_1 is unknown. Within the time period where the SNR of the pyruvate was high (first 12s), I determined a plateau of the $[1-^{13}\text{C}]$ pyruvate concentration, a decrease of the intermediate product ($[1-^{13}\text{C}]$ 2-hydroperoxy-2-hydroxypropanoate), and an increase of the final products ($[1-^{13}\text{C}]$ peroxymonocarbonate, and $^{13}\text{CO}_2$).

To monitor fast reactions by HP-MR, the HP solution must mix with the reactant un-

der study within seconds of reaching the science chambers. Our microfluidic device addressed this constraint by delivering the HP solution to each chamber in a cascade mode through eight channels (Fig. 7.2). For experiments where samples may need a convective flow for a proper mixing, I speculate that alternate infusion and withdrawal of the testing sample in the chambers using the additional channels included in our device would further enhance the mixing with the polarized sample. Hyperpolarization-enhanced MR techniques are rapidly evolving and are expected to transform current analytical tools. Increasing their throughput will help overcome the barrier that prevents these techniques from being more accessible. This work showed that combining dDNP-MRSI and microfluidics can increase the capacity of identify products from chemical reactions and demonstrated that multiple samples can be simultaneously and non-invasively interrogated. Reaction kinetics and in situ metabolomic studies are potential applications of our platform beyond the proof-of-principle in this work.

7.3.0.3 Microfluidic multiwell platform for the metabolic activity of HepG2 cell line by hyperpolarized spectroscopic imaging

We successfully parallelised the acquisition of metabolic imaging, understanding the role of rich media, cell lysis and extracellular NADH in metabolizing pyruvate to lactate 7.6. With this type of voxel spectroscopic metabolic imaging provided by CSI, I observed three different phenomena in a single experiment. First, I detected the increase of lactate production in a rich media supplemented with Glu and Gln due to an increase in glycolytic activity, as previously reported in literature[241]. Second, extracellular NADH helps to adjust the redox balance, in alive (indirectly) and lysed (directly) cells, resulting in an increase in lactate production[264]. Third, by lysing cells (and adding NADH), the metabolism of lactate was significantly increased thanks to avoiding the main limiting factor of the reaction, the transport of pyruvate into the cell tanks to the MCT1 transporter[265]. Yet, despite the advantages of the strategy, better detection coils with large areas (I employed a volume coil) and better k-space sampling with low pulsing are required to improve the resolution and aim for temporal imaging. Nonetheless, our results are the first to show such level of parallelisation with high spatial resolution for cellular studies using microfluidics and HP-MRSI, contributing to incorporating hyperpolarised

NMR into the field of precision medicine.

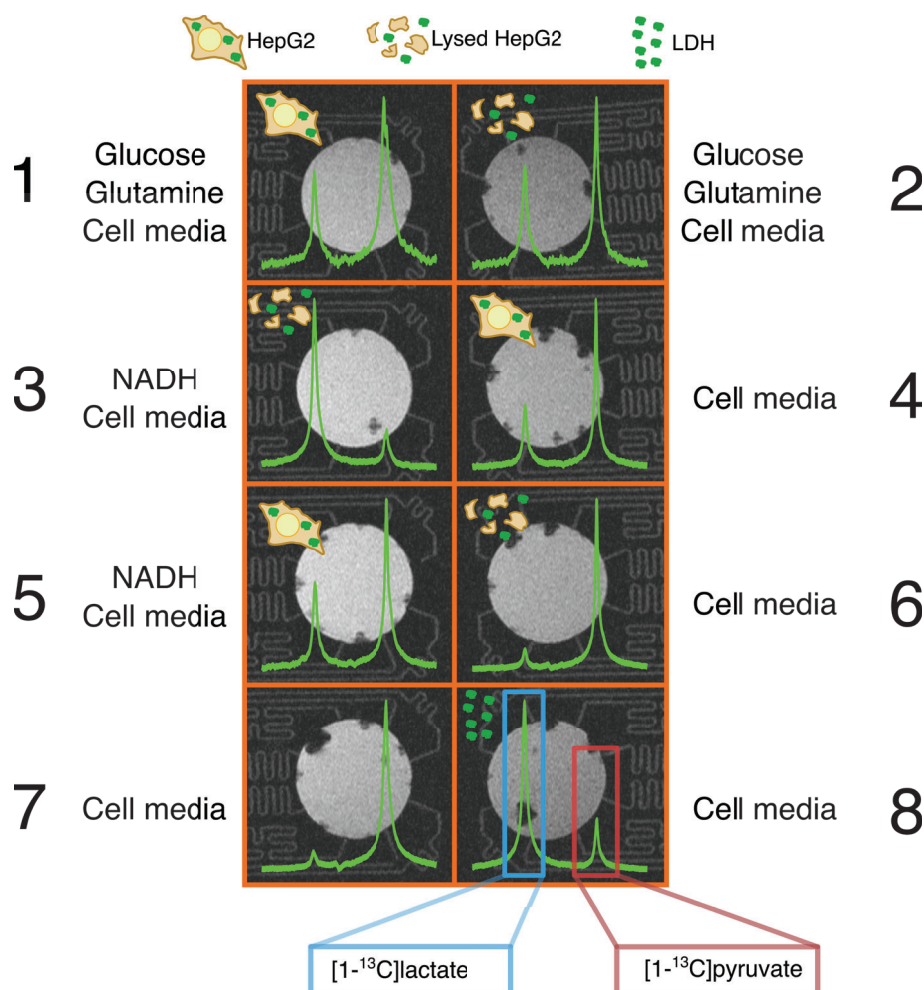


Figure 7.6: Representative figure of the results obtained with the multiwell microfluidic device with the cells study. At the top of the figure I made a legend of the drawings used to express whether live cells, lysed cells or LDH enzyme were used. Then we have the wells ordered numerically from 1 to 8 with the conditions specified next to the well. In addition in each well I show the ¹³C spectrum obtained 20 s after injecting the hyperpolarised [1-¹³C]pyruvate. The most unshielded peak corresponds to [1-¹³C]lactate (shown in blue) and the most shielded peak to [1-¹³C]pyruvate (shown in red).

7.4 CONCLUSIONS

In conclusion, this chapter demonstrates that hyperpolarized MRI is a suitable technique for conducting high-throughput analyses, enabling the acquisition of multiple conditions with a single hyperpolarized shot and measurement. Through spectroscopic localization within different regions of a microfluidic platform, diverse conditions were tested fol-

lowing a single polarization event. Specifically, in the oxidation of [1-¹³C]pyruvate with hydrogen peroxide, the reaction was dynamically monitored, tracking the evolution of reagents, intermediates, and products over time. This dynamic assessment was feasible by employing highly concentrated samples, and therefore, low flip angle measurements. We managed to take a metabolism snapshot at a specific time and obtain information about the different conditions involved in the wells of the microfluidic device. This novel experimental approach enables the conduct of hyperpolarization assays for metabolism measurement at a reduced expense, potentially making the technique more accessible to a larger number of people at reduced cost and time.

CONCLUSIONS

1. I have developed a robust, reliable, and biopsy-free protocol to quantify ammonium in biological fluids with a wide dynamic concentrations range, using quantitative ^1H NMR spectroscopy.
2. I demonstrated that the ammonium quantification method can be used to diagnose and discern between some stages of NAFLD and ArLD disease retrospectively.
3. I proved how magnetic resonance imaging is a promising tool to investigate diffusion and perfusion in porous bio-compatible materials commonly used to develop 3D cell culture models.
4. I studied the effect of metallic parts in the passage of magnetic solutions, and observed that in many cases the sample magnetization is diminished or lost due to nonadiabaticity of the passage.
5. I evaluated the efficiency of a 60 MHz modified benchtop NMR spectrometer to measure ^{13}C NMR acquisitions within a microfluidic device incorporating a double tuned saddle radiofrequency coil. We tested the setup with hyperpolarized $[1-^{13}\text{C}]$ pyruvate and fumarate.
6. I demonstrated that hyperpolarized MRI is a suitable technique for conducting high-throughput analyses, enabling the acquisition of multiple conditions with a single hyperpolarized shot and measurement.
7. We managed to take a metabolism snapshot at a specific time and obtain information about the different conditions involved in the wells of the microfluidic device using MRSI.

Bibliography

- [1] Felix Bloch. Nuclear induction. *Physical review*, 70(7-8):460, 1946.
- [2] James T Arnold, SS Dharmatti, and ME Packard. Chemical effects on nuclear induction signals from organic compounds. *The journal of chemical physics*, 19(4):507–507, 1951.
- [3] Edward Raymond Andrew. Nuclear magnetic resonance. *Nuclear Magnetic Resonance*, 2009.
- [4] E Matthias, B Olsen, DA Shirley, Ji E Templeton, and RM Steffen. Theory of nuclear magnetic resonance detected by nuclear radiations. *Physical Review A*, 4(4):1626, 1971.
- [5] Timothy DW Claridge. *High-resolution NMR techniques in organic chemistry*, volume 27. Elsevier, 2016.
- [6] Adam Allerhand and Michael Dohrenwend. Ultrahigh resolution nmr. 2. measurements of secondary isotope effects on chemical shifts, long-range carbon-carbon scalar coupling constants, and carbon-13 spin-spin relaxation times directly from line widths. *Journal of the American Chemical Society*, 107(23):6684–6688, 1985.
- [7] Toshimichi Fujiwara and Ayyalusamy Ramamoorthy. How far can the sensitivity of nmr be increased? *Annual Reports on NMR Spectroscopy*, 58:155–175, 2006.
- [8] Jung Ho Lee, Yusuke Okuno, and Silvia Cavagnero. Sensitivity enhancement in solution nmr: Emerging ideas and new frontiers. *Journal of Magnetic Resonance*, 241:18–31, 2014.

- [9] Jan H Ardenkjær-Larsen, Björn Fridlund, Andreas Gram, Georg Hansson, Lennart Hansson, Mathilde H Lerche, Rolf Servin, Mikkel Thaning, and Klaes Golman. Increase in signal-to-noise ratio of $> 10,000$ times in liquid-state nmr. *Proceedings of the National Academy of Sciences*, 100(18):10158–10163, 2003.
- [10] John S Rigden. Quantum states and precession: The two discoveries of nmr. *Reviews of modern physics*, 58(2):433, 1986.
- [11] Nicolaas Bloembergen, Edward Mills Purcell, and Robert V Pound. Relaxation effects in nuclear magnetic resonance absorption. *Physical review*, 73(7):679, 1948.
- [12] Armin M Nagel, Frank Lehmann-Horn, Marc-André Weber, Karin Jurkat-Rott, Maya B Wolf, Alexander Radbruch, Reiner Umathum, and Wolfhard Semmler. In vivo ^{35}Cl mr imaging in humans: a feasibility study. *Radiology*, 271(2):585–595, 2014.
- [13] Marianna Fekete, Fadi Ahwal, and Simon B Duckett. Remarkable levels of ^{15}N polarization delivered through sabre into unlabeled pyridine, pyrazine, or metronidazole enable single scan nmr quantification at the mm level. *The Journal of Physical Chemistry B*, 124(22):4573–4580, 2020.
- [14] T Jonsson, P Nordblad, and P Svedlindh. Dynamic study of dipole-dipole interaction effects in a magnetic nanoparticle system. *Physical Review B*, 57(1):497, 1998.
- [15] K Elbayed and D Canet. Accurate determination of interference terms between carbon-proton dipolar interactions and carbon or proton chemical shift anisotropy from longitudinal carbon-13 relaxation studies. *Molecular Physics*, 68(5):1033–1046, 1989.
- [16] Jan H Ardenkjaer-Larsen, Andrew M Leach, Neil Clarke, John Urbahn, Denise Anderson, and Timothy W Skloss. Dynamic nuclear polarization polarizer for sterile use intent. *NMR in biomedicine*, 24(8):927–932, 2011.
- [17] Yaotang Wu, Jerome L Ackerman, David A Chesler, Lila Graham, Yan Wang, and Melvin J Glimcher. Density of organic matrix of native mineralized bone mea-

- sured by water-and fat-suppressed proton projection mri. *Magnetic Resonance in Medicine: An Official Journal of the International Society for Magnetic Resonance in Medicine*, 50(1):59–68, 2003.
- [18] Mark A Brown and Richard C Semelka. *MRI: basic principles and applications*. John Wiley & Sons, 2011.
- [19] Simon Hu, Minhua Zhu, Hikari AI Yoshihara, David M Wilson, Kayvan R Keshari, Peter Shin, Galen Reed, Cornelius von Morze, Robert Bok, Peder EZ Larson, et al. In vivo measurement of normal rat intracellular pyruvate and lactate levels after injection of hyperpolarized [1-13c] alanine. *Magnetic resonance imaging*, 29(8):1035–1040, 2011.
- [20] Joseph P Hornak, Jerzy Szumowski, and Robert G Bryant. Magnetic field mapping. *Magnetic resonance in medicine*, 6(2):158–163, 1988.
- [21] Irene Marco-Rius, Cornelius von Morze, Renuka Sriram, Peng Cao, Gene-Yuan Chang, Eugene Milshteyn, Robert A Bok, Michael A Ohliger, David Pearce, John Kurhanewicz, et al. Monitoring acute metabolic changes in the liver and kidneys induced by fructose and glucose using hyperpolarized [2-13c] dihydroxyacetone. *Magnetic resonance in medicine*, 77(1):65–73, 2017.
- [22] Wanjie Bai, Peijie Xiang, Huijie Liu, Hangyu Guo, Ziran Tang, Peng Yang, Yuan Zou, Ye Yang, Zhipeng Gu, and Yiwen Li. Molecular hyperpolarization-directed photothermally enhanced melanin-inspired polymers. *Macromolecules*, 55(15):6426–6434, 2022.
- [23] Christian Hilty and Sean Bowen. Applications of dynamic nuclear polarization to the study of reactions and reagents in organic and biomolecular chemistry. *Organic & biomolecular chemistry*, 8(15):3361–3365, 2010.
- [24] Jiandu Hu, Jihyun Kim, and Christian Hilty. Detection of protein–ligand interactions by ¹⁹f nuclear magnetic resonance using hyperpolarized water. *The Journal of Physical Chemistry Letters*, 13(17):3819–3823, 2022.

- [25] Haifeng Zeng, Youngbok Lee, and Christian Hilty. Quantitative rate determination by dynamic nuclear polarization enhanced nmr of a diels- alder reaction. *Analytical chemistry*, 82(21):8897–8902, 2010.
- [26] Peter J Rayner, Marianna Fekete, Callum A Gater, Fadi Ahwal, Norman Turner, Aneurin J Kennerley, and Simon B Duckett. Real-time high-sensitivity reaction monitoring of important nitrogen-cycle synthons by ^{15}N hyperpolarized nuclear magnetic resonance. *Journal of the American Chemical Society*, 144(19):8756–8769, 2022.
- [27] Andrew E Derome. *Modern NMR techniques for chemistry research*. Elsevier, 2013.
- [28] Michael P Williamson and Jonathan P Waltho. Peptide structure from nmr. *Chemical Society Reviews*, 21(4):227–236, 1992.
- [29] Alexandra Svyatova, Vitaly P Kozinenko, Nikita V Chukanov, Dudari B Burueva, Eduard Y Chekmenev, Yu-Wen Chen, Dennis W Hwang, Kirill V Kovtunov, and Igor V Koptug. Phip hyperpolarized $[1-^{13}\text{C}]$ pyruvate and $[1-^{13}\text{C}]$ acetate esters via ph-inept polarization transfer monitored by ^{13}C nmr and mri. *Scientific Reports*, 11(1):5646, 2021.
- [30] Matthew L Hirsch, Neal Kalechofsky, Avrum Belzer, Melanie Rosay, and James G Kempf. Brute-force hyperpolarization for nmr and mri. *Journal of the American Chemical Society*, 137(26):8428–8434, 2015.
- [31] James Eills, Dmitry Budker, Silvia Cavagnero, Eduard Y. Chekmenev, Stuart J. Elliott, Sami Jannin, Anne Lesage, Jörg Matysik, Thomas Meersmann, Thomas Prisner, Jeffrey A. Reimer, Hanming Yang, and Igor V. Koptug. Spin hyperpolarization in modern magnetic resonance. *Chemical Reviews*, 123:1417–1551, 2023. PMID: 36701528.
- [32] Ozgur Sahin, Erica de Leon Sanchez, Sophie Conti, Amala Akkiraju, Paul Reshetikhin, Emanuel Druga, Aakriti Aggarwal, Benjamin Gilbert, Sunil Bhawe,

- and Ashok Ajoy. High field magnetometry with hyperpolarized nuclear spins. *Nature communications*, 13(1):5486, 2022.
- [33] Matthew L Hirsch, Bryce A Smith, Mark Mattingly, Artem G Goloshevsky, Melanie Rosay, and James G Kempf. Transport and imaging of brute-force ^{13}C hyperpolarization. *Journal of Magnetic Resonance*, 261:87–94, 2015.
- [34] David T Peat, Matthew L Hirsch, David G Gadian, Anthony J Horsewill, John R Owers-Bradley, and James G Kempf. Low-field thermal mixing in $[1-^{13}\text{C}]$ pyruvic acid for brute-force hyperpolarization. *Physical Chemistry Chemical Physics*, 18(28):19173–19182, 2016.
- [35] Lloyd Lumata, Matthew E Merritt, Craig R Malloy, A Dean Sherry, and Zoltan Kovacs. Impact of gd^{3+} on dnp of $[1-^{13}\text{C}]$ pyruvate doped with trityl ox063, bdpa, or 4-oxo-tempo. *The journal of physical chemistry A*, 116(21):5129–5138, 2012.
- [36] Albert P Chen, Justin YC Lau, Rohan DA Alvares, and Charles H Cunningham. Using $[1-^{13}\text{C}]$ lactic acid for hyperpolarized ^{13}C mr cardiac studies. *Magnetic resonance in medicine*, 73(6):2087–2093, 2015.
- [37] Peter Niedbalski, Christopher Parish, Andhika Kiswandhi, Zoltan Kovacs, and Lloyd Lumata. Influence of ^{13}C isotopic labeling location on dynamic nuclear polarization of acetate. *The Journal of Physical Chemistry A*, 121(17):3227–3233, 2017.
- [38] Thad G Walker and William Happer. Spin-exchange optical pumping of noble-gas nuclei. *Reviews of modern physics*, 69(2):629, 1997.
- [39] FD Colegrove, LD Schearer, and GK Walters. Polarization of ^3He gas by optical pumping. *Physical Review*, 132(6):2561, 1963.
- [40] Graham Norquay, GJ Collier, M Rao, NJ Stewart, and JM Wild. ^{129}Xe spin-exchange optical pumping with high photon efficiency. *Physical review letters*, 121(15):153201, 2018.

- [41] Earl Babcock, Ian Nelson, Steve Kadlecsek, Bastiaan Driehuys, LW Anderson, F William Hersman, and Thad G Walker. Hybrid spin-exchange optical pumping of ^3He . *Physical review letters*, 91(12):123003, 2003.
- [42] MS Rosen, TE Chupp, KP Coulter, RC Welsh, and SD Swanson. Polarized ^{129}Xe optical pumping/spin exchange and delivery system for magnetic resonance spectroscopy and imaging studies. *Review of Scientific Instruments*, 70(2):1546–1552, 1999.
- [43] Harald E Möller, X Josette Chen, Brian Saam, Klaus D Hagspiel, G Allan Johnson, Talissa A Altes, Eduard E de Lange, and Hans-Ulrich Kauczor. Mri of the lungs using hyperpolarized noble gases. *Magnetic Resonance in Medicine: An Official Journal of the International Society for Magnetic Resonance in Medicine*, 47(6):1029–1051, 2002.
- [44] Igor V Koptug, Kirill V Kovtunov, Scott R Burt, M Sabieh Anwar, Christian Hilty, Song-I Han, Alexander Pines, and Renad Z Sagdeev. Para-hydrogen-induced polarization in heterogeneous hydrogenation reactions. *Journal of the American Chemical Society*, 129(17):5580–5586, 2007.
- [45] Ralph W Adams, Juan A Aguilar, Kevin D Atkinson, Michael J Cowley, Paul IP Elliott, Simon B Duckett, Gary GR Green, Iman G Khazal, Joaquín López-Serrano, and David C Williamson. Reversible interactions with para-hydrogen enhance nmr sensitivity by polarization transfer. *Science*, 323(5922):1708–1711, 2009.
- [46] Zhen J. Wang, Michael A. Ohliger, Peder E. Z. Larson, Jeremy W. Gordon, Robert A. Bok, James Slater, Javier E. Villanueva-Meyer, Christopher P. Hess, John Kurhanewicz, and Daniel B. Vigneron. Hyperpolarized ^{13}C MRI: State of the Art and Future Directions. *Radiology*, 291(2):273–284, 2019.
- [47] Jae Mo Park, Sonal Josan, Thomas Grafendorfer, Yi-Fen Yen, Ralph E Hurd, Daniel M Spielman, and Dirk Mayer. Measuring mitochondrial metabolism in rat brain in vivo using mr spectroscopy of hyperpolarized $[2-^{13}\text{C}]$ pyruvate. *NMR in biomedicine*, 26(10):1197–1203, 2013.

- [48] Ferdia A Gallagher, Mikko I Kettunen, De-En Hu, Pernille R Jensen, Magnus Karlsson, Anna Gisselsson, Sarah K Nelson, Timothy H Witney, Sarah E Bohndiek, Georg Hansson, et al. Production of hyperpolarized [1, 4-¹³C₂] malate from [1, 4-¹³C₂] fumarate is a marker of cell necrosis and treatment response in tumors. *Proc. Natl. Acad. Sci. U.S.A.*, 106(47):19801–19806, 2009.
- [49] Marie A Schroeder, Pawel Swietach, Helen J Atherton, Ferdia A Gallagher, Phillip Lee, George K Radda, Kieran Clarke, and Damian J Tyler. Measuring intracellular pH in the heart using hyperpolarized carbon dioxide and bicarbonate: a ¹³C and ³¹P magnetic resonance spectroscopy study. *Cardiovascular research*, 86(1):82–91, 2010.
- [50] Kayvan R Keshari, John Kurhanewicz, Robert Bok, Peder EZ Larson, Daniel B Vigneron, and David M Wilson. Hyperpolarized ¹³C dehydroascorbate as an endogenous redox sensor for in vivo metabolic imaging. *Proceedings of the National Academy of Sciences*, 108(46):18606–18611, 2011.
- [51] Cornelius Von Morze, Peder EZ Larson, Simon Hu, Kayvan Keshari, David M Wilson, Jan Henrik Ardenkjaer-Larsen, Andrei Goga, Robert Bok, John Kurhanewicz, and Daniel B Vigneron. Imaging of blood flow using hyperpolarized [¹³C] urea in preclinical cancer models. *Journal of Magnetic Resonance Imaging*, 33(3):692–697, 2011.
- [52] Irene Marco-Rius, Jeremy W Gordon, Aras N Mattis, Robert Bok, Romelyn Delos Santos, Subramanian Sukumar, Peder EZ Larson, Daniel B Vigneron, and Michael A Ohliger. Diffusion-weighted imaging of hyperpolarized [¹³C] urea in mouse liver. *Journal of Magnetic Resonance Imaging*, 47(1):141–151, 2018.
- [53] Simon Hu, Peder EZ Larson, Mark VanCrickinge, Andrew M Leach, Ilwoo Park, Christine Leon, Jenny Zhou, Peter J Shin, Galen Reed, Paul Keselman, et al. Rapid sequential injections of hyperpolarized [1-¹³C] pyruvate in vivo using a sub-kelvin, multi-sample dnp polarizer. *Magnetic resonance imaging*, 31(4):490–496, 2013.
- [54] Marie A Schroeder, Lowri E Cochlin, Lisa C Heather, Kieran Clarke, George K Radda, and Damian J Tyler. In vivo assessment of pyruvate dehydrogenase flux in

- the heart using hyperpolarized carbon-13 magnetic resonance. *Proceedings of the National Academy of Sciences*, 105(33):12051–12056, 2008.
- [55] JS Clegg. Properties and metabolism of the aqueous cytoplasm and its boundaries. *American Journal of Physiology-Regulatory, Integrative and Comparative Physiology*, 246(2):R133–R151, 1984.
- [56] Richard L Hesketh and Kevin M Brindle. Magnetic resonance imaging of cancer metabolism with hyperpolarized ^{13}C -labeled cell metabolites. *Current opinion in chemical biology*, 45:187–194, 2018.
- [57] Per Mose Nielsen, Esben Søvsø Szocska Hansen, Thomas Stokholm Nørlinger, Rikke Nørregaard, Lotte Bonde Bertelsen, Hans Stødkilde Jørgensen, and Christoffer Laustsen. Renal ischemia and reperfusion assessment with three-dimensional hyperpolarized ^{13}C , ^{15}N -urea. *Magnetic resonance in medicine*, 76(5):1524–1530, 2016.
- [58] Zheng Ye, Bin Song, Philip M Lee, Michael A Ohliger, and Christoffer Laustsen. Hyperpolarized carbon ^{13}C mri in liver diseases: Recent advances and future opportunities. *Liver International*, 42(5):973–983, 2022.
- [59] Stephanie Anderson, James T Grist, Andrew Lewis, and Damian J Tyler. Hyperpolarized ^{13}C magnetic resonance imaging for noninvasive assessment of tissue inflammation. *NMR in Biomedicine*, 34(3):e4460, 2021.
- [60] David M Wilson and John Kurhanewicz. Hyperpolarized ^{13}C mr for molecular imaging of prostate cancer. *Journal of Nuclear Medicine*, 55(10):1567–1572, 2014.
- [61] John Kurhanewicz, Daniel B Vigneron, Jan Henrik Ardenkjaer-Larsen, James A Bankson, Kevin Brindle, Charles H Cunningham, Ferdia A Gallagher, Kayvan R Keshari, Andreas Kjaer, Christoffer Laustsen, et al. Hyperpolarized ^{13}C mri: path to clinical translation in oncology. *Neoplasia*, 21(1):1–16, 2019.
- [62] Katrina Ray. Nafld—the next global epidemic. *Nature reviews Gastroenterology & hepatology*, 10(11):621–622, 2013.

- [63] Paola Bertuccio, Federica Turati, Greta Carioli, Teresa Rodriguez, Carlo La Vecchia, Matteo Malvezzi, and Eva Negri. Global trends and predictions in hepatocellular carcinoma mortality. *Journal of hepatology*, 67(2):302–309, 2017.
- [64] Lindsey A Torre, Freddie Bray, Rebecca L Siegel, Jacques Ferlay, Joannie Lortet-Tieulent, and Ahmedin Jemal. Global cancer statistics, 2012. *CA: a cancer journal for clinicians*, 65(2):87–108, 2015.
- [65] Olga Khomich, Alexander V Ivanov, and Birke Bartosch. Metabolic hallmarks of hepatic stellate cells in liver fibrosis. *Cells*, 9(1):24, 2019.
- [66] Matthew E Merritt, Crystal Harrison, A Dean Sherry, Craig R Malloy, and Shawn C Burgess. Flux through hepatic pyruvate carboxylase and phosphoenolpyruvate carboxykinase detected by hyperpolarized ^{13}C magnetic resonance. *Proceedings of the National Academy of Sciences*, 108(47):19084–19089, 2011.
- [67] Hsin-Yu Chen, Rahul Aggarwal, Robert A Bok, Michael A Ohliger, Zi Zhu, Philip Lee, Jeremy W Gordon, Mark van Criekinge, Lucas Carvajal, James B Slater, et al. Hyperpolarized ^{13}C -pyruvate mri detects real-time metabolic flux in prostate cancer metastases to bone and liver: a clinical feasibility study. *Prostate cancer and prostatic diseases*, 23(2):269–276, 2020.
- [68] Liangyou Rui. Energy metabolism in the liver. *Comprehensive physiology*, 4(1):177, 2014.
- [69] Uffe Kjærgaard, Christoffer Laustsen, Thomas Nørtinger, Rasmus S Tougaard, Emmeli Mikkelsen, Haiyun Qi, Lotte B Bertelsen, Niels Jessen, and Hans Stødkilde-Jørgensen. Hyperpolarized $[1-^{13}\text{C}]$ pyruvate as a possible diagnostic tool in liver disease. *Physiological reports*, 6(23):e13943, 2018.
- [70] Sonal Josan, Kelvin Billingsley, Juan Orduna, Jae Mo Park, Richard Luong, Liqing Yu, Ralph Hurd, Adolf Pfefferbaum, Daniel Spielman, and Dirk Mayer. Assessing inflammatory liver injury in an acute ccl4 model using dynamic 3d metabolic imaging of hyperpolarized $[1-^{13}\text{C}]$ pyruvate. *NMR in Biomedicine*, 28(12):1671–1677, 2015.

- [71] Qianrang Lu, Xinyao Tian, Hao Wu, Jiacheng Huang, Mengxia Li, Zhibin Mei, Lin Zhou, Haiyang Xie, and Shusen Zheng. Metabolic changes of hepatocytes in nafl. *Frontiers in Physiology*, 12:710420, 2021.
- [72] Serena De Matteis, Andrea Ragusa, Giorgia Marisi, Stefania De Domenico, Andrea Casadei Gardini, Massimiliano Bonafè, Anna Maria Giudetti, et al. Aberrant metabolism in hepatocellular carcinoma provides diagnostic and therapeutic opportunities. *Oxidative medicine and cellular longevity*, 2018, 2018.
- [73] Eva M Serrao and Kevin M Brindle. Potential clinical roles for metabolic imaging with hyperpolarized [1-¹³C] pyruvate. *Front. Oncol.*, 6:59, 2016.
- [74] Francesca Cutruzzolà, Giorgio Giardina, Marina Marani, Alberto Macone, Alessandro Paiardini, Serena Rinaldo, and Alessio Paone. Glucose metabolism in the progression of prostate cancer. *Frontiers in physiology*, 8:97, 2017.
- [75] Zhao Chen, Weiqin Lu, Celia Garcia-Prieto, and Peng Huang. The warburg effect and its cancer therapeutic implications. *Journal of bioenergetics and biomembranes*, 39:267–274, 2007.
- [76] E Can, JAM Bastiaansen, DL Couturier, R Gruetter, HAI Yoshihara, and A Comment. [¹³ c] bicarbonate labelled from hyperpolarized [1-¹³ c] pyruvate is an in vivo marker of hepatic gluconeogenesis in fasted state. *Communications Biology*, 5(1):10–10, 2022.
- [77] Philip Lee, Waifook Leong, Trish Tan, Miangkee Lim, Weiping Han, and George K Radda. In vivo hyperpolarized carbon-13 magnetic resonance spectroscopy reveals increased pyruvate carboxylase flux in an insulin-resistant mouse model. *Hepatology*, 57(2):515–524, 2013.
- [78] Daniel M Spielman, Dirk Mayer, Yi-Fen Yen, James Tropp, Ralph E Hurd, and Adolf Pfefferbaum. In vivo measurement of ethanol metabolism in the rat liver using magnetic resonance spectroscopy of hyperpolarized [1-¹³c] pyruvate. *Magnetic Resonance in Medicine: An Official Journal of the International Society for Magnetic Resonance in Medicine*, 62(2):307–313, 2009.

- [79] Dominique Pessayre and Bernard Fromenty. Nash: a mitochondrial disease. *Journal of hepatology*, 42(6):928–940, 2005.
- [80] Francesco De Chiara, Sara Heebøll, Giusi Marrone, Carmina Montoliu, Stephen Hamilton-Dutoit, Antonio Ferrandez, Fausto Andreola, Krista Rombouts, Henning Grønbaek, Vicente Felipo, et al. Urea cycle dysregulation in non-alcoholic fatty liver disease. *Journal of hepatology*, 69(4):905–915, 2018.
- [81] Aparna H Kesarwala, Jenna L Carter, Graham H Read, Natsuko Miura, Kazutoshi Yamamoto, James B Mitchell, and M Krishna. Alginate hydrogels for three-dimensional culture and real-time monitoring of cancer cell metabolism and radiation response. *International Journal of Radiation Oncology, Biology, Physics*, 99(2):S148, 2017.
- [82] Georgia-Paraskevi Nikoleli, Christina G Siontorou, Dimitrios P Nikolelis, Spyridoula Bratakou, Stephanos Karapetis, and Nikolaos Tzamtzis. Biosensors based on microfluidic devices lab-on-a-chip and microfluidic technology. *Nanotechnology and biosensors*, pages 375–394, 2018.
- [83] Petra S Dittrich and Andreas Manz. Lab-on-a-chip: microfluidics in drug discovery. *Nature reviews Drug discovery*, 5(3):210–218, 2006.
- [84] Colin H Beckwitt, Amanda M Clark, Sarah Wheeler, D Lansing Taylor, Donna B Stolz, Linda Griffith, and Alan Wells. Liver ‘organ on a chip’. *Experimental cell research*, 363(1):15–25, 2018.
- [85] Erika Ferrari, Federico Nebuloni, Marco Rasponi, and Paola Occhetta. Photo and soft lithography for organ-on-chip applications. *Organ-on-a-Chip: Methods and Protocols*, pages 1–19, 2022.
- [86] Massimo Mastrangeli, Sylvie Millet, Janny van den Eijnden-van Raaij, et al. Organ-on-chip in development: Towards a roadmap for organs-on-chip. 2019.
- [87] Chao Ma, Yansong Peng, Hongtong Li, and Weiqiang Chen. Organ-on-a-chip: a new paradigm for drug development. *Trends in pharmacological sciences*, 42(2):119–133, 2021.

- [88] Jaewon Park, Jianrong Li, and Arum Han. Micro-macro hybrid soft-lithography master (mmhsm) fabrication for lab-on-a-chip applications. *Biomedical microdevices*, 12:345–351, 2010.
- [89] Kiran Raj M and Suman Chakraborty. Pdms microfluidics: A mini review. *Journal of Applied Polymer Science*, 137(27):48958, 2020.
- [90] Yu Hongbin, Zhou Guangya, Chau Fook Siong, Wang Shouhua, and Lee Feiwen. Novel polydimethylsiloxane (pdms) based microchannel fabrication method for lab-on-a-chip application. *Sensors and Actuators B: Chemical*, 137(2):754–761, 2009.
- [91] Germán Comina, Anke Suska, and Daniel Filippini. Pdms lab-on-a-chip fabrication using 3d printed templates. *Lab on a Chip*, 14(2):424–430, 2014.
- [92] WF Quirós-Solano, N Gaio, OMJA Stassen, YB Arik, C Silvestri, NCA Van Engeland, A Van der Meer, R Passier, CM Sahlgren, CVC Bouten, et al. Microfabricated tuneable and transferable porous pdms membranes for organs-on-chips. *Scientific reports*, 8(1):13524, 2018.
- [93] Bishal Kumar Nahak, Anshuman Mishra, Subham Preetam, and Ashutosh Tiwari. Advances in organ-on-a-chip materials and devices. *ACS applied bio materials*, 5(8):3576–3607, 2022.
- [94] Anthony Atala. Engineering tissues, organs and cells. *Journal of tissue engineering and regenerative medicine*, 1(2):83–96, 2007.
- [95] Alba Herrero-Gómez, Marc Azagra, and Irene Marco-Rius. A cryopreservation method for bioengineered 3d cell culture models. *Biomedical Materials*, 17(4):045023, 2022.
- [96] Ferran Velasco-Mallorquí, Júlia Rodríguez-Comas, and Javier Ramón-Azcón. Cellulose-based scaffolds enhance pseudoislets formation and functionality. *Biofabrication*, 13(3):035044, 2021.

- [97] Alzhan Baimenov, Dmitriy A Berillo, Stavros G Pouloupoulos, and Vassilis J Inglezakis. A review of cryogels synthesis, characterization and applications on the removal of heavy metals from aqueous solutions. *Advances in colloid and interface science*, 276:102088, 2020.
- [98] Marc Azagra, Elisa Pose, Francesco De Chiara, Martina Perez, Emma Avitabile, Joan-Marc Servitja, Laura Brugnara, Javier Ramon-Azcón, and Irene Marco-Rius. Ammonium quantification in human plasma by proton nuclear magnetic resonance for staging of liver fibrosis in alcohol-related liver disease and nonalcoholic fatty liver disease. *NMR in Biomedicine*, 35(9):e4745, 2022.
- [99] Sadaf G Sepanlou, Saeid Safiri, Catherine Bisignano, Kevin S Ikuta, Shahin Merat, Mehdi Saberifiroozi, Hossein Poustchi, Derrick Tsoi, Danny V Colombara, Amir Abdoli, et al. The global, regional, and national burden of cirrhosis by cause in 195 countries and territories, 1990–2017: a systematic analysis for the global burden of disease study 2017. *The Lancet gastroenterology & hepatology*, 5(3):245–266, 2020.
- [100] Zobair Younossi and Linda Henry. Contribution of alcoholic and nonalcoholic fatty liver disease to the burden of liver-related morbidity and mortality. *Gastroenterology*, 150(8):1778–1785, 2016.
- [101] Youngmin A Lee, Michael C Wallace, and Scott L Friedman. Pathobiology of liver fibrosis: a translational success story. *Gut*, 64(5):830–841, 2015.
- [102] Carolin Lackner and Dina Tiniakos. Fibrosis and alcohol-related liver disease. *Journal of hepatology*, 70(2):294–304, 2019.
- [103] Paul Angulo, David E Kleiner, Sanne Dam-Larsen, Leon A Adams, Einar S Bjornsson, Phunchai Charatcharoenwitthaya, Peter R Mills, Jill C Keach, Heather D Lafferty, Alisha Stahler, et al. Liver fibrosis, but no other histologic features, is associated with long-term outcomes of patients with nonalcoholic fatty liver disease. *Gastroenterology*, 149(2):389–397, 2015.

- [104] ILKe Nalbantoglu and Elizabeth M Brunt. Role of liver biopsy in nonalcoholic fatty liver disease. *World journal of gastroenterology: WJG*, 20(27):9026, 2014.
- [105] European Association for the Study of the Liver et al. Easl-aleh clinical practice guidelines: Non-invasive tests for evaluation of liver disease severity and prognosis. *Journal of hepatology*, 63(1):237–264, 2015.
- [106] Miquel Serra-Burriel, Isabel Graupera, Pere Torán, Maja Thiele, Dominique Roulot, Vincent Wai-Sun Wong, Indra Neil Guha, Núria Fabrellas, Anita Arslanow, Carmen Expósito, et al. Transient elastography for screening of liver fibrosis: cost-effectiveness analysis from six prospective cohorts in europe and asia. *Journal of hepatology*, 71(6):1141–1151, 2019.
- [107] D Haüssinger. Nitrogen metabolism in liver: structural and functional organization and physiological relevance. *Biochemical Journal*, 267(2):281, 1990.
- [108] Debbie L Shawcross, Shabnam S Shabbir, Nicholas J Taylor, and Robin D Hughes. Ammonia and the neutrophil in the pathogenesis of hepatic encephalopathy in cirrhosis. *Hepatology*, 51(3):1062–1069, 2010.
- [109] Robert J Barsotti. Measurement of ammonia in blood. *The Journal of pediatrics*, 138(1):S11–S20, 2001.
- [110] Dominic R Aldridge, Edward J Tranah, and Debbie L Shawcross. Pathogenesis of hepatic encephalopathy: role of ammonia and systemic inflammation. *Journal of clinical and experimental hepatology*, 5:S7–S20, 2015.
- [111] Pegah Golabi, Lynn Gerber, James M Paik, Rati Deshpande, Leyla de Avila, and Zobair M Younossi. Contribution of sarcopenia and physical inactivity to mortality in people with non-alcoholic fatty liver disease. *JHEP Reports*, 2(6):100171, 2020.
- [112] Jessica B Spinelli, Haejin Yoon, Alison E Ringel, Sarah Jeanfavre, Clary B Clish, and Marcia C Haigis. Metabolic recycling of ammonia via glutamate dehydrogenase supports breast cancer biomass. *Science*, 358(6365):941–946, 2017.

- [113] Daniel Juan Herrera, Tim Hutchin, Donna Fullerton, and George Gray. Non-specific interference in the measurement of plasma ammonia: importance of using a sample blank. *Annals of clinical biochemistry*, 47(1):81–83, 2010.
- [114] Dieter Müting, Johanna Heinze, Johanna Reikowski, Günter Betzien, Monica Schwarz, and Felix H Schmidt. Enzymatic ammonia determinations in the blood and cerebrospinal fluid of healthy persons. *Clinica Chimica Acta*, 19(3):391–395, 1968.
- [115] Nora Nikolac, Jelena Omazic, and Ana-Maria Simundic. The evidence based practice for optimal sample quality for ammonia measurement. *Clinical Biochemistry*, 47(12):991–995, 2014.
- [116] Rebecca Y Hodgetts, Alexey S Kiryutin, Peter Nichols, Hoang-Long Du, Jacinta M Bakker, Douglas R Macfarlane, and Alexandr N Simonov. Refining universal procedures for ammonium quantification via rapid 1h nmr analysis for dinitrogen reduction studies. *ACS Energy Letters*, 5(3):736–741, 2020.
- [117] Adam C Nielander, Joshua M McEnaney, Jay A Schwalbe, Jon G Baker, Sarah J Blair, Lei Wang, Jeffrey G Pelton, Suzanne Z Andersen, Kasper Enemark-Rasmussen, Viktor Colic, et al. A versatile method for ammonia detection in a range of relevant electrolytes via direct nuclear magnetic resonance techniques. *Acs Catalysis*, 9(7):5797–5802, 2019.
- [118] Annie Robert and Olivier Chazouilleres. Prothrombin time in liver failure: time, ratio, activity percentage, or international normalized ratio. *Hepatology*, 24(6):1392–1394, 1996.
- [119] Shanshan Sun, Mengxia Jin, Xia Zhou, Jinghua Ni, Xiangju Jin, Hongyue Liu, and Yinghong Wang. The application of quantitative 1h-nmr for the determination of orlistat in tablets. *Molecules*, 22(9):1517, 2017.
- [120] Keith E Whitener Jr, Michael Frunzi, Sho-ichi Iwamatsu, Shizuaki Murata, R James Cross, and Martin Saunders. Putting ammonia into a chemically opened fullerene. *Journal of the American Chemical Society*, 130(42):13996–13999, 2008.

- [121] Danila A Barskiy, Michael CD Tayler, Irene Marco-Rius, John Kurhanewicz, Daniel B Vigneron, Sevil Cikrikci, Ayca Aydogdu, Moritz Reh, Andrey N Pravdivtsev, Jan-Bernd Hövener, et al. Zero-field nuclear magnetic resonance of chemically exchanging systems. *Nature communications*, 10(1):3002, 2019.
- [122] Joscilin Mathew, Parvathy Sankar, and Matthew Varacallo. Physiology, blood plasma. 2018.
- [123] Ina Nemet, Lidija Varga-Defterdarović, and Zdenka Turk. Preparation and quantification of methylglyoxal in human plasma using reverse-phase high-performance liquid chromatography. *Clinical biochemistry*, 37(10):875–881, 2004.
- [124] Mohammed Bhogadia, Mark Edgar, Kayleigh Hunwin, Georgina Page, and Martin Grootveld. Detection and quantification of ammonia as the ammonium cation in human saliva by 1h nmr: A promising probe for health status monitoring, with special reference to cancer. *Metabolites*, 13(7):792, 2023.
- [125] Brian A Aguado, Joseph C Grim, Adrienne M Rosales, Jana J Watson-Capps, and Kristi S Anseth. Engineering precision biomaterials for personalized medicine. *Science translational medicine*, 10(424):eaam8645, 2018.
- [126] Cigdem Bilici, Mine Altunbek, Ferdows Afghah, Asena G Tatar, and Bahattin Koç. Embedded 3d printing of cryogel-based scaffolds. *ACS Biomaterials Science & Engineering*, 2023.
- [127] Ben Newland and Katherine R Long. Cryogel scaffolds: soft and easy to use tools for neural tissue culture. *Neural Regeneration Research*, 17(9):1981, 2022.
- [128] Nasim Annabi, Jason W Nichol, Xia Zhong, Chengdong Ji, Sandeep Koshy, Ali Khademhosseini, and Fariba Dehghani. Controlling the porosity and microarchitecture of hydrogels for tissue engineering. *Tissue Engineering Part B: Reviews*, 16(4):371–383, 2010.
- [129] Christopher D Spicer. Hydrogel scaffolds for tissue engineering: The importance of polymer choice. *Polymer Chemistry*, 11(2):184–219, 2020.

- [130] Timothy MA Henderson, Katharina Ladewig, David N Haylock, Keith M McLean, and Andrea J O'Connor. Cryogels for biomedical applications. *Journal of Materials Chemistry B*, 1(21):2682–2695, 2013.
- [131] Kan Yue, Grissel Trujillo-de Santiago, Mario Moisés Alvarez, Ali Tamayol, Nasim Annabi, and Ali Khademhosseini. Synthesis, properties, and biomedical applications of gelatin methacryloyl (gelma) hydrogels. *Biomaterials*, 73:254–271, 2015.
- [132] Weikang Hu, Zijian Wang, Yu Xiao, Shengmin Zhang, and Jianglin Wang. Advances in crosslinking strategies of biomedical hydrogels. *Biomaterials science*, 7(3):843–855, 2019.
- [133] Reza Foudazi, Ryan Zowada, Ica Manas-Zloczower, and Donald L Feke. Porous hydrogels: Present challenges and future opportunities. *Langmuir*, 39(6):2092–2111, 2023.
- [134] Louise Griveau, Marianne Lafont, Héloïse Le Goff, Clémence Drouglazet, Baptiste Robbiani, Aurore Berthier, Dominique Sigauco-Roussel, Najma Latif, Catherine Le Visage, Vincent Gache, et al. Design and characterization of an in vivo injectable hydrogel with effervescently generated porosity for regenerative medicine applications. *Acta Biomaterialia*, 140:324–337, 2022.
- [135] Fernando Yanez, Jose L Gomez-Amoza, Beatriz Magarinos, Angel Concheiro, and Carmen Alvarez-Lorenzo. Hydrogels porosity and bacteria penetration: Where is the pore size threshold? *Journal of Membrane Science*, 365(1-2):248–255, 2010.
- [136] Min Kyung Lee, Max H Rich, Kwanghyun Baek, Jonghwi Lee, and Hyunjoon Kong. Bioinspired tuning of hydrogel permeability-rigidity dependency for 3d cell culture. *Scientific reports*, 5(1):8948, 2015.
- [137] Rui Cao, Efstathios Avgoustiniatos, Klearchos Papas, Paul de Vos, and Jonathan RT Lakey. Mathematical predictions of oxygen availability in micro-and macro-encapsulated human and porcine pancreatic islets. *Journal of Biomedical Materials Research Part B: Applied Biomaterials*, 108(2):343–352, 2020.

- [138] Ashley L Farris, Alexandra N Rindone, and Warren L Grayson. Oxygen delivering biomaterials for tissue engineering. *Journal of materials chemistry B*, 4(20):3422–3432, 2016.
- [139] Mazaher Gholipourmalekabadi, Susan Zhao, Benjamin S Harrison, Masoud Mozafari, and Alexander M Seifalian. Oxygen-generating biomaterials: a new, viable paradigm for tissue engineering? *Trends in biotechnology*, 34(12):1010–1021, 2016.
- [140] Vladimir M Gun’ko, Irina N Savina, and Sergey V Mikhalovsky. Cryogels: Morphological, structural and adsorption characterisation. *Advances in colloid and interface science*, 187:1–46, 2013.
- [141] Siew-Leng Loo, Lía Vásquez, Muhammad Zahid, Federica Costantino, Athanasia Athanassiou, and Despina Fragouli. 3d photothermal cryogels for solar-driven desalination. *ACS Applied Materials & Interfaces*, 13(26):30542–30555, 2021.
- [142] Inseon Kim, Seunghun S Lee, Sunghoon Bae, Hoyon Lee, and Nathaniel S Hwang. Heparin functionalized injectable cryogel with rapid shape-recovery property for neovascularization. *Biomacromolecules*, 19(6):2257–2269, 2018.
- [143] Thai Duong Luong, Mohamed Zoughaib, Ruslan Garifullin, Svetlana Kuznetsova, Mustafa O Guler, and Timur I Abdullin. In situ functionalization of poly (hydroxyethyl methacrylate) cryogels with oligopeptides via β -cyclodextrin–adamantane complexation for studying cell-instructive peptide environment. *ACS applied bio materials*, 3(2):1116–1128, 2019.
- [144] Laura Martínez-Vidal, Valentina Magno, Petra B Welzel, Jens Friedrichs, Martin Bornhäuser, and Carsten Werner. Combining cryogel architecture and macromolecular crowding-enhanced extracellular matrix cues to mimic the bone marrow niche. *Macromolecular Chemistry and Physics*, 224(1):2200348, 2023.
- [145] Paul Tomlins, Paul Grant, Sergey Mikhalovsky, Stuart James, and Lyuba Mikhalovska. Measurement of pore size and porosity of tissue scaffolds. *Journal of ASTM International*, 1(1):JAI11510, 2004.

- [146] Mark Borden, SF El-Amin, Mohamed Attawia, and Cato T Laurencin. Structural and human cellular assessment of a novel microsphere-based tissue engineered scaffold for bone repair. *Biomaterials*, 24(4):597–609, 2003.
- [147] Hamed Lamei Ramandi, Peyman Mostaghimi, Ryan T Armstrong, Mohammad Saadatfar, and W Val Pinczewski. Porosity and permeability characterization of coal: a micro-computed tomography study. *International Journal of Coal Geology*, 154:57–68, 2016.
- [148] Erik L Ritman. Micro-computed tomography—current status and developments. *Annu. Rev. Biomed. Eng.*, 6:185–208, 2004.
- [149] YW Lui, ER Tang, AM Allmendinger, and V Spektor. Evaluation of ct perfusion in the setting of cerebral ischemia: patterns and pitfalls. *American journal of neuroradiology*, 31(9):1552–1563, 2010.
- [150] Eric N Landis and Denis T Keane. X-ray microtomography. *Materials characterization*, 61(12):1305–1316, 2010.
- [151] Hui Kian Wong, Chee Ren Ivan Lam, Feng Wen, Seow Khoon Mark Chong, Nguan Soon Tan, Chan Jerry, Mintu Pal, and Lay Poh Tan. Novel method to improve vascularization of tissue engineered constructs with biodegradable fibers. *Biofabrication*, 8(1):015004, 2016.
- [152] Aung Than, Chenghao Liu, Hao Chang, Phan Khanh Duong, Chui Ming Gemmy Cheung, Chenjie Xu, Xiaomeng Wang, and Peng Chen. Self-implantable double-layered micro-drug-reservoirs for efficient and controlled ocular drug delivery. *Nature communications*, 9(1):4433, 2018.
- [153] Shweta Tripathi, Denis Champagne, and Nathalie Tufenkji. Transport behavior of selected nanoparticles with different surface coatings in granular porous media coated with pseudomonas aeruginosa biofilm. *Environmental science & technology*, 46(13):6942–6949, 2012.
- [154] Moritz Waldecker, Stefan Rues, Peter Rammelsberg, and Wolfgang Bömicke. Accuracy of complete-arch intraoral scans based on confocal microscopy versus opti-

- cal triangulation: a comparative in vitro study. *The Journal of prosthetic dentistry*, 126(3):414–420, 2021.
- [155] MA Osborne, S Balasubramanian, WS Furey, and D Klenerman. Optically biased diffusion of single molecules studied by confocal fluorescence microscopy. *The Journal of Physical Chemistry B*, 102(17):3160–3167, 1998.
- [156] Alexander P Demchenko. Photobleaching of organic fluorophores: quantitative characterization, mechanisms, protection. *Methods and applications in fluorescence*, 8(2):022001, 2020.
- [157] Nectarios Klonis, Melanie Rug, Ian Harper, Mark Wickham, Alan Cowman, and Leann Tilley. Fluorescence photobleaching analysis for the study of cellular dynamics. *European Biophysics Journal*, 31:36–51, 2002.
- [158] Won C Bae, Shantanu Patil, Reni Biswas, Shihong Li, Eric Y Chang, Sheronda Statum, Darryl D D’Lima, Christine B Chung, and Jiang Du. Magnetic resonance imaging assessed cortical porosity is highly correlated with μ ct porosity. *Bone*, 66:56–61, 2014.
- [159] DML Cooper, CE Kawalilak, K Harrison, BD Johnston, and JD Johnston. Cortical bone porosity: what is it, why is it important, and how can we detect it? *Current osteoporosis reports*, 14:187–198, 2016.
- [160] Won C Bae, Peter C Chen, Christine B Chung, Koichi Masuda, Darryl D’Lima, and Jiang Du. Quantitative ultrashort echo time (ute) mri of human cortical bone: correlation with porosity and biomechanical properties. *Journal of Bone and Mineral Research*, 27(4):848–857, 2012.
- [161] Mara Camaiti, Villiam Bortolotti, and Paola Fantazzini. Stone porosity, wettability changes and other features detected by mri and nmr relaxometry: a more than 15-year study. *Magnetic Resonance in Chemistry*, 53(1):34–47, 2015.
- [162] Haitao Wang, Zengmin Lun, Chengyuan Lv, Dongjiang Lang, Bingyu Ji, Ming Luo, Weiyi Pan, Rui Wang, and Kai Gong. Measurement and visualization of tight

- rock exposed to co2 using nmr relaxometry and mri. *Scientific reports*, 7(1):44354, 2017.
- [163] R Adam Horch, Daniel F Gochberg, Jeffrey S Nyman, and Mark D Does. Clinically compatible mri strategies for discriminating bound and pore water in cortical bone. *Magnetic resonance in medicine*, 68(6):1774–1784, 2012.
- [164] Rebecca M Steele, Jean-Pierre Korb, Gianni Ferrante, and Salvatore Bubici. New applications and perspectives of fast field cycling nmr relaxometry. *Magnetic Resonance in Chemistry*, 54(6):502–509, 2016.
- [165] Sjoerd Hak, Honorius MHF Sanders, Prashant Agrawal, Sander Langereis, Holger Gröll, Henk M Keizer, Francesca Arena, Enzo Terreno, Gustav J Strijkers, and Klaas Nicolay. A high relaxivity gd (iii) dota-dspe-based liposomal contrast agent for magnetic resonance imaging. *European Journal of Pharmaceutics and Biopharmaceutics*, 72(2):397–404, 2009.
- [166] Frank G Shellock and Emanuel Kanal. Safety of magnetic resonance imaging contrast agents. *Journal of Magnetic Resonance Imaging: An Official Journal of the International Society for Magnetic Resonance in Medicine*, 10(3):477–484, 1999.
- [167] Andreas Pohlmeier, Dagmar van Dusschoten, Lutz Weihermüller, Ulrich Schurr, and Harry Vereecken. Imaging water fluxes in porous media by magnetic resonance imaging using d2o as a tracer. *Magnetic resonance imaging*, 27(2):285–292, 2009.
- [168] Fu-Nien Wang, Shin-Lei Peng, Chin-Tien Lu, Hsu-Hsia Peng, and Tzu-Chen Yeh. Water signal attenuation by d2o infusion as a novel contrast mechanism for 1h perfusion mri. *NMR in Biomedicine*, 26(6):692–698, 2013.
- [169] Lin Chen, Jing Liu, Chengyan Chu, Zheng Han, Nirhbay Yadav, Jiadi Xu, Renyuan Bai, Verena Staedtke, Monica Pearl, Piotr Walczak, et al. Deuterium oxide as a contrast medium for real-time mri-guided endovascular neurointervention. *Theranostics*, 11(13):6240, 2021.

- [170] Dong Qin, Younan Xia, and George M Whitesides. Soft lithography for micro-and nanoscale patterning. *Nature protocols*, 5(3):491, 2010.
- [171] Jose Yeste, Marc Azagra, Maria A Ortega, Alejandro Portela, Gergő Matajsz, Alba Herrero-Gómez, Yaewon Kim, Renuka Sriram, John Kurhanewicz, Daniel B Vigneron, et al. Parallel detection of chemical reactions in a microfluidic platform using hyperpolarized nuclear magnetic resonance. *Lab on a Chip*, 23(23):4950–4958, 2023.
- [172] Tarun Garg, Onkar Singh, Saahil Arora, and RSR Murthy. Scaffold: a novel carrier for cell and drug delivery. *Critical Reviews™ in Therapeutic Drug Carrier Systems*, 29(1), 2012.
- [173] Angela R Dixon, Shrinidhi Rajan, Chuan-Hsien Kuo, Tom Bersano, Rachel Wold, Nobuyuki Futai, Shuichi Takayama, and Geeta Mehta. Microfluidic device capable of medium recirculation for non-adherent cell culture. *Biomicrofluidics*, 8(1), 2014.
- [174] James Eills, Marc Azagra, David Gómez-Cabeza, Michael CD Tayler, and Irene Marco-Rius. Polarization losses from the nonadiabatic passage of hyperpolarized solutions through metallic components. *Journal of Magnetic Resonance Open*, 18:100144, 2024.
- [175] Sarah J Nelson, John Kurhanewicz, Daniel B Vigneron, Peder EZ Larson, Andrea L Harzstark, Marcus Ferrone, Mark Van Criekinge, Jose W Chang, Robert Bok, Ilwoo Park, et al. Metabolic imaging of patients with prostate cancer using hyperpolarized [1-¹³C] pyruvate. *Sci. Transl. Med.*, 5(198):198ra108–198ra108, 2013.
- [176] Eleonora Cavallari, Carla Carrera, Matteo Sorge, Gisèle Bonne, Antoine Muchir, Silvio Aime, and Francesca Reineri. The ¹³C hyperpolarized pyruvate generated by parahydrogen detects the response of the heart to altered metabolism in real time. *Scientific reports*, 8(1):1–9, 2018.
- [177] Martin Gierse, Luca Nagel, Michael Keim, Sebastian Lucas, Tobias Speidel, Tobias Lobmeyer, Gordon Winter, Felix Josten, Senay Karaali, Maximilian Fellermann,

- et al. Parahydrogen-polarized fumarate for preclinical in vivo metabolic magnetic resonance imaging. *Journal of the American Chemical Society*, 2023.
- [178] Gregory L Olsen, Or Szekely, Borja Mateos, Pavel Kadeřávek, Fabien Ferrage, Robert Konrat, Roberta Pierattelli, Isabella C Felli, Geoffrey Bodenhausen, Dennis Kurzbach, et al. Sensitivity-enhanced three-dimensional and carbon-detected two-dimensional nmr of proteins using hyperpolarized water. *Journal of Biomolecular NMR*, 74(2-3):161–171, 2020.
- [179] Christian Hilty, Dennis Kurzbach, and Lucio Frydman. Hyperpolarized water as universal sensitivity booster in biomolecular nmr. *Nature protocols*, 17(7):1621–1657, 2022.
- [180] Ratnamala Mandal, Pierce Pham, and Christian Hilty. Characterization of protein–ligand interactions by sabre. *Chemical science*, 12(39):12950–12958, 2021.
- [181] Ratnamala Mandal, Pierce Pham, and Christian Hilty. Screening of protein–ligand binding using a sabre hyperpolarized reporter. *Analytical Chemistry*, 94(32):11375–11381, 2022.
- [182] Bulat Gizatullin, Carlos Mattea, and Siegfried Stapf. Field-cycling nmr and dnp—a friendship with benefits. *Journal of Magnetic Resonance*, 322:106851, 2021.
- [183] Youngbok Lee, Gyu Seong Heo, Haifeng Zeng, Karen L Wooley, and Christian Hilty. Detection of living anionic species in polymerization reactions using hyperpolarized nmr. *Journal of the American Chemical Society*, 135(12):4636–4639, 2013.
- [184] Ekaterina V Pokochueva, Dudari B Burueva, Oleg G Salnikov, and Igor V Koptuyug. Heterogeneous catalysis and parahydrogen-induced polarization. *ChemPhysChem*, 22(14):1421–1440, 2021.
- [185] Weiyu Wang, Qiang Wang, Jun Xu, and Feng Deng. Understanding heterogeneous catalytic hydrogenation by parahydrogen-induced polarization nmr spectroscopy. *ACS Catalysis*, 13:3501–3519, 2023.

- [186] Alexandre Guthertz, Markus Leutzsch, Lawrence M Wolf, Puneet Gupta, Stephan M Rummelt, Richard Goddard, Christophe Farès, Walter Thiel, and Alois Fürstner. Half-sandwich ruthenium carbene complexes link trans-hydrogenation and gem-hydrogenation of internal alkynes. *Journal of the American Chemical Society*, 140(8):3156–3169, 2018.
- [187] Wenlong Jiang, Qiwei Peng, Huijun Sun, Qi Zhang, Chengda Huang, Shuohui Cao, Xinchang Wang, and Zhong Chen. Determining the enantioselectivity of asymmetric hydrogenation through parahydrogen-induced hyperpolarization. *The Journal of chemical physics*, 155(16):161101, 2021.
- [188] Irene Marco-Rius and Arnaud Comment. In vivo hyperpolarized ^{13}C mrs and mri applications. *Handbook of High Field Dynamic Nuclear Polarization*, page 405, 2019.
- [189] Bogdan A. Rodin, James Eills, Román Picazo-Frutos, Kirill F. Sheberstov, Dmitry Budker, and Konstantin L. Ivanov. Constant-adiabaticity ultralow magnetic field manipulations of parahydrogen-induced polarization: application to an aa'x spin system. *Phys. Chem. Chem. Phys.*, 23:7125–7134, 2021.
- [190] Benno Meier, Jean-Nicolas Dumez, Gabriele Stevanato, Joseph T Hill-Cousins, Soumya Singha Roy, Par Hakansson, Salvatore Mamone, Richard CD Brown, Giuseppe Pileio, and Malcolm H Levitt. Long-lived nuclear spin states in methyl groups and quantum-rotor-induced polarization. *Journal of the American Chemical Society*, 135(50):18746–18749, 2013.
- [191] Alexey S Kiryutin, Bogdan A Rodin, Alexandra V Yurkovskaya, Konstantin L Ivanov, Dennis Kurzbach, Sami Jannin, David Guarin, Daniel Abergel, and Geoffrey Bodenhausen. Transport of hyperpolarized samples in dissolution-dnp experiments. *Physical Chemistry Chemical Physics*, 21(25):13696–13705, 2019.
- [192] Morgan Ceillier, Olivier Cala, Théo El Daraï, Samuel F Cousin, Quentin Stern, Sylvie Guibert, Stuart J Elliott, Aurélien Bornet, Basile Vuichoud, Jonas Milani, et al. An automated system for fast transfer and injection of hyperpolarized solutions. *Journal of Magnetic Resonance Open*, 8:100017, 2021.

- [193] Talia Harris, Or Szekely, and Lucio Frydman. On the potential of hyperpolarized water in biomolecular nmr studies. *The Journal of Physical Chemistry B*, 118(12):3281–3290, 2014.
- [194] Pierce Pham, Ratnamala Mandal, Chang Qi, and Christian Hilty. Interfacing liquid state hyperpolarization methods with nmr instrumentation. *Journal of magnetic resonance open*, 10:100052, 2022.
- [195] Marcin Krajewski, Patrick Wespi, Julia Busch, Lukas Wissmann, Grzegorz Kwiatkowski, Jonas Steinhauser, Michael Batel, Matthias Ernst, and Sebastian Kozerke. A multisample dissolution dynamic nuclear polarization system for serial injections in small animals. *Magnetic resonance in medicine*, 77(2):904–910, 2017.
- [196] Eleonora Cavallari, Carla Carrera, Silvio Aime, and Francesca Reineri. Studies to enhance the hyperpolarization level in phip-sah-produced c13-pyruvate. *Journal of Magnetic Resonance*, 289:12–17, 2018.
- [197] Jonas Milani, Basile Vuichoud, Aurélien Bornet, Pascal Miéville, Roger Mottier, Sami Jannin, and Geoffrey Bodenhausen. A magnetic tunnel to shelter hyperpolarized fluids. *Review of Scientific Instruments*, 86(2):024101, 2015.
- [198] Fabian Jähnig, Grzegorz Kwiatkowski, and Matthias Ernst. Conceptual and instrumental progress in dissolution dnp. *Journal of Magnetic Resonance*, 264:22–29, 2016.
- [199] Arthur C Pinon, Andrea Capozzi, and Jan Henrik Ardenkjær-Larsen. Hyperpolarized water through dissolution dynamic nuclear polarization with uv-generated radicals. *Communications Chemistry*, 3(1):57, 2020.
- [200] Karel Kouřil, Hana Kouřilová, Samuel Bartram, Malcolm H Levitt, and Benno Meier. Scalable dissolution-dynamic nuclear polarization with rapid transfer of a polarized solid. *Nature communications*, 10(1):1733, 2019.

- [201] N Chattergoon, F Martínez-Santesteban, WB Handler, Jan Henrik Ardenkjær-Larsen, and TJ Scholl. Field dependence of t_1 for hyperpolarized [1- ^{13}C] pyruvate. *Contrast media & molecular imaging*, 8(1):57–62, 2013.
- [202] Bulat Gizatullin, Carlos Mattea, and Siegfried Stapf. Hyperpolarization by dnp and molecular dynamics: Eliminating the radical contribution in nmr relaxation studies. *The Journal of Physical Chemistry B*, 123(46):9963–9970, 2019.
- [203] Hong Shang, Timothy Skloss, Cornelius von Morze, Lucas Carvajal, Mark Van Criekinge, Eugene Milshteyn, Peder E. Z. Larson, Ralph E. Hurd, and Daniel B. Vigneron. Handheld electromagnet carrier for transfer of hyperpolarized carbon-13 samples. *Magnetic Resonance in Medicine*, 75(2):917–922, March 2015.
- [204] Kostas Mouloudakis, Sven Bodenstedt, Marc Azagra, Morgan W. Mitchell, Irene Marco-Rius, and Michael C. D. Tayler. Real-time polarimetry of hyperpolarized ^{13}C nuclear spins using an atomic magnetometer. *The Journal of Physical Chemistry Letters*, 14(5):1192–1197, January 2023.
- [205] Michael CD Tayler, Irene Marco-Rius, Mikko I Kettunen, Kevin M Brindle, Malcolm H Levitt, and Giuseppe Pileio. Direct enhancement of nuclear singlet order by dynamic nuclear polarization. *Journal of the American Chemical Society*, 134(18):7668–7671, 2012.
- [206] Irene Marco-Rius, Michael CD Tayler, Mikko I Kettunen, Timothy J Larkin, Kerstin N Timm, Eva M Serrao, Tiago B Rodrigues, Giuseppe Pileio, Jan Henrik Ardenkjær-Larsen, Malcolm H Levitt, et al. Hyperpolarized singlet lifetimes of pyruvate in human blood and in the mouse. *NMR in Biomedicine*, 26(12):1696–1704, 2013.
- [207] Wissam Iali, Soumya S Roy, Ben J Tickner, Fadi Ahwal, Aneurin J Kennerley, and Simon B Duckett. Hyperpolarising pyruvate through signal amplification by reversible exchange (sabre). *Angewandte Chemie*, 131(30):10377–10381, 2019.
- [208] Malcolm H Levitt. Singlet nuclear magnetic resonance. *Annual review of physical chemistry*, 63:89–105, 2012.

- [209] Giuseppe Pileio. Singlet nmr methodology in two-spin-1/2 systems. *Progress in nuclear magnetic resonance spectroscopy*, 98:1–19, 2017.
- [210] <https://github.com/MichaelTayler/RM3100-XIA0>.
- [211] Michael CD Tayler, Jordan Ward-Williams, and Lynn F Gladden. Ultralow-field nuclear magnetic resonance of liquids confined in ferromagnetic and paramagnetic materials. *Applied Physics Letters*, 115(7), 2019.
- [212] <https://www.industrialheating.com/articles/89463-hypodermic-the-hole-needle>. accessed: 30/08/23.
- [213] Christopher P Bidinosti, Jamal Choukeife, Geneviève Tastevin, P-J Nacher, and A Vignaud. Mri of the lung using hyperpolarized ^3He at very low magnetic field (3 mt). *Magnetic Resonance Materials in Physics, Biology and Medicine*, 16:255–258, 2004.
- [214] T O’Reilly, WM Teeuwisse, and AG Webb. Three-dimensional mri in a homogeneous 27 cm diameter bore halfbach array magnet. *Journal of Magnetic Resonance*, 307:106578, 2019.
- [215] Lionel M Broche, P James Ross, Gareth R Davies, Mary-Joan MacLeod, and David J Lurie. A whole-body fast field-cycling scanner for clinical molecular imaging studies. *Scientific Reports*, 9(1):1–11, 2019.
- [216] Yucheng He, Wei He, Liang Tan, Fangge Chen, Fanqin Meng, Hua Feng, and Zheng Xu. Use of 2.1 mhz mri scanner for brain imaging and its preliminary results in stroke. *Journal of Magnetic Resonance*, 319:106829, 2020.
- [217] Mathieu Sarracanie and Najat Salameh. Low-field mri: how low can we go? a fresh view on an old debate. *Frontiers in Physics*, 8:172, 2020.
- [218] Yilong Liu, Alex TL Leong, Yujiao Zhao, Linfang Xiao, Henry KF Mak, Anderson Chun On Tsang, Gary KK Lau, Gilberto KK Leung, and Ed X Wu. A low-cost and shielding-free ultra-low-field brain mri scanner. *Nature communications*, 12(1):7238, 2021.

- [219] Thomas Campbell Arnold, Colbey W Freeman, Brian Litt, and Joel M Stein. Low-field mri: Clinical promise and challenges. *Journal of Magnetic Resonance Imaging*, 57(1):25–44, 2023.
- [220] Kai Buckenmaier, Matthias Rudolph, Paul Fehling, Theodor Steffen, Christoph Back, Rebekka Bernard, Rolf Pohmann, Johannes Bernarding, Reinhold Kleiner, Dieter Koelle, et al. Mutual benefit achieved by combining ultralow-field magnetic resonance and hyperpolarizing techniques. *Review of Scientific Instruments*, 89(12):125103, 2018.
- [221] Seong-Joo Lee, Keunhong Jeong, Jeong Hyun Shim, Hyun Joon Lee, Sein Min, Heelim Chae, Sung Keon Namgoong, and Kiwoong Kim. Squid-based ultralow-field mri of a hyperpolarized material using signal amplification by reversible exchange. *Scientific Reports*, 9(1):12422, 2019.
- [222] Martin Grootveld, Benita Percival, Miles Gibson, Yasan Osman, Mark Edgar, Marco Molinari, Melissa L Mather, Federico Casanova, and Philippe B Wilson. Progress in low-field benchtop nmr spectroscopy in chemical and biochemical analysis. *Analytica chimica acta*, 1067:11–30, 2019.
- [223] Hyo-Yeon Yu, Sangki Myoung, and Sangdoo Ahn. Recent applications of benchtop nuclear magnetic resonance spectroscopy. *Magnetochemistry*, 7(9):121, 2021.
- [224] J Beau W Webber. A review of the use of simple time-domain nmr/mri for material-science: Time-domain benchtop and mobile nmr/mri for liquid and solid material science, and nano-to micro-pore-size measurement. *SN Applied Sciences*, 3(10):809, 2021.
- [225] Yejin Lee, Yevgen Matviychuk, and Daniel J Holland. Quantitative analysis using external standards with a benchtop nmr spectrometer. *Journal of Magnetic Resonance*, 320:106826, 2020.
- [226] José G Napolitano, Cassie Yang, Breanna Conklin, Yan He, and Jessica L Ochoa. Toward the development of rapid, automated identification tests for neat organic

- liquids using benchtop nmr instrumentation. *Analytical Chemistry*, 94(46):16095–16102, 2022.
- [227] Koki Hara, Shunji Yamada, Eisuke Chikayama, and Jun Kikuchi. Parameter visualization of benchtop nuclear magnetic resonance spectra toward food process monitoring. *Processes*, 10(7):1264, 2022.
- [228] Anne Friebel, Erik von Harbou, Kerstin Munnemann, and Hans Hasse. Reaction monitoring by benchtop nmr spectroscopy using a novel stationary flow reactor setup. *Industrial & Engineering Chemistry Research*, 58(39):18125–18133, 2019.
- [229] Justine Leenders, Martin Grootveld, Benita Percival, Miles Gibson, Federico Casanova, and Philippe B Wilson. Benchtop low-frequency 60 mhz nmr analysis of urine: A comparative metabolomics investigation. *Metabolites*, 10(4):155, 2020.
- [230] Seyma Alcicek, Erik Van Dyke, Jingyan Xu, Szymon Pustelny, and Danila A Barskiy. ¹³c and ¹⁵n benchtop nmr detection of metabolites via relayed hyperpolarization. *Chemistry-Methods*, page e202200075, 2023.
- [231] Roan Fraser, Floris PJT Rutjes, Martin C Feiters, and Marco Tessari. Analysis of complex mixtures by chemosensing nmr using para-hydrogen-induced hyperpolarization. *Accounts of Chemical Research*, 55(13):1832–1844, 2022.
- [232] Michael Salerno, Talissa A Altes, John P Mugler III, Masashi Nakatsu, Hiroto Hatabu, and Eduard E de Lange. Hyperpolarized noble gas mr imaging of the lung: potential clinical applications. *European journal of radiology*, 40(1):33–44, 2001.
- [233] KOLE Golman, Lars E Olsson, O Axelsson, S Mansson, Magnus Karlsson, and JS Petersson. Molecular imaging using hyperpolarized ¹³c. *The British journal of radiology*, 76(suppl_2):S118–S127, 2003.
- [234] Thorsten Jonischkeit and Klaus Woelk. Hydrogen induced polarization–nuclear-spin hyperpolarization in catalytic hydrogenations without the enrichment of para- or orthohydrogen. *Advanced Synthesis & Catalysis*, 346(8):960–969, 2004.

- [235] James Eills, William Hale, Manvendra Sharma, Matheus Rossetto, Malcolm H Levitt, and Marcel Utz. High-resolution nuclear magnetic resonance spectroscopy with picomole sensitivity by hyperpolarization on a chip. *J. Am. Chem. Soc.*, 141(25):9955–9963, 2019.
- [236] Ricardo Jiménez-Martínez, Daniel J Kennedy, Michael Rosenbluh, Elizabeth A Donley, Svenja Knappe, Scott J Seltzer, Hattie L Ring, Vikram S Bajaj, and John Kitching. Optical hyperpolarization and nmr detection of ^{129}Xe on a microfluidic chip. *Nature communications*, 5(1):3908, 2014.
- [237] M Victoria Gomez, Sander Baas, and Aldrik H Velders. Multinuclear ^1d and ^2d nmr with ^{19}f -photo-cidnp hyperpolarization in a microfluidic chip with untuned microcoil. *Nature Communications*, 14(1):3885, 2023.
- [238] Michael CD Tayler and Sven Bodenstedt. Nmrduino: A modular, open-source, low-field magnetic resonance platform. *Journal of Magnetic Resonance*, 362:107665, 2024.
- [239] Crystal Harrison, Chendong Yang, Ashish Jindal, Ralph J DeBerardinis, MA Hooshyar, Matthew Merritt, A Dean Sherry, and Craig R Malloy. Comparison of kinetic models for analysis of pyruvate-to-lactate exchange by hyperpolarized ^{13}c nmr. *NMR in Biomedicine*, 25(11):1286–1294, 2012.
- [240] Naeim Bahrami, Christine Leon Swisher, Cornelius Von Morze, Daniel B Vigneron, and Peder EZ Larson. Kinetic and perfusion modeling of hyperpolarized ^{13}c pyruvate and urea in cancer with arbitrary rf flip angles. *Quantitative imaging in medicine and surgery*, 4(1):24, 2014.
- [241] Martin Grashei, Philipp Biechl, Franz Schilling, and Angela M Otto. Conversion of hyperpolarized $[1-^{13}\text{c}]$ pyruvate in breast cancer cells depends on their malignancy, metabolic program and nutrient microenvironment. *Cancers*, 14(7):1845, 2022.
- [242] Talia Harris, Galit Eliyahu, Lucio Frydman, and Hadassa Degani. Kinetics of hyperpolarized $^{13}\text{c}1$ -pyruvate transport and metabolism in living human breast can-

- cer cells. *Proceedings of the National Academy of Sciences*, 106(43):18131–18136, 2009.
- [243] Isaac S Chan and Geoffrey S Ginsburg. Personalized medicine: progress and promise. *Annual review of genomics and human genetics*, 12:217–244, 2011.
- [244] Laura H Goetz and Nicholas J Schork. Personalized medicine: motivation, challenges, and progress. *Fertility and sterility*, 109(6):952–963, 2018.
- [245] Michele Simonato, Amy R Brooks-Kayal, Jerome Engel, Aristeia S Galanopoulou, Frances E Jensen, Solomon L Moshé, Terence J O’Brien, Asla Pitkanen, Karen S Wilcox, and Jacqueline A French. The challenge and promise of anti-epileptic therapy development in animal models. *The Lancet Neurology*, 13(9):949–960, 2014.
- [246] Isra Marei, Tala Abu Samaan, Maryam Ali Al-Quradaghi, Asmaa A Farah, Shamin Hayat Mahmud, Hong Ding, and Chris R Triggler. 3d tissue-engineered vascular drug screening platforms: promise and considerations. *Frontiers in cardiovascular medicine*, 9:847554, 2022.
- [247] Donald E Ingber. Human organs-on-chips for disease modelling, drug development and personalized medicine. *Nature Reviews Genetics*, 23(8):467–491, 2022.
- [248] Bailey C Buchanan and Jeong-Yeol Yoon. Microscopic imaging methods for organ-on-a-chip platforms. *Micromachines*, 13(2):328, 2022.
- [249] Yongchao Su, Loren Andreas, and Robert G Griffin. Magic angle spinning nmr of proteins: high-frequency dynamic nuclear polarization and 1h detection. *Annual review of biochemistry*, 84:465–497, 2015.
- [250] Susana Ros, Alan J Wright, Alejandra Bruna, Carlos Caldas, and Kevin M Brindle. Metabolic imaging with hyperpolarized [1-13c] pyruvate in patient-derived pre-clinical mouse models of breast cancer. *STAR protocols*, 2(3):100608, 2021.
- [251] Hannah Lees, Micaela Millan, Fayyaz Ahamed, Roozbeh Eskandari, Kristin L Granlund, Sangmoo Jeong, and Kayvan R Keshari. Multi-sample measurement of

- hyperpolarized pyruvate-to-lactate flux in melanoma cells. *NMR in Biomedicine*, 34(3):e4447, 2021.
- [252] James Eills, William Hale, Manvendra Sharma, Matheus Rossetto, Malcolm H Levitt, and Marcel Utz. High-resolution nuclear magnetic resonance spectroscopy with picomole sensitivity by hyperpolarization on a chip. *Journal of the American Chemical Society*, 141(25):9955–9963, 2019.
- [253] Jaehyuk Lee, Marc S Ramirez, Christopher M Walker, Yunyun Chen, Stacey Yi, Vlad C Sandulache, Stephen Y Lai, and James A Bankson. High-throughput hyperpolarized ^{13}C metabolic investigations using a multi-channel acquisition system. *Journal of magnetic resonance*, 260:20–27, 2015.
- [254] Yaewon Kim, Mengxiao Liu, and Christian Hilty. Determination of binding affinities using hyperpolarized nmr with simultaneous 4-channel detection. *Journal of Magnetic Resonance*, 295:80–86, 2018.
- [255] Sivic: open-source, standards-based software for dicom mr spectroscopy workflows.
- [256] James Friend and Leslie Yeo. Fabrication of microfluidic devices using polydimethylsiloxane. *Biomicrofluidics*, 4(2):026502, 2010.
- [257] Sangmoo Jeong, Roozbeh Eskandari, Sun Mi Park, Julio Alvarez, Sui Seng Tee, Ralph Weissleder, Michael G Kharas, Hakho Lee, and Kayvan R Keshari. Real-time quantitative analysis of metabolic flux in live cells using a hyperpolarized micromagnetic resonance spectrometer. *Science Advances*, 3(6):e1700341, 2017.
- [258] Victoria A Guarino, William M Oldham, Joseph Loscalzo, and Ying-Yi Zhang. Reaction rate of pyruvate and hydrogen peroxide: assessing antioxidant capacity of pyruvate under biological conditions. *Scientific reports*, 9(1):19568, 2019.
- [259] Robert T Mallet, Jeffrey E Squires, Shimona Bhatia, and Jie Sun. Pyruvate restores contractile function and antioxidant defenses of hydrogen peroxide-challenged myocardium. *Journal of molecular and cellular cardiology*, 34(9):1173–1184, 2002.

- [260] Solange Desagher, Jacques Glowinski, and Joël Prémont. Pyruvate protects neurons against hydrogen peroxide-induced toxicity. *Journal of Neuroscience*, 17(23):9060–9067, 1997.
- [261] Michael E Lacey, Raju Subramanian, Dean L Olson, Andrew G Webb, and Jonathan V Sweedler. High-resolution nmr spectroscopy of sample volumes from 1 nl to 10 μ l. *Chemical reviews*, 99(10):3133–3152, 1999.
- [262] Dean L Olson, Timothy L Peck, Andrew G Webb, Richard L Magin, and Jonathan V Sweedler. High-resolution microcoil 1h-nmr for mass-limited, nanoliter-volume samples. *Science*, 270(5244):1967–1970, 1995.
- [263] Miguel Mompeán, Rosa M Sánchez-Donoso, Antonio De La Hoz, Vittorio Saggiomo, Aldrik H Velders, and M Victoria Gomez. Pushing nuclear magnetic resonance sensitivity limits with microfluidics and photo-chemically induced dynamic nuclear polarization. *Nature communications*, 9(1):108, 2018.
- [264] Wusheng Xiao, Rui-Sheng Wang, Diane E Handy, and Joseph Loscalzo. Nad (h) and nadp (h) redox couples and cellular energy metabolism. *Antioxidants & redox signaling*, 28(3):251–272, 2018.
- [265] Yi Rao, Seth Gammon, Niki M Zacharias, Tracy Liu, Travis Salzillo, Yuanxin Xi, Jing Wang, Pratip Bhattacharya, and David Piwnica-Worms. Hyperpolarized [1-13c] pyruvate-to-[1-13c] lactate conversion is rate-limited by monocarboxylate transporter-1 in the plasma membrane. *Proceedings of the National Academy of Sciences*, 117(36):22378–22389, 2020.